ROMA TRE
UNIVERSITÀ DEGLI STUDI

Fisica

CORSO DI DOTTORATO DI RICERCA IN

XXXIII

CICLO DEL CORSO DI DOTTORATO

Multicomponent superconductivity at the unconventional Lifshitz transition in a three-dimensional heterostructure with tunable Rashba spin-orbit coupling

Titolo della tesi

M. Vittoria Mazziotti

Nome e Cognome del dottorando — firma

Roberto Raimondi

Docente Guida/Tutor: Prof. — firma

Giuseppe Degrassi

Coordinatore: Prof. — firma

"Science is a field which grows continuously with ever expanding frontiers. Further, it is truly international in scope. Any particular advance has been preceded by the contributions of those from many lands who have set firm foundations for further developments. The Nobel awards should be regarded as giving recognition to this general scientific progress as well as to the individuals involved. Further, science is a collaborative effort. The combined results of several people working together is often much more effective than could be that of an individual scientist working alone".

J. Bardeen

Contents

Abstract

In this thesis we consider a three-dimensional (3D) superlattice of metallic layers of thickness L separated by a spacer of width W and periodicity d. The presence of a confinement potential along the direction orthogonal to the layers is reflected in an electronic multiband structure which, as known, leads to multigap superconductivity and modulation of the critical temperature. Parallelly, interfacing different materials in the direction of confinement breaks the spatial inversion symmetry allowing a Rashba spin-orbit coupling (RSOC). The electrons in-plane are, thus, subjected to an effective magnetic field which orients the spin in a direction orthogonal to the momentum. This is reflected in a spin-splitting of the subbands that characterize the superlattice.

The main purpose of this thesis is to study the combined effect of multigaps superconductivity and RSOC and to see how, by appropriately varying the intensity of the Rashba coupling, the structural characteristics of the system and the parameters that define the superconducting phase, it is possible to obtain an amplification of the critical temperature.

As we will see, the interplay of the RSOC and superlattice structure leads to an extended van Hove singularity in the density of states (DOS) at the Brillouin zone edge with an unconventional Lifshitz transition for one of the two helicity states of the spin-orbit split electron spectrum. This is reflected in an amplification of the gaps and critical temperature where the DOS shows a maximum. The evaluation of the superconducting gap and the critical temperature is done by including in the Bogoliubov-de Gennes equation the quantum configuration interaction between the gaps. This is taken into account by considering an electron-phonon interaction dependent both on the band indices and on the wavevectors along the confinement direction. Therefore, unlike the Bardeen–Cooper–Schrieffer (BCS) theory, the superconducting coupling is not constant but has a matrix structure. The possibility to suitably vary each term of this matrix allows to study the effect on the superconducting phase of the coexistence of different condensates in different coupling regimes.

It is found that the presence of the RSOC amplifies both the gap and the critical temperature when the Fermi energy crosses the band edge of the higher energy subband. However, there is a limit to the variation of the Rashba coupling constant, as we will see, this quantity is inversely proportional to superlattice modulation parameter: increasing the first is equivalent to decreasing the second, this reduces the separation between adjacent subbands and generates overlapping and interference effects.

Having fixed a maximum coupling constant and, therefore, a minimum periodicity, we see how by suitably varying the thickness of the layers it is possible to increase both the electron-phonon coupling constant and the cut-off energy. This allows to reconstruct the *superconducting dome* typical of materials at high critical temperatures and to obtain critical temperatures close to room temperature.

Our results suggest, on the one hand, a method to effectively vary the effect of the RSOC via the tuning of the superlattice modulation parameter, on the other hand, they provide precise indications on the values of the parameters involved in view of possible practical realizations in a way potentially relevant for spintronics functionalities in several existing experimental platforms and materials.

1

Introduction

Several works [1–14] have shown that the critical temperature (T_C) of multigap superconductivity in 3D heterostructures at atomic limit, made of a superlattice of atomic layers with an electronic spectrum characterized by several quantum subbands, can be amplified by a shape-resonance driven by the contact exchange interaction between different gaps. The T_C amplification is achieved tuning the Fermi level near the singular nodal point [15,16] at a Lifshitz transition for opening a neck. Recently, high interest has been addressed to the breaking of inversion symmetry which leads to spin-splitting with a null magnetic field, the Rashba spin-orbit coupling (RSOC), also in 3D layered metals [17–19]. However the physics of multigap superconductivity near unconventional Lifshitz transitions in 3D heterostructures with RSOC, being in a non-BCS regime, is not known. In this thesis we obtain the superconducting gaps by the Bogoliubov-de Gennes theory and the 3D electron wavefunctions by solving the Schrödinger equation. This shows the feasibility of tuning multigap superconductivity by suitably matching the spin-orbit length with the 3D superlattice period. It is found that the presence of the RSOC amplifies both the k-dependent anisotropic gap function and the critical temperature when the Fermi energy is tuned near an electronic Lifshitz transition [20–22].

1.1 From the BCS theory to the multigap superconductivity with RSOC

The superconductivity is one of the most fascinating phenomena in solid state physics and has important conceptual and technological implications: from super-fast computers to new memory devices, from levitation trains to new medical imaging applications and many other possibilities. The key feature of the superconducting materials is to exhibit zero electrical resistance and perfect diamagnetism below a characteristic temperature, referred to as critical temperature and conventionally indicated with T_C (Fig. 1.1) [23,24].

Since the discovery of superconductivity in 1911 [23], numerous studies have been carried out in this field [1–14,21,22,24–49,49–91]. The purpose was both to find a theoretical model for the microscopic description of the phenomenon, and to search new materials with room critical temperature and ambient pressure superconductivity

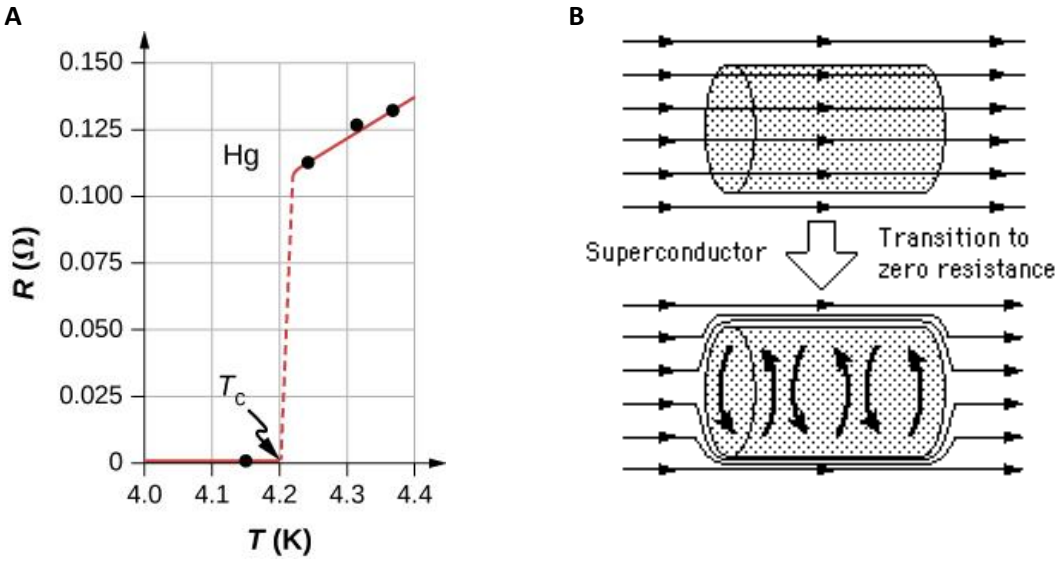

Figure 1.1: *Two requirements for superconductivity*: (**A**) vanishing of electrical resistivity below a critical temperature T_C, discovered in mercury by Kemerlingh Onnes et al. in 1911 [23]; and (**B**) expulsion of magnetic flux below a critical field H_C, discovered by Meissner and Ochsenfeld in 1933 [24].

in order to make the experimental results more easily reproducible, especially in view of practical applications.

In 1950 V. Ginzburg and L. Landau [26] developed a first phenomenological theory of superconductivity, based on the Landau theory of second-order phase transitions. The two scientists managed to formulate a series of equations that described the phenomenon, although, it was not possible to explain at a microscopic level why this would occur.

The first microscopic theory of superconductivity was proposed in 1957 by J. Bardeen, L. Cooper and R. Schrieffer (BCS theory) [27]. The BCS theory captures the essential physics which gives rise to the condensation of the Cooper pairs into a coherent superconducting macroscopic state. Specifically, it deals with homogeneous and single-band three-dimensional systems, the so called conventional superconductors, and it is essentially a self-consistent, mean-field treatment. In the original formulation, the attractive interaction between opposite spin electrons is a time-retarded interaction mediated by phonons. A passing electron, whose average velocity, given by the Fermi velocity, is much larger than the propagation speed of the phonons, polarizes the local ions of the lattice: before the lattice can relax, a second electron arrives and feels the attraction from the still-polarized positive ions. This attraction produces a pairing of electrons. The two electrons form a Cooper pair whose size is denoted by the superconducting coherence length ξ_0 (Fig. 1.2). In conventional superconductors the pair size is so large that a huge number of pairs is contained on the average within that distance. The large number of overlapping pairs permits to deal with the mutual effects of the pairs *on the average* by introducing an appropriate version of the so-called mean-field theory for phase transitions. The electron-phonon interaction leads to an effective electron-electron attraction in a narrow region around the Fermi wavevector, k_F, this attraction is of the order of the characteristic average phononic frequency of the lattice. The

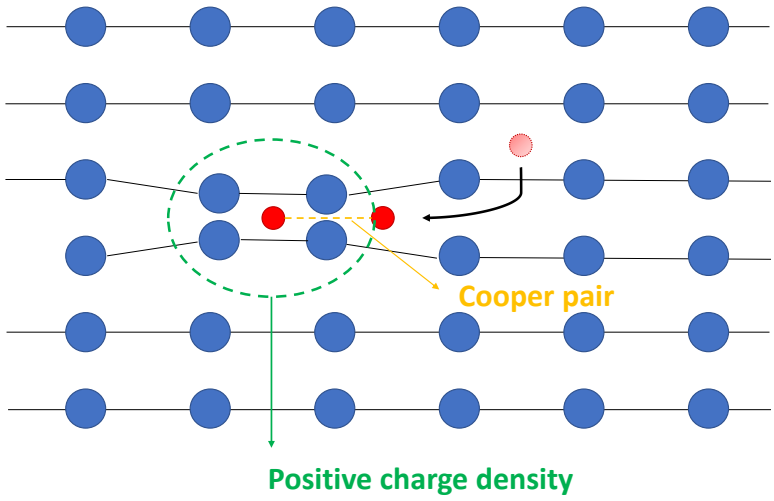

Figure 1.2: *The formation of Cooper pairs.* A conduction electron (red circle), passing through the lattice, perturbs some positive ions (blue circles) with respect to their equilibrium position, attracting them slightly towards it and forcing them to come closer. This creates a region of higher positive charge density. Local perturbation of charges in the lattice produces a weak short-range attractive potential capable of capturing a second electron. This causes an effective attraction between the two electrons leading to the formation of Cooper pairs. Pairs can flow faster in the lattice than unbound electrons.

Cooper pairs are, namely, strongly delocalized and interconnected in a weak coupling configuration which is reflected in the appearance of an energy gap, Δ, in the spectrum of the electronic excitations in correspondence with the Fermi wave vectors, $\pm k_F$ (Fig. 1.3).

The standard BCS theory relies an many approximations about the metallic phase: *i*) a simple homogeneous lattice; *ii*) a single electronic band; *iii*) a single value of the density of states at the Fermi level ($N(E_F)$), and *iv*) a constant electron-phonon coupling constant (g). The basic assumption is the *Migdal approximation* [28]: the phonon is supposed to have an energy, ω_0, very small, while the electron density is very high and the Fermi energy, E_F, is considered the highest energy scale, hence $\omega_0/E_F \ll 1$.

Several corrections, additions and clarifications have been introduced in the frame of the standard BCS theory [29–31, 35], but it has been accepted that the superconducting critical temperature cannot be larger than 23 K. In fact, in the single band approximation, T_C increases with both the phonon energy and the coupling strength, but for extreme strong electron-phonon coupling the electron liquid, at low temperature, prefers to order in the real space, forming electronic crystals which compete with the superconducting phase. Moreover if the superconductivity survives upon increasing the electron-phonon coupling, the critical temperature decreases since the phonon energy is pushed toward zero. In this regime the lattice structure collapses.

In 1986 G. Bednorz and K. A. Muller discovered that the $LaBaCuO$, a lanthanum, barium and copper oxide, becomes superconducting about 35 K, above the limit predicted by the BCS theory. Given the relevance of the discovery, the two physicists received the Nobel Prize for Physics in 1987.

In February 1987, a perovskite ceramic was identified capable of superconducting

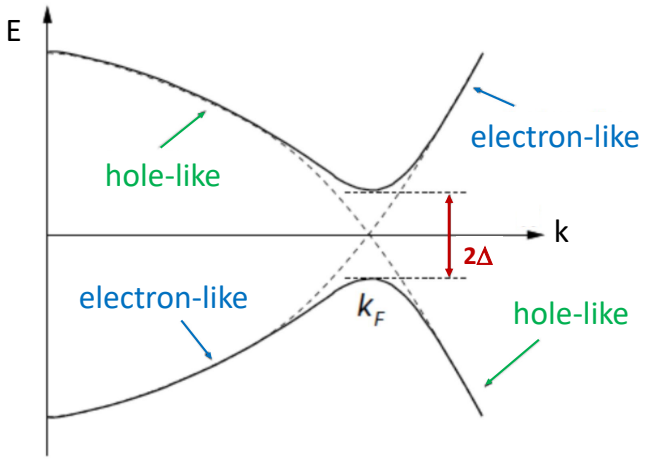

Figure 1.3: *The energy spectrum of a conventional superconductor.* The dashed lines represent the spectrum of the normal state, while the continuous curves represent the quasi-particle spectrum. Δ is the superconducting order parameter.

at 90 K (chemical formula $YBa_2Cu_3O_7$). This discovery was very important because it showed that liquid nitrogen could be used as the refrigerant. Given the temperatures involved, these materials began to be referred to as High Critical Temperature Superconductors (HT_CS). In the following years other materials were discovered with increasingly higher critical temperature (Fig. 1.4).

The HT_CS belong to the group of strongly correlated compounds. In these systems, complex repulsive electron interactions and a large number of degrees of freedom lead to a rich variety of states of matter. Exotic phases like the pseudogap, charge-, spin-, and pair-density waves, but also the remarkable phenomenon of superconductivity emerge, depending on the doping level and on the temperature.

The largest group of HT_CS are the cuprates, which are compounds in which the charge carriers are localized in copper oxide layers. Superconductivity in cuprates only emerges within a specific doping range. Undoped compounds are Mott-insulators, which indicates the existence of strong electronic correlations in these systems. The doping parameter is generally the amount of free charge carriers, but other factors, like pressure, can influence the doping level as well. The typical pair correlation length in these HT_CS is much smaller than in conventional superconductors. This indicates a different regime of pairing, locating the HT_CS in an intermediate regime between overlapping Cooper pairs in the BCS weak coupling regime and more localized pairs with bosonic character in the Bose-Einstein Condensation (BEC) strong coupling regime. Since there is no obvious symmetry breaking in continuously varying the distance between the fermions of the pairs, we expect to find a continuous transition between the two regimes, or a crossover.

The fundamental properties of superconductivity may be explained without introducing any unnecessary approximation using the general theory of superconductivity based on the self-consistent theory developed by Bogoliubov-de Gennes [35] and subsequently extended by Gor'kov [2], Josephson [3], Kondo [4], Blatt [5], Leggett [6] and others [7, 8]. This theory provides the spectrum of the excited quasiparticles and assumes that the transition from the normal phase to the superconductive phase is a real phase transition in which the electromagnetic gauge invariance is spontaneously

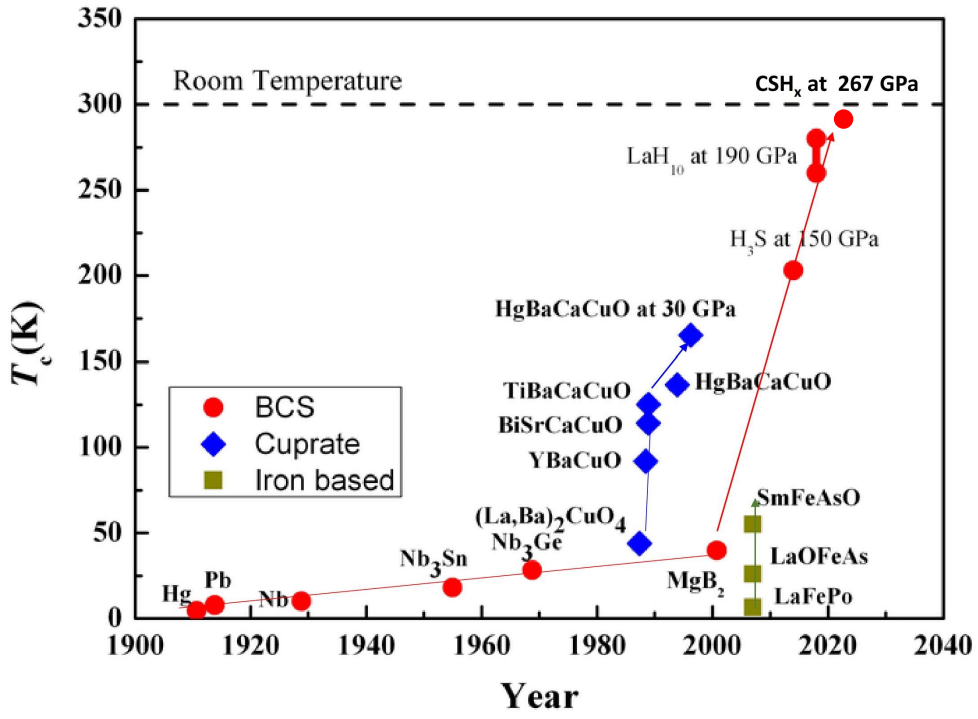

Figure 1.4: *The time evolution of the T_C of superconductors.* The superconductivity at $T_C = 203\ K$ is observed in the sulphur hydride system H_3S under a pressure of 155 GPa [32]. Significant drops in resistivity on cooling up to 260 K and $[180 - 200]\ GPa$ are observed recently in lanthanum superhydride LaH_{10} [33]. Room-temperature superconductivity with $T_C = 287.7\ K$ at $P = 267\ GPa$ was reported in October 2020 in a carbonaceous sulphur hydride CSH_x [34].

broken [36]. The general theory of superconductivity allows the description of superconductors with complex anisotropic or granular structure in the momentum space and in the real space [9]. The weak coupling limit of this theory reproduces the standard BCS superconductivity or the Ginzburg Landau regime, while the strong coupling limit gives the Bose-Einstein condensation.

In 2001 magnesium diboride MgB_2 was found to be superconducting at a temperature $T_C = 39\ K$. This discovery has been of great interest for its high critical temperature, but mostly because it marked the formal and definitive appearance of a new class of superconductors: multiband/multigap ones, to which many of discovered iron-based superconductors also belong [77].

Multiband and multigap superconductivity is emerging as a complex quantum coherent phenomenon with physical properties which are different or cannot be found in single-band conventional superconductors. In multiband and multigap systems the total superconducting condensate results from the coherent mixture of partial condensates forming in each band. Each partial condensate can have different properties with respect to the others, leading to interesting interference and resonance effects. The fundamental interaction in the general theory [5,6], missing in the standard BCS scenario, is the exchange terms due to configuration interaction between multiple condensate. It was based on experimental results showing that multiple electronic components coexist in cuprates at optimum doping level [10–13,13,14]. A first component is a Migdal condensate ($\omega_0/E_F \ll 1$) in the BCS limit and a second component is a strong interacting electronic liquid, where the Migdal approximation is violated, $\omega_0/E_F \sim 1$. The high temperature superconductivity was assigned to the role of the shape-resonance which is due to the exchange term between electrons in two different regime [67].

In 1996-1998 a theory for HT_CS in cuprates was developed by Bianconi, Perali and Valletta (the BPV theory) [62–66], in the frame of the general theory of superconductivity for multicomponents electronic systems. The variation of the critical temperature with doping is predicted considering Lifshitz transitions [64] for a new appearing Fermi arc driven by doping and misfit strain. While some Fermi arcs host BCS-like condensates, the new Fermi arc, appearing at the Lifshitz transition, hosts a condensate in the BEC or in the BCS-BEC crossover regime. The wavefunctions of electrons at the Fermi level are obtained by solving the Schrödinger equation in an artificial lattice superstructure. The exchange contact interaction, due to configuration interaction between pairs in different Fermi arcs, is evaluated numerically by the overlap of the pair wavefunctions without approximations. The exchange contact interaction increases the critical temperature giving high temperature superconductivity, with $k_BT_C/E_F \sim 0.2$, which was experimentally identified [67,68] and fully explained by the theory [69–71].

In 2015 Drozdov et al. [32] showed that the sulphur hydride compound H_3S reaches a maximum critical temperature of 203 K at a pressure of 155 GPa. This experimental discovery seems to agree with Ashcroft [49], Li et al. [50] and Duan et al. [51]. In particular Ashcroft pointed out that the high vibrational frequency of hydrogen atoms, linked to the small mass, provides a strong electron-phonon interaction. Subsequent studies [52] showed that hydrogen can become a HT_CS, $T_C = [100 - 240]\ K$, in the molecular state and will reach $T_C = [300 - 350]\ K$ in the atomic phase at pressures of 500 GPa. The work of Li et al. [50] has, in fact, estimated a critical temperature of about 80 K in high pressure sulphur hydride system. These compounds, such as hydrogen, have a high Debye temperature, but lower pressures are required to metallize them.

The latest research [32,48–52] has shown that hydrogen dominant materials apper to

be excellent candidates for the high critical temperature superconductivity. Therefore the materials research for room-temperature superconductivity was not driven simply by looking for a high phonon energy and a high coupling strength in the Cooper pairing. The theoretical predictions of high T_C in solid metallic hydrogen and hydrides at high pressure [53–55] were based on the search of materials characterized by high frequency phonons mediating the pairing and by a negative dielectric constant controlling the electron-electron interaction and the Coulomb energy [49,53–60].

The discovery of a room-temperature in a pressurized ternary hydride CSH_x metal with the critical temperature at 15 degree *Celsius* has been reported recently [34] and seems to be moving in this direction. As we will show below, the BPV theory is able to provide a theoretical explanation for the recent results of critical room-temperature superconductors, provides a numerical model capable of providing experimentally verifiable predictions and gives indications on the realization of new materials at high critical temperatures.

A central and new aspect of the work presented in this thesis will be to extend the concepts of the theory of multigap superconductivity in the presence of a spin-orbit Rashba coupling.

Usually, the spin-orbit coupling (SOC) is classified as extrinsic or intrinsic mechanism, depending on the origin of the electrical potential. The intrinsic SOC arises due to the crystalline potential of the host material or due to the confinement potential associated with the device structure. On the other hand, the extrinsic SOC is due to the atomic potential of random impurities, which determine the transport properties of a given material. The majority of the studies has focused on the Rashba spin-orbit coupling (RSOC) for electrons moving in the xy-plane, which was originally introduced by Rashba [92] to study the properties of the energy spectrum of non-centrosymmetric crystals of the CdS type and later successfully applied to the interpretation of the two-fold spin splitting of electrons and holes in asymmetric semiconducting heterostructures [93,94]. RSOC is classified as being due to the structure inversion asymmetry (SIA), which is responsible for the confinement of electrons in the xy-plane. In addition, one may also consider the SOC arising from the bulk inversion asymmetry (BIA), which is usually referred to as Dresselhaus SOC (DSOC) [95]. Both RSOC and DSOC modify the energy spectrum by introducing a momentum-dependent spin-splitting [96]. This can also be understood quite generally on the basis of symmetry considerations. In a solid, the spin degeneracy for a couple of states with opposite spin direction, comes from both time reversal invariance and space inversion invariance (parity). By breaking the parity, as for instance, in a confined two-dimensional electronic gas (2DEG), the spin degeneracy is lifted and the Hamiltonian requires an effective momentum-dependent magnetic field, which is the SOC. As a result, electron states can be classified with their helicity in the sense that their spin state depends on their wave vector.

An essential aspect that makes RSCO particularly attractive for spintronics and quantum computation [92–95,97–108] is its ability to be controlled by an external gate voltage placed on top of the 2DEG. Indeed, since the strength of the Rashba parameter is directly related to the interfacial potential drop, applying a gate voltage modifies the electron occupation, which in turn controls the magnitude of the RSOC, as experimentally demonstrated in InGaAs/InAlAs heterostructures [107,109]. The electric control of spin states is higher to the magnetic field control due to a better scalability, lower power consumption and the possibility for local manipulation of the spin states.

The spin-orbit interaction plays, moreover, a central role as a design element of topological states of matter, both recently discovered and proposed [109–129]. In partic-

ular, the topological insulator and topological superconductor states, both remarkable for their edge states, which are characterized by helical spin textures and Majorana fermions [110,130,131].

Over the past thirty years, ideas based on the work of Rashba [93] have been leading to a vast number of predictions, discoveries, and innovative concepts far beyond semiconductors. The past decade has been particularly creative with the realizations of means to manipulate spin orientation by moving electrons in space, controlling electron trajectories using spin as a steering wheel, and with the discovery of new topological classes of materials. These developments reinvigorated the interest of physicists and materials scientists in the development of inversion asymmetric structures ranging from layered graphene-like materials to cold atoms.

Given the important implications highlighted above, the aim of the thesis project has been the study of the RSOC in non-centrosymmetric superconductors starting from the following pioneering works in the field [94,95,128,129,132–135]. In non-centrosymmetric superconductors, where the crystal structure lacks a centre of inversion, parity is no longer a good quantum number and an electronic antisymmetric spin-orbit coupling (ASOC) is allowed to exist by symmetry. If this ASOC is sufficiently large, it has profound consequences on the superconducting state. For example, it generally leads to a superconducting pairing state which is a mixture of spin-singlet and spin-triplet components. The possibility of such novel pairing states, as well as the potential for observing a variety of unusual behaviours, led to intensive theoretical and experimental investigations. Here the focus is on evaluating the effect of ASOC on the superconducting properties.

As pointed above, it is known that the SIA, which stems from the inversion asymmetry of the confining potential in a 2DEG, induces a spin-orbit band splitting with states of different helicity [17,18,93,136–141] without the need for magnetic field. Giant spin-orbit induced spin splitting in the range $[150-450]\ meV$ have been found in metal alloys [142] and transition-metal dichalcogenides [143]. A three dimensional Rashba spin splitting has been observed in $PtBi_2$, $BiTeX$ ($X = Br$, Cl, or I) and $GeTe$ which show dispersion along the out-of-plane direction [144–146].

The realization of the three-dimensional Rashba-like spin splitting [19] in quantum materials and heterostructures potentially unfolds numerous promising applications. Following the first theoretical study of superconductivity [133] with spin-orbit band splitting in a 2D metallic layer or at the surface of doped WO_x oxides, several theoretical works have studied the emergence of superconductivity in the presence of spin-orbit coupling in a 2D metallic layer [147–153].

Recently, experimental evidence that the strength of spin-orbit interaction is correlated with quasi 2D superconductivity in the (111) $LaAlO_3/\ SrTiO_3$ interface has been reported [154] and confirmed in several systems [155–158]. The spin polarized energy bands near a topological Lifshitz transition can be detected experimentally by ARPES spectroscopy as it has been observed in complex oxide heterostructure interface [159] and in layered cuprate perovskite superconductors [160]. Today there is a high interest in the physics of quantum complex materials aimed at the realization of mesoscopic quantum heterostructures for novel superconductor Josephson junctions [161,162].

The theoretical studies of superconductivity coexisting with spin-orbit coupling have been limited to a 2D superconducting layer and to a single band metal [133,147–153], while it is not known how superconductivity will arise in a 3D Rashba system [1]. More-

[1] In the work [17] have studied the spectral and the transport properties of a quantum well in the presence of RSOC. The Hamiltonian they introduced is in some respects similar to the one proposed in

over, previous theoretical investigations have considered single-gap superconductors while, in multiband 3D superconductors, multigap superconductivity need to be considered in the presence of band spin splitting due to spin-orbit coupling.

In fact, in multigap superconductivity, it is no longer possible to neglect the key role of quantum configuration interaction between superconducting gaps as, for example, the BEC-BCS crossover gap at Lifshitz transitions near a band edge and other gaps in the BCS limit far from band edges [64, 81, 163–169]. Finally, all theoretical approaches have been developed in the BCS regime where the Fermi energy is much higher of both the spin-orbit energy band splitting and the energy gap, while the most interesting physics occurs in the regime where the Fermi energy is in the same energy range as the superconducting energy gaps and the spin-orbit-splitting.

The main results of this thesis is the theoretical description of multigap superconductivity [64, 81, 163–170, 170] at the unconventional Lifshitz transition [22] in a 3D heterostructure at the atomic limit with a periodicity of few nanometers with tunable spin-orbit strength. Our aim is to show that the interplay between the Rashba spin-orbit coupling and superlattice structure allows for a fine tuning of the critical temperature.

1.2 Outline

In this thesis, we will expand the numerical study proposed by A. Bianconi et al. in 1993 in the context of the BPV theory of HT_CS near a Lifshitz transition, to the case where there is a RSOC [170–174]. To this end, we will study the properties of the normal phase and the superconducting phase of a three-dimensional superlattice of quantum layers with RSOC.

The layout of the thesis is the following:

- The *second Chapter* is an introduction to the spin-orbit Rashba interaction.

  Firstly, we explain how effective spin-orbit Hamiltonians terms arise in solid state systems. At the end we pay some attention to two-dimensional systems which play an important role in spintronics. Starting from the work of L. P. Gor'kov and E. I. Rashba [133], in which the superconductivity theory for two-dimensional metals without inversion symmetry has been developed, we study the effect of the RSOC in the presence of a superconducting order in a two-dimensional system when the the twofold spin degeneracy is lifted by RSOC and singlet and triplet pairings are mixed in the wavefunction of the Cooper pairs.

- In the *third Chapter* we analyse the concepts and theoretical methods used in this thesis to explain and derive the properties of the normal and the superconducting phase in confined systems, both from an analytical and numerical point of view. The Bogoliubov-de Gennes equation is generalized to systems for which quantum size effects are not negligible. In particular, we study the BPV theory, proposed in the context of HT_CS near a Lifshitz transition in a multiband/multigap system in

this thesis, the differences consist in the fact that they have considered a reference system (x, z, y) rather than (x, y, z) (we will see the implications of this choice in *Appendix D*) and a single-hole potential rather than a periodic one, moreover the properties of the superconducting phase are not investigated. Same thing goes for the work of V. Brosco et al. [19] although they introduce a RSOC coupling in a 3D system, such a system is characterized by a Rashba coupling in the xy-plane and the electrons along the z direction are supposed to be free. They also limit their study to dc conductivity in the presence of static disorder (in *Appendix E* we will see how DOS and FS are obtained in this model) without analysing the superconducting phase.

which the shape-resonance idea is centred on the coexistence of at least one large Fermi surface and at least one small Fermi surface appearing or disappearing upon small changes in the chemical potential. The shape-resonance in superconducting gaps [171,175] is a type of Fano–Feshbach resonance between pairing channels at a Bose-Einstein to Bardeen-Cooper-Schrieffer crossover in multiband superconductors, appearing when the chemical potential is tuned to the proximity of a band edge. Here the Lifshitz transition occurs because of the variation of the Fermi surface topology as a function of the chemical potential. By changing the chemical potential, the critical temperature decreases towards 0 K when the chemical potential is tuned to the band edge, because of the Fano-antiresonance, and the T_C maximum appears (as in Fano-resonances) at higher energy, between one and two times the pairing interaction above the band edge [170–173].

- In the *fourth Chapter* we analyse the recently observed room-temperature superconductivity in two hydrogen-dominant compounds: H_3S and CSH_x. Underlining how the BPV theory, in the two-dimensional formulation, is able to explain the observed experimental results and predict the realization of new high T_C materials.

- The innovative idea of this work is to study the model described in the *third Chapter* in the presence of a spin-orbit Rashba coupling. In the *fifth Chapter* we describe the analytical and numerical results for the normal phase, while in the *sixth Chapter* we report the theoretical treatment developed to describe and subsequently implement the calculation of the quantities of interest in the superconducting phase. In this first phase we are interested in the calculation of the gap, then we also derive the expression of the critical temperature.

- In the *seventh Chapter* we see what happens in the superconducting properties of a quantum layered heterostructure as the superconducting coupling and, therefore, the cut-off energy vary. For the first time we rebuild the superconducting *dome* of a three-dimensional superconductor in the presence of a coupling RSOC.

- In the *eighth chapter* we see, instead, that it is possible to reach critical temperatures of the order of those observed in hydrogen dominated compounds even in a weak coupling regime as long as a Rashba spin-orbit coupling is considered and the geometry of the heterostructure is suitably varied. This gives important indications also in view of possible experimental realizations.

- Finally in *ninth Chapter* we list the salient results that this thesis work has allowed to obtain.

1.3 Main results: a brief overview

In this thesis we study a 3D superlattice of weakly interacting quantum layers in the presence of a RSOC coupling and a pairing interaction. The heterostructure is made of nanoscale superconducting layers, of thickness L, intercalated by insulating spacers, of amplitude W. The heterostucture can be described as superlattice of quantum wells with periodicity $d = L + W$. The system can be described by the following Hamiltonian

$$H = \tilde{H}_R + H_I, \tag{1.1}$$

where $\tilde{H}_R$ is the single-particle contribution, which includes both a periodic potential along z, $V_z = -V[\theta(z-d) - \theta(z-L)]$, and a RSOC coupling

$$\tilde{H}_R = H_{KP} + H_{RSOC} = \frac{p_z^2}{2m_z} + V(z) + \frac{\mathbf{p}_\parallel{}^2}{2m} - i\alpha(\sigma_x\partial_y - \sigma_y\partial_x), \tag{1.2}$$

where $\mathbf{p} = -i\hbar\nabla$ is the usual momentum operator, $\mathbf{p}_\parallel$ its projection in the xy-plane and α is the RSOC constant linked to the periodicity of the lattice by a relationship of the type

$$\alpha = 2\frac{\hbar^2}{2m}\frac{2\pi}{d}\alpha_{SO}, \tag{1.3}$$

α_{SO} is a dimensionless parameter which describes the strength of the Rashba momentum in units of the superlattice modulation parameter, d.

For the second contribution to the Hamiltonian in Eq.(1.1), we adopt the standard contact interaction with a cut-off energy $\hbar\omega_0$

$$H_I = \frac{U_0}{2}\int \mathrm{d}\mathbf{r}\ \Psi_\alpha^\dagger(\mathbf{r})\Psi_\beta^\dagger(\mathbf{r})\Psi_\beta(\mathbf{r})\Psi_\alpha(\mathbf{r}), \tag{1.4}$$

where $\Psi_\alpha(\mathbf{r})$ is the annihilation fermion field operator and summation over the repeated spin indices (α, β) is understood.

In *Chapter 2* we study the Rashba Hamiltonian, $H_{RSOC} + H_I$, and we derive the dispersion relation for the electrons in the xy-plane

$$\varepsilon_\lambda(p_\parallel) = \frac{p_\parallel^2}{2m} + \lambda\alpha p_\parallel, \tag{1.5}$$

where $\lambda = \pm 1$ is the helicity index.

The effect of RSOC is to remove the spin degeneracy, which this is reflected in a doubling of the spectrum into two bands of opposite helicity (see Fig. 2.2). By adding the electron-phonon interaction, that is H_I, we obtain the equation of the gap and of the critical temperature as a mean-field approximation (see Sec. 2.2).

The pairing potential in addition to allowing the formation of pairs only between electrons with the same helicity is a mixture of singlet and triplet components. It is therefore reasonable to expect an unconventional superconductivity.

In *Chapter 3* we study only the contribution to the Hamiltonian of the confinement potential, $H_{KP}+H_I$. The electrons in motion in the xy-plane of the layers are free, while in the z-direction they are affected by a periodic potential of the Kronig-Penney form. The geometry of the system is such that the quantum size effects are not negligible and are reflected in a multiband electronic structure. In fact the dispersion relation obtained has the following form

$$\varepsilon_n(\mathbf{p}) = E(p_x, p_y) + E_n(p_z),$$

where $E(p_x, p_y)$ is the dispersion of free electron along the plane of the layers and $E_n(p_z)$ is the dispersion along z that we calculate numerically.

The multiband structure means that the self-consistency equation for the gap (Sec. 3.2) has a BCS-like form in which, however, the electron-phonon coupling is no longer constant, but is a matrix that depends on the band indices and the wavevectors along the direction of the confinement. This allows to have a multicondensate system in different BCS-BEC coupling regimes.

In *Chapter 4* we see how the multicomponent structure is reflected in the properties of the normal and superconducting phase of a simpler system of quantum wires.

We show that the highest energy subband, in our case the third, has a two-dimensional dispersion, indeed, in addition to having a parabolic dispersion along x, it has a dispersion along z. This is reflected in the DOS trend which shows a widening between the band edge energy and the top of the third subband (Fig. 4.4). When the chemical potential reaches the top of the third subband there is a van Hove singularity that justifies the DOS peak. The evolution of the topology of the Fermi surface shows that, between the band edge and the van Hove singularity, the system undergoes two different Lifshitz transitions [20–22]. The first Lifshitz transition is of the first type in which a new 2D Fermi surface appears and a second Lifshitz transition in which the system crosses from a 2D geometry to a 1D one, this happens in correspondence with the van Hove singularity.

The unusual properties in the normal phase are reflected in the superconducting phase, the critical temperature shows, indeed, an asymmetrical trend that can be modelled with an antiresonance of the Fano-Fashbach type (Fig. 4.6). When the chemical potential reaches the Lifshitz transition of the first type, a new Fermi surface (FS) appears and the coexistence of condensates in a BCS-like regime and a condensate in a BEC-like regime becomes possible. In this case, the system is in an antiresonance regime and the critical temperature reaches a minimum. When the chemical potential is at the van Hove singularity, different BCS-like condensates coexist with a condensate in an intermediate BEC-BCS regime. The system is in a resonant regime where the critical temperature reaches the maximum. For large values of the chemical potential the system tends to a multicondensate system in the BCS-like regime, the critical temperature is indeed very small.

The model introduced allows to reproduce the critical temperature values recently observed in two hydrogen-rich compounds, H_3S to CSH_x, and to obtain the *superconducting dome*. A characteristic of high critical temperature superconductors is that of having a critical temperature value that is not univocal, but depends on the charge density and pressure. In accordance with the works [168, 176–178] we have described the variation of pressure with the simultaneous variation of the energy separation of the chemical potential from the Lifshitz transitions and of the electron-phonon interaction.

Finally, we solve the complete Hamiltonian (see equation (1.1)) for a two-bands system. In particular, in *Chapter 5* we study the normal phase, while in *Chapter 6* we investigate the properties of the superconducting phase, both from a theoretical and numerical point of view.

In the Fig. 1.5 we report the trend of the partial DOS for $\lambda = \pm 1$ for the second subband as a function of the energy. In the case of positive helicity the DOS shows the expected step trend for a generic 3D system in the absence of RSOC, while in the case of negative helicity the DOS shows a peak at a precise energy value. We show that the presence of this peak is related to an unusual variation in the topology of the FS. The *top panel* of Fig. 1.5 shows that when the chemical potential reaches the band edge, a 3D Fermi surface begins to form, the system is therefore in a Lifshitz transition of the first type. When the chemical potential reaches the top of the second subband we have a 3D-2D variation of the FS topology and finally for large values of the chemical potential the FS becomes 2D. At the second Lifshitz transition (3D-2D) we see an unusual van Hove singularity, we no longer have a single singular point, but a curve of singular points (dashed green curve). In *Chapter 5* we explain how this justifies the pronounced peak in DOS, we show that as the RSOC increases the peak shifts by an amount equal to the Rashba energy shift ($E_0 = -m\alpha^2/2$) and the radius of the circumference of singular points increases.

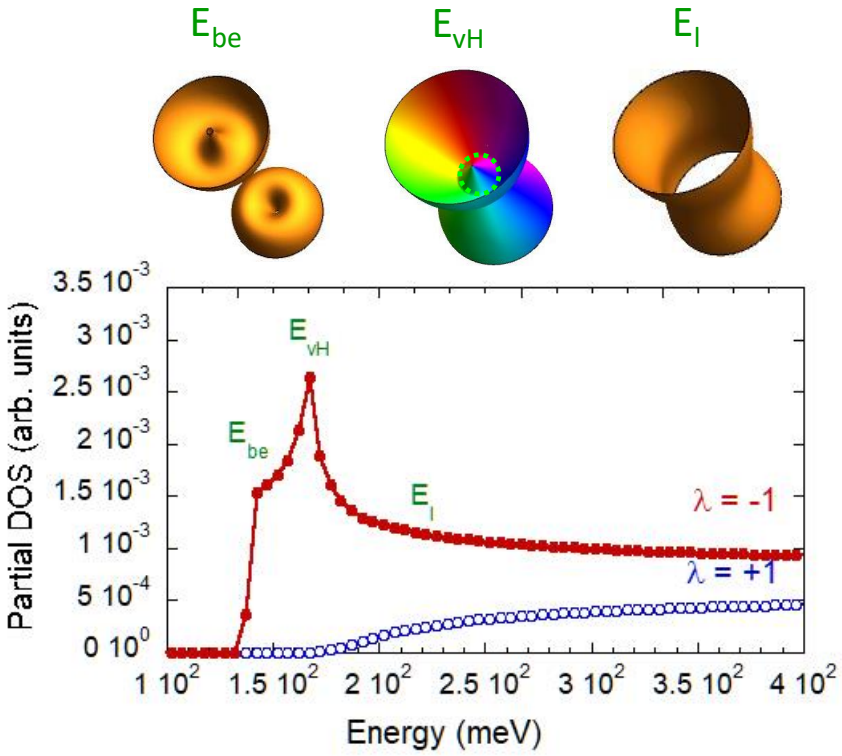

Figure 1.5: *Partial DOS and evolution of the Fermi surface.* In the *bottom panel* we plot the DOS for $\lambda = \pm 1$ for the second subband. The partial DOS relative to $\lambda = 1$ has the step behaviour expected for a normal 3D system, while the partial DOS relative to $\lambda = -1$ shows a pronounced pick. The unusual pattern of the latter DOS can be explained by observing the evolution of the FS for the three indicated energy values (*top panel*). When the DOS shows a peak we see an unusual van Hove singularity in which the FS develops a line of singular points dashed in green (the central FS).

The unusual properties of the normal phase are reflected in the superconducting phase. The trend of the gap and of the critical temperature have the form of a Fano-Fashbach antiresonance, with a minimum corresponding to the first Lifshitz transition and a maximum corresponding to the second Lifshitz transition (Fig. 6.3 and Fig. 6.4**A**). In this context, the increase of α amplifies the above parameters, while remaining in a weak coupling regime (Fig. 6.4**A** and **B**). Moreover, both the gap ratio $2\Delta/T_C$ and the isotopic coefficient deviate significantly from the values predicted by the BCS theory in an energy range close to the unusual van Hove singularity. With the choice of parameters made in this first phase we see that it is possible to reach critical temperatures of the order of 178 K.

In *Chapters 7* and *8* we see how to appropriately vary the RSOC coupling, the parameters that define the heterostructure and the parameters of the superconducting phase we reach critical temperatures close to room temperature in a BCS-like coupling regime. The most important result is to provide precise values of the parameters involved in order to define an optimal condition for the amplification of the critical temperature. We see that since the Rashba coupling is linked to the periodicity of the lattice (equation 1.3) it is not possible to increase it arbitrarily, but there is a value beyond which there is an overlap of the subbands (Fig. 7.2) which generates interference such as to limit the maximum value attributable to the energy cut-off (Fig. 7.2). In order to overcome this problem we vary the width of the layers and we find that there is a minimum value for this parameter that allows to work with cut-off energies such as to reach critical temperatures of the order of 208 K (Fig. 8.1, Fig. 8.2 and Fig. 8.3). The most surprising thing is that this is achieved in a weak coupling regime (Fig. 8.5).

2

Rashba spin-orbit coupling

In 1984 Yu. A. Bychkov and E. I. Rashba [92] studied the effect of spin-orbit coupling in a two-dimensional electron gas (2DEG). The absence of a centre of spatial inversion symmetry, due to an asymmetry in the confinement potential, removes the spin degeneracy by promoting spin-flipping with a null magnetic field. The most interesting aspect is that this effect can be varied through a transverse electric field. This explains the enormous interest that the works [92,93,179] have had over the past thirty years in inspiring a large number of innovative predictions, discoveries and concepts.

In 2001 Lev P. Gor'kov and E. I. Rashba [133] developed a theory of superconductivity for a 2DEG in the presence of a Rashba coupling, underlining the profound implications that it has on the superconducting state. For example, they showed how the pair wavefunction becomes a mixture of singlet and triplet states. The possibility of these new pairing states opens up an enormous variety of unusual behaviours and motivates the intensive theoretical and experimental research of recent years, summarized in Ref. [132].

The purpose of this thesis is to extend these concepts to an anisotropic 3D heterostructures in the presence of a RSOC coupling. In this system the symmetry breaking by inversion along the direction of the heterostructure generates a spin-orbit coupling. The consequent lifting of the spin degeneracy can lead to an amplification of the density of the states and therefore to unusual effects on the superconducting properties of the system. Before doing this, let us consider the special case of two-dimensional systems and we introduce the Rashba spin-orbit coupling Hamiltonians [180]. After, we discuss some of the consequences that the RSOC interaction has on a two-dimensional (2D) superconducting systems [92–94,109,133].

2.1 Intrinsic spin-orbit coupling in 2D systems: the Rashba model

In this section we introduce the Rashba spin-orbit coupling in a 2DEG.

There is a general argument connecting the inversion symmetry and spin degeneracy. Let us consider a state with wavevector $\mathbf{p}$ and spin $\uparrow$. In the presence of time reversal symmetry, by *Kramers theorem* the energy of an electron state obeys the following

relationship

$$\varepsilon(\mathbf{p},\uparrow) = \varepsilon(-\mathbf{p},\downarrow).$$

If the system has space inversion symmetry it obeys also

$$\varepsilon(\mathbf{p},\downarrow) = \varepsilon(-\mathbf{p},\downarrow).$$

Thus, if the system has both symmetries there is a degeneracy of the spin states in the absence of an external magnetic field. When space inversion symmetry is broken the energy is no longer spin degenerate due to a **p**-dependent Zeeman-like internal magnetic field. Then, the energy dispersion splits in two branches, $\varepsilon_+(\mathbf{p})$ and $\varepsilon_-(\mathbf{p})$. In 2D systems, this splitting can be the consequence of a bulk inversion asymmetry (BIA) of the underlying crystal (for example zinc blend structure [96, 181]), or of a structure inversion asymmetry (SIA) of the confinement potential. In this work we focus our attention on the latter case, which will be introduced in this section. For a more general treatment we refer to [181].

In the last twenty years, one of the most studied systems in spin-orbit based transport phenomena is the so-called 2DEG. This device is produced by growing materials with different band structures, whose properties can be fine-tuned through strains, external potential gates or doping, with the aim of creating a potential well for the conduction electrons.

In a 2DEG, Yu. A. Bychkov and E. I. Rashba [92, 93, 179] have proposed that the lack of inversion symmetry along the direction perpendicular to the gas plane, due to the confining potential, leads to a momentum-dependent spin splitting usually described by the so-called Rashba Hamiltonian (for a complete derivation see *Appendix A*)

$$H_R = \frac{p^2}{2m} - \mathbf{b}(\mathbf{p})\cdot\boldsymbol{\sigma}, \tag{2.1}$$

where $\mathbf{p}$ is the two-dimensional electron momentum, $\boldsymbol{\sigma}$ is the vector composed by Pauli matrices, m is the effective mass of electrons in the conduction band and $\mathbf{b}(\mathbf{p})$ is an internal magnetic field due to the **p**-dependent spin-orbit coupling. In a 2DEG Rashba case the potential V is given by the confining potential $V(z)$ due to the edge profile of the valence band along the growth direction[1]. Therefore, we have (see equation (A.9))

$$\mathbf{b}(\mathbf{p})\cdot\boldsymbol{\sigma} = \frac{e\tilde{\lambda}^2}{4}[(\partial_z V(z)\mathbf{e}_z \times \mathbf{p})\cdot\boldsymbol{\sigma}] = \tilde{\alpha}[(\mathbf{e}_z\times\mathbf{p})\cdot\boldsymbol{\sigma}], \tag{2.2}$$

where $\mathbf{e}_z$ is the unit vector directed along the growth direction, the parameter $\tilde{\alpha} = [\partial_z V(z)]e\tilde{\lambda}^2/4$ and $\tilde{\lambda}$ is the effective Compton wavelength, while e is the unit (positive or negative) charge. The importance of this mechanism lies in the fact that the asymmetry in the confinement potential can be varied by electrostatic means, allowing to tune the RSOC strength, $\tilde{\alpha}$, by an external voltage. Notice that the magnitude of the Rashba parameter $\tilde{\alpha}$ depends also on the crystal composition of the quantum well, in particular we have that the larger the spin splitting energy $\Delta E_{RSOC} = E_0$ is, the bigger $\tilde{\alpha}$ is.

[1] A more detailed description, based on the so-called *Kane model* for the s-p bands, shows us that the Rashba spin-orbit coupling is due to the confinement potential of the valence band $V(z)$. Thus, in a two-dimensional electron gas the coupling between the s-p bands leads to the effective conduction band Hamiltonian (2.1) with the **p**-dependent Zeeman coupling, given by equation (2.2). For further details we refer to [181].

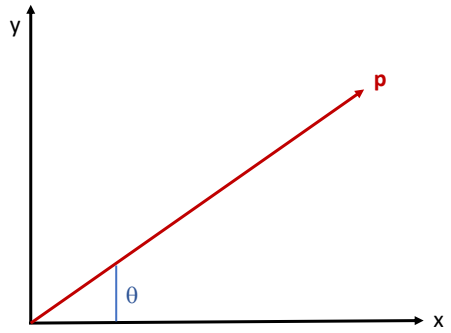

Figure 2.1: *The momentum orientation of the e charges in the xy-plane.*

We consider a 2DEG in the xy-plane. The non-interacting part of the Hamiltonian including the RSOC reads

$$\begin{aligned} H_R = H_0 + H_{RSOC} &= -\frac{\hbar^2}{2m}\left(\frac{\partial}{\partial x^2} + \frac{\partial}{\partial y^2}\right) + \tilde{\alpha}[(\boldsymbol{\sigma} \times \mathbf{p}) \cdot \mathbf{e}_z] \\ &= -\frac{\hbar^2}{2m}\left(\frac{\partial}{\partial x^2} + \frac{\partial}{\partial y^2}\right) + \tilde{\alpha}(\sigma_x \partial_y - \sigma_y \partial_x) \\ &= \frac{p_\parallel^2}{2m} - \mu + \tilde{\alpha}(\sigma^x p_y - \sigma^y p_x), \end{aligned} \tag{2.3}$$

where $\mathbf{p} = -i\hbar\vec{\nabla}$ is the momentum operator, $\tilde{\alpha} = -i\hbar\alpha$ is the Rashba coupling in the p-space and $\mathbf{p}_\parallel$ its projection in the xy-plane, ϑ is the angle formed by $\mathbf{p}$ and the x-axis (see Fig. 2.1).

We define $\xi_{p_\parallel} = p_\parallel^2/2m - \mu$ as the standard kinetic energy term, we introduce the Pauli matrix and the basis of the spins $(c^+_{p_\parallel\uparrow}, c^+_{p_\parallel\downarrow})$, so you can rewrite the Hamiltonian in matrix form as

$$H_R = \sum_p \begin{pmatrix} c^+_{p_\parallel\uparrow} & c^+_{p_\parallel\downarrow} \end{pmatrix} \begin{pmatrix} \xi_{p_\parallel} & i\tilde{\alpha}p_\parallel e^{-i\vartheta} \\ -i\tilde{\alpha}p_\parallel e^{i\vartheta} & \xi_{p_\parallel} \end{pmatrix} \begin{pmatrix} c_{p_\parallel\uparrow} \\ c_{p_\parallel\downarrow} \end{pmatrix}. \tag{2.4}$$

In the absence of a transversal confinement potential, the wavenumbers $k_x = p_x/\hbar$, $k_y = p_y/\hbar$ are still good quantum numbers. Then, the solutions of the time-independent Schrödinger equation are

$$\psi_{\mathbf{k}_\parallel\lambda}(\mathbf{r}_\parallel) = \frac{e^{i\mathbf{k}_\parallel\cdot\mathbf{r}_\parallel}}{\sqrt{\mathcal{A}}} \begin{pmatrix} 1 \\ i\lambda e^{i\vartheta_\mathbf{p}} \end{pmatrix} = \frac{e^{i\mathbf{k}_\parallel\cdot\mathbf{r}_\parallel}}{\sqrt{\mathcal{A}}} \boldsymbol{\eta}_\lambda(\vartheta), \tag{2.5}$$

with $\lambda = \pm 1$ and the dispersion relations

$$\varepsilon_\lambda(k_\parallel) = \frac{\hbar^2 k_\parallel^2}{2m} + \lambda\alpha k_\parallel = a k_\parallel^2 + b k_\parallel. \tag{2.6}$$

In the equation (2.5), $\mathcal{A}$ is the area of the two-dimensional quantum well and $\mathbf{r} = (x, y)$. While the equation (2.6) represents a parabola with $a = \hbar^2/2m$, $b = \lambda\alpha$ and vertex $P = (\mp m\alpha/\hbar^2, -m\alpha^2/2\hbar^2)$.

The matrix that diagonalizes the Hamiltonian H_R has the eigenvectors as columns

$$\mathcal{M} = \frac{1}{\sqrt{2}} \begin{pmatrix} 1 & 1 \\ ie^{i\vartheta} & -ie^{i\vartheta} \end{pmatrix}, \qquad \mathcal{M}_{\alpha\lambda} = \eta^\alpha_{\lambda k_\parallel} \tag{2.7}$$

and allows you to define new operators in the helicity basis

$$c_{k_\parallel\alpha} = \eta^{\alpha}_{\lambda k_\parallel} a_{\lambda k_\parallel}; \qquad c^{\dagger}_{k_\parallel\alpha} = (\eta^{\alpha}_{\lambda k_\parallel})^* a^{\dagger}_{\lambda k_\parallel}; \qquad \lambda = \pm 1,\ \alpha = \uparrow, \downarrow$$

$$\Rightarrow a_{\lambda k_\parallel} = (\eta^{\alpha}_{\lambda k_\parallel})^* c_{k_\parallel\alpha}; \qquad a^{\dagger}_{\lambda p} = \eta^{\alpha}_{\lambda k_\parallel} c^{\dagger}_{k_\parallel\alpha}. \tag{2.8}$$

Indeed, in this new basis

$$H_R = \sum_{k_\parallel,\lambda} \varepsilon_\lambda(k_\parallel) a^{\dagger}_{\lambda k_\parallel} a_{\lambda k_\parallel}. \tag{2.9}$$

As we can see in Fig. 2.2**A**, each eigenstate (2.5) has its spin orientation perpendicular to the direction of the momentum **p**. In fact, by calculating the spin projection on each eigenstate we have

$$< +|\sigma_z|+ >=< -|\sigma_z|- >= 0,$$

$$< +|\sigma_x|+ >= -\sin(\vartheta),\ < -|\sigma_x|- >= \sin(\vartheta),$$

$$< +|\sigma_y|+ >= \cos(\vartheta),\ < -|\sigma_y|- >= -\cos(\vartheta),$$

where $|+ >= \eta^{\alpha}_{+1,k_\parallel}$ and $|- >= \eta^{\alpha}_{-1,k_\parallel}$.

Hence, the spin lives in the xy-plane and its orientation with respect to the Fermi surface rotates as shown in Fig. 2.2**A**. Thus, we can classify the eigenstates and eigenvalues with the helicity $\lambda = \pm 1$. Looking at the Fig. 2.2**B** and Fig. 2.2**C** we can also see, as predicted in the previous section, that the twofold spin degeneracy is lifted by the splitting energy $E_0 = 2\alpha k_\parallel$, since these types of two-dimensional systems have no inversion symmetry. Hence, a removal of spin degeneracy is observed except at the invariant time-reversal point $\mathbf{k}_\parallel = 0$ due to the removal of the parity symmetry. An asymmetry in the interface potential breaks the spatial inversion symmetry allowing a RSOC coupling whose effect is to remove the spin degeneracy while preserving the T symmetry. In fact, acting as an effective magnetic field, it orients the spin of the conduction electrons in the direction orthogonal to their momentum. The spectrum is consequently doubled in the two bands of Fig. 2.2**B**. In Fig. 2.2**C** we have plotted the spectrum defined in equation (2.6) as k_x and k_y vary. For a given energy, the Fermi surface consists of two concentric circles with radii (see Fig. 2.2**A**)

$$k_{\parallel\pm} = \sqrt{2m\mu + m^2\alpha^2} \mp m\alpha, \tag{2.10}$$

with $k_F = \sqrt{2m\mu}$ the standard Fermi wavevector, and μ the chemical potential that a zero temperature is the Fermi energy, E_F. We notice that the spin rotates as we go along Fermi circles such that there is zero magnetic polarization.

As will be clarified below, the density of states (DOS) enters in the equation that defines the superconducting critical temperature. Given, therefore, the importance of this quantity we will first calculate it in this simple case and then for the more general model proposed in this work.

In the case in question we can define the DOS as

$$N(E) = \int \frac{d^2k_\parallel}{(2\pi)^2}[\delta(E - E_{k_\parallel+}) + \delta(E - E_{k_\parallel-})]$$

and we distinguish the two cases $E \lessgtr 0$. For $E < 0$ we have

$$N(E) = \frac{m}{2\pi} \frac{2m\alpha}{\sqrt{(m\alpha)^2 + 2mE}}. \tag{2.11}$$

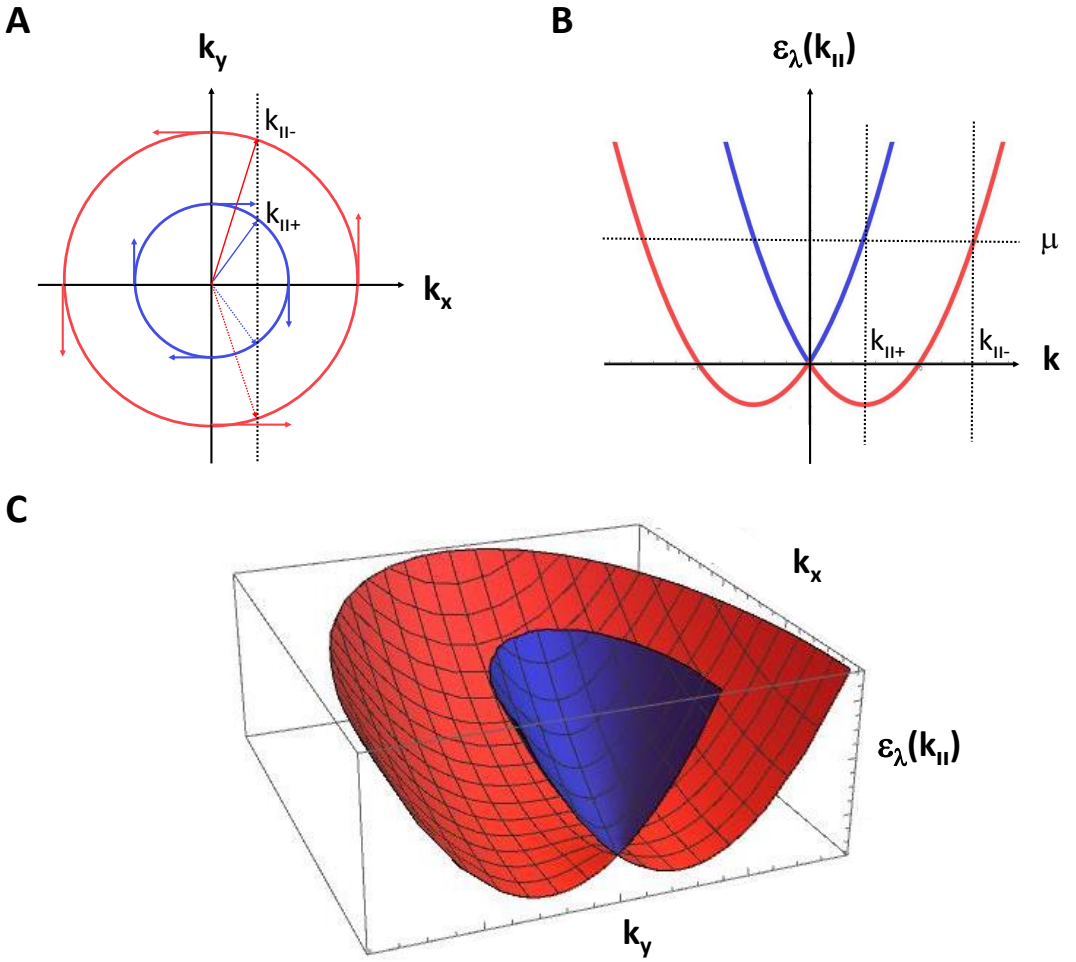

Figure 2.2: The *panel* **A** shows that each eigenstate has its spin orientation in the xy-plane and oriented perpendicular to momentum direction. As shown in *panel* **B**, the Rashba internal magnetic field, reported in equation (2.2), removes the twofold spin degeneracy and gives rise to two different energy bands: $\varepsilon_+(\mathbf{k}_\parallel)$ (blue line) and $\varepsilon_-(\mathbf{k}_\parallel)$ (red line). We have two different Fermi surface corresponding to the two different Fermi momenta $p_{F+} = \hbar k_{\parallel+}$ and $p_{F-} = \hbar k_{\parallel-}$. At fixed positive energy, the wavevectors of the mode (+) and (-) are two concentric circles with radius for (-) mode larger than that for the (+) mode. In the absence of Rashba spin-orbit coupling the two bands reduce to the twofold degenerate quadratic dispersion relation. In the *panel* **C** we have the spectrum of two-dimensional electron gas in the presence of RSOC interaction as a function of the wavevectors k_x and k_y.

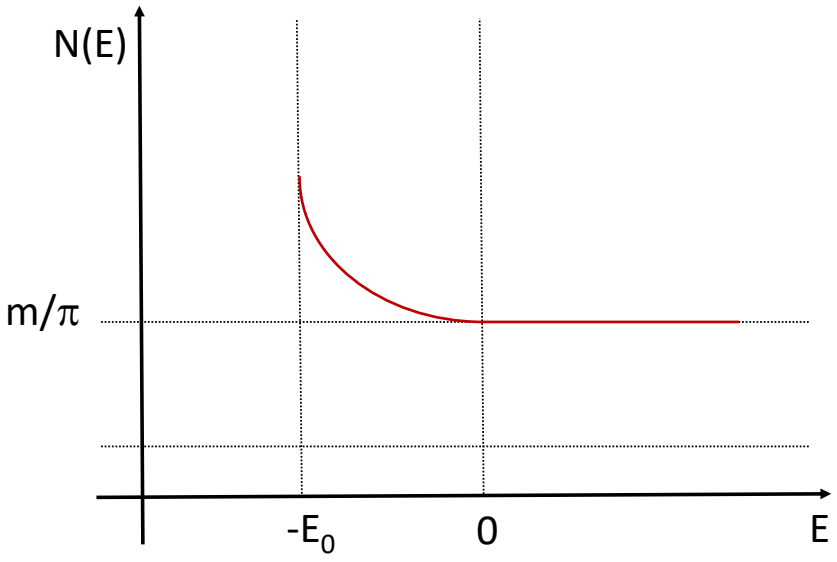

Figure 2.3: *The DOS for* $E \gtrless 0$.

This function tends to $+\infty$ when $E = -E_0$ and to m/π for $E = 0$.

For $E > 0$ we have

$$N(E) = \frac{m}{\pi}. \tag{2.12}$$

For a complete derivation of the DOS we refer to *Appendix B*, here instead we show the plot (Fig. 2.3).

Therefore, a discontinuity in the derivative is observed at $E = 0$ and a van Hove singularity at $-E_0$. This supports the idea that the presence of a RSOC coupling is reflected in the unconventional behaviour of the 2DEG.

In this thesis these concepts will be extended to the case of a three-dimensional system in which a periodic confinement potential is present along the additional direction z. In previous works [17, 18] a quasi-one-dimensional electron gas or quantum wire (QW) has been considered, in which the potential along z can be approximated with a single potential well, while in the work of V. Brosco et al. [19] a 3D Rashba metal was considered in the presence of static disorder. In both cases the transport properties have been studied without deepening the study of the superconducting phase, a central theme of this work.

In the following we will be analysed the superconducting phase of a 2DEG in the presence of RSOC.

2.2 The Nambu formalism in the presence of RSOC

In this section we see what it means to add a superconducting coupling to the Hamiltonian (2.9) that describes a 2DEG in the presence of RSOC [133]. Preliminarily, we apply the Nambu formalism to equation (2.9).

In general the Nambu formalism is used to introduce the hole degree of freedom besides the electron one. The basic idea is to consider states which are the time-reversal version of each other. The eigenvectors, $\boldsymbol{\eta}_\lambda(\vartheta)$ (equation (2.5)), have the following

feature: at fixed λ (helicity band), a state of momentum $\mathbf{p}$ has as time-reversed the state whit momentum $-\mathbf{p}$ as shown below (Fig. 2.4). The space of momenta can be

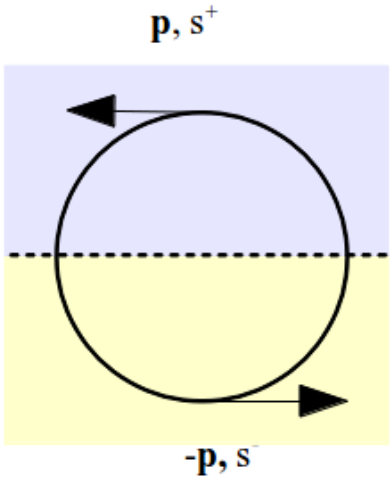

Figure 2.4: *States with opposite moments have also opposite spin.*

divided in two regions: s^+ and s^-. The momenta in s^- are related to those in s^+ by the time-inversion. Then, remembering that $\mathbf{k} = \mathbf{p}/\hbar$, we may write

$$H_R = \sum_{k_\parallel \lambda}{}' \varepsilon_\lambda(k_\parallel)[a^\dagger_{\lambda k_\parallel} a_{\lambda k_\parallel} + a^\dagger_{\lambda -k_\parallel} a_{\lambda -k_\parallel}] = \sum_{k_\parallel \lambda}{}' \varepsilon_\lambda(k_\parallel)[a^\dagger_{\lambda k_\parallel} a_{\lambda k_\parallel} - a_{\lambda -k_\parallel} a^\dagger_{\lambda -k_\parallel}], \quad (2.13)$$

where the $\sum'$ runs only on the region s^+, *i.e.*, half of the momentum space, while the second equality is defined up to a constant term and exploits the standard Nambu trick of reversing the order of operators[2].

The Hamiltonian (2.13) can be rewritten in the spin basis by exploiting the relations (2.8)

$$H_R = \sum_{k_\parallel \lambda}{}' (\xi_{k_\parallel} - \lambda\alpha k_\parallel)[\eta^\alpha_{\lambda k_\parallel} (\eta^\beta_{\lambda k_\parallel})^* c^\dagger_{k_\parallel \alpha} c_{k_\parallel \beta}] - (\xi_{k_\parallel} - \lambda\alpha k_\parallel)[(\eta^\alpha_{\lambda -k_\parallel})^* \eta^\beta_{\lambda -k_\parallel} c_{-k_\parallel \alpha} c^\dagger_{-k_\parallel \beta}]. \quad (2.14)$$

At this point introducing the projector in the particle-hole channel

$$P^{\alpha\beta}_\lambda = \eta^\alpha_{\lambda k_\parallel} (\eta^\beta_{\lambda k_\parallel})^* = \frac{1}{2}[\sigma^0_{\alpha\beta} + \lambda(\widehat{k_\parallel} \wedge \overrightarrow{\sigma} \cdot \hat{z})] \quad (2.15)$$

and noting that $\vartheta(-k_\parallel) = \pi + \vartheta(k_\parallel)$ so that $\eta^\alpha_{\lambda k_\parallel} (\eta^\beta_{\lambda k_\parallel})^* = (\eta^\alpha_{\lambda -k_\parallel})^* \eta^\beta_{\lambda -k_\parallel}$, we have that

$$\begin{aligned} H_R = & \sum_{k_\parallel}{}' \xi_{k_\parallel} (c^\dagger_{k_\parallel \alpha} c_{k_\parallel \beta} - c_{-k_\parallel \alpha} c^\dagger_{-k_\parallel \beta}) \sigma^0_{\alpha\beta} \\ & + \sum_{k_\parallel}{}' (\alpha k_\parallel)[c^\dagger_{k_\parallel \alpha} c_{k_\parallel \beta} (\sigma^x_{\alpha\beta} \widehat{k}_y - \sigma^y_{\alpha\beta} \widehat{k}_x) + c_{-k_\parallel \alpha} c^\dagger_{-k_\parallel \beta} (\sigma^x_{\alpha\beta} \widehat{k}_y - \sigma^y_{\alpha\beta} \widehat{k}_x)]. \end{aligned} \quad (2.16)$$

[2] In order to derive the Bogoliubov-De Gennes equation one could be tempted to go the real space representation of the helicity Hamiltonian. This is a bit difficult to implement because the energy $\varepsilon_\lambda(\mathbf{p})$ only depends on the absolute value of the momentum and in real space is not a convenient differential operator.

The Hamiltonian (2.16) can be rewritten in matrix form by introducing the four-component Nambu spinor, $\Psi_p^\dagger = (c_{k_\parallel\uparrow}^\dagger \; c_{k_\parallel\downarrow}^\dagger \; c_{-k_\parallel\downarrow} \; c_{-k_\parallel\uparrow})$, which explicitly includes the electron and hole degrees of freedom. Thus one has[3]

$$H_R = {\sum_{k_\parallel}}' \Psi_{k_\parallel}^\dagger h_{k_\parallel} \Psi_{k_\parallel}, \tag{2.17}$$

where

$$h_{k_\parallel} = \begin{pmatrix} \xi_{k_\parallel} & i\alpha k_\parallel e^{-i\vartheta} & 0 & 0 \\ -i\alpha k_\parallel e^{i\vartheta} & \xi_{k_\parallel} & 0 & 0 \\ 0 & 0 & -\xi_{k_\parallel} & -i\alpha k_\parallel e^{-i\vartheta} \\ 0 & 0 & i\alpha k_\parallel e^{i\vartheta} & -\xi_{k_\parallel} \end{pmatrix}. \tag{2.18}$$

We now ready to introduce the interaction in order to have the superconductive pairing. Assuming that the interaction is local and equal to U_0, we can write the interaction Hamiltonian in the basis of the spin states as

$$H_I = \frac{1}{2} \sum_{k_\parallel, k'_\parallel, q, \alpha, \beta} U_0 c_{k_\parallel\alpha}^\dagger c_{-k_\parallel - q\beta}^\dagger c_{-k'_\parallel - q\beta} c_{k'_\parallel\alpha}, \tag{2.19}$$

while in the basis of helicity it will be equal to

$$H_I = \frac{1}{2} \sum_{k_\parallel, k'_\parallel, q} U_{\lambda\mu\upsilon\rho}(k_\parallel, k'_\parallel, q) a_{\lambda k_\parallel}^\dagger a_{\mu - k_\parallel - q}^\dagger a_{\upsilon - k'_\parallel - q} a_{\rho k'_\parallel} \tag{2.20}$$

and the interaction potential reads

$$U_{\lambda\mu\upsilon\rho}(k_\parallel, k'_\parallel, q) = U_0 < \eta_{\lambda k_\parallel} | \eta_{\rho k'_\parallel} >< \eta_{\mu - k_\parallel - q} | \eta_{\upsilon - k'_\parallel - q} > . \tag{2.21}$$

Considering pairing only in the same branch with pairs having zero total momentum [133], the full Hamiltonian reads

$$H = \sum_{k_\parallel \lambda} \varepsilon_\lambda(k_\parallel) a_{\lambda k_\parallel}^\dagger a_{\lambda k_\parallel} + \frac{1}{2} \sum_{k_\parallel k'_\parallel} U_{\lambda\lambda\upsilon\upsilon} a_{\lambda k_\parallel}^\dagger a_{\lambda - k_\parallel}^\dagger a_{\upsilon - k'_\parallel} a_{\upsilon k'_\parallel}. \tag{2.22}$$

At this point we can use the standard pairing mean-field approximation

$$H_{MF} = {\sum_{k_\parallel}}' \varepsilon_\lambda(k_\parallel)(a_{\lambda k_\parallel}^\dagger a_{\lambda k_\parallel} - a_{\lambda - k_\parallel} a_{\lambda - k_\parallel}^\dagger) + {\sum_{k_\parallel}}' [\Delta_{\lambda k_\parallel} a_{\lambda k_\parallel}^\dagger a_{\lambda - p}^\dagger + \Delta_{\lambda p}^* a_{\lambda - k_\parallel}^\dagger a_{\lambda k_\parallel}], \tag{2.23}$$

where the pairing potential has been defined in each helicity band as

$$\Delta_{\lambda k_\parallel} = \frac{1}{2} \sum_{k'_\parallel \upsilon} [U_{\lambda\lambda\upsilon\upsilon}(k_\parallel, k'_\parallel) - U_{\lambda\lambda\upsilon\upsilon}(-k_\parallel, k'_\parallel)] < a_{\upsilon - k'_\parallel} a_{\upsilon k'_\parallel} > . \tag{2.24}$$

Notice that in the equation (2.24) there is no restriction on momentum in the sum. The two terms in square brackets originate from the division of the sum over momenta $\mathbf{p}$ in

[3] The Hamiltonian (2.17) with the matrix (2.18) can be transformed back to real space with no problems. $\xi_{k_\parallel}$ gives the standard Laplacian operator while $ik_\parallel e^{-i\vartheta} = k_y + ik_x$, $ik_\parallel e^{i\vartheta} = -k_y + ik_x$.

the two regions, as explained previously. By using the explicit form of the eigenvectors the potential in the helicity basis reads

$$U_{\lambda\lambda\upsilon\upsilon}(k_\parallel, k'_\parallel) - U_{\lambda\lambda\upsilon\upsilon}(-k_\parallel, k'_\parallel) = U_0 \lambda \upsilon e^{-i(\vartheta - \vartheta')}. \tag{2.25}$$

The pairing potential becomes

$$\Delta_{\lambda k_\parallel} = \frac{1}{2} \sum_{k'_\parallel \upsilon} U_0 \lambda \upsilon e^{-i(\vartheta - \vartheta')} < a_{\upsilon - k'_\parallel} a_{\upsilon k'_\parallel} >$$

or

$$\Delta_{\lambda k_\parallel} \equiv \lambda e^{-i\vartheta} \Delta_0, \qquad \Delta_0 = \sum_{k'_\parallel \upsilon} \frac{U_0}{2} e^{i\vartheta'} \upsilon < a_{\upsilon - k'_\parallel} a_{\upsilon k'_\parallel} > . \tag{2.26}$$

One notices that the pairing potential has a dependence on momentum via the factor $e^{i\vartheta}$ and a dependence on the helicity index via λ. The quantity Δ_0 does not depend explicitly on momentum and helicity.

It is useful to express the equation (2.26) in the origin basis. To this end we note that in accordance with the equation (2.8) we can write

$$\begin{aligned} e^{i\vartheta'} \sum_\upsilon \upsilon < a_{\upsilon - k'_\parallel} a_{\upsilon k'_\parallel} > &= e^{i\vartheta'} \sum_\upsilon \upsilon (\eta^\alpha_{\upsilon - k'_\parallel})^* (\eta^\beta_{\upsilon k'_\parallel})^* < c_{-k'_\parallel \alpha} a_{k'_\parallel \beta} > \\ &= \sigma^y_{\alpha\beta} < c_{-k'_\parallel \alpha} c_{k'_\parallel \beta} > . \end{aligned} \tag{2.27}$$

One sees that the pairing in the original basis has the standard form of a singlet and the gap equation reads

$$\Delta_0 = \frac{U_0}{2} \sum_{k'_\parallel} \sigma^y_{\alpha\beta} < c_{-k'_\parallel \alpha} c_{k'_\parallel \beta} > . \tag{2.28}$$

It is useful at this point to express the total Hamiltonian, $H = H_R + H_I$ in terms of the original basis of the $c_{k_\parallel \alpha}$ and $c^\dagger_{k_\parallel \alpha}$ operators, in order to obtain a matrix representation similar to equation (2.17), where, this time

$$\tilde{h}_{k_\parallel} = \begin{pmatrix} \xi_{k_\parallel} & i\alpha k_\parallel e^{-i\vartheta} & -i\Delta_0 & 0 \\ -i\alpha k_\parallel e^{i\vartheta} & \xi_{k_\parallel} & 0 & i\Delta_0 \\ i\Delta_0^* & 0 & -\xi_{k_\parallel} & -i\alpha k_\parallel e^{-i\vartheta} \\ 0 & -i\Delta_0^* & i\alpha k_\parallel e^{i\vartheta} & -\xi_{k_\parallel} \end{pmatrix}. \tag{2.29}$$

The equation (2.29) together with the equation (2.17) represents the pairing Hamiltonian with RSOC. By transforming back to the real space and assuming Δ_0 to be space dependent, one can write the Bogoliubov-De Gennes equation [133].

By using the relations (2.8) it is possible to examine the character of the pairing with respect to the spin quantisation axis in the original basis. The pairing function in the original basis is a matrix

$$\begin{aligned} F_{\alpha\beta k_\parallel} &= < c_{k_\parallel \alpha} c_{-k_\parallel \beta} > = \sum_\lambda \eta^\alpha_{\lambda k_\parallel} \eta^\beta_{\lambda - k_\parallel} < a_{\lambda k_\parallel} a_{\lambda - k_\parallel} > \\ &= \sum_\lambda \frac{1}{2} (\sigma^0_{\alpha\gamma} + \lambda \cos(\vartheta) \sigma^y_{\alpha\gamma} - \lambda \sin(\vartheta) \sigma^x_{\alpha\gamma}) \sigma^y_{\gamma\beta} e^{i\vartheta} \lambda < a_{\lambda k_\parallel} a_{\lambda - k_\parallel} > . \end{aligned} \tag{2.30}$$

Now we define the pairing function at fixed helicity λ as $f_{\lambda k_\parallel} = \lambda < a_{\lambda k_\parallel} a_{\lambda - k_\parallel} >$ and a new projector in the particle-particle channel

$$\tilde{P}^{\lambda}_{\alpha\beta} = \eta^{\alpha}_{\lambda k_\parallel} \eta^{\beta}_{\lambda - k_\parallel} = \frac{1}{2}(\sigma^0 + \lambda \widehat{k_\parallel} \wedge \overrightarrow{\sigma} \cdot \widehat{z}) \sigma^y e^{i\vartheta}$$

so that

$$F_{\alpha\beta k_\parallel} = \sum_{\lambda} \tilde{P}^{\lambda}_{\alpha\beta} f_{\lambda k_\parallel}. \tag{2.31}$$

The above equation expresses the decomposition of the pairing function in the original spin basis in terms of the two pairing functions in the helicity basis.

Following [133] it is useful to single out the singlet and triplet component in the following way

$$f_{\lambda k_\parallel} = f^S_{k_\parallel} + \lambda f^T_{k_\parallel}$$

so that

$$f^S_{k_\parallel} = \frac{1}{2} \sum_{\lambda} f_{\lambda k_\parallel}, \qquad f^T_{k_\parallel} = \frac{1}{2} \sum_{\lambda} \lambda f_{\lambda k_\parallel}.$$

In such a way

$$F_{\alpha\beta p} = \sum_{\lambda} P^{\lambda}_{\alpha\beta} (f^S_p + \lambda f^T_p) = f^S_p \sum_{\lambda} P^{\lambda}_{\alpha\beta} + f^T_p \sum_{\lambda} \lambda P^{\lambda}_{\alpha\beta}.$$

Now

$$\sum_{\lambda} \tilde{P}^{\lambda}_{\alpha\beta} = \sigma^y_{\alpha\beta} e^{i\vartheta},$$

$$\sum_{\lambda} \lambda \tilde{P}^{\lambda}_{\alpha\beta} = [(\widehat{k_\parallel} \wedge \overrightarrow{\sigma} \cdot \widehat{z}) \sigma^y]_{\alpha\beta} e^{i\vartheta}.$$

Hence in the projector operator the first term describes the singlet component, while the second the triplet component. So in each helicity band, the pairing is a mixture of singlet and triplet with respect to the original spin basis.

As pointed out above, the pairing potential has a singlet structure, this is apparent in the structure of the Hamiltonian (2.29), but the anomalous Green function has also a triplet component. This can be made explicit by computing the Matsubara Green function starting from the equation (2.29) (for more details see [133]).

The RSOC interaction by removing the spin degeneracy causes, on the one hand, the energy spectrum to be split into two branches of opposite helicity (except at the invariant time-reversal Dirac point), on the other hand, the pair wavefunction it is a mixture of singlet and triplet components. As underlined in [132], in the limit of strong spin-orbit coupling, magnetic field measurements are not able to give information on the relative weight of the singlet and triplet components and therefore do not allow to distinguish to which of the two components the superconducting behaviour is due. However, it has been seen that the triplet component can give rise to zero energy Majorana modes if suitable topological criteria are satisfied [124, 127, 130, 132]. This feature allows us to understand if non-centrosymmetric superconductors have a predominance of triplet or singlet components.

In the following chapter we will analyse in detail the multigap superconductivity that is evident in geometries in which the quantum size effects are reflected in a multiband electronic structure. We will then see how by varying the chemical potential close to a Lifshitz transition it is possible to obtain an amplification in the parameters of the superconducting phase, in particular, in the gap and in the critical temperature.

3

Superconductivity at the nanoscale: concepts and theoretical methods

Systems with dimension smaller than the Fermi wavelength, λ_F, in one direction are called quasi-2D systems or layers and can be defined nanoscale systems. One of the most important effect of reducing the size of materials to nanoscale dimensions is the appearance of quantization effects due to the confinement of the motion of electrons: the electron wavefunctions at the Fermi level near a band edge are strongly affected by the detail of the quantum confinement. In particular, these effects lead to discrete energy levels with consequent alteration of the electronic structure and a significant increase of the electronic density of states at the Fermi level resulting in sizeable variations of the physical properties.

In the BCS theory of superconductivity, the DOS at the Fermi level, $N(\mu)$[1], enters into the expression of the energy gap and of the transition temperature

$$\Delta = 1.76 k_B T_C = 2\hbar\omega_0 e^{-\frac{1}{N(\mu)g}}, \tag{3.1}$$

where $\hbar\omega_0$ is the Debye cut-off energy of the phonons, g is the phonon-mediated attractive interaction between the electrons and μ is the chemical potential. As we will see below, this relation no longer holds in reduced dimensions, but, when quantum size effects become important, the basic trend of the dependence is preserved. Thus, oscillations in the DOS can be reflected into sizeable oscillations in the energy gap, Δ, and in the critical temperature, T_C, particularly in the weak-coupling regime.

The study of superconductivity at nanoscale began in the 1963 with the pioneering work of Blatt and Thompson, soon after the formulation of the BCS theory [182, 183]. The predictions of these works of the oscillatory behaviour of T_C and of the energy gap as a function of the system thickness has been confirmed experimentally for superconducting nanofilms and nanowires [184] and was extended in 1993 by A. Bianconi, A. Perali and A. Valletta. The BPV theory provides a theoretical and numerical model to explain the high critical temperature observed in different compounds [10–14, 62–66, 69, 71, 73, 74, 81, 163–165, 167, 170–172, 175, 185–191]. The innovative idea of this work was to consider geometries in which the quantum size effects are reflected

[1] The chemical potential, μ, is equal to the Fermi energy, E_F, in the zero temperature limit.

on an electronic multiband structure. Under these conditions it is possible to vary the chemical potential, μ, around the Lifshitz electronic topological transition (ETT)[2], to yield a shape-resonance in the superconducting properties, such as the T_C and the gaps.

In these systems the shape-resonance is due to the configuration interaction between a closed and an open scattering channel. So, when the chemical potential is tuned between the band edge and the van Hove singularity, a new Fermi surface (FS) is made in which a very small number of electrons are confined and a coupling between delocalized (with a large Fermi wavevector) and localized (with a small Fermi wavevector) electrons is possible. The condensate in the FS 1D is in a BCS regime and coexists with a second condensate in small FS where the classical approximation BCS is violated. The Fermi energy is close to the band edge where the new FS appears near the ETT 1D/2D. This behaviour swings dramatically the critical temperature and becomes possible both an interband and an intraband coupling. The shape-resonance is so determined by the relative strength of these couplings.

Hence, in the BPV theory the maximum T_C amplification is expected when two conditions are verified:

- the materials are made up of the superquantum layers of dimensions such that the quantum size effects generate a multiband electronic structure;
- the chemical potential is tuned near an ETT.

The shape-resonances and multicomponent effects in the presence of Lifshitz transitions provide not only a mechanism for understanding the amplification of the critical temperature in many superconductors, but also an approach to synthesize new superconductors with high critical temperature made of heterostructures of quantum stripes without loss of superconducting coherence. These phenomena give a new approach to the study of superconductivity, as well as technological applications.

In particular, the BPV theory considers heterostuctures formed by superconducting stripes, parallel to the xy-plane, separated by insulating (or metallic) block wires. The electrons in the superconducting stripes form a two-dimensional electronic system because the effective electron mass in the z-direction is very large and the separation between superconducting wires is large enough to make small the single particle hopping along the z-direction.

In a recent work [81] we showed that the crystal structure of the organic compound *p-Terphenyl* can be modelled as a superlattice of quantum stripes. Also in this case, the T_C amplification seems being driven by shape-resonances between superconducting gaps near a Lifshitz transition. In the *Chapter 4*, we will see how the BPV theory for such two-dimensional (2D) heterostructures is suitable to reproduce also the experimental results recently observed in hydrogen-dominant materials (H_3S and CSH_x) which manifest, under appropriate conditions, critical temperature at room temperature [32, 34, 47]. Indeed, in this chapter we will extend the BPV theory to a heterostructure of quantum layers or to a three-dimensional (3D) system.

[2]Originally the ETT were related to the electron transition at $T = 0$ in metals, at which the topology of the Fermi surface (FS) changes abruptly. In the electronic materials (as topological semimetals, topological insulators and topological superconductors) different types of the ETT take place. They involve the other types of zeroes in the energy spectrum in addition to or instead of the FS, such as flat bands, Weyl and Dirac point nodes, Dirac nodal lines, zeroes in the spectrum of edges states, Majorana modes, etc. Each of these structures has its own topological invariant, which supports the stability of a given topological structure (for more information see [21, 22, 91]). The consequences of ETT are important in different areas of physics. The singularities emerging at the ETT may enhance the transition temperature to superconductivity.

The 3D structure of the superlattice has the advantage to suppress quantum fluctuations [192,193], that reduce the critical temperature in low dimensions, while keeping the key features of quantum confinement effects for superconductivity. While there are works on the theory of shape-resonances in 2D superlattices of quantum wires, called *superstripes* in cuprate superconductors, the theoretical investigation of shape-resonances in superlattices of quantum layers is missing. These are now of high interest since a 3D superlattice of quantum layers provide the simplest case of a 3D system showing multiband superconductivity near a band edge. Moreover, it has been recognized that diborides, intercalated graphite and pnictides are practical realizations of a superlattice of superconducting layers at atomic limit, where interband pairing is an essential ingredient for high-temperature superconductivity.

In this work, we study the properties of the normal and superconducting phase in a 3D multiband system with or without RSOC coupling, when the chemical potential μ is tuned in a narrow energy range around the edge E_{edge} of the higher in energy subband. This description applies to the situation when the first mini-bands produced by quantum size effects in a superlattice of quantum layers are well separated, *i.e.*, when the electron hopping between layers is small enough, so that the corresponding transversal band dispersion is smaller than the energy separation between the subbands.

Theoretically, the shape-resonance makes some approximations of the BCS theory are no longer valid. Hence, in this work we see that the crossover regime can be considered in a multiband scenario if the superconductive phase is treated avoiding all the standard BCS theory approximations, so for example the following:

- The Fermi energy is far from the band edge ($E_F/\hbar\omega_0 \gg 1$), so that the DOS can be considered constant in an energy range of $\hbar\omega_0$ order.
- Currently single band approximation is not expected for most high critical temperature superconductors.
- In multibands superconductors in addition to the interband attraction, an interband interaction, that can be repulsive or attractive, becomes relevant.
- In BCS theory the shift of the chemical potential from the normal to the superconducting phase is negligible, this approximation, here, is no longer valid.

In this *Chapter* we derive the equations of the BPV theory in the absence of RSOC for a 3D system suitable to describe the properties of the normal and the superconductive phase. In the *Chapter 4* we will see how this model is able to explain the recent results obtained for the 2D systems H_3S an CSH_x, before introducing the RSOC coupling in a 3D anisotropic system, *i.e.*, in a superlattice of quantum layers. In both cases we will analyze the numerical results obtained with a simulation implemented ad hoc (*Appendix G*) [10,14,62,64,66,81,163–165,170–172,175,185–189,191].

3.1 Electronic structure of a superlattice of quantum layers

In order to describe the properties of an electron confined in a potential well, for a single quantum layer, we observe that in the plane parallel to the layer, (x, y)-plane, the electron is free and has a parabolic dispersion. In the z-direction, perpendicular to the layers, the motion of electron is quantized, with formation of discrete energy levels, as given by the solution of the Schrödinger equation. Indeed, the electron wavevector

in the this direction is quantized, $k_n(z) = n\pi/L$ (where L is the thickness of the layer), and the electron dispersion for the n-th subband is

$$\varepsilon_n(\mathbf{k}) = \frac{\hbar^2 k^2}{2m} + E(k_n(z)), \tag{3.2}$$

where $E(k_n(z)) = \hbar^2/2m(n\pi/L)^2$ is the minimum energy for the n-th subband and $k^2 = (k_x^2 + k_y^2)$. The number of occupied subbands is given by $n = Int[2L/\lambda_F]$. If the Fermi energy E_F is close to the bottom of the n-th subband, only n main subbands will cross the Fermi level.

The previous observation can be generalized to a superlattice of quantum layers. A superlattice of quantum layers, like the one shown in the Fig. 5.1, can be modelled as a periodic potential barrier. The one-electron potential $V(z)$ for the superlattice is a periodic function in the z-direction, as shown in the Fig. 5.1**A**.

The two-dimensional electronic gas (2DEG) in the xy-plane will therefore be subjected to a potential of the form

$$V(z) = \begin{cases} -V & -W \leq z \leq 0 \quad I \\ 0 & 0 \leq z \leq b \quad II \end{cases}, \tag{3.3}$$

which compactly can be rewritten as

$$V(z) = V \sum_{-\infty}^{\infty} \theta(W/2 - |md - z|),$$

i.e., we consider a free electron gas with an effective mass m moving in a superlattice of quantum wires of width L separated by a periodic potential barrier $V(x, z)$ of amplitude V and width W along the z-direction and constant in the xy-plane with periodicity d.

The Schrödinger equation for this system is

$$-\frac{\hbar^2 \boldsymbol{\nabla}^2}{2m}\psi(x, y, z) + V(z)\psi(x, y, z) = E\psi(x, y, z), \tag{3.4}$$

that is, the Hamiltonian of the system is separable

$$H_{KP} = H_x + H_y + H_z = (-\frac{\hbar^2}{2m}\frac{\partial^2}{\partial^2 x}) + (-\frac{\hbar^2}{2m}\frac{\partial^2}{\partial^2 y}) + (-\frac{\hbar^2}{2m}\frac{\partial^2}{\partial^2 z} + V(z)), \tag{3.5}$$

and for the eigenstates and the eigenfunctions the following relations are valid

$$E_{KP} = E(k_x) + E(k_y) + E(k_z),$$

$$\psi(x, y, z) = \psi(x)\psi(y)\psi(z).$$

It is therefore possible to solve the three Hamiltonians, $H_{x,y,z}$, separately. Along the x-direction the Hamiltonian that describes the motion is that the free particle ($V(x) = 0$)

$$\frac{d^2\psi(x)}{dx^2} + k^2\psi(x) = 0, \tag{3.6}$$

where

$$\begin{cases} k_x = \sqrt{\frac{2mE(k_x)}{\hbar^2}} \Rightarrow E(k_x) = \frac{\hbar^2}{2mk_x^2} \\ \psi(x) = \frac{1}{L_x}e^{ik_x x} \end{cases}. \tag{3.7}$$

An analogous result holds for the electrons in motion in the y-direction. Along the z-direction, as we will see, we get subbands, $E_n(k_z)$ with wavefunctions which will be linear combinations of plane waves, so the solution of the equation (3.4) will have the following form

$$\psi(x,y,z) \propto e^{ik_x x + ik_y y}\psi_{nk_z}(z). \tag{3.8}$$

To determine the subbands along z we observe that the potential is periodic with periodicity $d = L + W$ and therefore the following condition must be verified

$$\psi(z+d) = e^{i\varphi}\psi(z) \quad \varphi = k_z d. \tag{3.9}$$

Schrödinger equations for zones I and II are

$$\frac{d^2\psi_{I,nk_z}(z)}{d^2z} + \alpha^2\psi_{I,nk_z}(z) = 0 \Rightarrow \begin{cases} \psi_{I,nk_z}(z) = Ae^{i\alpha z} + Be^{-i\alpha z} & for \quad -W \le z \le 0 \\ \alpha = \sqrt{\frac{2mE_n(k_z)}{\hbar^2}} \end{cases} \tag{3.10}$$

$$\frac{d^2\psi_{II,nk_z}(z)}{d^2z} + \beta^2\psi_{II,nk_z}(z) = 0 \Rightarrow \begin{cases} \psi_{II,nk_z}(z) = Ce^{i\beta z} + De^{-i\beta z} & for \quad 0 \le z \le b \\ \beta = \sqrt{\frac{2m(E_n(k_z)+V)}{\hbar^2}} \end{cases}. \tag{3.11}$$

For negative energies α is an imaginary quantity, while the β root argument cannot take negative values. The equation (3.10) and (3.11) are the wavefunction relative to the first period, whereas in the second period, indicated by the condition $L \le z \le L + d$, according to equation (3.9), we have

$$\psi_{nk_z}(z) = e^{i\varphi}\begin{cases} Ae^{i\alpha(z+d)} + Be^{-i\alpha(z+d)} & for \quad L \le z \le d \\ Ce^{i\beta(z+d)} + De^{-i\beta(z+d)} & for \quad d \le z \le L+d \end{cases} \tag{3.12}$$

By imposing the continuity of the wavefunction and its first derivatives in $z = 0$ and the two conditions that connect the wavefunction and its first derivatives in $z = -W$ and $z = L$ through the phase factor $e^{i\varphi} = e^{ik_z d}$, as required by the *Bloch theorem*

$$\begin{cases} \psi_{I,n,k_z}(0) = \psi_{II,nk_z}(0) \\ \left.\frac{d\psi_{I,nk_z}(z)}{dz}\right|_{z=0} = \left.\frac{d\psi_{II,nk_z}(z)}{dz}\right|_{z=0} \\ \psi_{II,nk_z}(L) = e^{ik_z d}\psi_{I,nk_z}(-W) \\ \left.\frac{d\psi_{II,nk_z}(z)}{dz}\right|_{z=L} = e^{ik_z d}\left.\frac{d\psi_{I,nk_z}(z)}{dz}\right|_{z=-W} \end{cases} \tag{3.13}$$

the following conditions are obtained

$$\begin{cases} A + B = C + D \\ \alpha(A - B) = \beta(C - D) \\ C(e^{i\beta L} + De^{-i\beta L}) = e^{ik_z d}(Ae^{-i\alpha W} + Be^{i\alpha W}) \\ \beta(Ce^{i\beta L} - De^{-i\beta L}) = \alpha e^{ik_z d}(Ae^{-i\alpha W} - Be^{i\alpha W}) \end{cases} \tag{3.14}$$

Writing the coefficient matrix, the system admits non-trivial solutions if and only if the determinant of the matrix that multiplies the vector of the coefficients is zero. By imposing this condition we obtain that the solution of the implicit equation for positive energies is given by

$$\cos(k_z d) = \cos(\alpha W)\cos(\beta L) - \frac{1}{2}\left(\xi - \frac{1}{\xi}\right)\sin(\alpha W)\sin(\beta L), \tag{3.15}$$

while for negative energies, we have

$$\cos(k_z d) = \cosh(\alpha W)\cos(\beta L) - \frac{1}{2}\left(\xi - \frac{1}{\xi}\right)\sinh(\alpha W)\sin(\beta L), \tag{3.16}$$

where $\xi = \alpha/\beta$. The solution of the eigenvalue equations from the electronic dispersion for the n subbands is obtained numerically and provides the energy spectrum $\varepsilon_n(\mathbf{k}) = E(k_x, k_y) + E_n(k_z)$ where $E(k_x, k_y)$ is the dispersion of electron free along the layers plane and $E_n(k_z)$ is the dispersion along z. In *Appendix C* we considered the limit case of a *the Dirac Comb* periodic potential.

Hence, in the periodic potential we assume that the full single-particle wavefunction can be written as

$$\psi_{n,\mathbf{k},\alpha}(\mathbf{r}) = \frac{1}{\sqrt{L_x L_y L_z}} e^{i\mathbf{k}_\parallel \cdot \mathbf{r}_\parallel} \psi_{nk_z}(z)\boldsymbol{\chi}_\alpha, \tag{3.17}$$

where $\mathcal{A} = L_x L_y L_z$ are the spatial dimensions of the system, n is the band index, $\mathbf{k}_\parallel = (k_x, k_y)$ is the wavevector, and $\boldsymbol{\chi}_\alpha$ is the spinor part with spin $\alpha = \uparrow$ or $\downarrow$. The corresponding energy eigenvalues, independents from the spin, are given by

$$\varepsilon_n(\mathbf{k}) = \frac{\hbar^2 k_\parallel^2}{2m} + E_n(k_z). \tag{3.18}$$

The eigenfunctions $\psi_{nk_z}(z)$ and the eigenvalues $E_n(k_z)$ are computed numerically by solving a corresponding Kronig-Penney model. The solution of the eigenvalues equation gives the electronic dispersion for the n subbands.

3.2 Superconducting properties of a superlattice of quantum layers

The key point of this thesis is to predict the properties of the superconducting phase with numerical calculations, solving the Bogoliubov-de Gennes (BdG) equations without standard approximations, using the theoretical model described in the following. This provides high T_C states with multicondensate and multigaps in different coupling regimes.

Bogoliubov-de Gennes equations for nanoscale superconductors cannot be solved analytically and even numerically the solution is very demanding. Then, we must introduce an appropriate ansatz to get an approximate solution of the BdG equations.

A direct consequence of quantum confinement is a non-uniform spatial distribution of the superconducting order parameter $\Delta = \Delta(\mathbf{r})$. The Bogoliubov-de Gennes (BdG) equations are a very powerful formalism which is able to describe a position-dependent order parameter. The BdG equations result to be

$$\begin{pmatrix} H(\mathbf{r}) & \Delta(\mathbf{r}) \\ \Delta^*(\mathbf{r}) & -H(\mathbf{r}) \end{pmatrix} \begin{pmatrix} u_\mathbf{k}(\mathbf{r}) \\ v_\mathbf{k}(\mathbf{r}) \end{pmatrix} = E \begin{pmatrix} u_\mathbf{k}(\mathbf{r}) \\ v_\mathbf{k}(\mathbf{r}) \end{pmatrix}, \tag{3.19}$$

where the single-electron Hamiltonian is

$$H(r) = -\frac{\hbar^2 \boldsymbol{\nabla}^2}{2m} - \mu + U_{ext}(\mathbf{r}) \tag{3.20}$$

and $u_\mathbf{k}(\mathbf{r})$ and $v_\mathbf{k}(\mathbf{r})$ are the eigenfunctions of the BdG equations and satisfy the orthonormalization condition, while $\Delta = \Delta(\mathbf{r})$ is the superconducting order parameter

which has a non-uniform spatial distribution as a result of quantum confinement and is related to the eigenfunctions $u_{\mathbf{k}}$, $v_{\mathbf{k}}$ from the self-consistency relation

$$\Delta(\mathbf{r}) = U_0 \sum_{\mathbf{k}} u_{\mathbf{k}}(\mathbf{r}) v^*_{\mathbf{k}}(\mathbf{r}), \tag{3.21}$$

where $U_0 > 0$ is the strength of the pairing potential.

In the approximation we will use below, the single particle Schrödinger equation is solved

$$H(\mathbf{r})\psi_{\mathbf{k}}(\mathbf{r}) = \xi_{\mathbf{k}}(\mathbf{r})\psi_{\mathbf{k}}(\mathbf{r}). \tag{3.22}$$

Considering the following ansatz

$$u_{\mathbf{k}}(\mathbf{r}) = c_{\mathbf{k}}\psi_{\mathbf{k}}(\mathbf{r}); \qquad v_{\mathbf{k}}(\mathbf{r}) = d_{\mathbf{k}}\psi_{\mathbf{k}}(\mathbf{r}), \tag{3.23}$$

with

$$\int d\mathbf{r}\psi^*_{\mathbf{k}}(\mathbf{r})\psi_{\mathbf{k}'}(\mathbf{r}) = \delta_{\mathbf{k}\mathbf{k}'} \tag{3.24}$$

and defining

$$\Delta_{\mathbf{k}} = \int d\mathbf{r}\Delta(\mathbf{r})|\psi_{\mathbf{k}}(\mathbf{r})|^2 \tag{3.25}$$

we can reduce the equation (3.19) to the following system of equations rewritten in matrix form as

$$\begin{pmatrix} \xi_{\mathbf{k}} & \Delta_{\mathbf{k}} \\ \Delta^*_{\mathbf{k}} & -\xi_{\mathbf{k}} \end{pmatrix} \begin{pmatrix} c_{\mathbf{k}} \\ d_{\mathbf{k}} \end{pmatrix} = \varepsilon_{\mathbf{k}} \begin{pmatrix} c_{\mathbf{k}} \\ d_{\mathbf{k}} \end{pmatrix}. \tag{3.26}$$

By solving this linear system it is possible to determine $\varepsilon_{\mathbf{k}}$, $c_{\mathbf{k}}$ e $d_{\mathbf{k}}$

$$\varepsilon_{\mathbf{k}} = \sqrt{\xi^2_{\mathbf{k}} + |\Delta_{\mathbf{k}}|^2}, \tag{3.27}$$

$$c_{\mathbf{k}} = \sqrt{\frac{1}{2}\left(1 + \frac{\xi_{\mathbf{k}}}{\varepsilon_{\mathbf{k}}}\right)}, \tag{3.28}$$

$$d_{\mathbf{k}} = \sqrt{\frac{1}{2}\left(1 - \frac{\xi_{\mathbf{k}}}{\varepsilon_{\mathbf{k}}}\right)}. \tag{3.29}$$

Taking into account (3.23) and that

$$c_{\mathbf{k}} d^*_{\mathbf{k}} = \frac{|\Delta_{\mathbf{k}}|}{\varepsilon_{\mathbf{k}}},$$

we have

$$\Delta_{\mathbf{k}} = \sum_{\mathbf{k}'} U_{\mathbf{k}\mathbf{k}'} \frac{|\Delta_{\mathbf{k}'}|}{\sqrt{\xi^2_{\mathbf{k}'} + \Delta^2_{\mathbf{k}'}}}. \tag{3.30}$$

We have thus determined the equation of self-consistency at zero temperature for the superconducting gap $\Delta_{\mathbf{k}}$, whose expression turns out to be analogous to that of the BCS model. The actual pairing is given by the following matrix elements

$$U_{\mathbf{k}\mathbf{k}'} = \frac{U_0}{2} \int d\mathbf{r}|\psi_{\mathbf{k}}(\mathbf{r})|^2 |\psi_{\mathbf{k}'}(\mathbf{r})|^2. \tag{3.31}$$

In the approximation used, the actual pairing interaction, which enters in the definition of the gap, is reconfigured by the effects of quantization through the single particle wavefunctions, determined by the external confinement potential.

The BPV theory evaluates the properties of the superconductive phase by solving the BdG equations numerically, without the standard approximations. The coupling is due to an attractive interaction for each Fermi surface, while the interaction between different Fermi surfaces can be both attractive and repulsive. The coupling terms are calculated considering the interference between the electron wavefunctions in different subbands, as will be clarified below.

In the previous section we saw that in a heterostructure of quantum layers the wavefunctions also depend on the band indices, n, (see equation (3.17)) therefore the interaction becomes a matrix whose elements are described by the following equation obtained by generalizing the equation (3.31)

$$U^{nn'}_{k_z k'_z} = -\frac{U_0}{2}\int_S |\psi_{nk_z}(z)|^2 |\psi_{n'k'_z}(z)|^2 dxdz = -U_0 I^{nn'}_{k_z k'_z}. \tag{3.32}$$

In this equation remains only a dependence on k_z since, as seen in the equation (3.17), the wavefunctions in the xy-plane are plane waves that cancel each other out in the calculation of the square modulus of the wavefunctions. $I^{nn'}_{k_z k'_z}$ is the pair superposition integral. The coupling terms are calculated considering the interference between the electron wavefunctions in different subbands. Indeed, the intrinsic **k**-dependence of the pairing interaction $U^{nn'}_{k_z k'_z}$ in the superlattice with wavevector k_z induces a structure in the **k**-dependent interband coupling interaction for the electrons that determines the quantum interference between electron pair wavefunction in different subbands of the superlattice.

In an homogeneous system the factor U_0 is related to the effective coupling, g, and the effective density of states per spin at Fermi energy, $N(\mu)$

$$g = N(\mu)U_0.$$

In turn, we allow for the possibility that, in the modulated system, the effective coupling has a dependence upon the band index, $g = g_{nn'}$. Hence the matrix elements becomes

$$U^{nn'}_{k_z k'_z} = \frac{g_{nn'}}{N(\mu)} I^{nn'}_{k_z k'_z}. \tag{3.33}$$

The coefficients A, B, C and D of the single-electron wavefunctions $\psi_{nk_z}(z)$ (3.14) in the transverse direction of the superlattice are obtained by imposing the continuity condition of the wavefunction and of its derivative at $z = 0$, the Bloch condition with periodicity d and by normalization of the wavefunction in the period d (see equation (3.14)). Then, single-electron wavefunctions $\psi_{nk_z}(z)$ are obtained in order to calculate the pairing interaction matrix elements from the overlap integral.

The matrix elements $I^{nn'}_{k_z k'_z}$ depend on the subband index and on the wavevector k_z transversal to the stripes. For a periodic potential barrier associated with the superlattice of layers, the density histogram of the pairing interaction matrix elements between subbands is illustrated in Fig. 3.1. The interband and intraband distributions show different shapes and widths and have different range of values.

The results here reported can be extended to any superconducting superlattice of quantum layers.

In the equation (3.33) the dimensionless factor $g_{nn'} = (-1)^{\delta_{nn'}} g^0_{nn'}$ assumes positive values for $n = n'$ (intraband Cooper pairing) and negative values for $(n \neq n')$ (repulsive

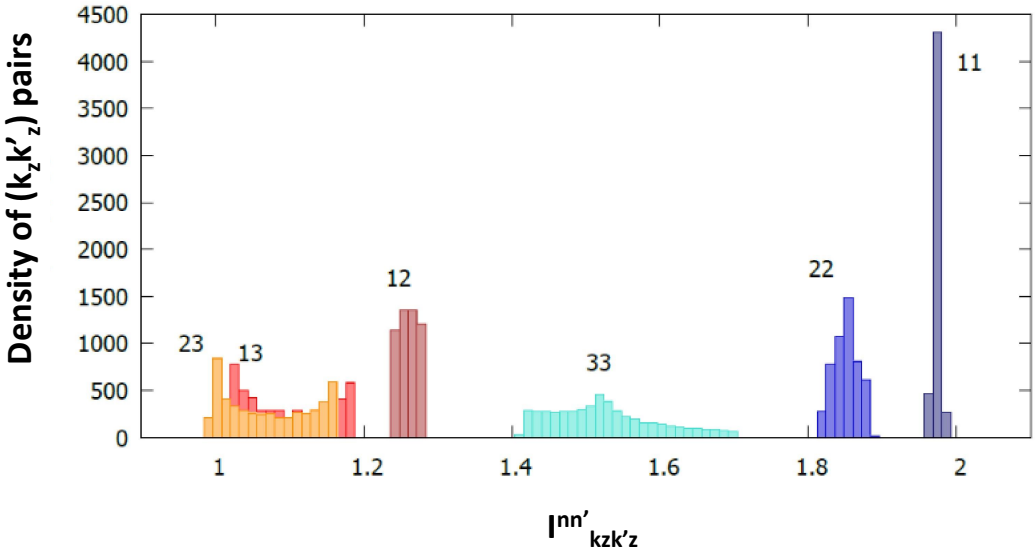

Figure 3.1: *Density histograms of the pairing interaction matrix elements* $I^{nn'}_{k_z k'_z}$.

exchange-like interband pairing, whit $g_{nn'} = g_{n'n}$) and measures the relative intensity of intraband and interband pairing strength. In fact, it multiplies the **k**-dependent integral and therefore permits us to simulate the behaviour of different superconductive multilayer compounds controlling the ratio between intensities of intraband and interband pairing.

In three dimensions it is assumed that $N(\mu)$ is equal to the density of states per spin of a normal, three dimensional, homogeneous system. Hence, we use the value of the barrier height V as a typical value for the Fermi energy for the particles in the system, obtaining

$$N(\mu) = N_{0,3D}(\mu \approx V) = \frac{1}{4\pi^2}\left(\frac{\hbar^2}{2m}\right)^{-3/2}\sqrt{V}.$$

In order to determine the gaps self-consistently and to calculate the critical temperature we use iterative solving methods for the coupled BCS-like equations, hence, as an extension of equation (3.30) we get

$$\Delta_{n\mathbf{k}} = -\frac{1}{M}\sum_{n'\mathbf{k}'}\frac{U^{nn'}_{k_z k'_z}\Delta_{n'\mathbf{k}'}}{\sqrt{(\varepsilon_n(\mathbf{k}')-\mu)^2+\Delta^2_{n'\mathbf{k}'}}},$$

starting with an initial gap parameter equal to a constant and assuming that the convergence occurred for relative variation of the gap less than 10^{-6}. In the previous equation for the gap, M is the total number of wavevectors $\mathbf{k}'$ and is understood that the summation is made only on the states whose distance in energy from the Fermi level is smaller than the cut-off energy ω_0 (except in cases where it is specified from here on we will use units such that $\hbar = 1$).

The superconducting critical temperature is calculated by iteratively solving the linearised equation

$$\Delta_{n\mathbf{k}} = -\frac{1}{2M}\sum_{n'\mathbf{k}'}\frac{(U^{nn'}_{k_z k'_z} tanh((\varepsilon_n(\mathbf{k}')-\mu)/2T_C))(\Delta_{n'\mathbf{k}'})}{(\varepsilon_n(\mathbf{k}')-\mu)}$$

until the vanishing solution is reached with increasing temperature.

The BPV theory predicts hence complex superconductivity that shows anisotropic gaps varying in the **k**-space and in the **r**-space.

In the following chapter we see how these theoretical results are able to provide predictions in agreement with the experimental results observed for two compounds in particular. These systems constitute a simplification of the equations previously obtained by being approximable to 2D heterostructures of quantum wires.

4

The superconducting dome in sulphur hydrides driven by a shape-resonance in a superlattice of wires

In 2015, Drozov et al. have found that pressurized sulphur hydride H_3S reaches a maximum critical temperature $T_C = 203\ K$ [32] higher than the record found before in pressurized cuprate perovskites. Although this discovery does not provide indications on the superconducting mechanism responsible for very heigh T_C, it confirms predictions that manipulation of hydrogen-rich materials [49–52] could drive toward room-temperature superconductivity.

In a recent paper it has been shown that in the pressurized compound CSH_x, which can be considered as a carbon doped H_yS, the critical temperature reaches the surprising value of 15 °C [34]. This material is obtained by photodoping and pressurization of an heterogeneous mixture of van der Waals solids, obtained by introducing methane CH_4 at low pressures into the $H_2S + H_2$ mixture, needed for the synthesis of H_3S [194]. The superconducting transition temperature increases slowly from 140 GPa to 220 GPa where it shows un upturn reaching the maximum of 287.7 K at 267 GPa [34]. The present discovery falsifies a popular dogma that macroscopic quantum coherence in a many-body system cannot occur at room temperature. This new compound belong to the class of intrinsic inhomogeneous materials like perovskites [195, 196] and hydrides [197]. Today there is the need for a roadmap for material design of room-temperature superconductors which could be validated of falsified by experiments.

A characteristic feature of high temperature superconductors is that the critical temperature does not have a unique value independent on the position of the Fermi level, like in homogeneous BCS-crystalline superconductors. On the contrary, the critical temperature is a function of the position of the Fermi level. Therefore, the critical temperature in the room-temperature superconductors is aspected to show a *superconducting dome* where the T_C is a function of two main physical thermodynamic parameters: pressure and charge density.

Here we present a first principles theoretical prediction of the *superconducting dome* for H_3S and CSH_x, by tuning doping and pressure in a multigap superconductor made of a superlattice of wires forming an heterostructure at atomic limit.

The critical temperature, in a multigap superconductor, reaches the maximum of the *dome* when the chemical potential is near a Lifshitz transition. In fact, the maximum critical temperature occurs near a Fano-resonance or Feshbach-resonance or shape-resonance in the superconducting gaps.

According to the BPV theory [10–14, 62–66, 69, 71, 73, 74, 81, 163–165, 167, 170–172, 175, 185–191], the shape-resonances are driven by optimized repulsive or attractive exchange interaction between gaps in different regimes. The critical temperature decreases out of the maximum of the *dome* by changing either *i*) the *charge density* which pushes the chemical potential toward the band edge of one of the multiple bands, where its Fermi energy goes toward zero or *ii*) the *strain* which drives the system toward a lattice instability where the electron-phonon coupling increases with softening of the phonon.

The results may provide a theoretical explanation of the *superconducting dome* in H_3S and CSH_x and show that this new experimental result validate the roadmap proposed by the BPV approach.

In the Fig. 4.1 we plot the T_C as a function of the pressure for three different compounds: D_3S, H_3S and CSH_x [32, 34, 47, 168, 176, 177, 198]. We can observe that in the case of the H_3S for pressures between 120 GPa and 160 GPa the critical temperature increases rapidly until it reaches the maximum value of 203 K; while in the case of CSH_x the critical temperature, after a discontinuity, sharply increases reaching the highest value of $T_C = 287.7$ K at 267 GPa [34].

In *panel* **B** of Fig. 4.1 we report the compressive strain of the SHS bond in H_3S at 120 GPa, where the sulphur hydrides start to show high temperature superconductivity [199–201]. The band structure calculations have shown that the lattice compressive strain (controlled by high pressure) tunes the chemical potential around a van Hove singularity [14, 32, 168, 188, 199–203] which has been confirmed by several authors [198, 204]. Therefore, in a pressurized heterogeneous multigap superconductor, the external pressure tunes the chemical potential near two topological Lifshitz transitions [20–22]: the first type of Lifshitz transition (type I) occurs tuning the chemical potential near the edge of a subband with a critical point where a new Fermi surface spot appears. The second type of Lifshitz transition (type II) occurs at the opening of a neck in the small Fermi surface with the appearing of a singular nodal point or nodal line.

Guige et al. [205] and Goncharov et al. [199] showed that the structure of H_3S depends on the pressure at which the sample is heated. In particular, at pressures greater than 140 GPa, H_3S has a $Im\bar{3}m$ lattice symmetry [51]. This justifies the key role of short hydrogen bond SHS and it is consistent with the fact that high T_C materials are characterized by strong hydrogen bonds with high frequency modes in the phonon spectrum. Moreover, the results mentioned confirm the idea that to reach critical high temperatures it is necessary to compress H_2S in order to have a molecular dissociation into superconductive H_3S and sulphur ($3H_2S \rightarrow 2H_3S + S$).

Band structure calculations [168] have shown that, in the zero temperature limit, the pressure induces a shift of the order of hundreds meV of the Lifshitz energy $\tilde{\eta}$ (according to the equation (4.6), $\tilde{\eta} = \mu - E_L$). This parameter corresponds to the energy difference between the chemical potential and the topological Lifshitz transition at E_L, where E_L is the band edge energy of the highest energy subband. The Fig. 4.2 shows the linear relation between $\tilde{\eta}$, calculated by band structure calculation [168], and the external pressure.

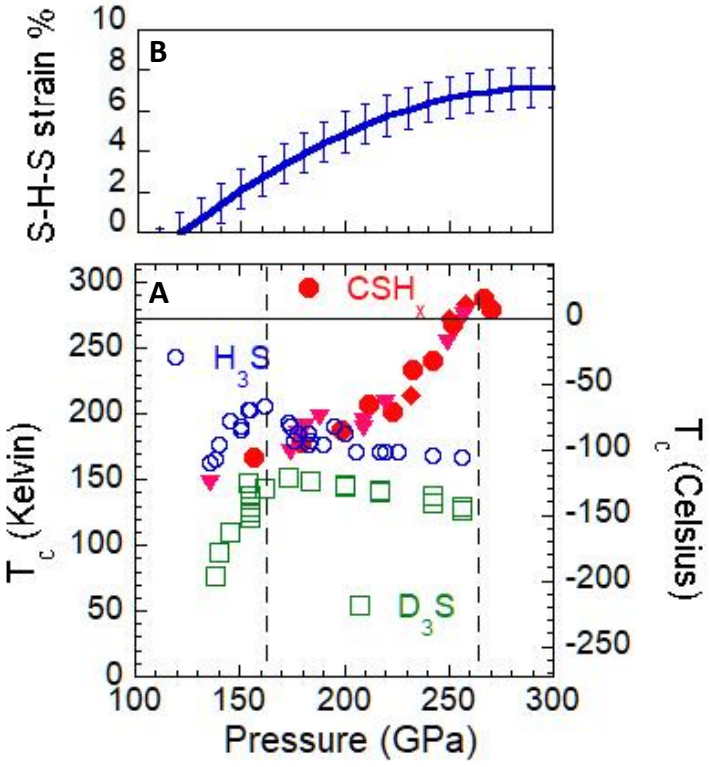

Figure 4.1: The *panel* **A** shows the experimental results obtained for three different cuprates: D_3S, H_3S and CSH_x. The critical temperature expressed in Kelvin (left axis) and in Celsius (right axis) is plotted as a function of the pressure expressed in GPa. Both D_3S and H_3S reach a maximum critical temperature around 150 GPa. Although the values of T_C remain lower for the D_3S the dependence as a function of the pressure is almost the same for the two compounds. As for CSH_x, the maximum critical temperature, about equal to 287.7 K, is reached at 265 GPa. For this compound there are two phase transitions: one at about 150 GPa (first phase transition) and one at about 250 GPa (second phase transition). In the *panel* **B** we report the bond strength SHS as a function of the pressure. It is noted that as the pressure increases, the bond strength increases until a saturation value equal to 8 percent is reached for pressures greater than 200 GPa.

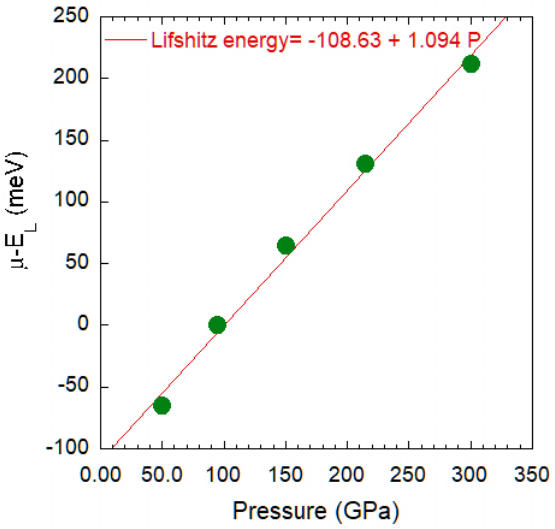

Figure 4.2: *The variation of the Lifshitz energy as a function of the applied external pressure.* The Lifshitz energy $\tilde{\eta}$ is given by the energy difference between the chemical potential at zero temperature μ and the Lifshitz electronic transition for the appearing of a new Fermi surface spot at E_L calculated by band structure calculations [168]. The figure shows the linear relation between the energy difference $(\mu - E_L)$, and the pressure.

From the data shown in Fig. 4.1 and Fig. 4.2 for H_3S and CSH_x, we assume that the variation of the external pressure induces the variation of *i*) the electron phonon coupling driven by strain of the electrons in the small Fermi surface spot in the new appearing upper subband and *ii*) the energy shift of the Lifshitz parameter. Therefore, we propose a simple theoretical model of multigap superconductivity predicting the variation of the critical temperature as a function of both *i*) the proximity to a Lifshitz transition and *ii*) the electron phonon coupling for electrons in the upper subband.

The multigap superconductivity in H_3S, is indicated by the unusual dependence of the isotope coefficient on the pressure. In particular, in the range of 130 $GPa < P <$ 200 GPa the isotope coefficient decreases from 2.37 to 0.31 [47,168,177,178], therefore it deviates markedly from the 0.5 value predicted by the BCS theory, valid for a metal with a single effective Fermi surface and for the energy cut-off much smaller than the Fermi energy. The anomalous behaviour of the isotope coefficient in cuprate perovskites as a function of the doping [163,171,190] and in hydrides as a function of the pressure [168, 176–178] has been associated by some authors to multigap superconductivity. In fact, both the chemical doping and the compressive strain could lead the chemical potential to cross a Lifshitz transition in a multiband system [171,191,198,204]. The anomalous doping dependence of the isotope coefficient as function of charge density or pressure has been considered to be a key experimental result which validates the proposed roadmap for room temperature superconductivity driven by the shape-resonances [10, 62, 64, 81, 163–165,169,170,172,175,186,192,206–217].

The shape-resonances appear in room-temperature superconductors, where at least two different electronic components with different symmetry coexist at the Fermi level forming two different Fermi surfaces [10,62,64,81,163,164,164,165,169,170,172,175,186, 187,192,206–217]. The resonances can be tuned by changing either the charge density or the strain. The chemical potential can be changed by a voltage gate or chemical doping or by external pressure, chemical pressure or lattice misfit strain between two different units of a composite material [61, 66, 185, 218–226]. Many works have shown

that tuning of superconductivity by high pressure in hydrides can be described as tuning the chemical potential near a Lifshitz transition [20–22] in a system where both the electronic structure and the phonon branches are changed by pressure [28–31, 46, 47, 189, 189, 227–240]. Therefore, we present here a scenario where the pressure changes in the same time the energy separation of the chemical potential from a Lifshitz transition and the electron-phonon coupling.

In agreement with the BPV theory, here we assume that H_3S and CSH_x are multigap superconductors in which condensates in the BCS regime, in the lower subbands, coexist with a condensate in a regime in which the BCS approximations are no longer valid. The key point is to solve the Bogoliubov-de Gennes equations in a multigap system. The coupling terms, due to the contact exchange interaction between condensates and usually neglected in standard single band approximation, are calculated by first principles. In particular, it is considered the interference between the electron wavefunctions in different subbands. The wavefunctions are calculated by solving the Schrödinger equation in the periodic potential determined by the lattice structure of the heterostructure at atomic limit. The coupling is supposed due to an attractive interaction due to Cooper pairing within each subband, while the exchange interaction between different subbands can be both attractive, like in diborides, or repulsive, like in iron based superconductors. The amplification of T_C is, thus, determined by the relative strength of different retarded Cooper pairing mediated by phonons within different subbands and the contact non retarded couplings between different condensates.

In the following we show how the BPV theory is able to explain both the high T_C observed in the H_3S and in the CSH_x, and the anomalous behaviour of the isotopic coefficient with pressure. This could open up new directions for design of new room-temperature superconductors made of heterostructures at atomic limit.

4.1 The model

The BPV theory goes beyond the standard BCS appoximations for simple homogeneous metals and beyond the previous extensions of the BCS theory. In this way allows to study the properties of the normal phase and the superconductive phase even for more complex systems characterized by an electronic multiband structure.

The BPV theory has proposed a simple practical realization of multigap superconductivity near a Lifshitz transition: composite materials made of superlattice of weakly interacting nanoscale units, where quantum size effects create a multiband electronic structure. The superlattice is made up of insulating spacers, of amplitude W, between superconducting nanoscale modules, of amplitude L. Therefore, the system can be modelled with a periodic potential in the confinement z-direction, of periodicity $d = W + L$ and amplitude V. The theoretical model is the same as that introduced in *Chapter 3* with the difference that, in this case, the system is 2D, *i.e.*, we are in the presence of an heterostructure of quantum wires rather than quantum layers, therefore the components do not appear along the y-direction.

For this system we assume that: *i*) the periodicity of the quantum wires lattice is comparable to the correlation length, so that the electrons in the transverse direction can be considered weakly interacting; *ii*) the size of the conductive wires, L, is of the same order as the Fermi wavelength. Hence, the effects of quantum size are not negligible. This is reflected in the spectrum that appears splitted in n subbands characterized by quantized values of the transverse moment that depend on the band index and the dimensions of the wires.

In an heterostructure of quantum wires the electrons along the x-direction are free, while along the z-direction they are subjected to a periodic potential $V(z)$ (equation (3.3)).

According to the discussion in *Chapter 3*, in the periodic potential we assume that the full single-particle wavefunction can be written as

$$\psi_{n,\mathbf{k},\alpha}(\mathbf{r}) = \frac{1}{\sqrt{L_x L_z}} e^{ik_x x} \psi_{nk_z}(z) \boldsymbol{\chi}_\alpha, \tag{4.1}$$

where L_x and L_z are the spatial dimensions of the system, n is the band index, $\mathbf{k} = (k_x, k_z)$ is the wavevector, and $\boldsymbol{\chi}_\alpha$ is the spinor part with spin $\alpha =\uparrow$ or $\downarrow$. The corresponding energy eigenvalues, independents from the spin, are given by

$$\varepsilon_n(\mathbf{k}) = \frac{\hbar^2}{2m_x} k_x^2 + E_n(k_z). \tag{4.2}$$

The eigenfunctions $\psi_{nk_z}(z)$ and the eigenvalues $E_n(k_z)$ are computed numerically by solving a corresponding Kronig-Penney model. The solution of the eigenvalues equation gives the electronic dispersion for the n subbands.

In order to reproduce the experimental values of H_3S we have chosen the following values for the parameters of the model: $L = 8.50$ Å, $W = 5.50$ Å, $V = 4.16\ eV$, $\omega_0 = \Delta E$, $g_{ii} = g_{ij} = 0.1$, $g_{33} = 0.25$. Where ω_0 is the cut-off energy and ΔE is the dispersion along z of the third subband. Several papers show that there is an optimal condition for the amplification of T_C: $\omega_0 = \Delta E$ [14, 163, 188]. On the other hand, $g_{nn'}$ is the superconducting adimesional coupling constant for a three-band system and has a matrix structure that depends on the band indices n and n'. We, also, choose a value equal to $m_b = 1.00$ for the effective mass of the electron on the barrier, the effective mass in the well is instead chosen equal to $m_w = 0.86$, equal to the effective mass in the free x-direction. The pressure induces a strain in superconducting modules and can be tuned by changing the lattice parameters of the spacers.

As regards the superconducting phase we can refer to *Sec.*(3.2), in which we have seen that the pairing interaction depends only on the band indices and on the wavevector along the z-direction

$$U^{nn'}_{k_z k'_z} = -\frac{U_0}{2} \int_S |\psi_{nk_z}(z)|^2 |\psi_{n'k'_z}(z)|^2 dx dz = -\frac{U_0}{2} I^{nn'}_{k_z k'_z}, \tag{4.3}$$

where $I^{nn'}_{k_z k'_z}$ is the pair superposition integral.

In Fig. 4.3**A** we show the dependence on the band indices of the exchange integral, while in Fig. 4.3**B** we plot the dependence on the wavevectors. The diagonal elements of the matrix defined by the equation (4.3) are greater than those off-diagonal except for the term $I^{33}_{k_z k'_z}$ and for the interband there is a curve of values of k_z and k'_z for which $I^{ij}_{k_z k'_z} = I^{ji}_{k_z k'_z}$.

As seen in the *Sec.*(3.2), the self-consistent equation for the superconducting gap at $0\ K$ can be written as

$$\Delta_{nk_z} = -\frac{1}{2} \sum_{n',k'_x,k'_z} \frac{U^{nn'}_{k_z k'_z} \Delta_{n'k'_z}}{\sqrt{(\varepsilon_{n'}(\mathbf{k'}) - \mu)^2 + |\Delta_{n'k'_z}|^2}}. \tag{4.4}$$

Instead, the superconducting critical temperature is calculated by iteratively solving the linearised equation

$$\Delta_{n\mathbf{k}} = -\frac{1}{2M} \sum_{n'k'_x k'_z} \frac{U^{nn'}_{k_z k'_z} tanh((\varepsilon_{n'}(\mathbf{k'}) - \mu)/2T_C)(\Delta_{n'k'_z})}{(\varepsilon_{n'}(\mathbf{k'}) - \mu)} \tag{4.5}$$

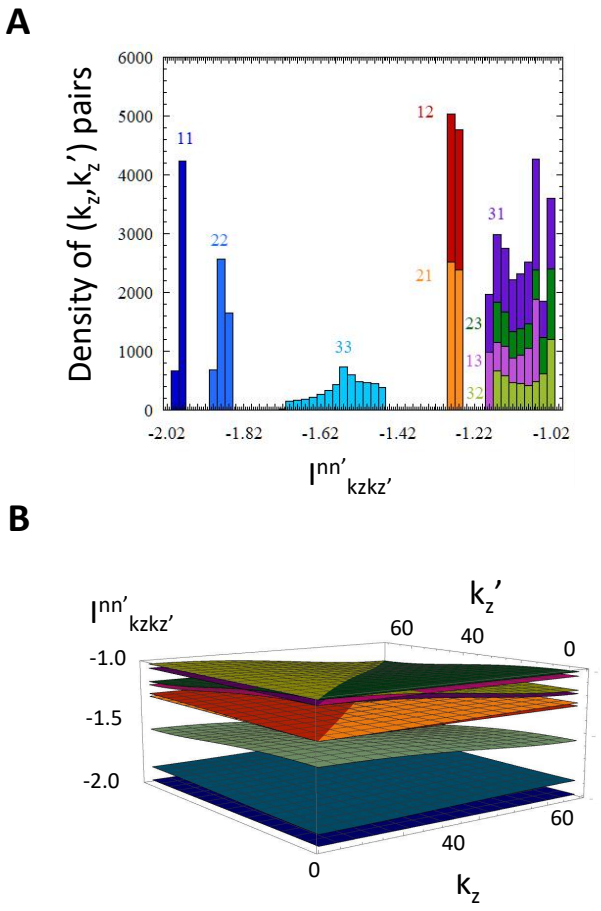

Figure 4.3: *Panel* **A**: histogram of the superposition integral of equation (4.3). The numbers indicate the different elements of the matrix of the intraband pairings $I^{n,n'}_{k_z k'_z}$ and the interband couplings $I^{n,n'}_{k_z k'_z}$. *Panel* **B**: the matrix elements of the exchange integral as a function of the wavevectors in the direction of the confinement potential. The colours used correspond to those of the histogram.

until the vanishing solution is reached with increasing temperature (see *Sec.*(3.2)).

4.2 Numerical results of the BPV theory

In the heterostructure of quantum wires the quantum size effects yield a multiband electronic structure, in which the subband with higher energy shows a two-dimensional behaviour. Indeed, plotted the DOS as the Lifshitz parameter changes (Fig. 4.4), we can be observe that the first and seconds subbands are an one-dimensional behaviour. Instead, when the Lifshitz parameter is tuned between the bottom and the top of third subband, the DOS shows a two-dimensional behaviour. For values greater than Lifshitz parameter the behaviour returns to one-dimensional (diverge as $E^{-1/2}$). The Lifshitz parameter is defined as

$$\eta = \frac{\mu - E_L}{\Delta E}, \tag{4.6}$$

where μ is the chemical potential, E_L is the band edge energy for the third subband, while ΔE is the dispersion along the confinement direction for the third subband, for our choice of parameters $\Delta E = 145\ meV = \omega_0$[1].

When the Lifshitz parameter is tuned over the band edge (η_1), there is a variation in the topology of the Fermi surface, the electronic gas is subjected to topological transition called first type Lifshitz transition or spot apparing. When the Lifshitz parameter reaches the Von Hove singularity (η_2) we have a second Lifshitz transition where the Fermi surface changes her topology from 1D to 2D configuration, this transition is called the second type Lifshitz transition or neck collapsing.

When the Lifshitz parameter is tuned between the band edge and the Von Hove singularity, a new Fermi surface is made in which a very small number of electrons are confined and a coupling between delocalized and localized electrons is possible. The condensate in the large Fermi surface (second subband) is in a BCS-regime and coexists with a second condensate in the small Fermi surface (third subband) where the classical approximation BCS is violated. This behaviour swings dramatically the critical temperature and becomes possible both an interband and an intraband coupling. The T_C amplification is, hence, determined by the relative strength of these couplings.

In the following we analyse the properties of the superconducting phase. For this purpose, we suppose that the first and second subband are in a weak coupling regime, *i.e.*, we use for dimensionless coupling constants the following values: $g_{11} = g_{22} = 0.1$, while in the third subband we change the coupling in the third subbands $g_{33} = g$, in the range of values [0.100, 0.150, 0.200, 0.250, 0.300, 0.330, 0.400, 0.450, 0.460, 0.470, 0.486], parallel we vary the cut-off energy ω_0 according to the *Migdal theorem* [28]. This theorem gives a relation between the renormalized cut-off energy, ω_0, the bare cut-off energy, $\tilde{\omega_0}$, and the pairing constant g, according to the following relation:

$$\omega_0 = \tilde{\omega}_0 \sqrt{1 - 2g}, \tag{4.7}$$

where we use $\omega_0 = \Delta E = 145\ meV$ as renormalized cut-off energy at $g = 0.4$. At this point it is necessary to make a clarification, in this thesis whit **cut-off energy** we refer to the value of the renormalized cut-off energy, ω_0, obtained by the *Migdal theorem* by imposing $g = 0.4$.

[1] Several works [11–13, 64, 165, 191] have shown that there is an optimal condition for the amplification of the critical temperature in heterostructures of quantum wires, this corresponds to when the dispersion in the confinement direction of the highest energy subband coincides with the pairing energy.

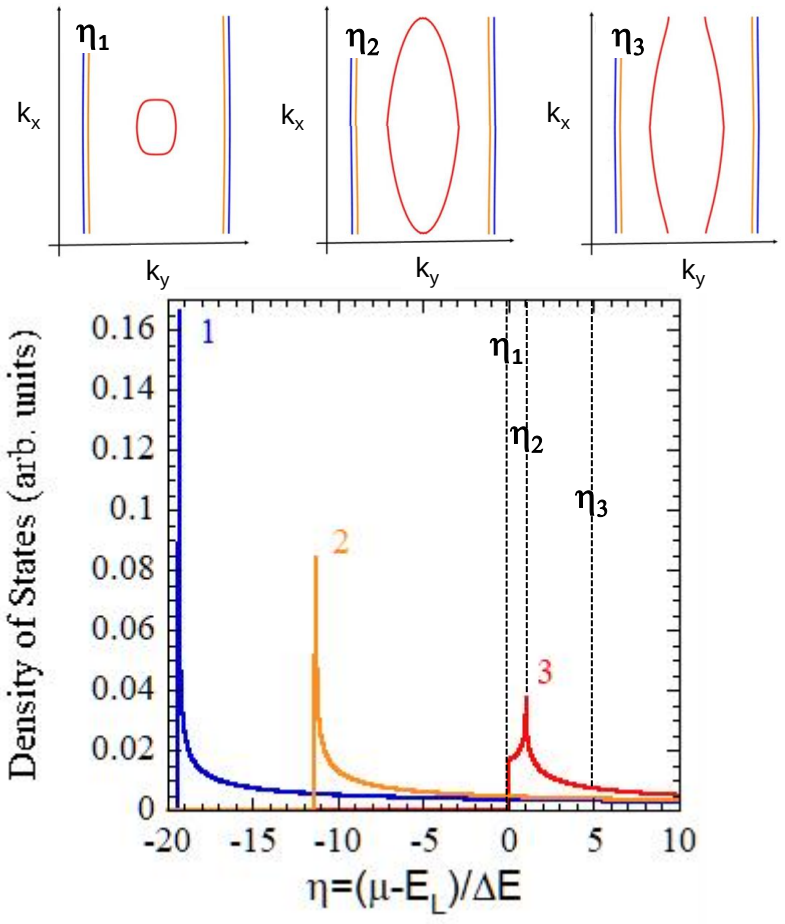

Figure 4.4: *Bottom panel*: Density of states for the first (blue), for the second (orange) and for the third subband (red) as a function of the Lifshitz parameter. For the third subband, in correspondence with the three indicated renormalized energy values, we plot the corresponding Fermi surfaces (*top panel*). For the third subband η_1 corresponds to the value for which we have the first Lifshitz transition called spot appearing, while η_2 is the energy in which we have in the DOS the van Hove singularity or a Lifshitz transition of the second type in which the geometry of the system changes from 2D to 1D.

The above relation is stems from the screening effect of the electrons in the phonon propagator which was derived for the Fermi gas model of a typical metal. Hence the relation contains the coupling constant for the 3D homogeneous metal forming the superconducting layers and is strictly valid only in the BCS limit. With this warning in mind, we use it here to qualitatively estimated the effect of the coupling constant on the phonon frequency.

In Fig. 4.5 we plot the critical temperature as a function of the coupling in the third subband and as a function of the Lifshitz parameter. The critical temperature appears an asymmetric function of the Lifshitz parameter and reaches a maximum for $\eta = 1$, when the system passes from a 2D to a 1D geometry in a Lifshitz transition of the second type. Furthermore, the maximum of T_C increases with coupling. The *superconductive dome* obtained in this figure can represent the behaviour of different compounds. In particular the experimental values obtained for the H_3S and for the CSH_x are reproduced in the BPV theory for precise values of the Lifshitz parameter and of the coupling on the third subband. Indeed, by plotting the critical temperature as a function of the Lifshitz parameter (Fig. 4.6**A**), the maximum value of the critical temperature obtained experimentally for the compound H_3S is reached with our model for $\eta = 1$ and $g = 1/4$, while the maximum value of the critical temperature obtained experimentally for the compound CSH_x is obtained for $\eta = 1$ if $g = 1/3$. In the Fig. 4.6**B** we show the critical temperature as a function of g and two fixed values of η. For the H_3S compound the critical temperature is maximum at $\eta = 1.7$ if $g = 0.40$, while for the compound CSH_x the critical temperature is maximum at $\eta = 1.3$ if $g = 0.33$.

The T_C maximum is located at the 2D-1D dimensional crossover, or when the chemical potential trough the second Lifshitz transition, and is an asymmetric function of the Lifshitz parameter. We can observe that the values of the gap of the first and second subband coincide, while the value of the gap of the third subband is about an order of magnitude higher. Furthermore, an amplification of the superconducting parameters is observed in a range of values $0 < \eta < 1$, amplification that increases as g increases.

When the chemical potential, μ, is tuned around the band edge, different regimes are reached, which can be distinguished by the Lifshitz parameters. In the first Lifshitz transition there is a coexistence of a BCS-like condensate in the second subband with a BEC-like condensate in the third subband. In this regime the critical temperature is extremely low and small variations of the parameters can lead to large variations in the gaps and in the T_C. This determines a large peaked value of the isotope coefficient. At the second Lifshitz transition, the resonant regime of maximum T_C is obtained. A BCS-like pair condensate of the second subband coexists with a condensate of the third subband in a coupling regime in which the BCS approximations are no longer valid (as we will see in Fig. 4.6). For larger chemical potential, a third regime of conventional two-band superconductivity is reached with the coexistence of two-particles condensates having both BCS-like character. This is confirmed by small values of the gaps, typical of weakly coupled superconductors.

When the system switches from an antiresonant to a multiband BCS regime, T_C increases as the g (Fig. 4.5) up to a value of the coupling constant of the order of 0.4, then T_C starts to decrease again as the validity limit of the *Migdal theorem* is reached. Furthermore, we observe that the critical temperature reaches high values even for small coupling thanks to the exchange integral. The critical temperature vs g for different values of the Lifshitz parameter, confirms that there are large variations of T_C only around the singularity of van Hove.

In Fig. 4.7 we summarize the properties of the superconducting phase. The *panel*

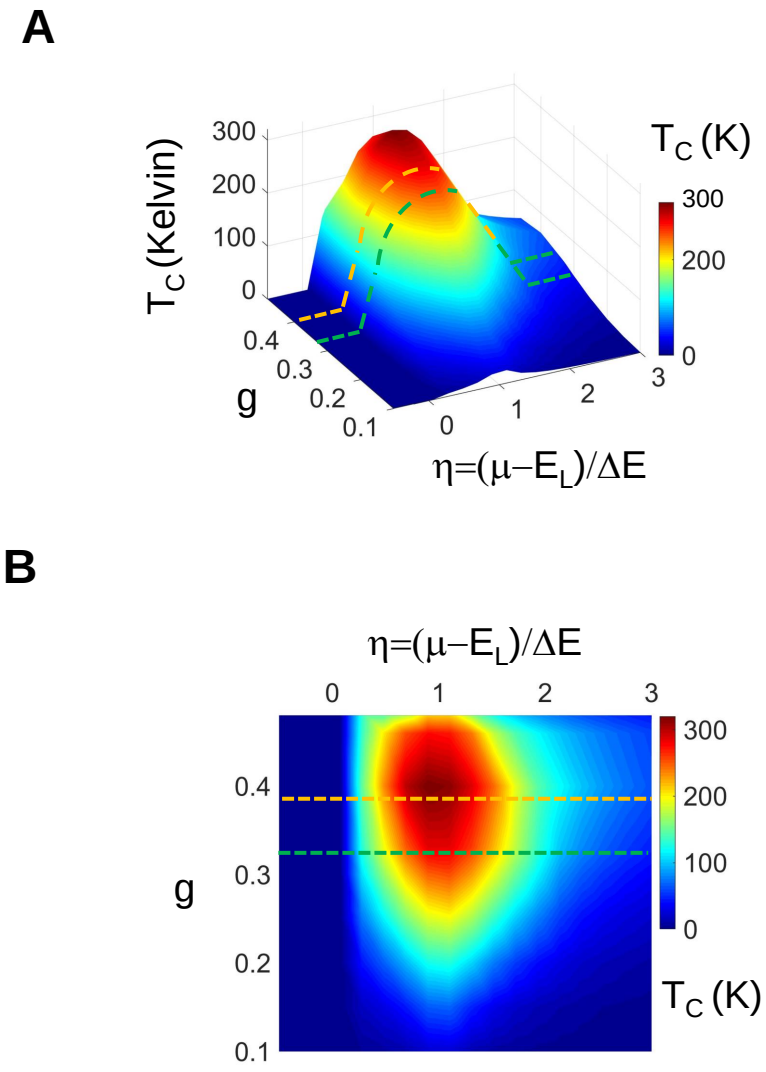

Figure 4.5: In the *panel* **A** we plot the critical temperature predicted by the BPV theory as a function of the coupling g and the Lifshitz parameter η. The *panel* **B** is a projection of the dome obtained in the (η, g) plane. The critical temperature increases from blue ($T_C = 0\ K$) to red ($T_C = 300\ K$) and can be varied either by changing the coupling on the third subband or the Lifshitz parameter. The critical temperature reaches a maximum when the multiband superconductor is close to a Lifshitz transition of the second type, for $0 < \eta < 1$. For both panels the yellow dashed line represents H_3S, the green one CSH_x.

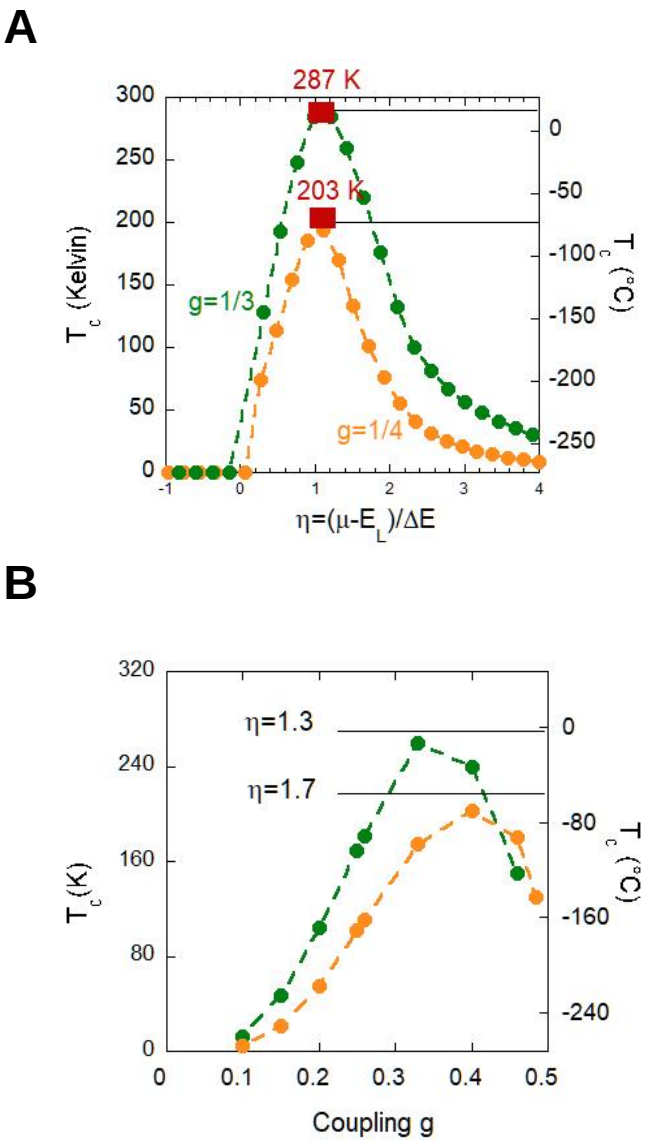

Figure 4.6: *Panel* **A**: the values of the critical temperature, for the proposed three-subband system, as a function of the Lifshitz parameter in linear scale for the coupling values $g = 1/4,\ 1/3$ in the third subband. In this figure we compare the experimental values obtained for the compounds H_3S (*yellow line*) and CSH_x (*green line*) with the data obtained from the proposed model. If in the proposed theoretical model we choose a coupling $g = 1/4$ and then $\omega_0 = 1286\ cm^{-1}$ we reproduce the experimental values of H_3S and then we can be to reach a maximum critical temperature of 203 K. If in the proposed theoretical model we choose a coupling $g = 1/3$ and then $\omega_0 = 1071\ cm^{-1}$ we reproduce the experimental values of CSH_x and then we manage to reach a maximum critical temperature of 287.7 K. *Panel* **B**: the critical temperature as a function of the coupling for a fixed value of the Lifshitz parameter ($\eta = 1.7,\ 1.3$). It can be observed that the maximum critical temperature of 203 K and 287.7 K, observed in the cuprate H_3S and CSH_x, respectively, is reached for $\eta = 1.7,\ 1.3$ and $g = 0.40,\ 0.33$.

A shows the values of the gap ratio, $2\Delta/T_C$, for the second and third subband, while the *panel* **B** shows the trend of the isotope coefficient as η varies. All these graphs were obtained at a fixed coupling value equal to $g = 1/4$ for the H_3S compound and at $g = 1/3$ for the CSH_x.

The gap ratio of the second and third subband coincide in $\eta = 0$ and reach the value predicted by the BCS theory ($2\Delta/T_C = 3.5$), above this value, the anisotropy of the gaps becomes evident, in fact, $2\Delta_2/T_C$ reaches a very small value, between 0 and 1, while $2\Delta_3/T_C$ remains approximately constant at the BCS value. This behaviour emphasizes the non-trivial role of the exchange integral.

Unlike the prediction of the BCS theory for which the isotope coefficient remains constant at a value of 0.5, in this case there is a variation of the critical temperature as a function of the cut-off energy which becomes marked in the range $0 < \eta < 1$, that is, when the system is in a Lifshitz transition of the second type.

Experimentally, the isotope coefficient shows an anomalous behaviour as a function of pressure. In our case this translates into the fact that the pressure brings the energy separation between the chemical potential at the Lifshitz topological transition [168]. In fact, in correspondence with the values of the Lifshitz parameter in which there is a Lifshitz transition of the second type, the isotopic coefficient, obtained using the BPV theory, deviates significantly from the value predicted by the BCS theory. The data in Fig. 4.7 in addition to reproducing the experimental behaviour, therefore indicate the possible presence of a topological transition showing near room-temperature superconductivity.

Finally, in the Fig. 4.8 we plot the critical temperature as a function of the ratio between the gap of the third subband and the gap of the second subband. In order to have a high critical temperature, there must be a strong anisotropy[2] between the gaps, the graph shows, in fact, that the maximum of T_C is reached when the ratio Δ_3/Δ_2 is maximum.

In this *Chapter* we have considered an heterostructure of quantum wires of dimensions such that the quantum size effects determine a multibands electronic structure, this system closely approximates the superlattice of nanoscale structural modules of perovskites, in general, and of the H_3S and CSH_x, in particular. In this compounds the pressure induces a strain in superconducting modules, in the model proposed, this parameter can be tuned by changing the lattice parameters of the spacers inserted between the superconducting nanoscale modules. In this way, we have shown that it is possible to reach very high critical temperatures at a critical point where the chemical potential and strain tune the Fermi level at a Fano-Feshbach shape-resonance between the multiple superconducting gaps in proximity of the Lifshitz transition.

In conclusion, this work shows that BPV theory is able to provide a theoretical explanation for the recent results on high critical temperature superconductors, provides a numerical model capable of providing experimentally verifiable predictions and gives indications on the realization of new materials at high critical temperatures.

In the following *Chapters* we will see what happens both theoretically and numerically for the quantum layers systems described in the *Chapter 3*, when a Rashba spin-orbit coupling is introduced between the electrons in the xy-plane. To this end, we will analyse both the normal and the superconductive phase.

[2] By anisotropy we mean that the studies we conducted have shown that by choosing g small for the intraband and interband exchange integral and increasing the interaction only for the highest energy subband, it is possible to amplify the gap for this subband, this is related to the factors $I^{nn'}_{k_z k'_z}$ that appear in the gap equation.

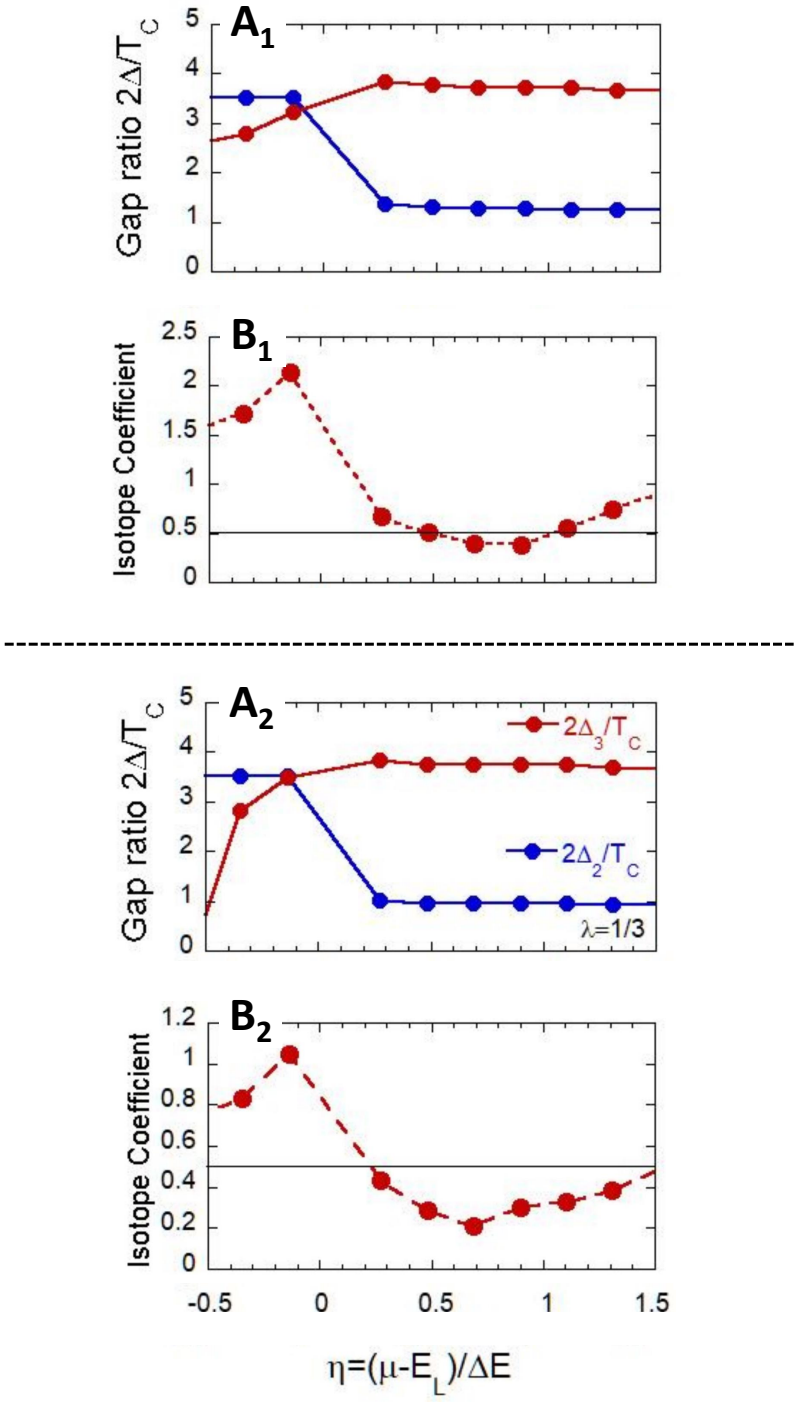

Figure 4.7: *Panel* $\mathbf{A_1}$: gap ratio as a function of the Lifshitz parameter for $g = 1/4$ (H_3S) for the second and third subband. *Panel* $\mathbf{B_1}$: isotope coefficient as a function of the Lifshitz parameter for $g = 1/4$ (H_3S). *Panel* $\mathbf{A_2}$: gap ratio as a function of the Lifshitz parameter for $g = 1/3$ (CSH_x) for the second and third subband. *Panel* $\mathbf{B_2}$: isotope coefficient as a function of the Lifshitz parameter for $g = 1/3$ (CSH_x).

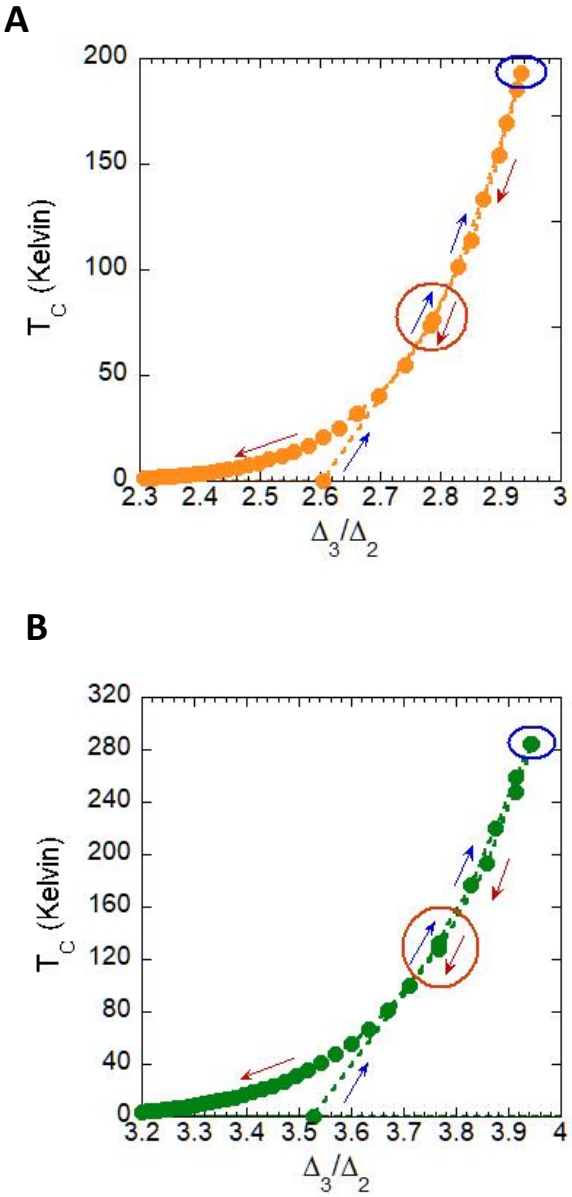

Figure 4.8: *The critical temperature as a function of the ratio between the gap of the third subband and the gap of the second subband. Panel* **A** represents the trend for the compound H_3S, while *panel* **B** represents CSH_x. It can be noted that in the range $2.6 < \Delta_3/\Delta_2 < 2.9$ (for H_3S) or $3.5 < \Delta_3/\Delta_2 < 3.9$ (for CSH_x) the critical temperature increases as the anisotropy between the gaps increases (blue arrows) until it reaches a maximum value when Δ_3/Δ_2 is maximum, from this point on then the T_C decreases almost exponentially as the ratio between the gaps decreases (red arrow). The blue circle represents the point where T_C is maximum, the red circle the point of intersection of the two opposite trends.

5

Multigaps superconductivity at unconventional Lifshitz transition in a 3D Rashba heterostructure at atomic limit: normal phase

The innovative idea of this work is to consider a three-dimensional superconductive anisotropic system in the presence of a Rashba type coupling.

In this and subsequent chapters we introduce the model proposed that synthesizes the properties of a 2DEG in the presence of RSOC and multigap superconductivity, concepts introduced separately in *Chapters 2* and *3*. To this end, we consider a 3D superlattice of metallic layers of thickness L separated by spacers of width W and periodicity d, schematized in Fig. 5.1. For the first time, both an additional dimension are added, passing from an heterostructure of quantum wires to one of quantum layers, and the degree of freedom of spin, which in addition to making the discussion closer to real systems has, as we will see, very important implications.

The electronic gas in the xy-plane is subjected to a Rashba spin-orbit coupling as a consequence of the breaking of the inversion symmetry at the interface between the insulating and conducting modules that characterize the heterostructure.

As seen in *Chapter 2*, spin degeneracy is a consequence of Hamiltonian symmetry with respect to parity (P) and time reversal symmetry (T). Both of these operators change the direction of the momentum, but T also acts with a spin-flip. However, if the potential that confines the electrons at the interface is asymmetric, the spin degeneracy is removed and the spectrum appears to be split into two bands with opposite helicity. The system, therefore, while violating P preserves T. The general form of the Rashba Hamiltonian can be derived with a very general argument: an electron in motion with velocity $\mathbf{v}$, subjected to an electric field $\mathbf{E}$, perceives an effective magnetic field, $\mathbf{B}$, proportional to $\mathbf{v}\times\mathbf{E}$. This, coupled with the intrinsic moment of the electron, modifies the energy by a quantity proportional to $\mathbf{B}\cdot\boldsymbol{\sigma}$, where $\boldsymbol{\sigma}$ is the vector of the Pauli matrices. The Rashba Hamiltonian will therefore be equal to:

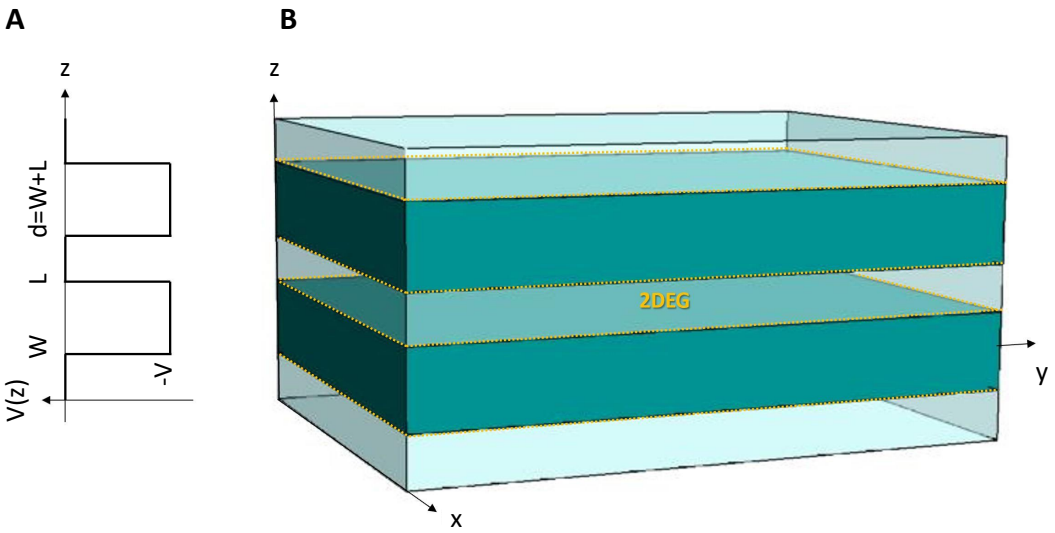

Figure 5.1: *Heterostructure of quantum layers made of conductive layers of thickness L (transparent light green layers) separated by insulating slabs of width W (opaque green layers), with periodicity d.* In this systems the electron in the xy-plane are free, but we have an anisotropy due to the fact that along the z-axis there is a potential for periodic confinement. In order for quantum size effects to be obtained, the thickness of the layers must be of the same order as the Fermi wavelength, while the periodicity must be of the order of the coherence length so that the electrons in the z-direction are weakly interacting and therefore the hopping amplitude is of the same order of magnitude as the superconducting pairing. The figure represents a three-dimensional system: (*panel* **A)** along the z-direction the structure is periodic and the electrons are confined to a periodic Kronig-Penney potential of periodicity d, (*panel* **B)** in the xy-plane at the interface between insulating layers and conductors it forms a two-dimensional electronic gas (highlighted with yellow dotted line).

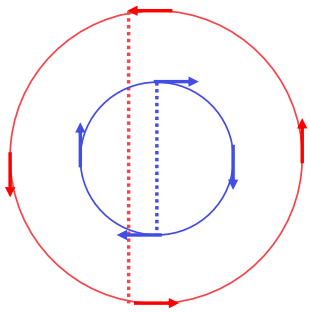

Figure 5.2: *Helicity bands with a RSOC interaction.* The arrows indicate the direction of the spin eigenstates. The dashed lines indicate the Cooper pairs from these states [132].

$$H_{RSOC} = \tilde{\alpha}(\mathbf{p} \times \mathbf{E}) \cdot \boldsymbol{\sigma}$$

The Rashba effect is therefore to orient the spin of the conduction electrons in the direction orthogonal to their momentum. The energy spectrum is therefore split into two branches. Thus, for a given energy the Fermi surface consists of two concentric circles. We notice that the spin rotates as we go along Fermi circles such that there is zero magnetic polarization (see Fig. 2.1).

Different works show that by adding to such a system a superconductive order you can get a Cooper pair unconventional [19, 132, 241, 242]. As the Fig. 5.2 shows, it is possible to couple only electrons with the same helicity or one time-reversal of the other. In particular, the generic state will be a linear combination of the spin-singlet Cooper pair and only one of the three possible spin-triplet Cooper pair (see *Chapter 2*).

Most of the theoretical studies on the coexistence of a Rashba spin-orbit coupling and superconductivity have however limited themselves to considering a single-band two-dimensional electronic system [133, 147–153]. There have been works that have extended the analysis to three-dimensional systems. In the work [17], for example, C. A. Perroni et al. have studied the spectral and the transport properties of a quantum well in the presence of RSOC. The Hamiltonian they introduced is in some aspects similar to the one proposed in this thesis, the differences consist in the fact that they have considered a reference system (x, z, y) rather than (x, y, z) (we will see the implications of this choice in *Appendix D*) and a single-hole potential rather than a periodic one, moreover the properties of the superconducting phase are not investigated. Same thing goes for the work of V. Brosco et al. [19] although they introduce a RSOC coupling in a 3D system, such a system is characterized by a Rashba coupling in the xy-plane and the electrons along the z-direction are supposed to be free. They also limit their study to dc conductivity in the presence of static disorder (in *Appendix E* we will see how DOS and FS are obtained in this model) without analysing the superconducting phase.

The most interesting and innovative purpose of this thesis is to see how the properties of the normal and superconducting phase are changed in a 3D Rashba system in which the geometry of the system is such as to create a multiband electronic structure. Indeed, the main results of this work is the theoretical description of multigap superconductivity [64, 81, 163–170, 170] at the unconventional Lifshitz transition [22] in a 3D

heterostructure at the atomic limit with a periodicity of few nanometers with tunable spin-orbit strength.

Our aim is to show that the interplay between the Rashba spin-orbit coupling and superlattice structure allows for a fine tuning of the critical temperature. To appreciate this point, consider the energy splitting due to the RSOC and the corresponding difference of the Fermi momenta of the two spin eigenstates. This difference introduces a typical SOC length scale l_{SOC}, which may be compared with the modulation of the superlattice d. In a bulk system l_{SOC} can be compared only with the Fermi wavelength, which is typically of the order of 0.1 nm. In contrast in a superlattice, the modulation is of the order of tens of nm, which matches the order of magnitude of the RSOC. The RSOC energy is linear in the wavevector $\epsilon \sim \alpha k$, with the constant $\alpha \sim 0.01$ eV nm. By defining $l_{SOC} = 2\pi\hbar^2/(\alpha m)$, m being the electron mass, one estimates $l_{SOC} \sim 10$ nm. As a result the tuning of the RSOC may be achieved via the variation of the modulation of the superlattice structure.

In the next section, we introduce the model Hamiltonian of a 3D layered superconductor in the presence of RSOC. Later, we study the normal phase paying special attention to the topology of the Fermi surface and to the associated features in the single-particle density of states (DOS). Finally, in the *Chapters 6*, *7* and *8* we turn our attention to the superconducting phase where we derive the superconducting gap equation and discuss its numerical solution in the multiband case.

5.1 The Model

In this work we studied the properties of the normal and superconductive phase of an heterostructure of quantum layers (Fig. 5.1) in which we have a two-dimensional electron gas (2DEG) in the xy-plane and a periodic potential, $V(z)$, in the z-direction (for a different convention on axes see *Appendix D*).

Furthermore, along the z-axis there is an electrostatic field which induces a spin-orbit Rashba coupling for the electrons in the xy-plane.

The system introduced can be described by the following Hamiltonian

$$H = \tilde{H}_R + H_I, \tag{5.1}$$

where H_I is the interaction Hamiltonian, as we will see later, while $\tilde{H}_R$ is the single-particle contribution, which includes the RSOC (see *Chapter 3*)

$$\begin{aligned}
\tilde{H}_R &= H_{KP}(z) + H_R(x,y) \\
&= \left(-\frac{\hbar^2}{2m}\frac{\partial^2}{\partial z^2} + V(z) \right) + \left[-\frac{\hbar^2}{2m}\left(\frac{\partial^2}{\partial x^2} + \frac{\partial^2}{\partial y^2} \right) + \alpha(\boldsymbol{\sigma} \wedge \mathbf{k}) \cdot \widehat{n} \right] \\
&= \left(-\frac{\hbar^2}{2m}\frac{\partial^2}{\partial z^2} + V(z) \right) + \left[-\frac{\hbar^2}{2m}\left(\frac{\partial^2}{\partial x^2} + \frac{\partial^2}{\partial y^2} \right) + \alpha(\sigma_x k_y - \sigma_y k_x) \right] \\
&= \frac{{p_\parallel}^2}{2m} + \frac{p_z^2}{2m_z} + V(z) - i\alpha\hbar\left(\sigma_x\partial_y - \sigma_y\partial_x\right).
\end{aligned} \tag{5.2}$$

In the above equation, $\mathbf{p} = -i\hbar\boldsymbol{\nabla}$ is the usual momentum operator and $p_\parallel = (p_x, p_y)$ its projection in the xy-plane (see Fig. 2.1)

$$\begin{cases} p_x = |p_\parallel| \cos(\vartheta) \\ p_y = |p_\parallel| \sin(\vartheta), \end{cases} \tag{5.3}$$

$V(z) = V(z+d)$ is the periodic potential modelling the superlattice structure $V(z) = -V[\theta(z-d) - \theta(z-L)]$, where $d = L + W$ and V is a positive constant.

In the absence of interaction the Hamiltonian $\tilde{H}_R$ can be separated into a contribution of the Kronig-Penney form due to a periodic potential along z and a contribution due to the RSOC which, on the other hand, acts only on the electrons in the xy-plane. In the equation (5.2), $\boldsymbol{\sigma}$ is the vector of the Pauli matrices, α is the coupling constant RSOC in $eV{\cdot}$Å

$$\begin{cases} K_{SO} = \frac{2\alpha_{SO}\pi}{d} \\ \alpha = 2\frac{\hbar^2}{2m}K_{SO}, \end{cases} \tag{5.4}$$

where α_{SO} is a dimensionless constant which can be changed arbitrarily, while d is the periodicity.

As a first step we solved the Hamiltonian in the absence of interaction, that is $\tilde{H}_R$, analysing separately the two contributions previously described, H_{KP} and H_R.

In particular we have solved the following two equations (see *Sec.*(3.1))

$$H_{KP}(z)\psi_{nk_z}(z) = E_n(k_z)\psi_{nk_z}(z), \tag{5.5}$$

where n is the band index because the long confinement z determines a multiband electronic structure characterized by discrete energy values, and (see *Sec.*(2.1))

$$H_R[\psi_{k_\parallel}(r_\parallel)\boldsymbol{\eta}_\lambda(\vartheta)] = \varepsilon_\lambda(k_\parallel)[\psi_{k_\parallel}(r_\parallel)\boldsymbol{\eta}_\lambda(\vartheta)], \tag{5.6}$$

where $\lambda = \pm 1$ is the helix index, while $\boldsymbol{\eta}_\lambda(\vartheta)$ is a two-component spinor as will be clarified below and $r_\parallel = (x, y)$.

Along the z-direction, as we will see, we get n subbands, $E_n(k_z)$, with wavefunctions which will be linear combinations of plane waves, so the solution of the equation (5.5) will have the following form

$$\psi_{nk_z}(z), \tag{5.7}$$

while, as seen, the eigenvalues can be obtained by solving the Kronig-Penney model (*Sec.*(3.1)) which provides two implicit equations for energy:

$$1. \qquad \cos(k_z d) = \cos(\alpha W)\cos(\beta L) - \frac{1}{2}\left(\xi - \frac{1}{\xi}\right)\sin(\alpha W)\sin(\beta L), \tag{5.8}$$

valid for positive energies, and

$$2. \qquad \cos(k_z d) = \cosh(\alpha W)\cos(\beta L) - \frac{1}{2}\left(\xi - \frac{1}{\xi}\right)\sinh(\alpha W)\sin(\beta L), \tag{5.9}$$

valid for negative energies, where $\xi = \alpha/\beta$.

In our model, both the eigenvalues and the eigenfunctions of H_{KP} are computed numerically with an ad hoc *Fortran* program (*Appendix G*).

Now all that remains is to solve the equation (5.6) relating to the RSOC contribution, to this end we report below the basic steps of the calculation that we analysed in detail in *Chapter 2*. As a first step we rewrite the Hamilonian in matrix form

$$H_R(r_\parallel) = \begin{pmatrix} -\frac{\hbar^2}{2m}\left(\frac{\partial^2}{\partial x^2} + \frac{\partial^2}{\partial y^2}\right) & \alpha(k_y + ik_x) \\ \alpha(k_y + ik_x) & -\frac{\hbar^2}{2m}\left(\frac{\partial^2}{\partial x^2} + \frac{\partial^2}{\partial y^2}\right) \end{pmatrix} = H_0(r_\parallel) + H_{RSOC}(r_\parallel). \tag{5.10}$$

H_0 is the free particle Hamiltonian which admits the following eigenvalues

$$E(k_\parallel) = -\frac{\hbar^2}{2m}k_\parallel^2 \tag{5.11}$$

and the following wavefunctions

$$\psi_{k_\parallel}(r_\parallel) = -\frac{1}{\sqrt{L_\parallel}}e^{ik_\parallel r_\parallel}, \tag{5.12}$$

where $L_\parallel = L_x L_y$ represents the area of the layer section in the xy-plane.

All that remains is to resolve the Hamiltonian properly RSOC, H_{RSOC}

$$H_{RSOC} = \alpha k_\parallel \begin{pmatrix} 0 & \sin(\vartheta) + i\cos(\vartheta) \\ \sin(\vartheta) - i\cos(\vartheta) & 0 \end{pmatrix} = \begin{pmatrix} 0 & i\alpha k_\parallel e^{-i\vartheta} \\ -i\alpha k_\parallel e^{i\vartheta} & 0 \end{pmatrix}. \tag{5.13}$$

Diagonalizing this Hamiltonian is obtained for the eigenvalues

$$E_\lambda(k_\parallel) = \lambda\alpha k_\parallel \qquad \lambda = \pm 1 \tag{5.14}$$

and for eigenvectors a two-component spinor is obtained in the helicity base

$$\boldsymbol{\eta}_\lambda(\vartheta) = \frac{1}{\sqrt{2}}\begin{pmatrix} 1 \\ i\lambda e^{i\vartheta} \end{pmatrix}. \tag{5.15}$$

Finally, the solution of the non-interacting Hamiltonian, $\tilde{H}_R$, is

$$\tilde{H}_R\psi_{n,\lambda,k_x,k_y,k_z}(x,y,z) = (H_{KP}(z)+H_R(x,y))\psi_{n,\lambda,\mathbf{k}}(\mathbf{r}) = (E_n(k_z)+\varepsilon_\lambda(k_x,k_y))\psi_{n,\lambda,\mathbf{k}}(\mathbf{r}), \tag{5.16}$$

with:

$$\varepsilon_\lambda(k_\parallel) = \frac{\hbar^2}{2m}k_\parallel^2 - \lambda\alpha k_\parallel = a(k_\parallel + \lambda k_0) + E_0, \tag{5.17}$$

where $E_0 = m\alpha^2/2$, $a = \hbar^2/m$ and $k_0 = m\alpha/\hbar$.

Hence, overall we have that the single-particle Hamiltonian $\tilde{H}_R$ has solutions of the form

$$\varepsilon_{n\lambda}(\mathbf{k}) = E_n(k_z) + \frac{\hbar^2 k_\parallel^2}{2m} + \lambda\alpha k_\parallel \equiv E_n(k_z) + \varepsilon_\lambda(k_\parallel) \tag{5.18}$$

and

$$\psi_{n\mathbf{k}\lambda}(\mathbf{r}) = \psi_{nk_z}(z)\frac{e^{i\mathbf{k}_\parallel\cdot\mathrm{r}_\parallel}}{\sqrt{\mathcal{A}}}\boldsymbol{\eta}_\lambda(\theta), \tag{5.19}$$

where the wavevector components $\mathbf{k} = (k_x, k_y, k_z) \equiv (\mathbf{k}_\parallel, k_z)$ label plane waves in the xy-plane of area $\mathcal{A}$ and the Bloch functions $\psi_{nk_z}(z)$ along the z-axis, n being a subband index.

As for the second contribution to the Hamiltonian in equation (5.1), we adopt the standard contact interaction with a cut-off energy $\hbar\omega_0$

$$H_I = \frac{U_0}{2}\int \mathrm{d}\mathbf{r}\ \Psi_\alpha^\dagger(\mathbf{r})\Psi_\beta^\dagger(\mathbf{r})\Psi_\beta(\mathbf{r})\Psi_\alpha(\mathbf{r}), \tag{5.20}$$

where $\Psi_\alpha(\mathbf{r})$ is the annihilation fermion field operator and summation over the repeated spin indices (α, β) is understood.

Before considering the superconducting phase in the *Chapter 6*, it is useful to analyse first in the next section the effects of the RSOC in the normal phase and in particular

on the density of states. To this end, we first consider a simplified tight-binding model and then we turn our attention to the model defined in equation (3.10), by confining to the two lowest subbands for numerical reasons.

For the following discussion it is useful to introduce two dimensionless parameters: the Lifshitz parameter defined as

$$\eta = \frac{\mu - E_2}{\Delta E} \tag{5.21}$$

and the rescaled Lifshitz parameter

$$\eta = \frac{\mu - E_R}{\Delta E}, \quad with \quad E_R = E_2 - \Delta E_{RSOC}, \tag{5.22}$$

where μ is the chemical potential which at zero temperature coincides with the Fermi energy, E_2 is the band edge energy of the second subband in the absence of RSOC. ΔE is the dispersion of the highest energy band, in our case the second as we will limit our analysis to a two-band system, which we will fix equal to the reference cut-off energy $\hbar\omega_0$ since, as previously said, several works have demonstrated that this is the optimal condition for the amplification of superconducting parameters. Finally ΔE_{RSOC} is the energy shift due to the RSOC.

5.2 The Normal Phase

In the presence of a RSOC, the trend of the DOS can be understood by considering the evolution of the Fermi surface. In this context we will limit our analysis to a two-band system obtained by taking the two lowest subbands.

The starting point is the single-particle energy dispersion (5.18), which we report here for the sake of clarity

$$\varepsilon_{n\lambda}(\mathbf{k}) = \frac{k_{\parallel}^2}{2m} + \lambda\alpha k_{\parallel} + E_n(k_z), \tag{5.23}$$

where for simplicity we adopt units such that $\hbar = 1$.

For both the first and second subband, the energy dispersion along the z-axis, which is numerically solved as shown below, can be fitted in terms of a tight-binding model. In particular, for odd n the agreement is obtained with a two-harmonic expansion, while for n even the agreement is obtained with a three-harmonic expansion. All this can be combined with the observation that, for the purpose of the subsequent discussion, we do not need to specify the precise form of the dispersion along the z-axis, but for the fact the $E_n(k_z)$ increases (for n odd) or decreases (for n even) monotonically between $k_z = 0$ and $k_z = \pi/d$ and, furthermore, is an even function with respect to $k_z \longrightarrow -k_z$, for both even and odd n.

Hence, in order to illustrate the key features of the DOS, we start our analysis with a simplified expression of $E_n(k_z)$, namely

$$E_1(k_z) = t(1 - \cos(d \cdot k_z)), \quad t = 1 \ \text{ and } 0 < k_z < \pi/d, \tag{5.24}$$

for the first subband, and

$$E_2(k_z) = t(1 + \cos(d \cdot k_z)), \quad t = 1 \ \text{ and } 0 < k_z < \pi/d, \tag{5.25}$$

for the second subband.

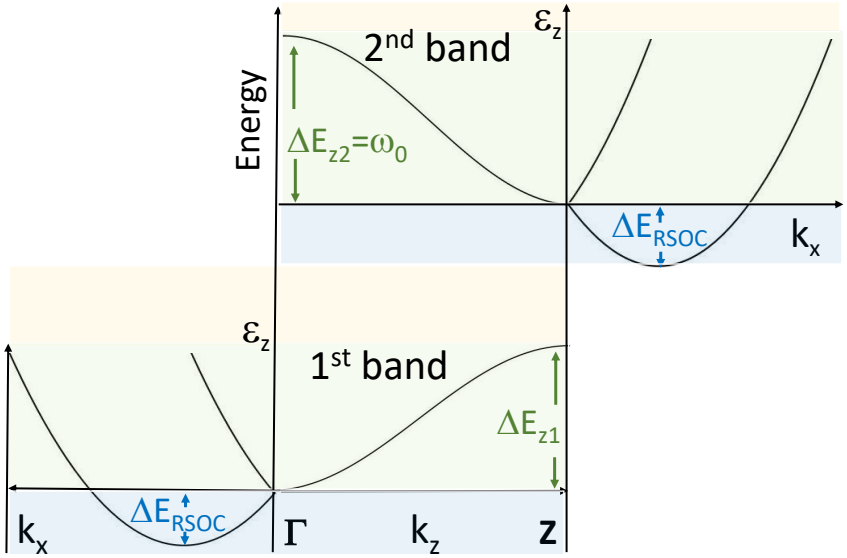

Figure 5.3: The dispersion along k_x is shown together with the dispersion along k_z, in arbitrary units, both for n odd (top panel) and for n even (bottom panel). In this figure ΔE_{zn} is the dispersion in the z direction equal to ε_z for both n even and odd (in the numerical model we will assume that ΔE_{z2} is equal to the cut-off energy ω_0). $\Delta E_{RSOC} = -k_0^2$ is, instead, the shift of the Dirac point (defined as the point at which the in-plane dispersions with opposite helicity meet) as a consequence of the dispersion along k_z. The Γ and Z points are the center and the edge of the first Brillouin zone (IZB). We then indicate the three different regimes in which to study the system: I) $\varepsilon_z < \mu$ (light-yellow box); II) $0 < \mu < \varepsilon_z$ (light-green box); III) $-k_0^2 < \mu < 0$ (light-blue box).

To simplify the notation in the following discussion, the parameters of the in-plane dispersion in equation (5.23) are expressed in units such that $2m = 1$ and we define the spin-orbit typical momentum $k_0 = m\alpha$.

For the sake of definiteness we assume that the minimum energy for the z-axis is zero and the maximum is ε_z, *i.e.*, $E_{2n+1}(0) = 0$ and $E_{2n+1}(\pi/d) = \varepsilon_z$ for the odd subbands, while we have $E_{2n}(0) = \varepsilon_z$ and $E_{2n}(\pi/d) = 0$ for the even subbands. Hence from (5.23) we take the zero of the energy at the origin in the in-plane momentum space. Thus the dispersion along z for the first and second subband will be equal to $\Delta E_{zn} = \varepsilon_z$.

The quasi-particle energy (5.23) has axial symmetry so that we may first study it in the $(k_\parallel, k_z)$-plane. From the isoenergetic curves in this plane one can obtain the isoenergetic surfaces by performing a rotation around the k_z-axis. At a given chemical potential μ, from the expression of the quasiparticle energy we derive the values of $k_\parallel$ at fixed k_z and helicity λ

$$k_\parallel(k_z, \lambda) = -\lambda k_0 \pm \sqrt{k_0^2 + (\mu - E_n(k_z))}, \tag{5.26}$$

from which we start our discussion. It is useful to distinguish three separate regimes for the Fermi energy: I) $\varepsilon_z < \mu$; II) $0 < \mu < \varepsilon_z$; III) $-k_0^2 < \mu < 0$, where, in this simplified model, $\Delta E_{RSOC} = -k_0^2$ is the energy shift due to RSOC coupling (see the Fig. 5.3).

Let us examine them in detail.

5.2.1 Regime I

When selecting the sign in equation (5.26) we must keep in mind that $k_{\parallel} \geq 0$. Let us start with the helicity $\lambda = 1$. In this case for both even and odd n the only allowed sign is the positive one

$$k_{\parallel}(k_z, \lambda) = -k_0 + \sqrt{k_0^2 + (\mu - E_n(k_z))}. \tag{5.27}$$

For n odd at $k_z = 0$ one has $k_{\parallel}(0,1) = -k_0 + \sqrt{k_0^2 + \mu}$, wehereas at $k_z = \pi/d$ one has $k_{\parallel}(\pi/d, 1) = -k_0 + \sqrt{k_0^2 + (\mu - \varepsilon_z)}$, so that $k_{\parallel}(\pi/d, 1) < k_{\parallel}(0,1)$. Hence the isoenergetic curve, when rotated around the k_z-axis generates a corrugated cylinder wider in $k_z = 0$ and narrower in $k_z = \pm\pi/d$. For n even we have a diametrically opposite situation, *i.e.*, we still have a corrugated cylinder which, however, is narrower in $k_z = 0$ and wider in $k_z = \pm\pi/d$ (Fig. 5.4).

Let us consider next the case $\lambda = -1$. Since $\mu > E_n(k_z)$, the radicand is always greater than k_0, and, therefore, the only allowed sign is the positive one

$$k_{\parallel}(k_z, \lambda) = k_0 + \sqrt{k_0^2 + (\mu - E_n(k_z))}. \tag{5.28}$$

For n odd at $k_z = 0$, one has $k_{\parallel}(0, -1) = k_0 + \sqrt{k_0^2 + \mu}$, whereas at $k_z = \pi/d$ one has $k_{\parallel}(\pi/d, -1) = k_0 + \sqrt{k_0^2 + (\mu - \varepsilon_z)}$. Hence, also in this case, the isoenergetic curve, when rotated around the k_z-axis generates a corrugated cylinder, which is bigger than the previous one.

For n even at $k_z = 0$ one has $k_{\parallel}(0, -1) = k_0 + \sqrt{k_0^2 + (\mu - \varepsilon_z)}$, whereas at $k_z = \pi/d$ one has $k_{\parallel}(\pi/d, -1) = k_0 + \sqrt{k_0^2 + \mu}$. Hence, also in this case, the isoenergetic curve, when rotated around the k_z-axis generates a corrugated cylinder, with opposite curvature compared to the case of odd n (Fig. 5.4).

5.2.2 Regime II

Let us begin again by considering first the helicity $\lambda = 1$. Clearly the only sign allowed is the positive one. One notices that exactly at $\mu = \varepsilon_z$ one has $k_{\parallel}(\pi/d, 1) = 0$, which implies a Lifshitz transition for the Fermi surface. For the energies in this regime we see that not all the values of k_z are allowed. The maximum $k_z = k_z^*$ is determined by the condition $k_{\parallel}(k_z^*, 1) = 0$ *i.e.* $k_0 = \sqrt{k_0^2 + (\mu - E_n(k_z^*))}$. For odd n, the isoenergetic curve starts at a point $(0, k_z^*)$ on the k_z-axis and ends at a point $k_{\parallel}(0,1), 0$ in the $k_{\parallel}$-axis. The Fermi surface has a fuse-like shape (Fig. 5.4).

For even n, the isoenergetic curve starts at a point $(0, k_z^*)$ on the k_z-axis and ends at a point $k_{\parallel}(\pi/d, 1), \pi/d$ on the $k_{\parallel}$-axis. In this case, for Fermi surfaces, we obtain half of a spindle that has the tip in $(0,0)$ and reaches the maximum diameter in $k_z = \pi/d$ (Fig. 5.4).

In this regime the case for helicity $\lambda = -1$ is more complex. The positive sign is of course allowed. The branch with the positive sign starts at the point $(k_{\parallel}(\pi/d, -1), \pi/d)$ and ends at the point $(k_{\parallel}(0, -1), 0)$ for odd n, while per even n the positive sign starts at the point $(k_{\parallel}(0, -1), 0)$ and ends at the point $(k_{\parallel}(\pi/d, -1), \pi/d)$. In both cases these curves generate corrugated cylinders by rotation around k_z (Fig. 5.4). For this helicity there is also a possibility of the other branch with the negative sign

$$k_{\parallel}(k_z, \lambda) = k_0 - \sqrt{k_0^2 + (\mu - E_n(k_z))}. \tag{5.29}$$

However this branch is only allowed for a restricted range of k_z values, *i.e.* $(k_z^*, \pi/d)$ which is the complementary range with respect to that allowed for the other helicity.

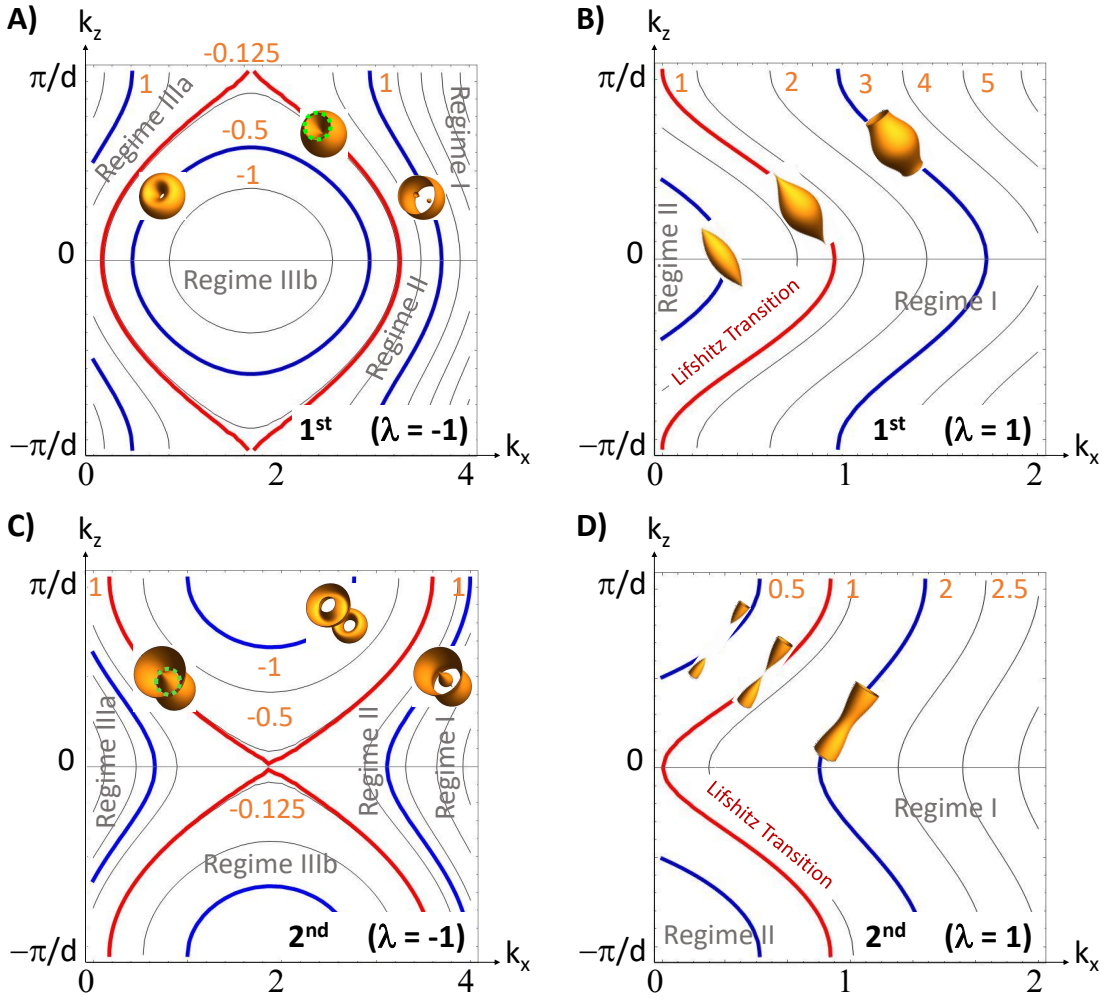

Figure 5.4: *Top panel*: contour plots in the $(k_{\parallel}, k_z)$ plane for $\lambda = -1$ (left) and $\lambda = +1$ (right) for a single-harmonic tight-binding model for the first subband of equation (5.24). Parameters are $d = 1$, $t = 1$ so that $\varepsilon_z = 2$. The RSOC momentum $k_0 = 1.5$. On top of some of the isoenergetic curves are shown the corresponding Fermi surfaces. *Bottom panel*: contour plots as above for the second subband of equation (5.25). The orange numbers are the values of the Lifshitz parameter, defined in the equation (5.21) of the different level curves, for the choice of the parameters made in this simplified model, while the dashed green curves on the 3D Fermi surfaces of panels **A)** and **C)** are represents the nodal line of singular points at an unusual van Hove singularity.

Hence in this regime of energies the helicity $\lambda = 1$ does not exists for the range $(k_z^*, \pi/d)$, when the helicity$\lambda = -1$ develops another branch exactly in this range. As a result the Fermi surface for the $\lambda = -1$ gets a apple-like shape with the poles pushed inwards. This is due to the fact that the points where the phase velocity vanishes are no longer isolated points, but due to the rotation around k_z they form circles with finite measure.

5.2.3 Regime III

In this regime there is only the helicity $\lambda = -1$, which however has two branches

$$k_{\|}(k_z, \lambda) = k_0 - \sqrt{k_0^2 + (\mu - E_n(k_z))}, \tag{5.30}$$

$$k_{\|}(k_z, \lambda) = k_0 + \sqrt{k_0^2 + (\mu - E_n(k_z))}. \tag{5.31}$$

If $k_0^2 + \mu - \varepsilon_z = 0$ then both branches start at the same point $(k_0, \pi/d)$ for odd n ($(k_0, 0)$ for even n) and from there depart ending at the points $(k_0 + \sqrt{k_0^2 + \mu}, 0)$ and $(k_0 - \sqrt{k_0^2 + \mu}, 0)$ for odd n ($(k_0 + \sqrt{k_0^2 + \mu}, \pi/d)$ and $(k_0 - \sqrt{k_0^2 + \mu}, \pi/d)$ for even n) in the $k_{\|}$-axis, respectively. This is the case when the singularity in the phase velocity, which in the absence of RSOC is at the isolated point $(0, \pi/d)$ for odd n or $(\pi/d, 0)$ for even n, becomes a finite-measure manifold and develops a van Hove singularity in the DOS (Fig. 5.4). Hence we may distinguish two cases: IIIa) $0 < k_0^2 + \mu < \varepsilon_z$ and IIIb) $0 < k_0^2 + \mu > \varepsilon_z$. In the case IIIa) the argument of the square root is negative, hence the two branches start at a point (k_0, k_z^{**}) with k_z^{**} given by the condition $k_0^2 + \mu = E_n(k_z^{**})$. Then the two branches end on the $k_{\|}$-axis. The Fermi surface generated by these curves has a torus-like shape. In regime IIIb) instead, the two branches remain disconnected from each other. The Fermi surface has an external and internal part and has a torus-like shape, with the toruses of neighboring zones touching each other (Fig. 5.4).

Our aim is to evaluate the density of states in order to compare it with the detailed calculations made with the more realistic periodic potential model. Therefore, we derive the analytical DOS expression for both helicity values, $\lambda = \pm 1$.

The energy dispersion in suitable reduced units reads

$$E(p, k, \lambda) = t(1 - \cos(p)) + (k + \lambda k_0)^2 - k_0^2, \tag{5.32}$$

where $-\pi < p < \pi$ is the momentum along the z-axis, $0 < k < \infty$ the momentum in the xy-plane, $\lambda = \pm 1$ is the helicity index. Here t is the hopping parameter and describe a tight-binding motion along the z-axis. This is the opposite limit with respect to the parabolic dispersion considered by V. Brosco et al. [19] (see *Appendix E*). Also the parameter k_0 describes the spin-orbit interaction. Let us start with the helicity $\lambda = -1$. The DOS reads

$$N_-(\mu) = \int_0^\infty \frac{kdk}{2\pi} \int_{-\pi}^{\pi} \frac{dp}{2\pi} \delta(t(1 - \cos(p)) + (k - k_0)^2 - k_0^2 - \mu). \tag{5.33}$$

In order to evaluate the integrals for the DOS, we observe that the dispersion in p is an even function and we confine to positive values. Also it is useful to change varable

$$x = k - k_0 \Rightarrow k = x + k_0. \tag{5.34}$$

We can also make the following change of variable

$$\eta = t(1 - \cos(p)) \Rightarrow \cos(p) = 1 - \frac{\eta}{t} \tag{5.35}$$

from which it is easy to get

$$dp = \frac{d\eta}{\sqrt{t^2 - (t-\eta)^2}}. \tag{5.36}$$

Then, the DOS becomes

$$N_-(\mu) = \frac{1}{2\pi^2}\int_{-k_0}^{\infty} dx(x+k_0)\int_0^{2t} d\eta \frac{\delta(\eta + x^2 - k_0^2 - \mu)}{t^2-(t-\eta)^2}. \tag{5.37}$$

The evaluation of the integral over the variable η is trivial due to the Dirac delta function, but because $0 < \eta < 2t$ one is left with a condition on the variable x to be integrated next: $0 < \mu + k_0^2 - x^2 < 2t$. As a result the DOS reads

$$N_-(\mu) = \frac{1}{2\pi^2}\int_{-k_0}^{\infty} dx(x+k_0) \frac{\theta(\mu + k_0^2 - x^2)\theta(x^2 + 2t - \mu + k_0^2)}{\sqrt{(\mu + k_0^2 - x^2)(x^2 + 2t - \mu + k_0^2)}}. \tag{5.38}$$

In the above $\theta(x)$ is the Heaviside step function. The evaluation of the integral depends on the relative values of the parameters μ, t, k_0. It is useful to define the following integral, which depends parametrically on the integration limits a, b and implicitly on all other parameters

$$I_-(a,b) = \int_a^b dx(x+k_0)\frac{1}{(\mu + k_0^2 - x^2)(x^2 + 2t - \mu + k_0^2)}. \tag{5.39}$$

Let us analyze the integral defined in equation (5.39). As a function of the variable x, the integrand has singularities at $x = \pm\sqrt{\mu + k_0^2}$ and $x = \pm\sqrt{\mu + k_0^2 - 2t}$. All singularities have index $-1/2$ and hence are integrable. When $\mu + k_0^2 = 2t$, the denominator acquires a zero at the origin. In the absence of spin-orbit interaction, the $1/|x|$ behaviour of the denominator is compensated by the numerator and the integral is finite. However, in the presence of spin-orbit interaction, there is a term proportional to k_0 in the numerator and a van Hove singularity develops. The singularity has a logarithmic behaviour.

A better intuition can be developed by considering that the dispersion has an axial symmetry in the xy-plane. Hence we may consider the Fermi surface projected in the k and p plane. In such a plane the Fermi surface is a curve. The 3D Fermi surface (Fig. 5.5) is then obtained by rotating the curve around the p axis. This is shown in Fig. 5.6. Given the dispersion (5.32) the band velocity reads

$$v(k,p) = (2(k-k_0), t\sin(p)). \tag{5.40}$$

Then it is clear that for $k_0 = 0$, the velocity vanishes at $(0,\pi)$ and $(0,-\pi)$. Clearly these are two isolated points. They can be seen in the 3D representation of the left plot of Fig. 5.5. For $k_0 = 0.3$ the velocity of the $s = -1$ subband vanishes at point $(0.3,\pi)$ and $(0.3,-\pi)$.

To evaluate equation (5.33) let us first distinguish two regime for the Fermi energy: *i)* $\mu + k_0^2 > 2t$; *ii)* $\mu + k_0^2 < 2t$. Let us consider first regime *i)* $\mu + k_0^2 > 2t$. The Heaviside functions in equation (5.33) restrict the integration over the variable x. For $x > 0$ the restriction is $\sqrt{\mu + k_0^2 - 2t} < x < \sqrt{\mu + k_0^2}$. For $x < 0$, restriction depends on the value of k_0. One must distinguish in turn three cases: a) $\sqrt{\mu + k_0^2 - 2t} < k_0 < \sqrt{\mu + k_0^2}$; b) $k_0 < \sqrt{\mu + k_0^2 - 2t}$; c) $k_0 > \sqrt{\mu + k_0^2}$. For regime *ii)* $\mu + k_0^2 < 2t$ the Heaviside functions give the following restrictions. For $x > 0$, one has $0 < x < \sqrt{\mu + k_0^2}$. For $x < 0$, we

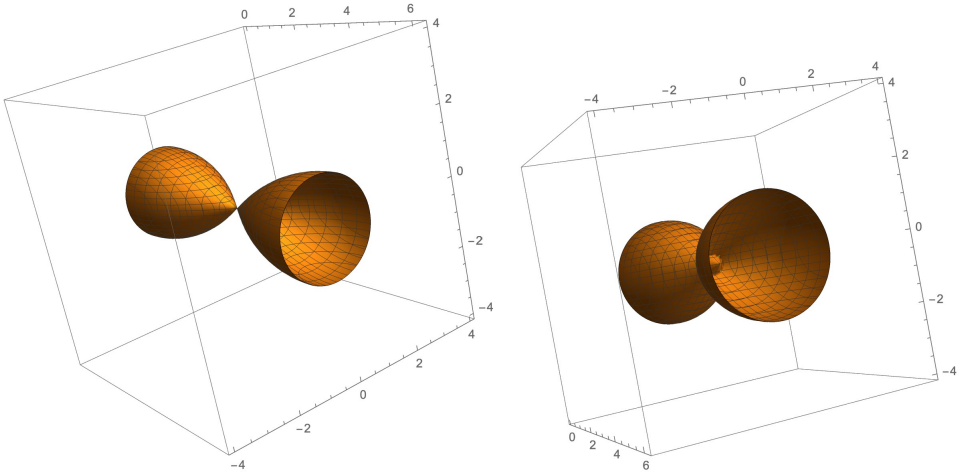

Figure 5.5: The Fermi surfaces for $\mu = 2t$ with $t = 1$. The image on the left is in the absence of spin-orbit interaction, $k_0 = 0$. The image to the right has spin-orbit interaction with $k_0 = 0.3$. In the absence of spin-orbit interaction, at the zone edge, the Fermi surface shrinks to a point, whereas with spin-orbit interaction there is a circle.

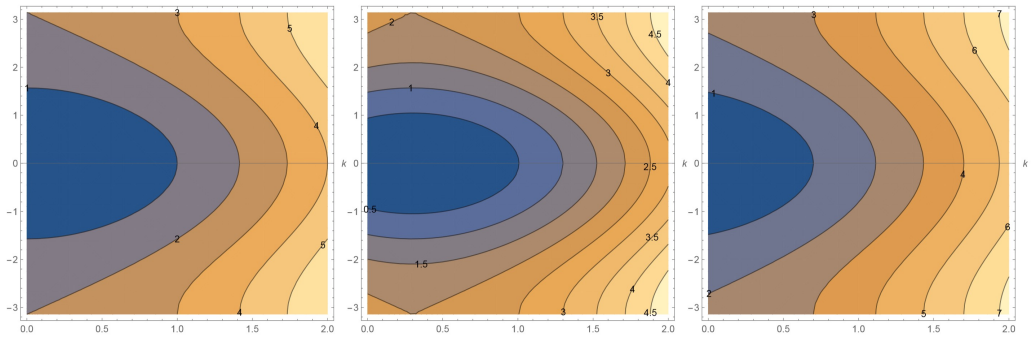

Figure 5.6: The contour plots of the 2D cut of the Fermi surface in the kp plane. The value of the hopping is set $t = 1$. The plot on the left is for the case with no spin-orbit interaction, $k_0 = 0$. The other two case are for $k_0 = 0.3$, for $s = -1$ (centre), $s = 1$ (right). The van Hove singularity occurs at $\mu = 2$ (in units of t) only for the helicity $s = -1$. This is clearly evident in the centre plot at points (k_0, π) and $(k_0, -\pi)$. These are the points where the band velocity vanishes signalling the van Hove singularity.

must consider two cases: a) $k_0 > \sqrt{\mu + k_0^2}$ one has $-\sqrt{\mu + k_0^2} < x < \sqrt{\mu + k_0^2}$; b) $k_0 < \sqrt{\mu + k_0^2}$ one has $-k_0 < x < \sqrt{\mu + k_0^2}$. We may then write the DOS in the final following form

$$\begin{aligned} N_-(\mu) = \theta(\mu + k_0^2 - 2t)[&\theta(\sqrt{\mu + k_0^2} - k_0)\theta(k_0 - \sqrt{\mu + k_0^2 - 2t})I_-(\sqrt{\mu + k_0^2 - 2t}, \sqrt{\mu + k_0^2}) \\ &+ I_-(-k_0, -\sqrt{\mu + k_0^2 - 2t}) + \theta(\sqrt{\mu + k_0^2 - 2t} - k_0)I_-(\sqrt{\mu + k_0^2 - 2t}, \sqrt{\mu + k_0^2}) \\ &+ \theta(k_0 - \sqrt{\mu + k_0^2})(I_-(\sqrt{\mu + k_0^2 - 2t}, \sqrt{\mu + k_0^2}) + I_-(-\sqrt{\mu + k_0^2}, -\sqrt{\mu + k_0^2 - 2t}))] \\ &+ \theta(2t - \mu - k_0^2)[\theta(k_0 - \sqrt{\mu + k_0^2})I_-(-\sqrt{\mu + k_0^2}, \sqrt{\mu + k_0^2}) + \theta(\mu + k_0^2 - k_0)I_-(-k_0, \sqrt{\mu + k_0^2})]. \end{aligned} \tag{5.41}$$

A similar analysis can be done for helicity $\lambda = 1$. One has

$$\begin{aligned} N_+(\mu) = \frac{1}{2\pi^2} \int_{k_0}^{\infty} dx(x - k_0) \\ \frac{\theta(\mu + k_0^2 - x^2)\theta(x^2 + 2t - \mu + k_0^2)}{\sqrt{(\mu + k_0^2 - x^2)(x^2 + 2t - \mu + k_0^2)}}, \end{aligned} \tag{5.42}$$

where $x = k_{\parallel} \mp k_0$ for $\lambda = \mp 1$ and $\theta(x)$ is the Heaviside step function.

The DOS expression can be computed with Mathematica by using the built-in Heaviside function and numerical integration command. In Fig. 5.7 are reported the plots of N_-, N_+ (partial DOS), and $N_- + N_+$ (total DOS), respectively for four values of $k_0 = 0.1,\ 0.2,\ 0.3,\ 0.41,\ 0.5,\ 0.6,\ 0.7,\ 0.8$ and $t = 1$. The partial and the total DOS are reported as a function of the rescaled Lifshitz parameter defined in the equation (5.22) where, in this case, $E_2 = 0$, $\Delta E_{RSOC} = -k_0^2$ and $\Delta E = \omega_0 = \Delta E_{z2} = \varepsilon_z = 2t$.

The black curve corresponds to the case when there is no spin-orbit present. Clearly, the value $\eta_R = 1$ (in units of t) marks the point of the band edge for the dispersion along the z-axis. The spin-orbit interaction develops a van Hove singularity exactly at this point. This behaviour, as we will see below, appears in agreement with the more realistic model. This point, $\eta_R = 2t/\Delta E_{z2}$, corresponds to the singularity in the two-dimensional Rashba model at the bottom of the lower band with helicity $\lambda = -1$. In the 3D case the singularity appears at the edge of the band due to the motion along z.

The Fig. 5.7, also, shows that as k_0 increases, N_+ increases while N_- decreases, in the sum this involves a change only in the proximity of the van Hove singularity. More precisely, while at the Lifshitz transition the partial densities combine to yield a strong change in the DOS, at high energies they compensate, so that the total DOS coincides with the total DOS in the absence of RSOC. This means that in the high-energy limit the parameters of the normal phase and, as we will see below, of the superconducting phase do not depend on k_0, in accordance with the work of Gor'kov and Rashba [133].

5.2.4 Numerical results for the full model

After the analysis of the simplified tight-binding model, we study the properties of the normal phase starting from the solution of the model of equation (5.2) obtained numerically.

For the numerical solution of the normal phase the chosen parameters are: the barrier $V = 0.5\ eV$, the thicknesses of the metallic and insulating layers $L = 23$ Å, $W = 7$ Å, respectively, with total periodicity $d = 30$ Å, the effective masses $m = m_z = m_e$, the cut-off energy $\omega_0 = 30\ meV$ and the coupling constant $g = 0.4$.

According to the works [18, 137], we express the Rashba coupling constant in the form of the equation (5.4).

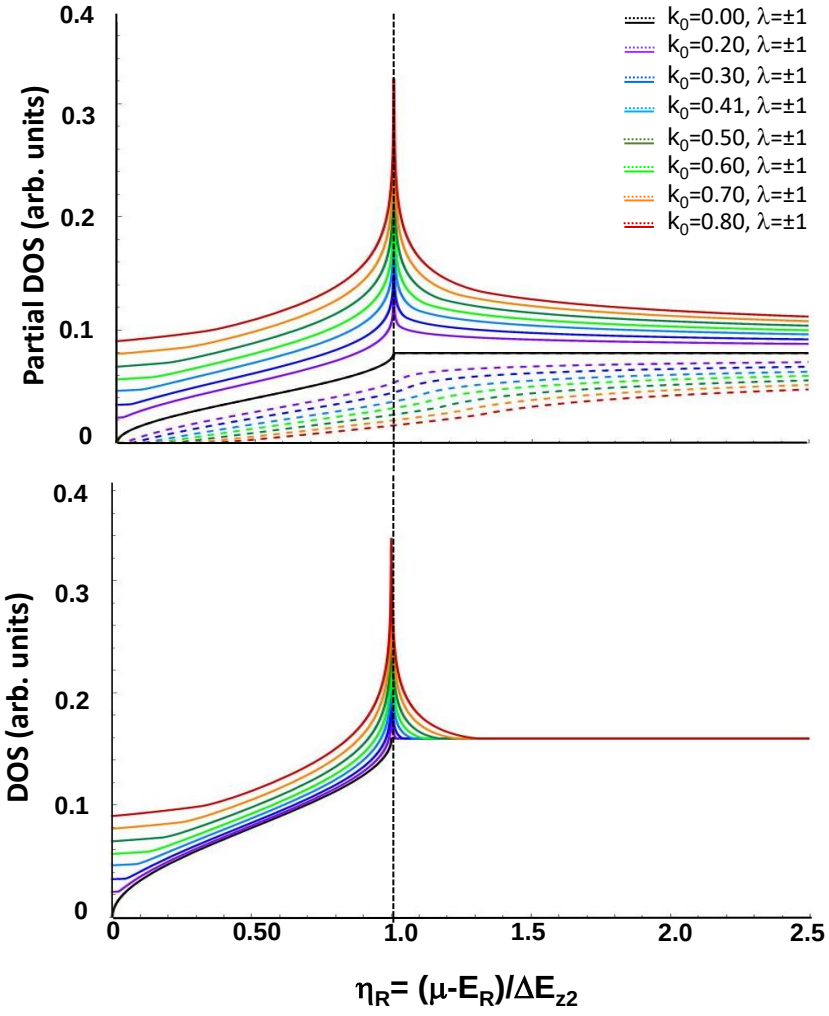

Figure 5.7: *Total and partial DOS as a function of* η_R (equation (5.22)). *Top panel*: the partial DOS N_- (equation (5.38)) and N_+ (equation (5.42)) as function of the rescaled Lifshitz parameter η_R. The black curve is $k_0 = 0$. The other curves have increasing values of $k_0 = 0.1,\ 0.2,\ 0.3,\ 0.41,\ 0.5,\ 0.6,\ 0.7,\ 0.8$. Here $t = 1$. *Bottom panel*: the total DOS $N_- + N_+$ given in Eqs.(5.38), (5.42) as function of rescaled Lifshitz parameter η_R. The black curve is $k_0 = 0$. The other curves have increasing values of $k_0 = 0.1,\ 0.2,\ 0.3,\ 0.41,\ 0.5,\ 0.6,\ 0.7,\ 0.8$. Here $t = 1$.

where α_{SO} is a dimensionless parameter which describes the strength of the Rashba momentum in units of the inverse lattice spacing along the z-direction.

Similarly to what has been done for the tight-binding model, we carry out the analysis of the evolution of Fermi surfaces for $E_2(k_z)$ obtained numerically by distinguishing for each of the listed regimes three distinct cases: $\Delta E_{z2} \gtreqless \Delta E_{RSOC}$, where $\Delta E_{z2} = E_{2,max}(k_z) - E_{2,min}(k_z)$ is the bandwidth of the dispersion along the axis of confinement z in the presence of a potential of the Kronig-Penney form, while in this case $\Delta E_{RSOC} = E_0 = -(m\alpha^2)/(2\hbar^2)$ is the energy shift due to the RSOC. The model parameters are chosen so that ΔE_{z2} is of the same order of magnitude as the cut-off energy.

This study concerns a two-band system, where the first subband has a s-symmetry, while the second one has p-symmetry. The results are shown in the Fig. 5.8: in the *panels* **A)**, **B)**, **C)** and **D)** we plot the isoenergetic curves in the $(k_{\|}, k_z)$-*plane* for $\lambda = \pm 1$ and for the first and the second subbands versus the Lifshitz parameter, η, equation (5.21) where $E_2 = 163.64\ meV$ is the band edge of the second subband in the absence of RSOC and ω_0 is the cut-off energy for $\hbar = 1$. In this figure we also report the evolution of Fermi surfaces for three distinct values of the parameter η. The analysis is made for $\alpha_{SO} = 0.41$ value for which the condition $\Delta E_{RSOC} = \Delta E_{z2} = \omega_0$ is verified. In the case of the second subband for an energy value close to the van Hove singularity (η_L) we take into account that in the presence of RSOC the spinor (equation (5.15)), and the gap (equation (6.18)), depend on a phase factor $e^{i\vartheta}$ and the removal of the spin degeneracy splits the dispersion in two bands with opposite helicity. To take this into account we plot the FS with a colour that varies with ϑ. In particular, for $\lambda = 1$ it varies from red to purple, while for $\lambda = -1$ it varies from purple to red.

We highlight the three regimes analysed previously and a change in symmetry in passing from the first to the second subband. Such a change, for the first subband, occurs at the point Γ, origin of the first Brillouin zone (IBZ), while, in the second subband, it occurs at the point Z, edge of the IBZ in the z-direction. As the Rashba coupling changes ($\Delta E_z \gtreqless \Delta E_{RSOC}$), only a flattening of the contour lines and Fermi surfaces is observed to the left and a shift to the right of the singular points. The latter are the points where the phase velocity vanishes and which generate, for rotation around the k_z-axis, circles whose radius increases with α_{SO}. The energy in which this van Hove unusual singularity occurs is indicated in the figure with η_L and in the literature it is called neck opening energy. We can note that for the bands with positive helicity η_L is independent of the value of α_{SO}, while for the bands with negative helicity it varies as the RSOC varies.

This behaviour is confirmed by Fig. 5.9 where we plot the partial DOS for $\alpha_{SO} = 0.20$ ($\Delta E_{RSOC} > \Delta E_{z2}$), $\alpha_{SO} = 0.41$ ($\Delta E_{RSOC} > \Delta E_{z2}$) and $\alpha_{SO} = 0.50$ ($\Delta E_{RSOC} > \Delta E_{z2}$). In this figure η_L coincides with the value for which the partial DOS relative to $\lambda = -1$ for the first and second subband have a maximum. As you can see, as α_{SO} increases, the η_L parameter decreases while the value of the partial DOS peak $\lambda = -1$ increases. In particular, in the case of the first subband for $\lambda = -1$, $\eta_L = -5.2$ for $\alpha_{SO} = 0.50$, $\eta_L = -4.6$ for $\alpha_{SO} = 0.41$ and $\eta_L = -4.0$ for $\alpha_{SO} = 0.20$. Indeed, in the case of the second subband for $\lambda = -1$, $\eta_L = -0.37$ for $\alpha_{SO} = 0.50$, $\eta_L = 0.11$ for $\alpha_{SO} = 0.41$ and $\eta_L = 0.78$ for $\alpha_{SO} = 0.20$. In the right panel of Fig. 5.9 we report the projection of the Fermi surfaces in the plane (k_x, k_y) at the point Z of the IZB for $\eta = 3$, where we have highlighted the two possible values of helicity with different colours (light blue for $\lambda = -1$ and orange for $\lambda = 1$).

What can be seen from the graphs in the Fig. 5.9 is a peak in the partial DOS, and

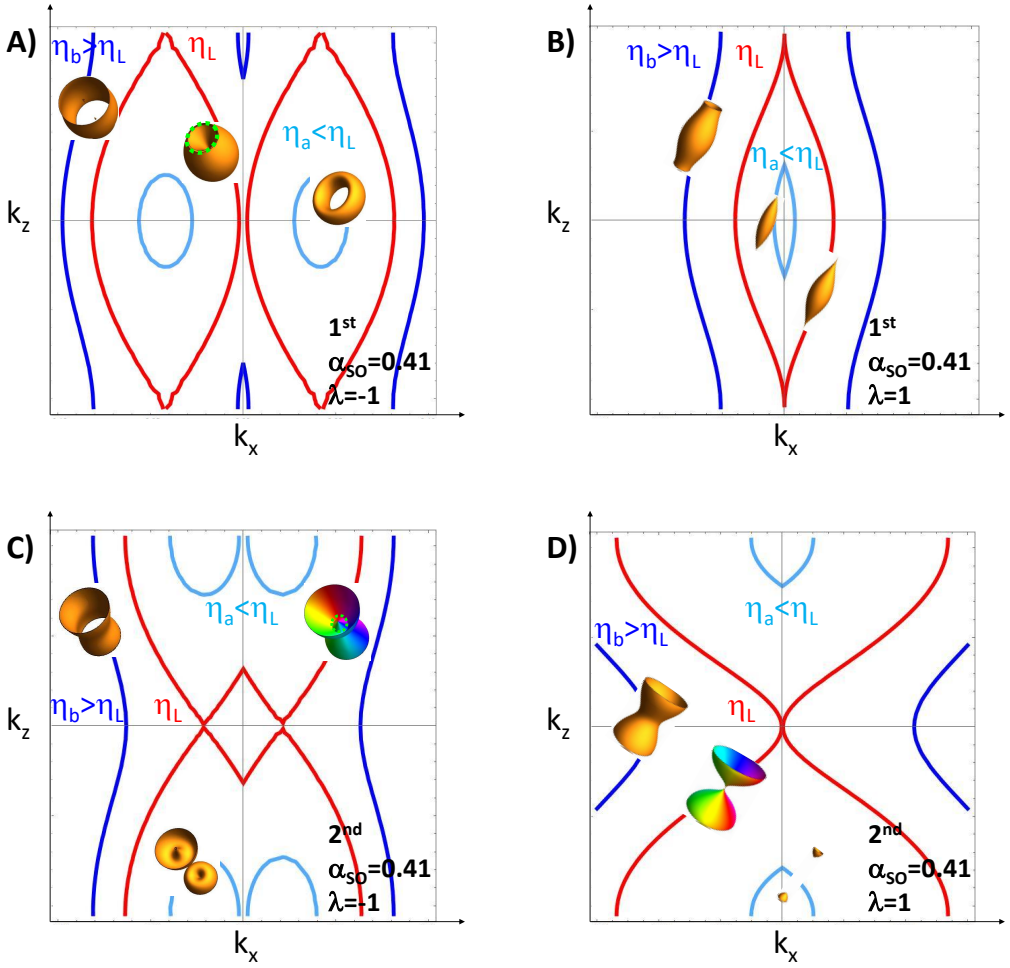

Figure 5.8: *Isoenergetic curves, Fermi surfaces for the first and second subbands at three differents values of Lifshitz parameter.* The *top panels* show the case of $\lambda = 1$ (left) and $\lambda = -1$ (right) for the first subband and for $\Delta E_{RSOC} = \Delta E_{2z}$ ($\alpha_{SO} = 0.41$). The *bottom panels* show the same analysis carried out for the second subband. The DOS maximum is observed at η_L where the system develops a van Hove singularity. In this case the Fermi surface develops a nodal line highlighted in panels **A)** and **C)** with a dashed green line. For $\lambda = 1$, both for the first and for the second subband, η_L is independently of the value of α_{SO} and it's equal to $-3.9\ meV$ and $0.92\ meV$, respectively. While for $\lambda = -1$, η_L changes with α_{SO} (as underlined in Fig. 5.9), for the first subband $\eta_L = -4.6\ meV$, for the second $\eta_L = -0.11\ meV$. In the panel **C)** and **D)**, for $\eta = \eta_L$ we highlight the phase factor with the colours of the rainbow and the nodal line (white dashed curve) of the singular points.

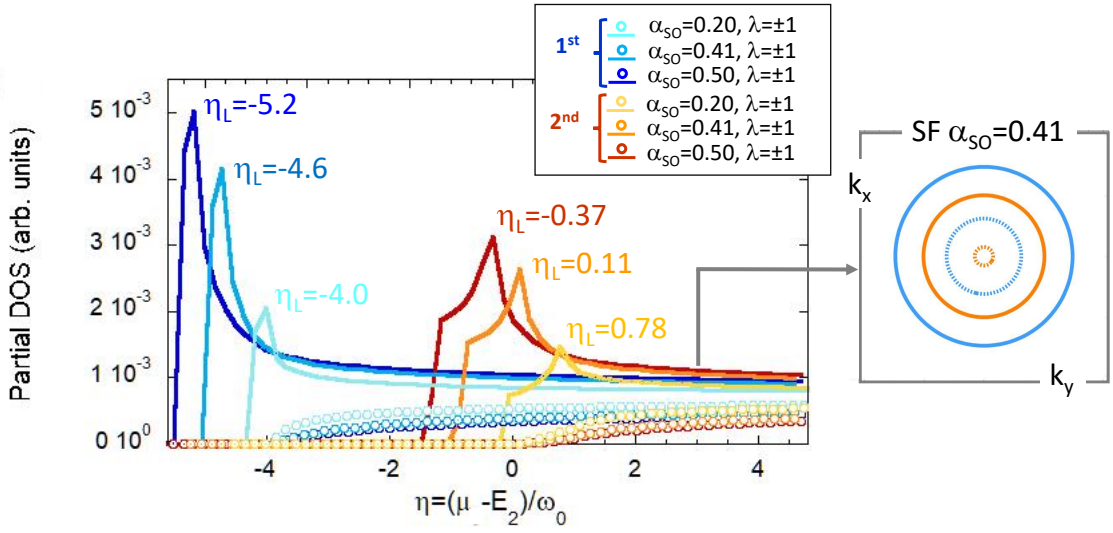

Figure 5.9: *Partial density of the states vs* η *and projection of the FS in the plane* (k_x, k_y) *at* $k_z = Z$. In the *left panel* the continuous curves represent the partial DOS for $\lambda = -1$, the dots those for $\lambda = 1$, the shades of blue refer to the first subband for three different values of $\alpha_{SO} = 0.20,\ 0.41,\ 0.50$, while the shades of red to the second subband. The figure shows that the value of η_L, for which the FS have a nodal line (Fig. 5.8), decreases as α_{SO} increases by an amount equal to E_0/ω_0, while the peak of the partial DOS $\lambda = +1$ increases. In the *right panel* the light blue curve represents the projection of the FS relative to $\lambda = -1$ in the (k_x, k_y)-plane for the first subband, the light blue dashed curve is relative to $\lambda = 1$. Similarly, the orange curves refer to the second subband. This panel is built for $\alpha_{SO} = 0.41$ and $\eta = 3$.

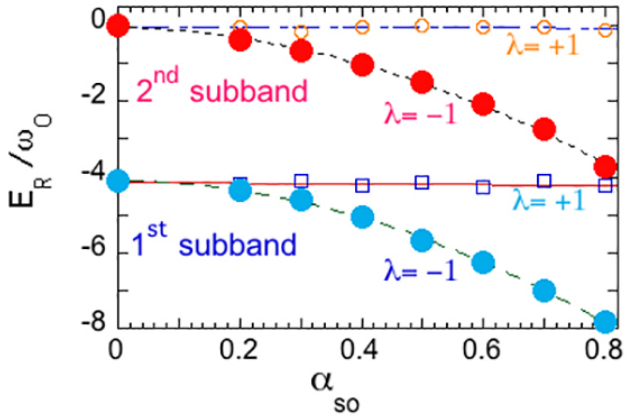

Figure 5.10: *Normalized band-edge energy as a function of the RSOC constant.* The orange empty circles represent the band edge energy *vs* α_{SO} (bottom axis) or *vs* α (top axis) for the second subband and $\lambda = 1$, while the blue empty squares are relative to the first subband at the same helicity value. The red dots, on the other hand, represent the band edge energy for the second subband at $\lambda = -1$, the light blue dots refer to the first subband for the same helicity value. As noted earlier, a Rashba shift can only be observed for negative helicity bands.

then in the total DOS, corresponding to an energy value equal to $E_0/\Delta E_{z2} = E_0/\Delta E = E_0/\omega_0 = -(m\alpha^2)/(2\omega_0)$ which, as the coupling constant Rashba increases, it increases and shifts to gradually smaller Lifshitz parameter values, and the shift involves only the negative helicity bands. This is underlined in the Fig. 5.10, in which we have reported the normalized band-edge energy, E_R in the equation (5.22), for the first and the second subband for the two distinct helicity values as a function of the RSOC constant.

Finally, note that, for the values of the normalized band-edge energy, from this point on, we report the results in terms of the rescaled Lifshitz parameter (equation (5.22)).

In the normal phase for a two-band system we plot the total density of the states (DOS) and the partial DOS as the Rashba coupling changes ($\Delta E_z \gtreqless \Delta E_{RSOC}$) and compare it with the case without RSOC (Fig. 5.11). In Fig. 5.11 the DOS is plotted versus the rescaled Lifshitz parameter, η_R for different values of α_{SO}.

In the case of positive helicity the DOS trend is that of a sloped step, very similar to the trend observed in the absence of RSOC, while in the case of negative helicity we can observe a peak in the density of the states and a shift of the latter towards the left as the parameter α_{SO} increases. This confirms what has been commented for the figures 5.6, 5.7, 5.8, 5.9, or that the effects of a Rashba spin-orbit coupling become more marked for the negative helicity subband.

In a generic 3D system with free-electron like dispersion relation, the DOS behaves as the square root of energy, whereas in a quantum layer ($2D$) the DOS is constant and so that it jumps sharply every time a new quantum number from a new layer takes over. In present case, the DOS shows almost a $2D$-like behaviour for the first subband. In fact, this is nearly pure 2D subbands with a negligible transversal hopping between the layers. Instead, at the bottom of the second subband appears a sharp step due to contribution of the partial density of states of the second subband to the total density of states. The total energy dispersion of the second subband, ΔE_{z2} determines the energy separation between the top and the band edge energy for the second subband. In the energy range $\eta_{2edge} < \eta < \eta_{2top}$ (where η_{2edge} and η_{2top} are, respectively, the Lifshitz parameter at the edge and at the top of the second subband), the electronic structure is like that of an anisotropic 3D electron gas, while the 2D character appears at higher

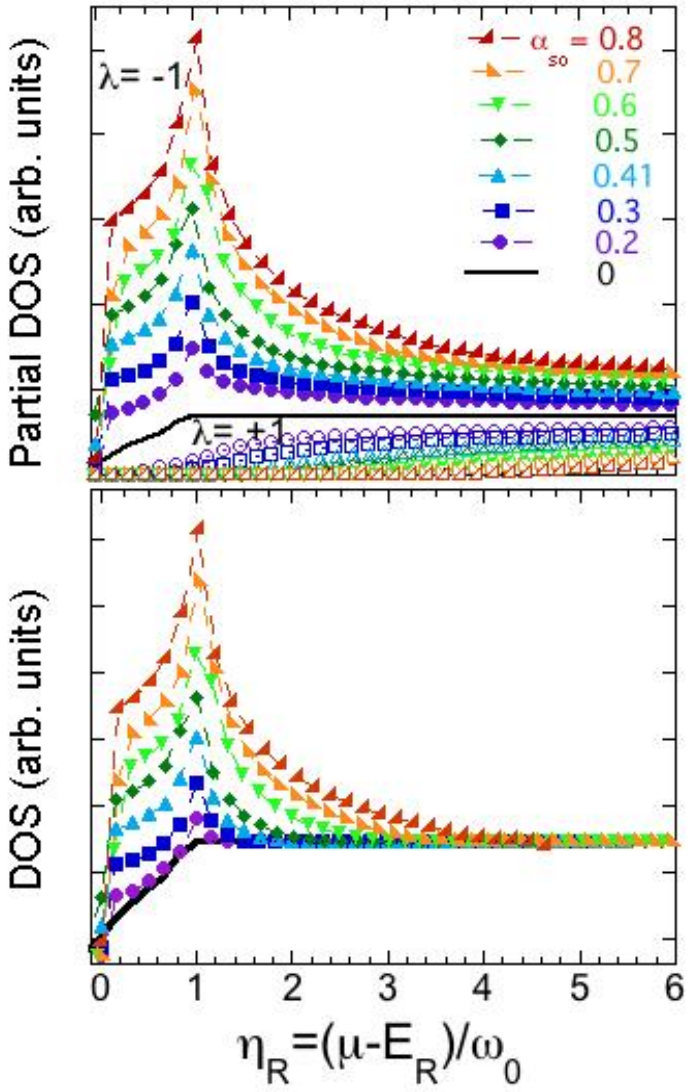

Figure 5.11: *The DOS for the first and the second subband as the α_{SO} changes.* In particular, we have chosen values for this parameter between 0.2 and 0.8 in order to reproduce the three cases previously discussed $\Delta E_z \gtrless \Delta E_{RSOC}$ and compare them with the case of no RSOC, $\alpha_{SO} = 0$. What is observed is that as the RSOC increases, the DOS peak becomes more pronounced and shifts to gradually smaller energies, since the peak occurs at E_0/ω_0.

energy $\eta > \eta_{2top}$.

The observed Rashba shift can be understood by considering the simplified model previously introduced. In the absence of RSOC the vanishing of the energy gradient occurs in an isolated point and, therefore, there are no singularities in the DOS. In contrast in the presence of RSOC, the energy gradient vanishes at finite values of the absolute values in-plane momentum, $k_{\|}$, therefore we have singular points distributed on circumferences that generate van Hove peaks in the DOS. As the RSOC increases, the energy in which van Hove peaks occur move to the left, but, as underlined in the discussion of the tight-binding model, the difference in energy between the band edge and the maximum DOS value remains constant and equal to the dispersion along z.

The shape of the Fermi surface is crucial for understanding the electronic properties of metals. As first noticed by Lifshitz [91], changes in the Fermi surface topology cause anomalous behavior of thermodynamic, transport and elastic properties of materials. Intuitively, the simplest way to observe such an electronic topological transition, also known as Lifshitz transition, is by tuning the Fermi level to the singular point in the band structure where the change of topology takes place. This requires considerable variations of the electron density. A quantum critical point appears in the proximity of a Lifshitz transition with typical quantum criticalities and possible quantum tricritical behavior in itinerant electron systems.

There are two types of Lifschitz transition: type I, the appearance of a new detached Fermi surface region or appearance or disappearance of a new Fermi surface (FS) spot, and type II, the disruption of the neck-collapsing-type of Lifschitz transition that can be induced by orbital symmetry breaking in lightly hole doped bands. In the Fig. 5.8 we show that a new 3D FS opens when the chemical potential crosses the band edge energy, and the electron gas in the metallic phase undergoes an electronic topological transition (ETT). When the chemical potential is beyond the band edge in an anisotropic system at a higher energy threshold, the electronic structure undergoes a second ETT, the 3D-2D ETT, where the FS changes topology from 3D to 2D or viceversa, called also the opening or closing of a neck in a tubular FS or neck collapsing. This ETT is a common feature of all existing high-temperature superconductors and novel materials synthesized by material design in the search for room-temperature superconductivity.

However, the analysis made in this section highlights some surprising results, the first is that there is a change in symmetry of the evolution of the FS topology in passing from the first to the second subband. The second is that in the proximity of a second-type Lifshitz transition we have a curve of critical points and no longer an isolated point, this explains the appearance of a very pronounced peak in DOS values. The radius of this curve increases with the intensity of the RSOC and this is reflected in an increase and at the same time a true right shift of the DOS maximum. In this situation, the variation in the Fermi surface (FS) topology is absolutely non-trivial.

Clearly, we want to see how the above features of the electron spectrum and of the DOS are reflected in the properties of the superconducting phase. Therefore, after having analysed in detail the structure of the FS and the DOS in the normal phase, we turn, in the next section, to the study of the superconducting phase.

6

Multigaps superconductivity at unconventional Lifshitz transition in a 3D Rashba heterostructure at atomic limit: superconductive phase

In order to investigate how the shape of the Fermi surface and the behaviour of the DOS manifest in the superconducting properties of the system with RSOC, we first derive the equations for computing the energy gap. The approach used is the one illustrated in Ref. [165, 170] by D. Innocenti et al., where the Bogoliubov-de Gennes equations are solved analytically and numerically without the typical approximations of the BCS theory and extended by us to the 3D case (*Chapter 3*). The entirely new thing in the following discussion, however, consists in using non-relativistic Dirac wavefunctions in order to take into account the additional spin degree of freedom.

The field operators of equation (5.20) can be written in terms of the single-particles states

$$\psi_{n\mathbf{k}\alpha}(\mathbf{r}) = \psi_{nk_z}(z)\frac{e^{i\mathbf{k}_\parallel\cdot\mathbf{r}_\parallel}}{\sqrt{\mathcal{A}}}\boldsymbol{\chi}_\alpha \equiv \tilde{\psi}_{n\mathbf{k}}(\mathbf{r})\boldsymbol{\chi}_\alpha, \tag{6.1}$$

where $\boldsymbol{\chi}_\alpha$ with $\alpha = \uparrow, \downarrow$ are the usual spinors associated to the quantization of the spin along the z-axis. This is a legitimate expression for the field operators since the functions $\psi_{n\mathbf{k}\alpha}(\mathbf{r})$ are the eigenfunctions of the Hamiltonian $\tilde{H}_R$ obtained by setting $\alpha = 0$ in equation (5.2), *i.e.*, completely neglecting the Rashba term. If we indicate with $c_{n\mathbf{k}\alpha}$ the operators that destroy a particle in the state (6.1) then the field operators becomes

$$\Psi_\alpha(\mathbf{r}) = \sum_{n,\mathbf{k}} \psi_{n\mathbf{k}\alpha}(\mathbf{r})\, c_{n\mathbf{k}\alpha} \tag{6.2}$$

and the interaction term can be written as[1]

$$H_I = \frac{U_0}{2} \sum_{\mathbf{k}_1,\mathbf{k}_2,\mathbf{k_3},\mathbf{k_4}} \sum_{\alpha,\beta} I^{n_1,\mathbf{k}_1;n_2,\mathbf{k}_2}_{n_3,\mathbf{k}_3;n_4,\mathbf{k}_4} \cdot \\ \cdot \; c^\dagger_{n_1,\mathbf{k}_1,\alpha} c^\dagger_{n_2,\mathbf{k}_2,\beta} c_{n_3,\mathbf{k}_3,\beta} c_{n_4,\mathbf{k}_4,\alpha}, \tag{6.3}$$

with the overlap integrals defined by

$$I^{n_1,\mathbf{k}_1;n_2,\mathbf{k}_2}_{n_3,\mathbf{k}_3;n_4,\mathbf{k}_4} = \int \tilde{\psi}^*_{n_1,\mathbf{k}_1}(\mathbf{r})\, \tilde{\psi}^*_{n_2,\mathbf{k}_2}(\mathbf{r}) \cdot \\ \cdot\, \tilde{\psi}_{n_3,\mathbf{k}_3}(\mathbf{r})\, \tilde{\psi}_{n_4,\mathbf{k}_4}(\mathbf{r})\, d\mathbf{r}. \tag{6.4}$$

The integrals in equation (6.4) appear in the treatment of the superconductive phase transition in the presence of a periodic potential and have been extensively discussed [165]. The operators $a^\dagger_{n,\mathbf{k},\lambda}$ that create a particle in the state equation (6.1), are related to the $c^\dagger_{n,\mathbf{k},\alpha}$ operators by an unitary transformation

$$a^\dagger_{n,\mathbf{k},\lambda} = \sum_\alpha c^\dagger_{n,\mathbf{k},\alpha} \mathcal{M}_{\alpha,\lambda}(\mathbf{k}), \tag{6.5}$$

where the matrix element of the change of basis is equal to $\mathcal{M}_{\alpha,\lambda}(\mathbf{k}) = \boldsymbol{\chi}^\dagger_\alpha \cdot \boldsymbol{\eta}_\lambda\left(\theta_{\mathbf{k}_\parallel}\right)$. As a result, the four operator products that appear in the expansion of the right hand side of equation (5.20) can be written as

$$c^\dagger_{n_1,\mathbf{k}_1,\alpha} c^\dagger_{n_2,\mathbf{k}_2,\beta} c_{n_3,\mathbf{k}_3,\beta} c_{n_4,\mathbf{k}_4,\alpha} = \\ \sum_{\lambda_1,\lambda_2,\lambda_3,\lambda_4} M_{\lambda_1,\lambda_4}\left(\theta_{\mathbf{k_1}_\parallel} - \theta_{\mathbf{k_4}_\parallel}\right) M_{\lambda_2,\lambda_3}\left(\theta_{\mathbf{k_2}_\parallel} - \theta_{\mathbf{k_3}_\parallel}\right) \cdot \\ \cdot\, a^\dagger_{n_1,\mathbf{k_1},\lambda_1} a^\dagger_{n_2,\mathbf{k_2},\lambda_2} a_{n_3,\mathbf{k_3},\lambda_3} a_{n_4,\mathbf{k_4},\lambda_4}, \tag{6.6}$$

where we have defined

$$M_{\lambda_1,\lambda_4}(\theta_{\mathbf{k}_{1\parallel}} - \theta_{\mathbf{k}_{4\parallel}}) = \sum_\alpha U^\dagger_{\lambda_1,\alpha}(\mathbf{k}_1) U_{\lambda_4,\alpha}(\mathbf{k}_4), \tag{6.7}$$

and similarly for $M_{\lambda_2,\lambda_3}\left(\theta_{\mathbf{k_2},\parallel} - \theta_{\mathbf{k_3},\parallel}\right)$. Since the φ_{n,k_z} are Bloch wavefunctions, the integral (6.4) is different from zero only for $\mathbf{k}_1 + \mathbf{k}_2 = \mathbf{k}_3 + \mathbf{k}_4$ and the expression for H_I becomes

$$H_I = \frac{1}{2} \sum_{n_1,n_2,n_3,n_4,\mathbf{k}_1,\mathbf{k}_2,\mathbf{K}} U^{n_1,\lambda_1;n_2,\lambda_2}_{n_3,\lambda_3;n_4,\lambda_4}(\mathbf{k}_1,\mathbf{k}_2;\mathbf{K}) \\ a^\dagger_{n_1,\mathbf{k}_1,\lambda_1} a^\dagger_{n_2,-\mathbf{k}_1+\mathbf{K},\lambda_2} a_{n_3,-\mathbf{k}_2+\mathbf{K},\lambda_3} a_{n_4,\mathbf{k}_2,\lambda_4}, \tag{6.8}$$

where the effective potential reads

$$U^{n_1,\lambda_1;n_2,\lambda_2}_{n_3,\lambda_3;n_4,\lambda_4}(\mathbf{k}_1,\mathbf{k}_2;\mathbf{K}) = U_0 I^{n_1,\mathbf{k}_1;n_2,-\mathbf{k}_1+\mathbf{K}}_{n_3,-\mathbf{k}_2+\mathbf{K};n_4,\mathbf{k}_2} \\ M_{\lambda_1,\lambda_4}(\theta_{\mathbf{k}_{1\parallel}} - \theta_{\mathbf{k}_{2\parallel}}) M_{\lambda_2,\lambda_3}(\theta_{-\mathbf{k}_{1\parallel}+\mathbf{K}_\parallel} - \theta_{-\mathbf{k}_{2\parallel}+\mathbf{K}_\parallel}). \tag{6.9}$$

[1] In the *Appendix F* is it possible to find the complete derivation of the interaction Hamiltonian, while in the *Appendix D* you can see what changes for a different choice of axes.

Equation (6.8) is the expression of the interaction term when both RSOC and a periodic potential are present. It can be viewed as the *natural* extension to a multiband system of equation (4) of [133] and, from this point on, the computation of the superconducting gap follows the same steps. In agreement with Gor'kov and Rashba [133] we assume that the normal and the anomalous Green functions are diagonal in the helicity base. Hence we consider only Cooper pairs with zero net momentum ($\mathbf{K} = 0$), formed with particles in the same band and with the same helicity, $\{(n, \mathbf{k}, \lambda), (n, -\mathbf{k}, \lambda)\}$, which are connected by the time reversal symmetry operator. We allow for the contact exchange interaction H_I to connect pairs in different bands with different helicity: the pair $\{(n, \mathbf{k}, \lambda), (n, -\mathbf{k}, \lambda)\}$ can be scattered into the pair $\{(l, \mathbf{q}, \nu), (l, -\mathbf{q}, \nu)\}$ where n, λ, l, and ν can assume any allowed value. We emphasize that, as discussed in Ref. [133], the existence of a different pairing function in each helicity band implies a mixture of singlet and triplet pairing. Symmetric and antisymmetric combinations (see equation (22)) of Ref. [133]) of the pairing functions for the two helicity bands correspond to the singlet and triplet component with respect to the original spin quantization axis taken along the z-direction. This can be seen by using the transformation (6.5) connecting the electron operators between the original spin basis and the helicity basis.

Following the *standard* Gor'kov approach at finite temperature, we introduce the Matsubara imaginary time operators $a_{n,\mathbf{k},\lambda}(\tau)$ that follows the imaginary time evolution equation $-\partial_\tau a_{n,\mathbf{k},\lambda}(\tau) = [a_{n,\mathbf{k},\lambda}(\tau), H]$. In terms of these operators the *normal* $[G_{n,\lambda}(\mathbf{k}, \tau - \tau')]$ and the *anomalous* $[F^\dagger_{n,\lambda}(\mathbf{k}, \tau - \tau')$ and $F_{n,\lambda}(\mathbf{k}, \tau - \tau')]$ Green's functions are defined as

$$G_{n,\lambda}(\mathbf{k}, \tau - \tau') \equiv -\langle T_\tau a_{n,\mathbf{k},\lambda}(\tau) a^\dagger_{n,\mathbf{k},\lambda}(\tau')\rangle, \tag{6.10}$$

$$F^\dagger_{n,\lambda}(\mathbf{k}, \tau - \tau') \equiv \langle T_\tau a^\dagger_{n,-\mathbf{k},\lambda}(\tau) a^\dagger_{n,\mathbf{k},\lambda}(\tau')\rangle, \tag{6.11}$$

$$F_{n,\lambda}(\mathbf{k}, \tau - \tau') \equiv \langle T_\tau a_{n,-\mathbf{k},\lambda}(\tau) a_{n,\mathbf{k},\lambda}(\tau')\rangle, \tag{6.12}$$

where T_τ denotes the imaginary-time ordering operator. By using a mean-field approach, we arrive, after a lengthy algebra (see *Appendix F* for a complete derivation), to the self-consistent gap equation

$$\Delta_{n,\lambda}(\mathbf{k}) = -\frac{1}{2} \sum_{l,\mathbf{q},\nu} U'_{n,\lambda;l,\nu}(\mathbf{k}, \mathbf{q}) \frac{\Delta_{l,\nu}(\mathbf{q})}{2E_{l,\nu}(\mathbf{q})} \tanh\left(\frac{\beta E_{l,\nu}(\mathbf{q})}{2}\right), \tag{6.13}$$

where $\Delta_{n,\lambda}(\mathbf{k})$ is defined as

$$\Delta_{n,\lambda}(\mathbf{k}) \equiv \frac{1}{2} \sum_{l,\mathbf{q},\nu} U'_{n,\lambda;l,\nu}(\mathbf{k}, \mathbf{q}) F_{l,\nu}\left(\mathbf{q}, 0^+\right), \tag{6.14}$$

and the quasiparticle energy is

$$E_{l,\nu}(\mathbf{q}) = \sqrt{(\varepsilon_{\nu,\mathbf{q}_\parallel} + \varepsilon_{l,q_z} - \mu)^2 + |\Delta_{l,\nu}(\mathbf{q})|^2} \tag{6.15}$$

and the pairing potential reads

$$\begin{aligned} U'_{n,\lambda;l,\nu}(\mathbf{k}, \mathbf{q}) &\equiv U^{n,\lambda;n,\lambda}_{l,\nu;l,\nu}(\mathbf{k}, \mathbf{q}; \mathbf{0}) - U^{n,\lambda;n,\lambda}_{l,\nu;l,\nu}(-\mathbf{k}, \mathbf{q}; \mathbf{0}) \\ &= U_0 I_{n,l}(k_z, q_z) \lambda\nu e^{-i(\theta_{\mathbf{k}_\parallel} - \theta_{\mathbf{q}_\parallel})}, \end{aligned} \tag{6.16}$$

with the overlap integral

$$I_{n,l}(k_z, q_z) \equiv I^{n,\mathbf{k};n,-\mathbf{k}}_{l,\mathbf{q};l,-\mathbf{q}}. \tag{6.17}$$

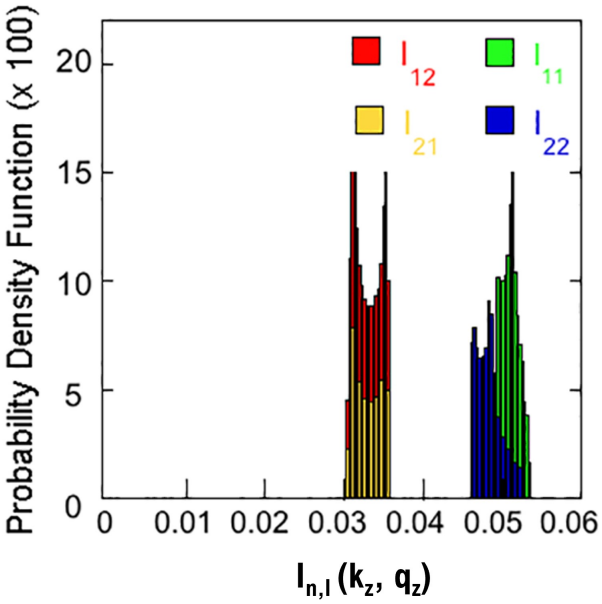

Figure 6.1: *Histogram of the matrix elements defining the superposition integral of* equation (6.17). The green and blue bars refer, respectively, to the intraband pairings $I_{1,1}(k_z, q_z)$ and $I_{2,2}(k_z, q_z)$, while the red and yellow bars refer to, respectively, to the interband couplings $I_{1,2}(k_z, q_z)$ and $I_{2,1}(k_z, q_z)$. The histogram shows a marked anisotropy.

The matrix elements defined in the equation (6.17) depend on the subband index (n and l) and on the wavevector transversal to the layers (k_z and q_z). In the superposition integrals (equation (6.17)) only the dependence on the transverse moment remains, since the wavefunctions in the plane are plane waves which compensate for the choice made on $\mathbf{K}$. For a periodic potential barrier associated with the superlattice of layers the density histogram of pairing interaction matrix elements between subbands is illustrated in the Fig. 6.1. The intraband (diagonal elements of matrix) and interband (off-diagonal elements of matrix) distributions show different shapes and widths and have different range of values. In particular, the off-diagonal elements have a probability density function which is about half of the diagonal elements which instead are of the same order of magnitude.

While in the Fig. 6.1 the dependence on the band indices of the exchange integral is highlighted, in the Fig. 6.2 the dependence on wavevectors is highlighted. This last figure clearly shows that the diagonal elements of the matrix defined by the superposition integral are greater than those off-diagonal, whatever the value of the wavevectors. Furthermore, for both the intraband and the interband there is a curve of values of k_z and q_z for which $I_{11} = I_{22}$ and $I_{12} = I_{21}$, whereas on the right of this curve $I_{11} < I_{22}$ and $I_{12} < I_{21}$, the opposite being true on the left.

The integral equation (6.13) shows a dependence of the gap $\Delta_{n,\lambda}(\mathbf{k})$, reminiscent of the Rashba spinor equation (5.15), upon the helicity and the in-plane component of the wavevector through a phase factor $\lambda e^{i\theta_{\mathbf{k}_\parallel}}$. To get rid of this dependence in the self-consistent equation, we define an auxiliary gap function Δ_{nk_z} as

$$\lambda e^{i\theta_{\mathbf{k}_\parallel}} \Delta_{nk_z} \equiv \Delta_{n,\lambda}(\mathbf{k}). \tag{6.18}$$

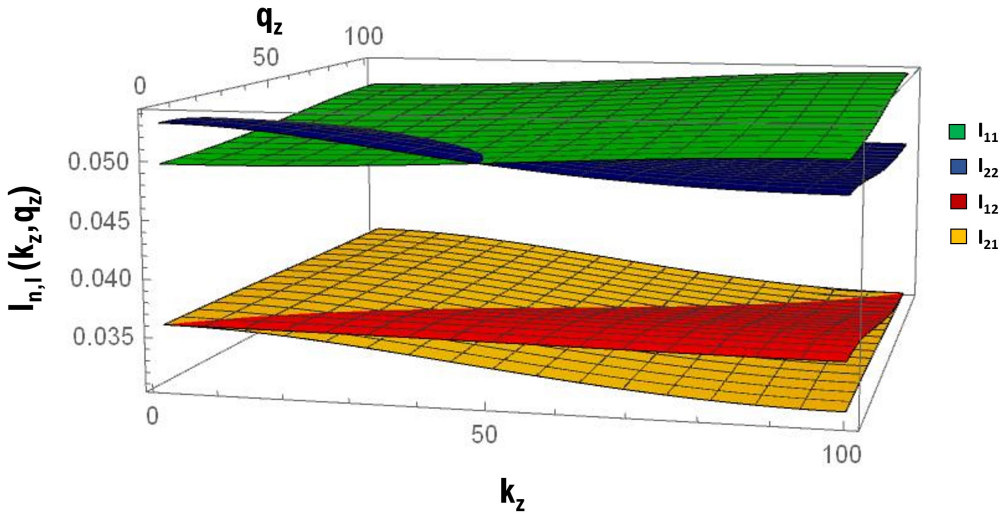

Figure 6.2: Terms of the matrix of the exchange integral defined in equation (6.17) as a function of the wavevectors in the direction of the confinement potential. The green plan corresponds to $I_{1,1}(k_z, q_z)$, the blue plan corresponds to $I_{2,2}(k_z, q_z)$, the red plan corresponds to $I_{1,2}(k_z, q_z)$ and the yellow plan corresponds to $I_{2,1}(k_z, q_z)$.

Then, the self-consistent equation for Δ_{nk_z} can be cast in the form

$$\Delta_n(k_z) = -\frac{U_0}{2} \sum_{l,q_z} I_{n,l}(k_z, q_z)\Delta_l(q_z) \times \sum_{\nu} \sum_{q_x,q_y} \frac{\tanh\left(\frac{\beta}{2} E_{l,\nu}(\mathbf{q})\right)}{2E_{l,\nu}(\mathbf{q})}, \tag{6.19}$$

where it is understood that the wavevector $\mathbf{q}$ appearing in the last term is $\mathbf{q} = (q_x, q_y, q_z)$. The solution of equation (6.19) is obtained numerically by starting with a guess for Δ_{nk_z} and iterating until convergence is reached. Since the computational effort is considerable, it becomes important to speed-up the calculations by reducing the dimensionality of the summations. In fact, once q_z has been fixed, the argument of the last sum depends on $q_\parallel$ only trough the in-plane dispersion energy $\varepsilon_{\nu,q_\parallel}$. It is, then, convenient to define a *partial* density of states $g_\nu(\varepsilon_\parallel)$ that allows a transformation of the double sum in equation (6.19) into a one-dimensional integral

$$\sum_{q_x,q_y} f(\varepsilon_{\nu,q_\parallel}) = \frac{\mathcal{A}}{4\pi^2} \int_{\varepsilon_{\parallel,min}}^{\varepsilon_{\parallel,max}} g_\nu(\varepsilon_\parallel) f(\varepsilon_\parallel) d\varepsilon_\parallel. \tag{6.20}$$

The integration extrema, $\varepsilon_{\parallel,min}$ and $\varepsilon_{\parallel,max}$, are computed by introducing the contact interaction energy cut-off in the sense that the condition $\varepsilon_{\parallel,min} < \varepsilon_\parallel < \varepsilon_{\parallel,max}$ implies the inequality $|\varepsilon_\parallel + \varepsilon_{l,q_z} - \mu| < \hbar\omega_0$.

It is worth to point out that $g_\nu(\varepsilon_\parallel)$ cannot be formulated as a single analytical function but it has to be defined with a piecewise expression that reflects the topology change of the Fermi Surface when switching from one regime to another (see sections

III.A, III.B, and III.C). In fact, the expression defining the partial density of states is

$$\begin{aligned}\frac{\mathcal{A}}{4\pi^2}g_\nu(\varepsilon_\parallel) &= \sum_{q_x,q_y}\delta(\varepsilon_\parallel-\varepsilon_{\nu,\mathbf{q}_\parallel}) \\ &= \frac{\mathcal{A}}{4\pi^2}\int_0^\infty 2\pi\mathbf{q}_\parallel\delta\left(\varepsilon_\parallel-\varepsilon_{\nu,q_\parallel}\right)d\mathbf{q}_\parallel,\end{aligned} \tag{6.21}$$

where the double sum has been transformed in a integral in polar coordinates in the last line. This leads to the following expression for $g_\nu(\varepsilon_\parallel)$

$$g_\nu(\varepsilon_\parallel)=\begin{cases}4\pi m\frac{-2\nu k_0}{\sqrt{2m\varepsilon_\parallel+k_0^2}} & \text{if } -\frac{k_0^2}{2m}\le\varepsilon_\parallel<0,\ \nu=-1\\ 4\pi m\frac{\nu k_0+\sqrt{2m\varepsilon_\parallel+k_0^2}}{\sqrt{2m\varepsilon_\parallel+k_0^2}} & \text{if } \varepsilon_\parallel>0\\ 0 & \text{otherwise}\end{cases} \tag{6.22}$$

where k_0 is defined as in the discussion preceding equation (5.26), but this time we do not set $2m=1$.

The equation (6.19) has been solved both in the limit $T\to 0$, (that is $\beta\to\infty$), and in the limit $T\to T_C$, (that is $\Delta_{nk_z}\to 0$ for every n and k_z). The first limit allows to determine the gaps while the second allows to determine the critical temperature.

The results of the numerical computations for the gaps are shown in the Fig. 6.3**A**, in which we plot both partial DOS and Δ_{nk_z} for the first and second subbands in $k_z=\pi/2d$ as a function of the rescaled Lifshitz parameter, η_R (equation (5.22)). The numerical values of the shift due to the Rashba coupling are indicated in the various panels which differ in the value of the α_{SO} parameter. Furthermore, in this discussion, we set the value of the superconducting coupling at $g=0.4$, where g is defined as $g=g_{3D}(\mu)U_0$ with $g_{3D}=\frac{1}{(2\pi)^2(\sqrt{\hbar^2/2m})^3}\sqrt{\mu}$ being the DOS at the Fermi level for a homogeneous system (no RSOC, no periodic potential along z). In the numerical simulation we assume that g is a constant, so as the chemical potential changes both g_{3D} and U_0 are continuously recalculated.

We emphasize that, in order to have the full gap, i.e., $\Delta_{\lambda n}(\mathbf{k})$, we must also consider the dependence on the phase factor and on the helicity, for this purpose we keep in mind the Fig. 5.8.

The Fig. 6.3**A** shows that both for the gap of the first subband (Δ_1) and for the gap of the second subband (Δ_2) it is possible to distinguish three distinct regimes of multigap superconductivity as a function of the rescaled Lifshitz parameter when is tuned around the unusual van Hove singularity: an antiresonant regime in which the gaps reach a minimum value for $\eta_R<\eta_L$, where η_L is the value of the van Hove energy for which the DOS shows a peak, a resonant regime for $\eta_R=\eta_L$ in which the gaps reach their maximum value and, finally, a multiband BCS-like regime for $\eta_R>\eta_L$.

In particular, it can be observed that Δ_1 has a minimum when the chemical potential is near the bottom of the second subband. The partial DOS relative to the first subband, both for $\lambda=1$ and for $\lambda=-1$, does not change as the chemical potential changes, therefore, the presence of a such pronounced minimum may be due to the existence of a Fano-type antiresonance in superconducting gaps. An antiresonance can be due to an interband exchange term that generates interference effects between the wavefunctions of a single particle by coupling in a non-trivial way the parameters of the superconducting phase relating to different bands. Both the depth and the position of the minimum in the Δ_1 depend on this term.

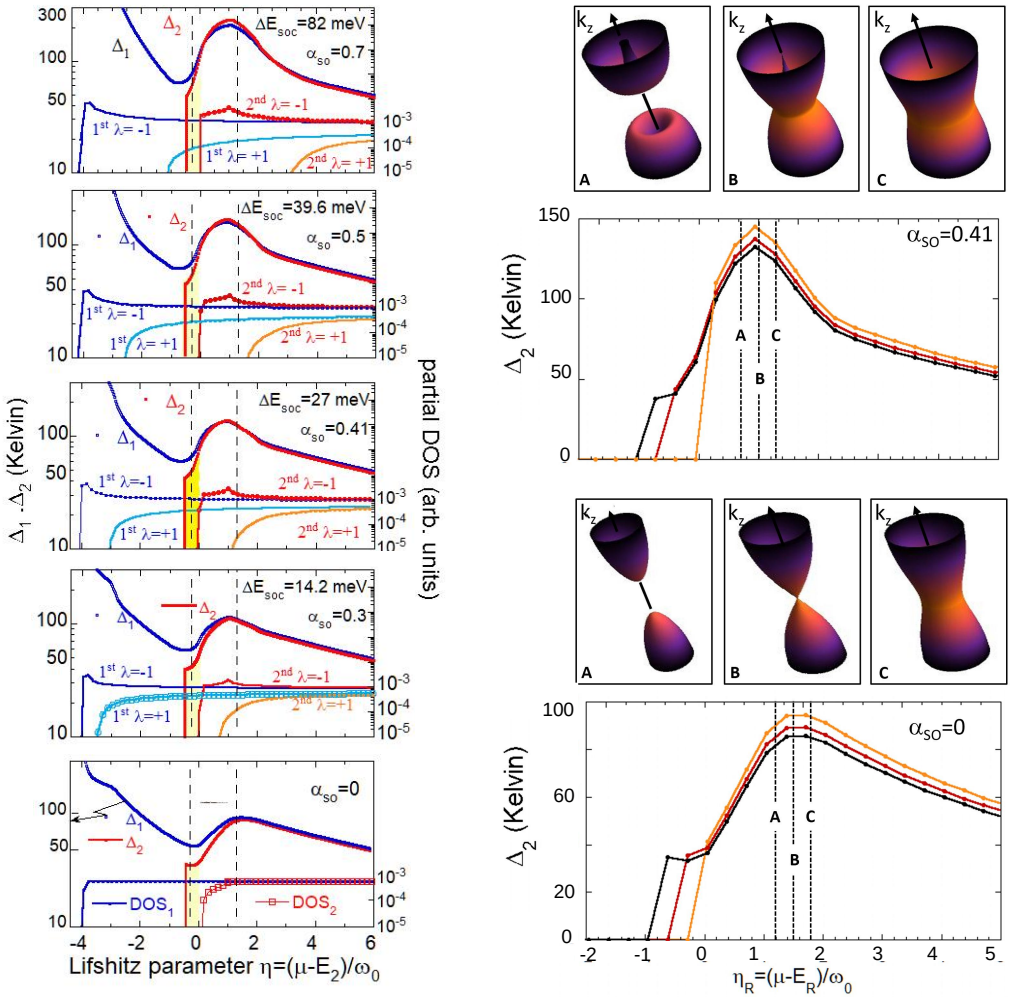

Figure 6.3: *Properties of the normal phase and the superconductive phase vs the rescaled Lifshitz parameter without and with RSOC for different α_{SO} values such that $\Delta E_{RSOC} \lessgtr \Delta E_{2z}$. Panel* **A**: starting from the bottom, the first panel shows the DOS for the first subband (blue curve) and the second subband (red curve) and the trend of the gap relative to the first subband (blue curve) and to the second subband (red curve) as a function of the rescaled Lifshitz parameter. The other panels are related to the four values of α_{SO} previously discussed, $\alpha_{SO} = 0.30,\ 0.41,\ 0.50,\ 0.70$, and show the partial DOS for the first subband with positive helicity (light blue curves) and with negative helicity (blue curves) and the partial DOS for the second subband with positive helicity (orange curve) and with negative helicity (red curves). We also report the trend of the gap relative to the first subband (blue curve) and to the second subband (red curve) as a function of the rescaled Lifshitz parameter. An anomalous behaviour and an amplification of the parameters of the superconductive phase are observed in a range of rescaled Lifshitz parameter $0 < \eta_R < 1$, i.e., in the proximity to the unusual van Hove singularity. *Panel* **B**: the values of the gaps for the second subbands at $\alpha_{SO} = 0$ and $\alpha_{SO} = 0.41$ *versus* the rescaled Lifshitz parameter for different values of $k_z = 0,\ \pi/2d,\ \pi/d$ show a small variation in a neighbourhood of van Hove unusual singularity. We have highlighted this variation on the Fermi surface in $\eta_R = \eta_L$ and $\eta_R = \eta_L \pm 0.5$ by choosing the black colour for $k_z = \pi/d$, the red colour for $k_z = \pi/2d$ and the orang colour for $k_z = 0$ consistent with the trends of the gaps.

A minimum in Δ_1 appears below the band edge where the DOS of the second subband changes abruptly and the Fermi surfaces, as seen above, are in a Lifshitz transition of the first type. That is, the partial filling of the second subband is reflected in the appearance of two new three-dimensional (3D) Fermi surfaces, one for each helicity.

As for the gap of the second subband (Δ_2), the Fig. 6.3**A** shows that it starts to assume non-zero values when the chemical potential has not yet reached the bottom of the second subband. This effect emphasizes, once again, the non-banal role of interband coupling in a multicomponent system.

Δ_2 reaches the maximum corresponding to the maximum of the partial DOS relative to the second subband and to a negative helicity, i.e., when the chemical potential is near the unusual van Hove singularity, in which the Fermi surfaces changes topology passing from a 3D to a two-dimensional (2D) geometry. As the Rashba parameter α_{SO} varies, as seen previously, the radius of the circumference of the singular points that characterizes the Fermi surface in a Lifshitz transition of the second type (3D-2D ETT) increases, and, as shows the Fig. 6.3**A**, the maximum values of Δ_1 and Δ_2 also increase. By varying the parameter α_{SO}, we distinguish three different regimes: if α_{SO} is such that $\Delta E_{RSOC} < \Delta E_{z2}$ the maximum of Δ_1 has a value greater than the maximum of Δ_2, for $\Delta E_{RSOC} = \Delta E_{z2} = \omega_0$ the maximum of the two gaps coincide within the limits of the numerical approximations made and, finally, for $\Delta E_{RSOC} > \Delta E_{z2}$ the maximum of Δ_2 exceeds the value of the maximum of Δ_1.

It can also be noted that in the high energy limit the values of the gaps are to a good approximation close to the BCS limit, i.e., in the high energy limit the gaps no longer depend on α [133].

In Fig. 6.3**B**, we plot the values of Δ_2 as a function of η_R for different values of k_z. It can be observed that Δ_1 does not vary as k_z varies from point Γ to point Z of the IZB, while it is possible to notice a small variation of Δ_2 in a neighbourhood of η_L, where the role of exchange integrals (equation (6.4)) becomes crucial.

For values of the Lifshitz parameter close to the van Hove singularity, for the second subband and for a helicity $\lambda = -1$ (the only one present) we plot the corresponding FS highlighting the dependence of Δ_2 from k_z with three different colours. In proximity of the unusual van Hove singularity the gap is not constant in k_z since the partial filling of the second subband causes the weight of ε_{l,q_z} in the equation (6.15) to be not negligible.

By solving the equation (6.19) in the limit $\Delta_{nk_z} \to 0$ we can be compute the critical temperature, T_C.

In the Fig. 6.4, *panel* **A**, we plot the values of the critical temperature at different values of the Rashba parameter, α_{SO}, as a function of the rescaled Lifshitz parameter. The critical temperature appears as an asymmetric function of the Lifshitz parameter regardless of the value of the α_{SO} parameter and shows the typical trend of a Fano antiresonance with a minimum at the first Lifshitz transition and a maximum at the second Lifshitz transition where the Fermi surfaces switch from 3D geometry to 2D geometry. From the Fig. 6.4**A** one can observe that in the presence of RSOC the energies are shifted to the left by an amount equal to $E_0 = -(m\alpha^2)/(2\hbar^2)$ and that the values of the T_C are amplified with respect to the case in which there is no RSOC. In particular, a maximum T_C value is observed in correspondence with the van Hove singularity in the DOS because we have assumed the energy cut-off and the energy dispersion in the z-direction to be the same. The BCS theory predicts a value of about 32 $Kelvin$ for the critical temperature, with the model parameters chosen in this work, for $\alpha_{SO} = 0.4$ this value increases about four times.

In the *panel* **B** of Fig. 6.4 we show in a log-log plot the critical temperature T_C

as a function of the effective Fermi temperature $T_F = E_F/k_B$ where the Fermi level is calculated from the bottom of the first subband and k_B is the Boltzmann constant. The critical temperature is calculated for different values of the Rashba coupling constant, $\alpha_{SO} = 0,\ 0.30,\ 0.41,\ 0.50,\ 0.70$. The Fano-resonance at the bottom of the second subband occurs in this so called Uemura plot [243] T_C versus T_F. In this figure the dashed line indicates the BEC-BCS crossover predicted to be $T_C = T_F/(k_F\xi_0)$ [71,244, 245]. The Fano-resonance clearly occurs on the BCS side of the BCS-BEC crossover where the ratio between T_F and T_C is in the range between 10 and 20. The calculated Fano resonance in the white region occurs on the BCS side up to the largest spin-orbit coupling. In fact the Fano-resonance occurs in the range between the BEC crossover and the line $T_C = T_F/20$ in the BCS side. From the figure it can be seen that the critical temperature values remain included in a BCS regime although as α_{SO} increases the Fano-resonance appears increasingly shifted towards the BEC limit.

Furthermore, it is possible to observe that the value of α_{SO} for which $\Delta E_{RSOC} = \Delta E_{z2} = \omega_0$ *i.e.* $\alpha_{SO} = 0.41$ marks the boundary between two distinct situations: if $\alpha_{SO} < 0.41$ the maximum of T_C grows slowly, while if $\alpha_{SO} > 0.41$ it grows faster and faster. All this is highlighted in the Fig. 6.5 in which we report the maximum of the T_C as a function of the Rashba coupling constant (red curve). The maximum of critical temperature increases linearly with RSOC for $\alpha_{SO} \geq 0.41$.

Previously we underlined the fact that near η_L the gaps vary with k_z, this being strongly reflected in the calculation of the gap ratio, $2\Delta/T_C$. Therefore, in order to plot this parameter correctly we consider Δ averaged over k_z. So, starting from the bottom of the Fig. 6.6 we plot the gap ratio, $2\Delta/T_C$, where T_C is the critical temperature, for the first and the second subband for different values of the α_{SO} parameter as a function of the rescaled Lifshitz parameter.

We observe that the gap ratio differs from the constant value 3.5 foreseen by the BCS theory when the rescaled Lifshitz parameter is closed to $0 < \eta_R < 1$. In particular, the $2\Delta_1/T_C$ ratio for the first subband reaches a minimum, greater than the value predicted by BCS theory, when the rescaled Lifshitz parameter is approximately equal to zero. That is, when Δ_1 is in an antiresonant regime and the system is close to a Lifshitz transition of the first type. The $2\Delta_1/T_C$ ratio reaches a maximum value for $\eta_R \approx 1$, when the superconducting parameter Δ_1 is in a resonant regime, this occurs close to the second-type Lifshitz transition.

Regarding to the gap ratio for the second subband, $2\Delta_2/T_C$, we observe a significant deviation from the value predicted by the BCS theory in a range of values of the rescaled Lifshitz parameter equal to $0 < \eta_R < 1$. In particular, when the system is in an antiresonant regime $2\Delta_2/T_C$ diverges, while when Δ_2 is in a resonant regime it shows a maximum. By contrast, such a maximum is not present in the absence of the RSOC as the bottom panel of Fig. 6.6 shows. As the parameter α_{SO} changes, the maximum of $2\Delta_2/T_C$ increases and, as in the case of the Fig. 6.3, we observe three distinct regimes: when $\Delta E_{RSOC} < \Delta E_{z2}$ we have $2\Delta_2/T_C < 2\Delta_1/T_C$, when $\Delta E_{RSOC} < \Delta E_{z2} = \omega_0$ the two gap ratios intersect and, finally, for $\Delta E_{RSOC} > \Delta E_{z2}$ we have $2\Delta_2/T_C > 2\Delta_1/T_C$.

We see in Fig. 6.6 that the gap ratio to the transition temperature $2\Delta_2/T_C < 3.9$ in the second subband, at the maximum critical temperature, in spite of the peak of the partial DOS in the second subband due the van Hove singularity brought about by the largest spin-orbit coupling $\alpha_{SO} = 0.7$, does not show a large deviation from the standard weak coupling universal value 3.52 predicted by the single-band BCS theory. This is in agreement with the corresponding gap ratio $2\Delta_1/T_C = 3.4$ in the first subband. We plot T_C versus the Δ_2/Δ_1 ratio for different values of the parameter α_{SO}

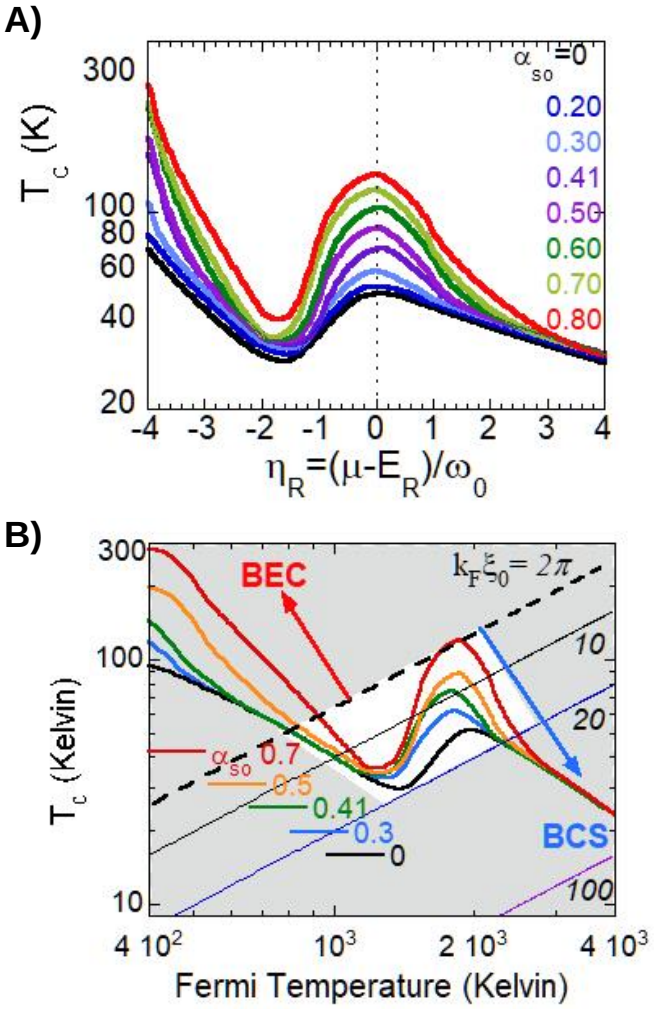

Figure 6.4: *Panel* **A**: the critical temperature T_C versus Lifshitz parameter for different values of Rashba coupling α_{SO} on a semi-logarithmic scale. The critical temperature appears as an asymmetric function of the Lifshitz parameter and if $\alpha_{SO} < 0.41$ the maximum of T_C grows slowly, while if $\alpha_{SO} > 0.41$ it grows faster and faster. *Panel* **B**: In this Uemura plot the critical temperature T_C is plotted on a log-log scale versus the Fermi temperature for different values of Rashba coupling α_{SO}. The white box refers to the Fano-resonance appearing near the BEC-BCS crossover indicated by the dashed line.

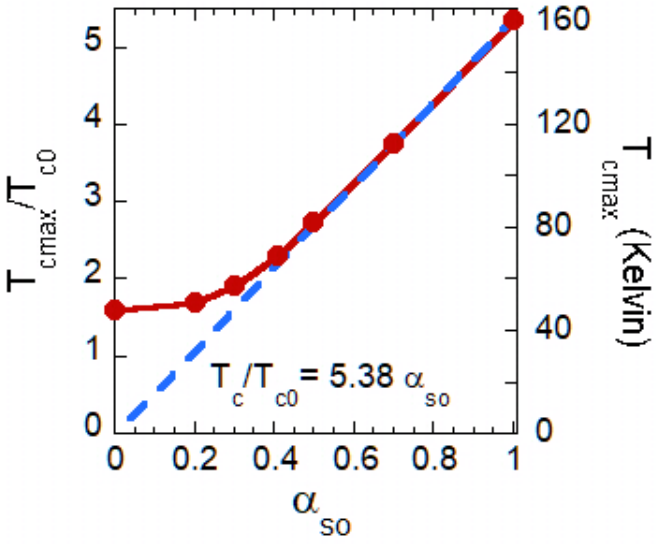

Figure 6.5: *The maximum value of the critical temperature (red curve) and the critical temperature predicted by the BCS theory ratio for different values of α_{SO} parameter.* What is observed is a marked amplification of the maximum of the T_C when a Rashba coupling is introduced into the system. In particular, the maximum of the critical temperature increases slowly for $\alpha_{SO} < 0.41$ and always becomes faster for $\alpha_{SO} > 0.41$.

in Fig. 6.7, which shows that Δ_2/Δ_1 ratio is only 1.12, at maximum T_C, for $\alpha_{SO} = 0.7$. Moreover we want to point out that for $\alpha_{SO} = 0.41$ the gap ratio $\Delta_2/\Delta_1 < 1$, while the ratio between the partial DOS $N_2/N_1 > 1$ due to the van Hove singularity in the second subband. These results show that the present superconducting scenario is in the weak coupling regime where the mean field approximation is valid. In fact the aim of this work is to show a scenario with weak electron-phonon coupling, where the amplification of the critical temperature has been driven by interband pairing in the presence of strong spin-orbit coupling. It is well known that in the multigap Bogoliubov-de Gennes superconductivity [246–248] the Δ_2/Δ_1 ratio becomes proportional to N_1/N_2 where the contact non retarded-exchange interaction (interband pairing) becomes more relevant that the retarded bosonic exchange pairing. From Fig. 6.7 we can see a marked anisotropy in the trend of the critical temperature which shows a maximum corresponding to the maximum value of the Δ_2/Δ_1 ratio.

Further work is in progress to study the cooperative role of contact and retarded interactions in anisotropic superconductivity related with the anisotropic k-space pairing in the Fermi surface topology at unconventional Lifshitz transitions.

As we have just seen, the Fig. 6.3 and the Fig. 6.6 clearly show a quantum resonance characterized by a Fano-type asymmetry in the superconducting parameters and a considerable deviation from the predictions of the BCS theory. To further highlight this last aspect we plot the isotopic coefficient, $\gamma = \partial ln T_C / \partial ln M$, as a function of the rescaled Lifshitz parameter for different values of the parameter α_{SO}, assuming that the cut-off energy depend on the isotopic mass as $\omega_0 \propto M^{-1/2}$ [171, 191] (Fig. 6.8).

In the BCS theory, the isotope coefficient has a constant value as the chemical potential changes equal to 0.5, in our case instead we can notice a considerable deviation from this value when the rescaled Lifshitz parameter is in the range $0 < \eta_R < 1$ (for this range of values, the behavior of the γ parameter is that typical of the Fano antiresonance), that is, when the system is close to a Lifshitz transition. These deviations

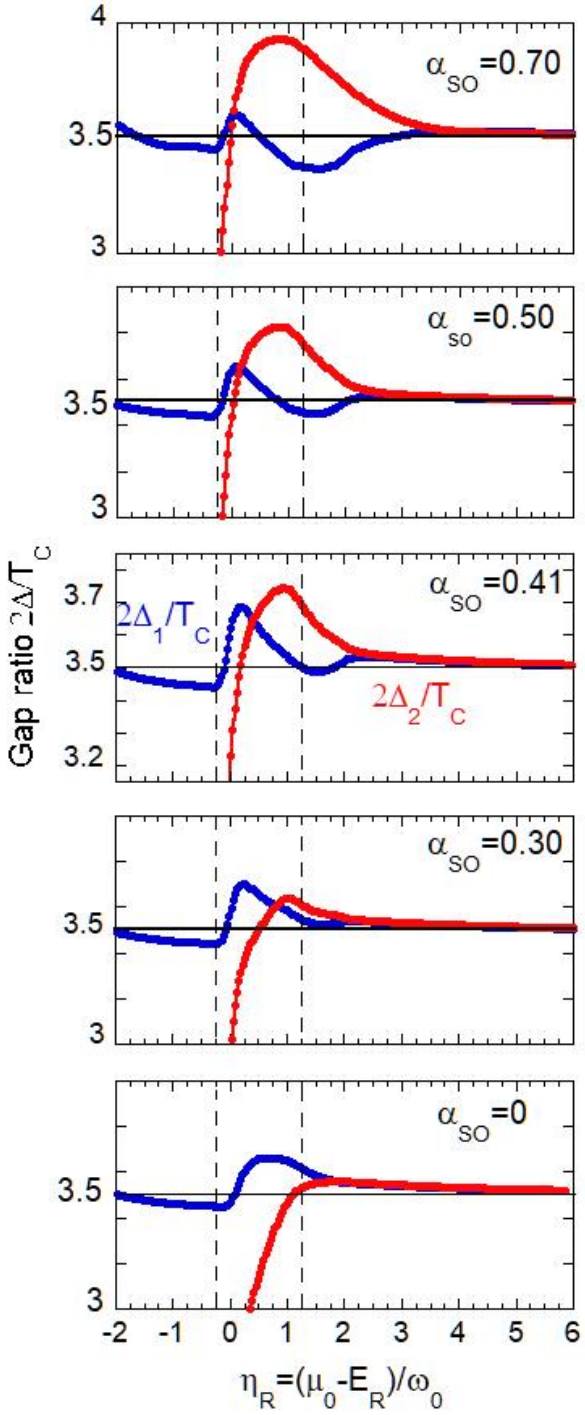

Figure 6.6: *Properties of the superconductive phase vs the Lifshitz parameter without and with RSOC for different α_{SO} values such that $\Delta E_{RSOC} \gtreqless \Delta E_{2z}$.* This figure shows both the trend of the gap ratio for the first subband (blue curves) and the second subband (red curves) compared to the constant value predicted by the BCS theory (black curves).

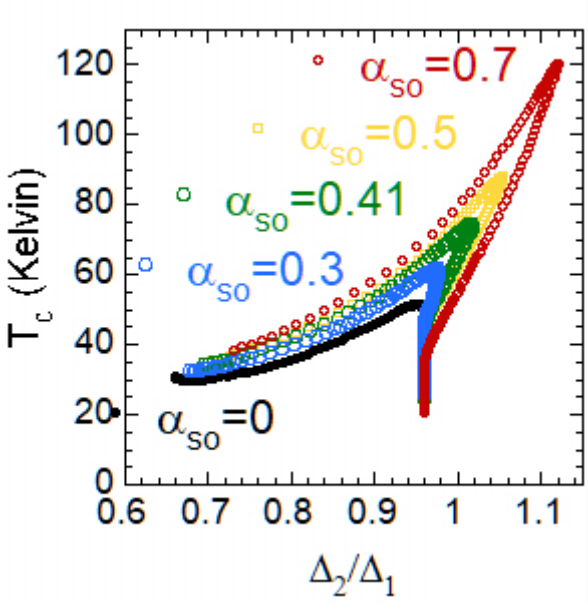

Figure 6.7: *The trend of the critical temperature versus the* Δ_2/Δ_1 *ratio for different values of the parameter* α_{SO}. The T_C trend shows a strong asymmetry which becomes maximum when the Δ_2/Δ_1 ratio is maximum.

from the BCS theory increase as the Rashba coupling, α_{SO}, increases, therefore there exists an unconventional dependence of the critical temperature on the cut-off energy unlike what is proposed in the BCS theory.

In the high-energy limit, the gap ratio and the isotope coefficient tend to the values predicted by the BCS theory, so we are dealing with two BCS-like condensates.

In Fig. 6.9 we plot the isotope coefficient as a function of the critical temperature for different values of α_{SO} for the range of energies delimited in Fig. 6.8 by the dashed lines. This parameter, in this range of energies, can be measured and this prediction can be experimentally verified.

These results confirm that in correspondence with the van Hove singularity there is an amplification of the characteristic parameters of the superconductive phase which becomes more and more evident when the Rashba coupling exceeds a limit value of 0.4.

In the works [165,170] D. Innocenti *et al.* investigated the superconducting properties for a superlattice of quantum wells and observed that there is an optimum condition for the amplification of the critical temperature that is obtained when the cut-off energy is equal to the dispersion along the confinement direction of the higher energy band. The particular geometry considered creates, in fact, a multicomponent system. Here, instead, by introducing the degree of freedom of spin in the solution of the Bogoliubov-de Gennes equations, as well as having the possibility of dealing with realistic cases, we can overcome the limit imposed by previous works simply by suitably increasing the Rashba coupling that exists by definition at the interface between different materials that make up an heterostructure.

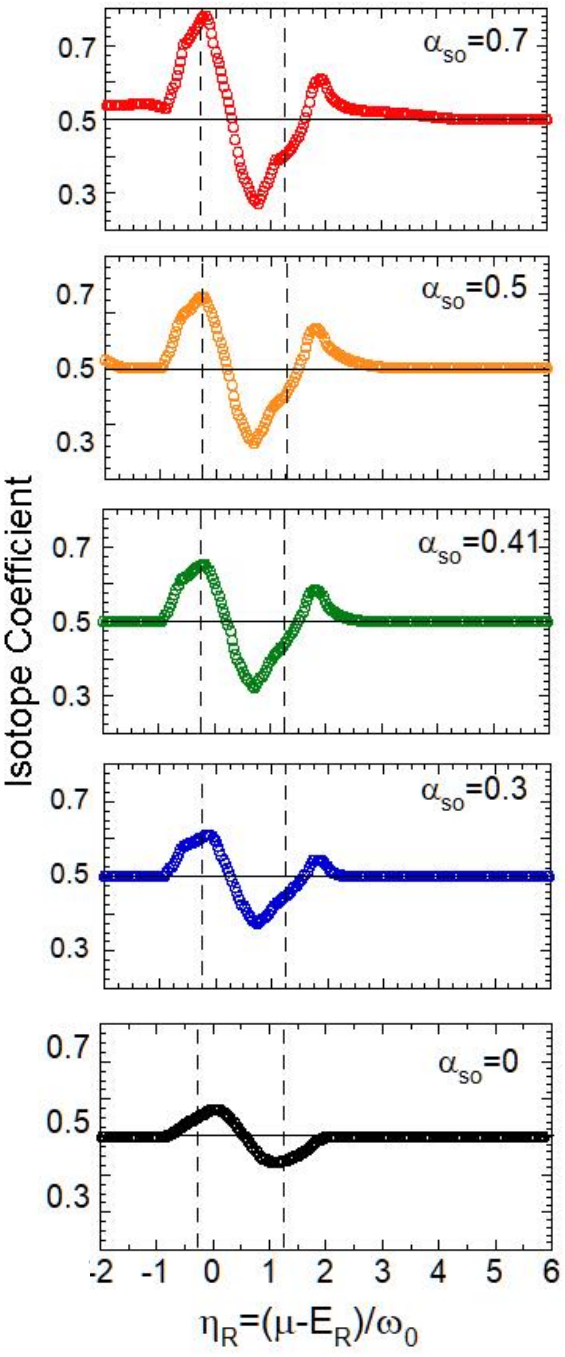

Figure 6.8: Properties of the superconductive phase vs the Lifshitz parameter without and with RSOC for different α_{SO} values such that $\Delta E_{RSOC} \gtreqless \Delta E_{2z}$. This figure shows the variation of the critical temperature with the cut-off energy via the isotope coefficient. The constant value predicted by the BCS theory is the black line.

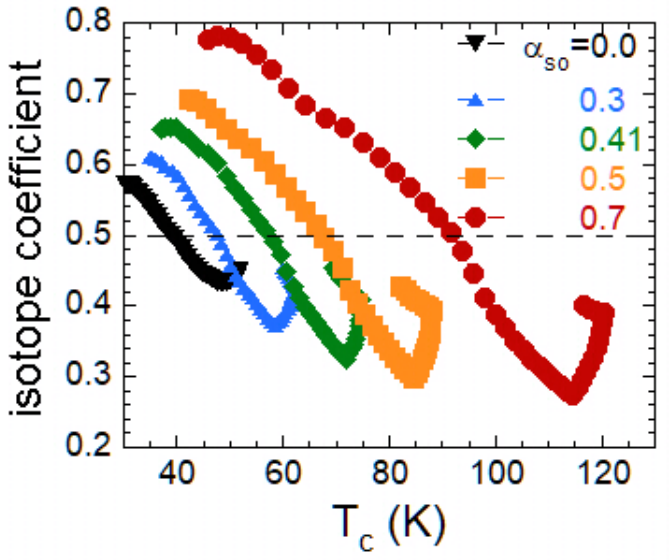

Figure 6.9: *The isotope coefficient as a function of the critical temperature for different values of* α_{SO}.

7

Variation of the critical temperature as a function of the parameters that characterize the superconducting phase

In this chapter we will see how it is possible to increase the values of the critical temperature by appropriately varying some parameters of the model. As a first step, we will see what happens by varying the cut-off energy, ω_0. Next we will reconstruct the *superconducting dome*, as we did in *Chapter 4*, this time introducing a RSOC coupling in a 3D heterostructure. This allows us to make predictions on the T_C trend for the design of new materials. To this end, in *Chapter 8* we will see what is the effect of the variation of the structural parameters of the heterostructure of quantum layers, in order to provide precise indications for future practical applications.

7.1 Trend of the critical temperature by tuning the pairing energy

The purpose of this section is to see how the trend of the critical temperature changes by increasing the cut-off energy, ω_0. Hence, we plot the T_C as a function of the rescaled Lifshitz parameter (equation (5.34)) which we report here for reasons of clarity

$$\eta_R = \frac{\mu - E_R}{\Delta E}, \tag{7.1}$$

where μ is the chemical potential or the Fermi energy in the zero temperature limit, $E_R = E_2 - E_0$, E_2 is the energy of the bottom of the second subband in the absence of a Rashba coupling, E_0 is the energy shift due to RSOC splitting and ΔE is the dispersion along z of the highest energy subband, in our case the second, having considered a two-band system. In all the discussion that follows, we chose for the constant RSOC the maximum acceptable value for our model, $\alpha_{SO} = 0.7$, value beyond which the first and the second subband begin to overlap (see Fig. 7.1) and we will see what happens by

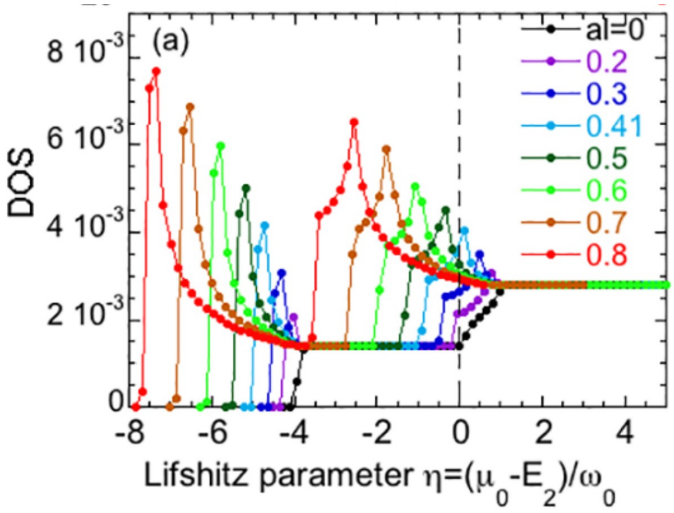

Figure 7.1: *The density of states for the first and the second subband for different values of* α_{SO}. For $\alpha_{SO} = 0.8$ the band edge of the second subband coincides with the band edge of the first subband in the absence of RSOC (black curve), therefore, from this value onwards, the overlapping effects of the bands are not negligible.

varying the parameters that define the superconducting phase: ω_0 and g. As a first step we investigate the effect of the variation of the pairing energy.

The plot in Fig. 7.2 is obtained for different values of the cut-off energy, $\omega_0 = [30,\ 60,\ 90,\ 120]\ meV$. What is observed is that as ω_0 increases, the critical temperature increase.

When $\omega_0 = \Delta E = 30\ meV$ it is possible to observe the typical bell-shaped pattern of the shape-resonance, while as ω_0 increases the resonance widens to include that of the first subband. For $\omega_0 > 60\ meV$ it is no longer possible to distinguish the typical bell-shape as the unrevealing of the T_C trend is due to a superposition of several resonances. This is clear evidence that everything is governed by the difference in energy between the first and second subband which in this case is approximately 150 meV. Therefore, in order to reach a critical temperature typical of high T_C superconductors we will see in *Chapter 8* that it will be appropriate to increase the separation between the subbands without violating any requirement of quantum mechanics. In fact, for example, the value of the coupling constant chosen is $g = 0.4$ less than the limit imposed by the *Migdal theorem* of 0.5 [28].

The Fig. 7.2 shows that, with the choice of parameters made in this section, it is possible to reach a maximum critical temperature equal to $T_{C,MAX} = 160\ K$, a value typically observed in cuprates. Because the maximum electron-phonon interaction that we can choose, before interference effects take place, is $\omega_0 = 60\ meV$.

7.2 Construction of the *superconducting dome* in the presence of RSOC

As seen in the *Chapter 4*, the *Migdal theorem* [28] gives a relation between the renormalized cut-off energy, ω_0, the bare cut-off energy, $\tilde{\omega}_0$, and the pairing constant, g, according to the relation (4.7), than for convenience we recall here

$$\omega_0 = \tilde{\omega}_0 \sqrt{1 - 2g}. \tag{7.2}$$

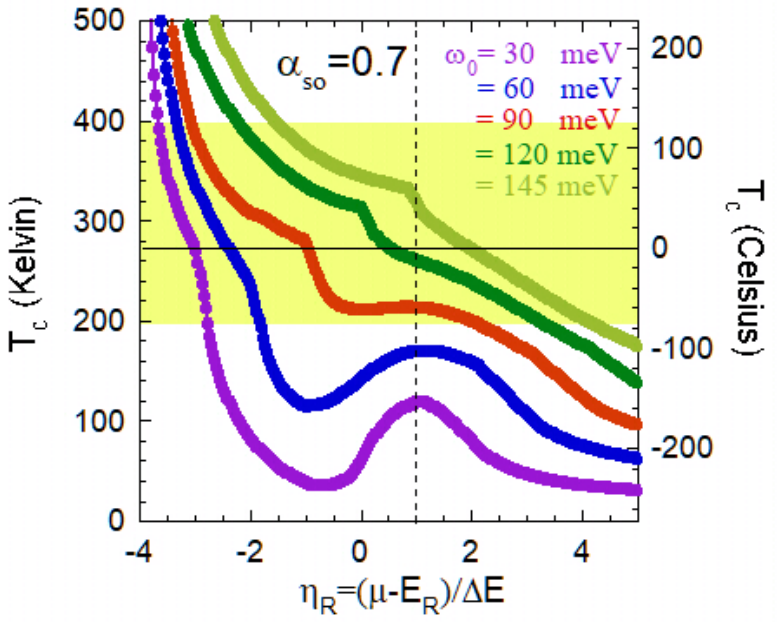

Figure 7.2: *Variable boson pairing strength* This figure show the effect of the variable boson energy in the range 30 $meV < \omega_0 < 145$ meV as a function of the chemical potential measured from the bottom of the potential well normalized of the transversal energy dispersion (rescaled Lifshitz parameter η_R) due to interlayer hopping modulated by the potential barrier due to intercalated layers separating the superconducting layers. The green box highlights the typical temperatures in which life can exist.

Here we fix $\tilde{\omega}_0 \simeq 134$ meV and, as shown in the Fig. 7.2, the renormalized cut-off energy is $\omega_0 = 60$ meV at $g = 0.4$. The relation (7.2) tells us that it is not possible to arbitrarily vary the pairing energy without appropriately modifying the electron-phonon interaction constant. In the Fig. 7.3 we shows how ω_0 varies as g varies in the range $0.150 < g < 0.495$.

In Fig. 7.4 *top panel* we plot the trend of the critical temperature as a function of the rescaled Lifshitz parameter, η_R (equation (7.1)), for different values of the dimensionless coupling constant g by varying ω_0 according to the *Migdal theorem*, setting as the bare cut-off energy $\tilde{\omega}_0 = 134$ meV in order to avoid interference effects between the resonances in the first two subbands that characterize our system. It can be observed that as g increases the shape-resonance expands and the critical temperature values increase up to a limit value of g equal to 0.4, for g greater the trend decreases and the resonance tightens. All this is made even clearer by the *bottom panel* of Fig. 7.4 in which we have reported the maximum value of T_C as g varies.

As pointed out in the introduction to *Chapter 4*, in high T_C superconductors the critical temperature does not have a unique value but as the pressure and charge density vary it describes a *dome*. The *dome* allows to synthesize the properties of several high critical temperature superconductors. In this work, for the first time, the *superconducting dome* is constructed for a 3D superlattice that exhibits both multigap superconductivity and strong RSOC coupling. To do this, we plot the trend of T_C as a function of the rescaled Lifshitz parameter (this is equivalent to varying the chemical potential and therefore the charge density) and of the electron-phonon interaction (this is equivalent to varying the thermodynamic parameter pressure). The result is shown in Fig. 7.5. The theoretically traced *superconducting dome* could be useful for com-

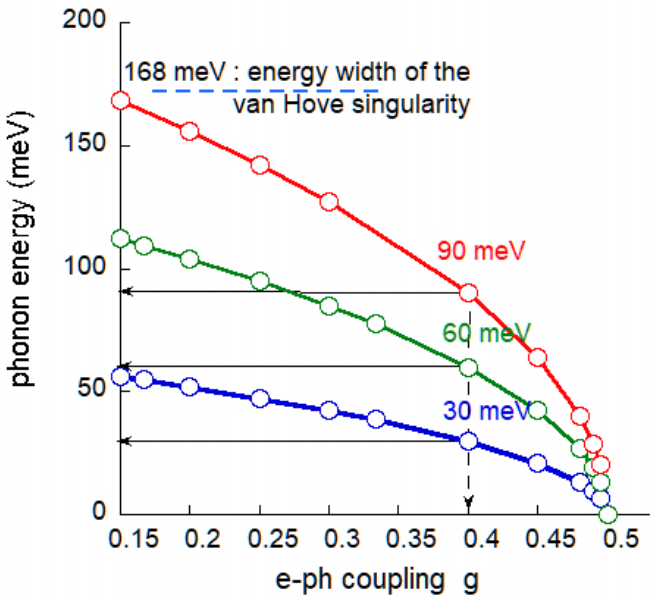

Figure 7.3: *Variation of the renormalized cut-off energy as a function of the electron-phonon coupling.* In this figure we report the trend of ω_0 vs g described by the equation (7.2) for three different values of $\tilde{\omega_0} = [64, 134, 201]\ meV$ (which correspond to fix the cut-off energy, i.e. the renormalized cut-off energy for $g = 0.4$, to the values $\omega_0 = [30, 60, 90]\ meV$). All three trends show a decrease of ω_0 as g increases which becomes more pronounced as ω_0 increases.

paring future experimental trends, which makes our theoretical-numerical model highly predictive.

We stress that with the parameters chosen for our model it is possible to reach a maximum T_C of about 170 K. In order to increase this value, in *Chapter 8* we change the parameters that define the geometry of the heterostructure of quantum layers. This allows us to increase the difference in energy between the first and second subband, hence to reduce the interference effects between the resonances of the two subbands and, in accordance with Fig. 7.2, to choose values of the cut-off energy, ω_0, higher.

Finally, in Fig. 7.6 we plot in log-log scale the T_C as a function of the effective Fermi temperature $T_F = \mu/k_B$, where μ is the Fermi energy in the zero-temperature limit computed from the bottom of the first subband and k_B is the Boltzmann constant. The graph is obtained for $\alpha_{SO} = 0.7$ and for $0.150 < g < 0.495$, *i.e.* for different cut-off energies (see Fig. 7.2). The continuous curves, as before, represent the trends of T_C increasing with g, the others the trends that decreasing with g. In this figure we also indicate the regimes of strong and weak superconducting coupling: the shape-resonance clearly manifests in a BEC-BCS crossover regime, according to the fact that the maximum of T_C occurs in correspondence with the maximum of DOS, *i.e.*, when the chemical potential reaches the unusual van Hove singularity. For g which tends to the value of 0.4, the resonance shifts towards a BEC regime, while for values of g greater, the resonance gradually moves towards a BCS regime.

7.3 Discussion

The analysis conducted so far allows us to show that to increase the T_C it is necessary to increase both the RSOC coupling and the characteristic parameters of the superconducting phase, such as ω_0 and g. At the same time it highlights how structural parameters

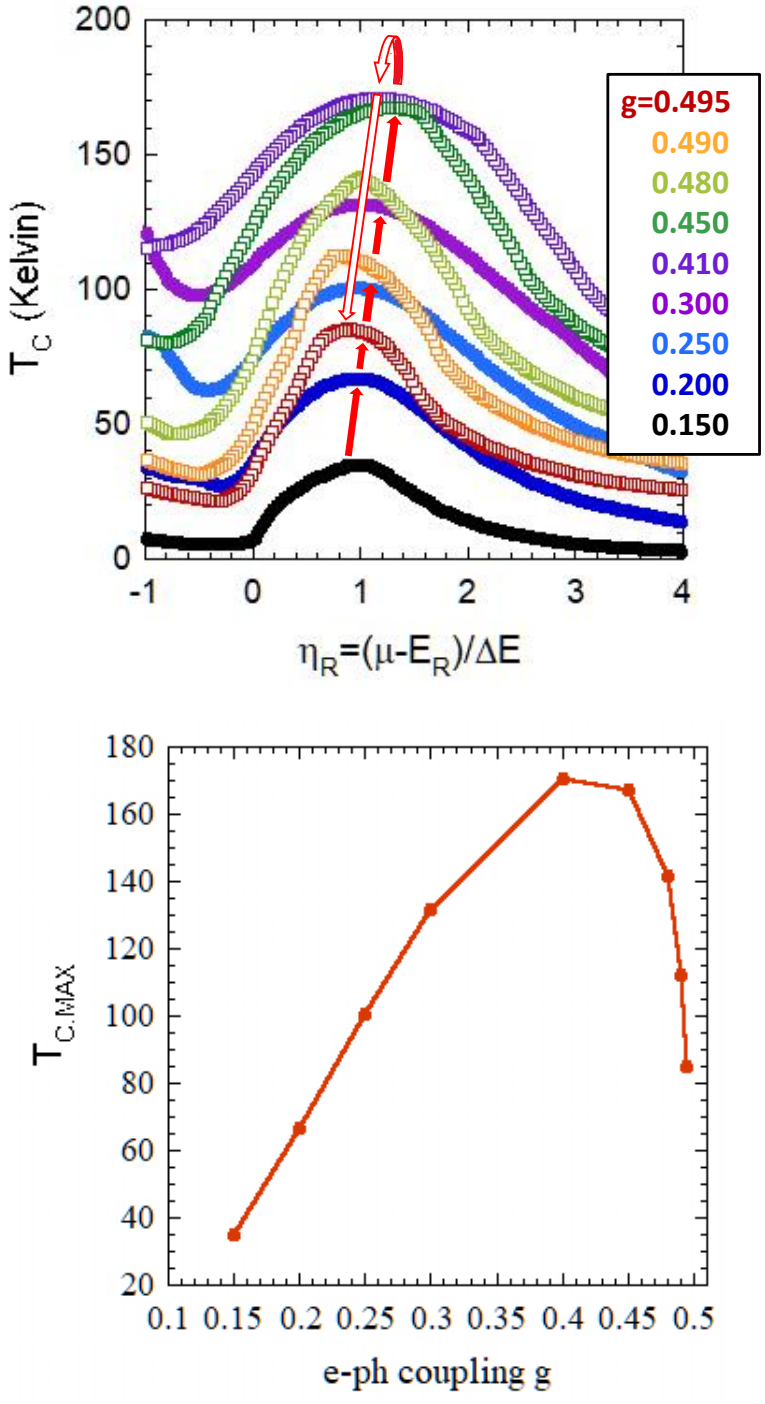

Figure 7.4: *Top panel*: the critical temperature vs η_R for several g in the range $0.150 < g < 0.495$, for $\alpha_{SO} = 0.7$, $\tilde{\omega}_0 = 134\ meV$ and different values of ω_0 obtained from equation (7.2). The continuous curves represent the values of g for which the trend of T_C increases as g increases, while the square curves represent the opposite trend, as indicated by the arrow. *Bottom panel*: we plot the maximum value reached by the critical temperature as g and therefore ω_0 vary. This parameter grows almost linearly up to $g = 0.4$, the point in which there is the maximum critical temperature, above this value $T_{C,MAX}$ starts to decrease again.

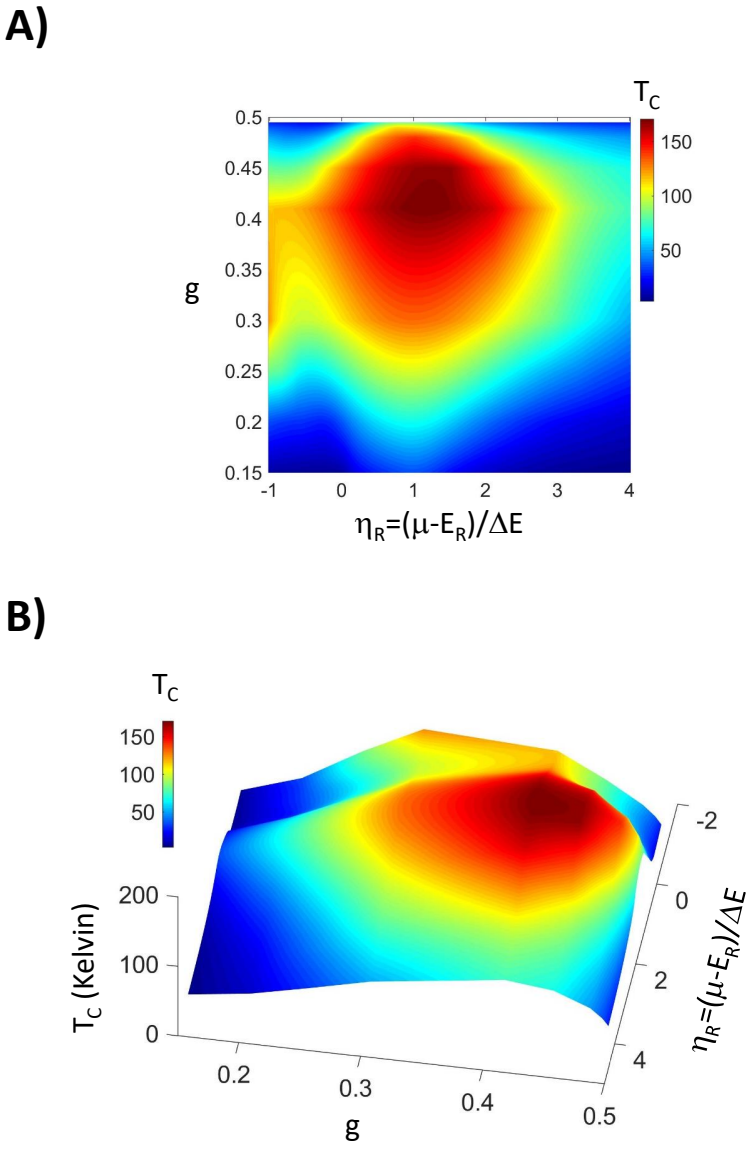

Figure 7.5: *Superconducting dome in the presence of RSOC for* $\alpha_{SO} = 0.7$. In the *panel* **A** we report the projection of the critical temperature in the $(g - \eta_R)$-plane, the colours from blue to red represent increasing critical temperatures. A marked anisotropy of the critical temperature can be observed as a function of both g and the rescaled Lifshitz parameter. The maximum of the critical temperature occurs in $0.40 < g < 0.45$ and $\eta_R = 1$ where the DOS shows a maximum, *i.e.* an anomalous van Hove singularity (see *Chapter 5*). The *panel* **B** represents the same trend but in a 3D chart. A first shape-resonance is observed in $\eta_R = 1$ and a second, less pronounced, in $\eta_R < -1$. The first shape-resonance is, as seen in the *Chapter 5*, due to a Lifshitz transition of the second type, in which the Fermi surface passes from a 3D to a 2D geometry. The second resonance is imputable to interference effects between the resonances in the first and second subband in our two-band model (see Fig. 7.2).

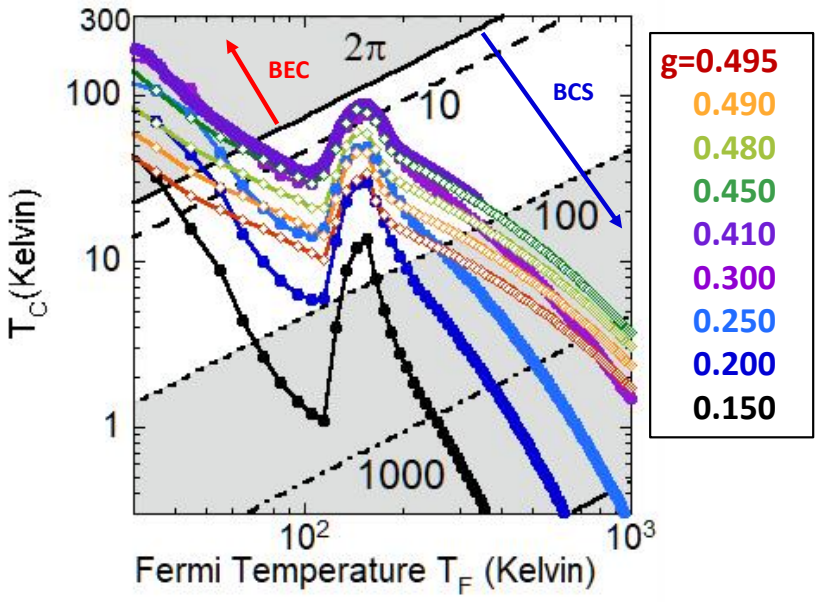

Figure 7.6: *Uemura plot* [243]. We plot in log-log scale the trend of T_C vs T_F for different electron-phonon coupling values. The white box highlights that the shape-resonance occurs in a crossover BEC-BCS regime, an intermediate regime between a strong coupling regime, BEC-like, and the weak coupling regime, BCS-like. The dotted line indicates, in fact, this crossover regime which is predicted to be $T_C = T_F/k_F\xi_0$, where ξ_0 is the coherence length of the Cooper pair [69, 244, 245].

considerably limit the increase of the critical temperature due to interference effects between shape-resonances in two different subbands. This is consistent with the fact that with this thesis we have tried to unify two distinct fields of condensed matter, namely multigap superconductivity and Rashba spin-orbit coupling. In the following *Chapter* we will see how the critical temperature varies with the variation of the geometry of the superlattice in order to provide precise indications for the fabrication of new materials with an high critical temperature.

8

Tuning the superlattice parameters for materials design

As previously anticipated, in this chapter we will see what is the effect produced on the properties of the superconducting phase by varying the structural characteristics of the quantum layer heterostructure schematized in Fig. 5.1.

8.1 Study of the critical temperature as the potential barrier width changes

In this section we analyse the trend of T_C as the potential barrier width varies, or rather as the parameter L changes (see Fig. 5.1) considering the periodicity of the superlattice constant and equal to $d = 30$ Å. In equation (5.4) we have, in fact, seen that there is a relationship between the constant Rashba, α_{SO} and the periodicity of the confinement potential along z. In this case, with the aim to limit ourselves to the case of strong RSOC coupling ($\alpha_{SO} = 0.7$) we must impose that d remains constant. This allows to isolate only the effect of the confinement geometry on the T_C trend.

We therefore consider a potential barrier of amplitude $V = 500\ meV$ and width L variable in the range $15 < L < 23$. The well width will vary according to the formula $d = L + h = 30$. We consider a Rashba coupling constant $\alpha_{SO} = 0.7$, a cut-off energy $\omega_0 = 60\ meV$ and a phonon-electron interaction $g = 0.4$. For this choice of parameters, the Fig. 8.1 represents the T_C trend as a function of the Lifshitz parameter rescaled for the different values of L[1].

In *Chapter 7* we underlined that it is not possible to increase the cut-off energy beyond 60 meV because the difference in energy between the first and second subband is such as to produce overlaps between the resonances of the two subbands of which it is composed our system. The Fig. 8.1 shows that decreasing the width of the barrier allows to widen the distance between two adjacent subbands as well as the range of

[1] With reference to equation (7.1) which defines the rescaled Lifshitz parameter, it is necessary to consider that, having changed L, the energy distance between the first and second subband varies, but at the same time, the dispersion of the second subband also varies along the z-direction that goes from a value of 30 meV to a value of 25 meV

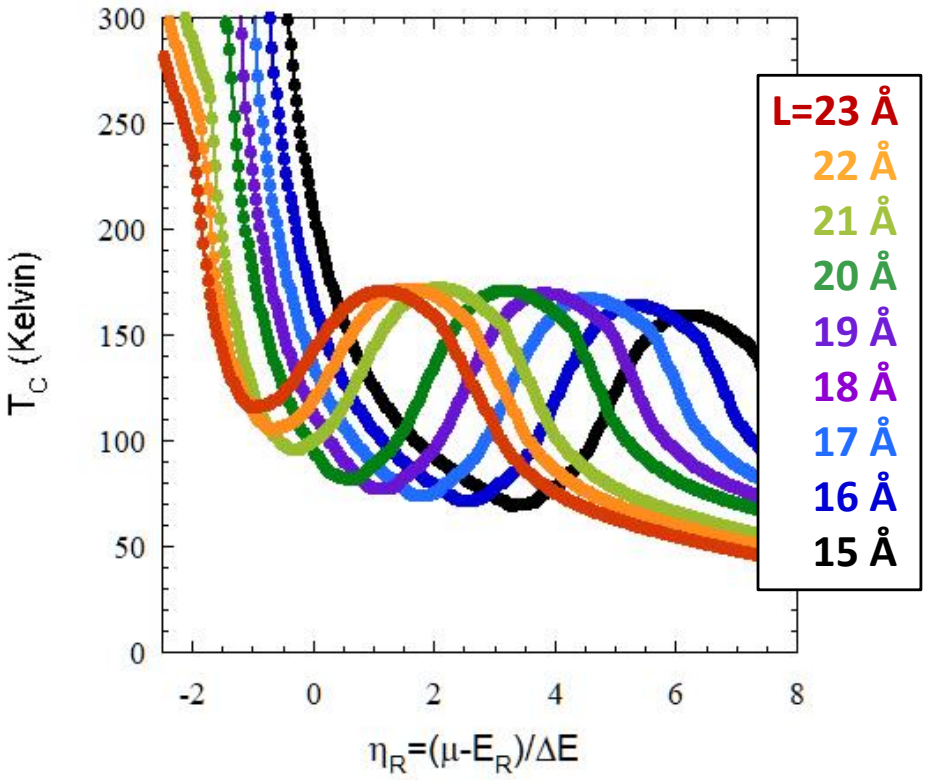

Figure 8.1: *The critical temperature trend as a function of η_R for different L values.* As the width of the potential barrier decreases, the resonance widens and the maximum of the critical temperature, while remaining almost constant, shifts to increasing values of the Lifshitz energy. This is related to the fact that the distance between the first and second subband increases. For the choice of parameters made so far, we have seen that this difference was approximately equal to 150 meV now it turns out to be equal to 250 meV in the most extreme case of $L = 15$.

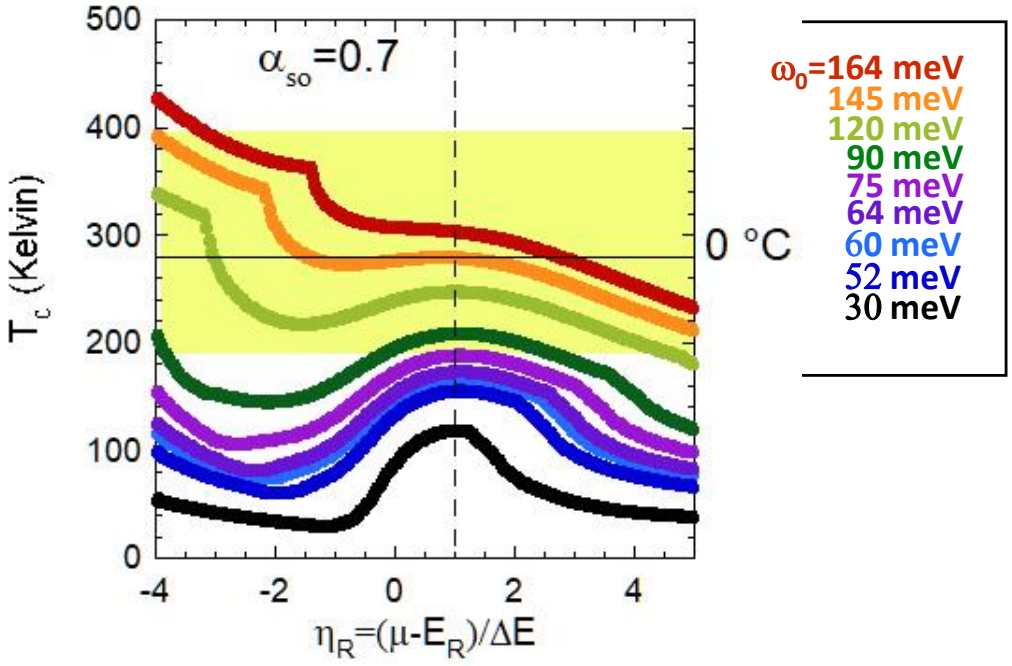

Figure 8.2: *Variable boson pairing.* The figure shows the effect on T_C of the variation of the pairing energy, made to vary in the range 30 $meV < \omega_0 < 164$ meV as a function of the rescaled chemical potential (equation (7.1)) measured from the bottom of the potential well $V(z)$ (Fig.(5.1)).

energies in which the T_C shows a shape-antiresonance. This results in a reduction of the interference effects, as the shape-resonance of the first subband is more distant than the second. All this has no significant effects on the maximum T_C, but allows to work with higher pairing energies and therefore to further increase the critical temperature, as will be clarified below.

8.2 Changes in the trend of the critical temperature as a function of the cut-off energy

In this section we choose a suitable value for L equal to 17 Å which allows us to have a satisfactory separation in energy between the first and second subband, $\Delta E_{1,2} = 216$ meV. We vary the cut-off energy. The aim is to find the optimal choice of the parameters involved in order to reach a maximum critical temperature close to the room temperature.

In Fig. 8.2 we plot the trend of the critical temperature as a function of the rescaled Lifshitz parameter for different values of the pairing energy, setting $\alpha_{SO} = 0.7$ and $g = 0.4$, in a completely similar way to Fig. 7.2. It can be noted that with this choice of L it is possible to choose a cut-off energy greater than that seen in *Chapter 7* and precisely equal to 90 meV. So, with reference to equation (7.2) it is possible to fix $\tilde{\omega}_0 = 201$ meV.

According to the Fig. 7.3 we plot, therefore, the critical temperature for different values of the electron-phonon interaction and therefore for different values of ω_0 (equa-

tion (7.2)). By setting $\alpha_{SO} = 0.7$, $\tilde{\omega}_0 = 201\ meV$, $L = 17$ Å and leaving all the other parameters of the model unchanged we obtain the Fig. 8.3.

The same considerations made in the comment of Fig. 7.4 are valid, *i.e.* that the critical temperature increases as g increases for values in the range $0.15 < g < 0.40$ and then decreases again. At the same time there is a widening of the shape-resonance for this range of g values and a subsequent narrowing for $g > 0.40$. The whole is summarized in *panel* **B** of Fig. 8.3. The T_C, as seen in *Chapters 4* and *5*, is an asymmetric function of the Lifshitz parameter with a maximum reached in correspondence of $\eta_R = 1$ where the DOS shows a peak due to an anomalous van Hove singularity. The most surprising thing is that the choice of parameters used for the model in question allows to work with a pairing energy such that a maximum critical temperature of about 208 K can be reached, the same value observed for the H_3S and confirmed in several papers [32,47].

Also in this case we have reconstructed the *superconducting dome*. The Fig. 8.4 shows how RSOC coupling allows to work with 3D heterostructures of quantum layers and not be limited to 2D systems of quantum layers as seen in *Chapter 4*. In fact, our model is able to reproduce the experimental data collected for the H_3S to predict the behaviour of future materials with high T_C and to provide precise indications on the realization of new 3D heterostructures.

In Fig. 8.5 we report the Uemura plot, compared to what we saw in *Chapter 7* it is possible to notice a shift of the critical temperature trends towards the weak coupling regime, BCS-like. The only resonances that completely fall into a BEC-BCS crossover regime (white box) are those that occur for $g = 0.45\ meV,\ 0.40\ meV,\ 0.3\ meV$. This fact is very important as it tells us that considering the RSOC effect in a 3D heterostructure it is possible to reach critical temperatures typical of the most recent experimentally reported high T_C materials while remaining in a weak coupling regime and considering model parameters easily reproducible experimentally.

8.3 Study of the isotope effect

In *Chapter 4* we saw that sulfur hydride metal H_3S reaches a maximum critical temperature of about 208 K for pressures of the order of 160 GPa and we show how a 2D heterostructure of quantum wires in the absence of RSOC is able to reproduce both the high value of the T_C and the anomalous trend of the isotopic coefficient. Experimentally it has in fact been seen that the value of the isotopic coefficient of H_3S deviates significantly from the value of 0.5 predicted by the BCS theory [32], we have underlined how this deviation occurs where the chemical potential reaches a topological Lifshitz transition.

In this section we show that similar results, but for several more surprising aspects, can be obtained in a 3D geometry, or in an heterostructure of quantum layers, as long as a Rashba coupling is added in the equations that describe the system, also necessary to describe in the behaviour of real systems is more realistic and accurate. In the previous section we have already seen that our model allows to reach the critical temperatures expected for compounds rich in hydrogen as well as to predict the possibility of finding new materials with even higher T_C. The new and most interesting aspect is that all this can be achieved in a weak coupling regime (Fig. 8.5).

In the Fig. 8.6 we report the theoretical values of T_C and of the isotopic coefficient. The theoretical results are qualitatively in agreement with the experimental results show in the Fig. 8.7. The behaviour of H_3S and of D_3S has been simulated by choosing different values for the energy of the phonon: $\omega_0 = 52\ meV$ for the D_3S and

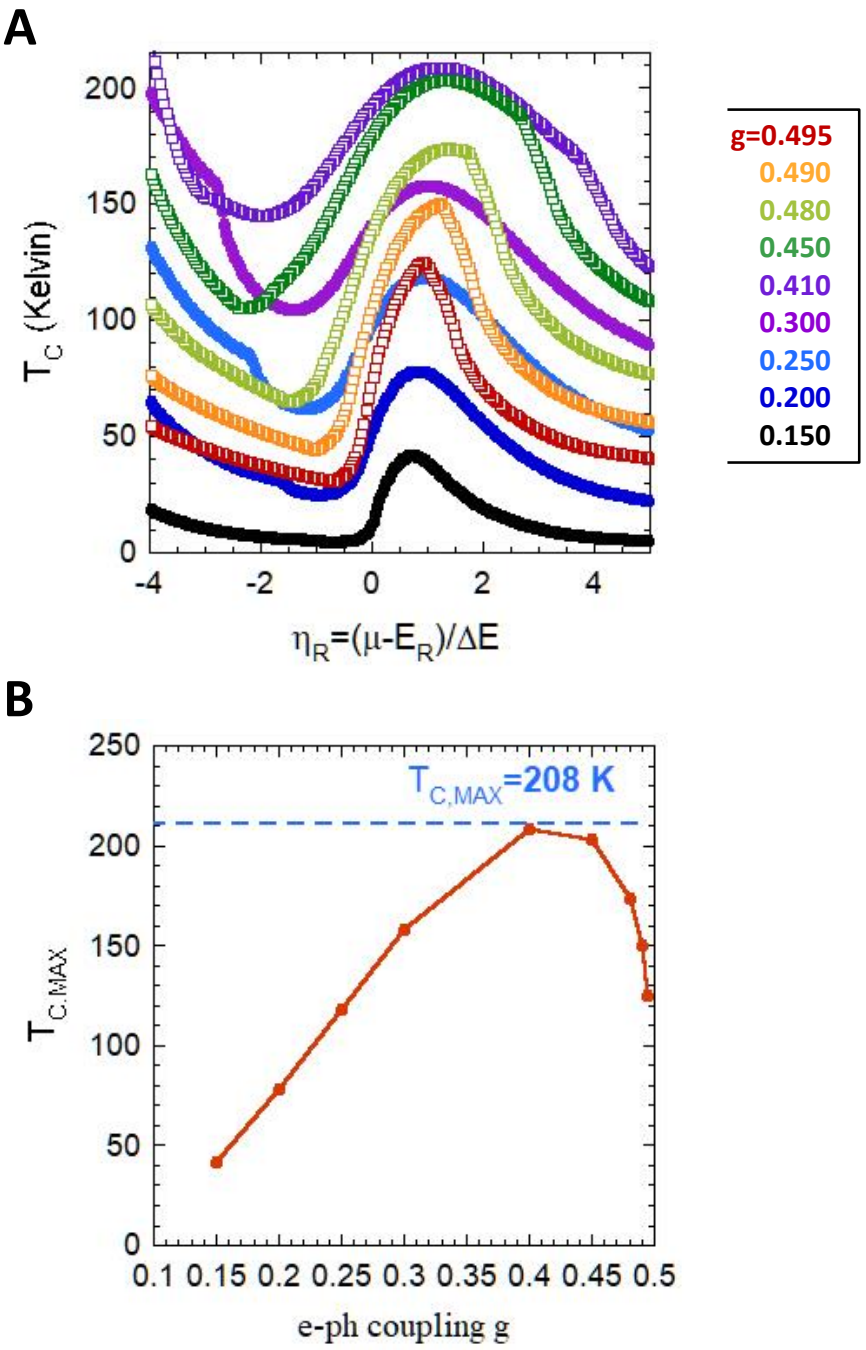

Figure 8.3: *The critical temperatures for different values of the electron-phonon interaction.* The *Figure* **A** shows how as g increases and therefore the pairing energy ω_0 increases, the shape-resonance gets wider. For $0.15 < g < 0.40$ the maximum value of the critical temperature increases, while for greater electron-phonon interactions the resonance decreases and tightens again. In the *panel* **B** we plot the maximum value of the critical temperature as a function of g, highlighting what was said previously, that is, there is an optimal value for g equal to 0.4. With this choice we are able to reach the critical temperature expected for H_3S, about equal to 208 K (see Chapter 4).

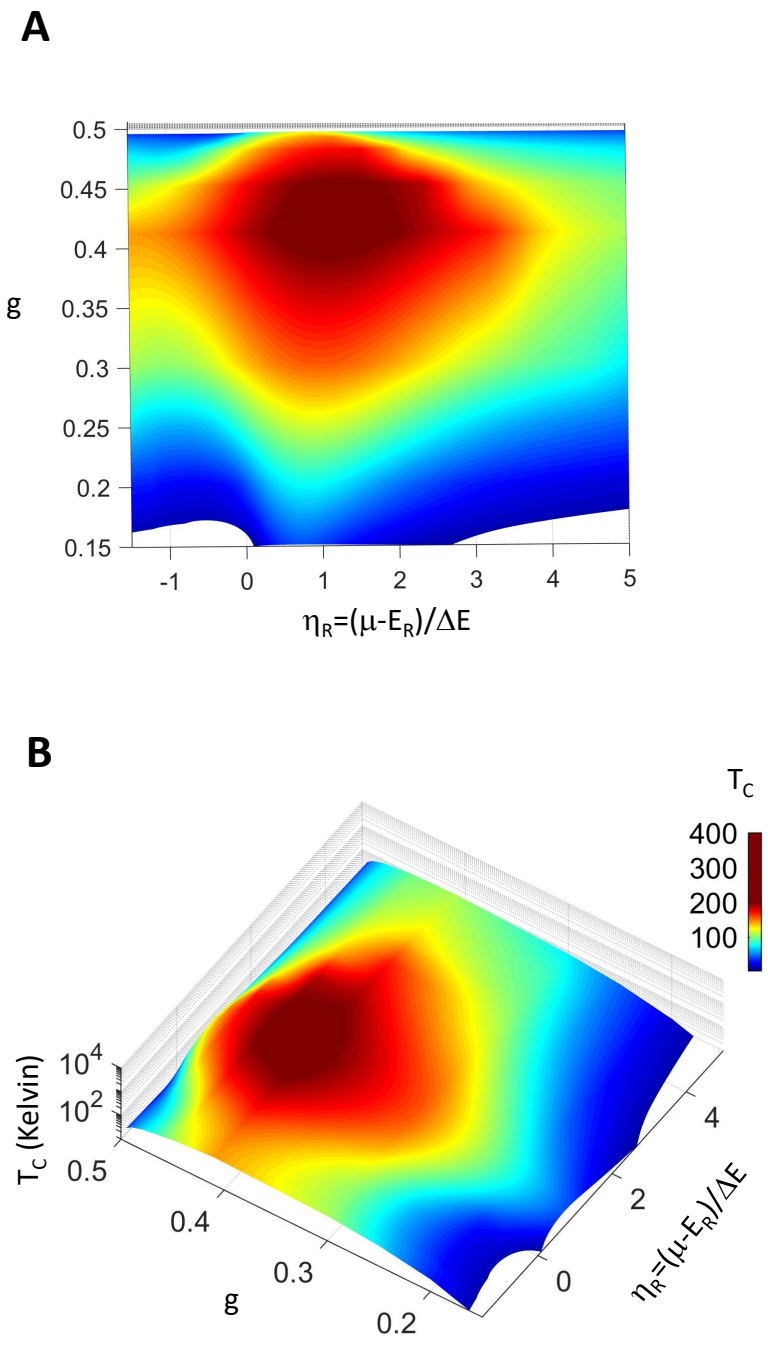

Figure 8.4: *Superconducting dome.* In *panel* **A** we plot the propjection of the critical temperature in the $(g - \eta_R)$-plane, while *panel* **B** is the 3D reconstruction of the *superconducting dome*. It can be observed that by choosing the parameters made it is possible to reach critical temperatures close to the ambient temperature and observed in compounds rich in hydrogen, such as H_3S, and to predict the behaviour of future materials with an high T_C.

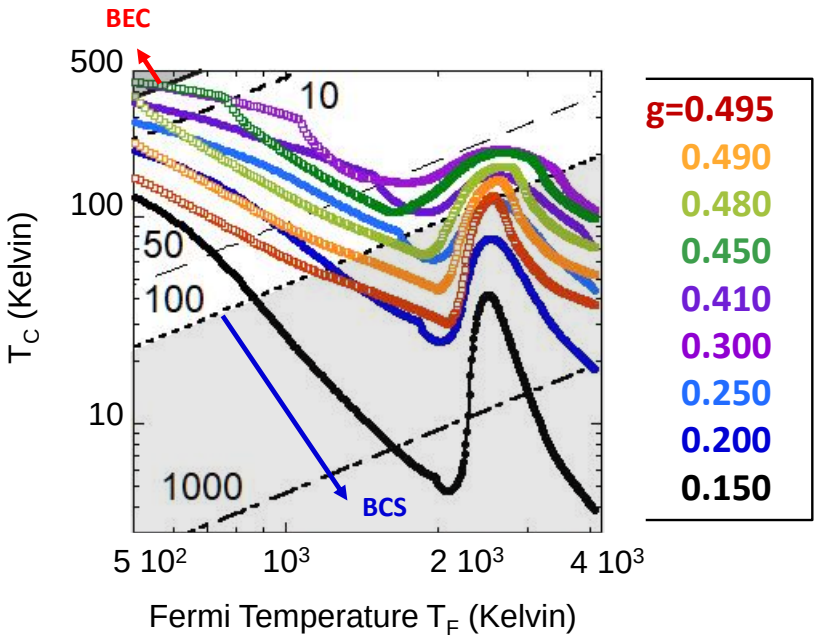

Figure 8.5: *Uemura plot.* We plot in log-log scale the trend of the critical temperature as a function of the Fermi temperature (defined in *Chapters 6 and 7*) for different values of the electron-phonon interaction. The black continuous diagonal line represents the limit at which a BEC-like regime begins, therefore it is possible to observe a shift of the T_C towards a weak coupling regime.

$\omega_0 = 90\ meV$ for the H_3S. The ratio of these values is, in fact, approximately equal to the difference in mass between deuterium and hydrogen. As seen in the previous sections, increasing the energy cut-off widens the shape-resonance producing unconventional shape of the temperature dependent isotopic coefficient and a large variation by changing the pressure from the expected BCS coefficient 0.5 [2].

Fig. 8.7 shows the experimental data obtained for the isotope coefficient in the pressure range between 120 GPa and 180 GPa [32, 168, 203]. The isotope coefficient gradually decreases with increasing pressure passing from a value of 1 to a value of about 0.3, showing a significant variation from the predicted value of the BCS theory of 0.5. As seen above, this anomalous behaviour can only be explained in the reference of the general theory of multigap superconductivity near a Lifshitz transition. The same thing can be said in reference to the experimental trends of the critical temperature. In particular, T_C decreases by about 40 K in H_3S and by about 60 K in D_3S in a range of about 30 GPa, between 160 GPa and 130 GPa . While BCS calculations foresee that in this range of pressures the variation of T_C is of the order of 10 K [168], in a multigap superconductor the T_C tends to zero (see the antiresonance of shape in Fig. 8.3**A**) in correspondence with a Lifshitz transition of the first type and a marked resonance in correspondence with a Lifshitz transition of the second type; when the FS passes from a 3D geometry to a 2D one and two condensed in different coupling regimes coexist. In particular, the condensate in the first subband is in the BCS-like regime, while the condensate in the second subband is in a BEC-BCS crossover regime.

The comparison between experimental and theoretical trends shows how the Rashba interaction gives an important contribution to the theoretical explanation of superconductivity at room temperature in a weak coupling regime.

[2] As pointed out in *Chapter 4*, in a 2016 paper published in Scientific Reports T. Jarborg and A. Bianconi [168] have seen that in the zero temperature limit, the pressure shifts the energetic distance of the chemical potential from the Lifshitz transition by a few meV. In Fig. 4.2 we reconstruct the relation between pressure and energy distance of the chemical potential with respect to the topological Lifshitz transitions ($(\mu - E_L)$ where E_L is the band edge energy of the highest energy subband, in our case the second). This allows us to simulate the pressure variation with a variation of the Lifshitz parameter, η_R.

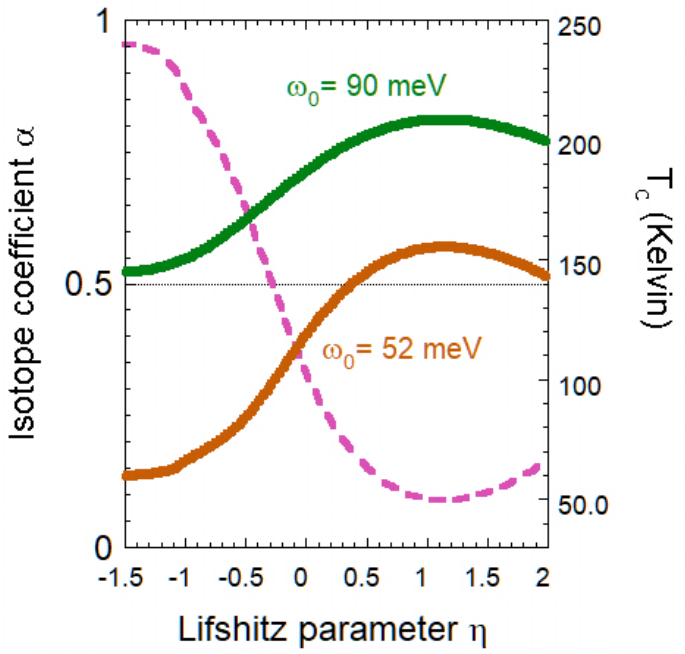

Figure 8.6: *The critical temperature and the isotope coefficient as a function of the pressure and the Lifshitz parameter for two different compounds:* H_3S and D_3S. The trend of T_C vs the pressure obtained theoretically by modelling the difference in the isotopic weight of the two compounds with two different phononic frequencies, whose ratio is $\omega_0(D_3S)/\omega_0(H_3S) = 0.59$.

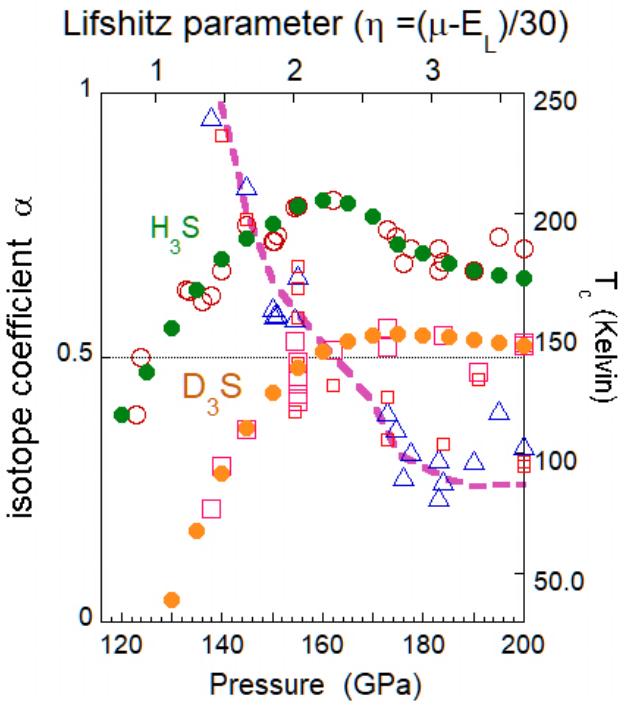

Figure 8.7: *The critical temperature and the isotope coefficient as a function of the pressure and the Lifshitz parameter for two different compounds:* H_3S and D_3S. The experimental results, reported in [32, 47, 203], show a difference in the trend of the T_C vs the pressure in the two samples with different isotopic weight. The difference in mass between deuterium and hydrogen is $90\sqrt{1/2} = 63$. This difference manifests itself in an isotope coefficient that varies a lot in a small range of pressures. It is possible to note an excellent agreement between experimental data and theoretical predictions.

9

Conclusions and future prospectives

The aim of the work presented in this thesis has been to investigate theoretically and numerically the electronic structure and the superconducting properties of a nanostructured superlattice of quantum layers in the presence of RSOC. We have described the unconventional Lifshitz transition in a 3D superlattice of metallic layers characterized by the length of the circular nodal line increasing with RSOC in the negative helicity states of the spin-orbit split electron spectrum. Here we have been able to provide the theoretical description of tuning multigap Bogolioubov-de Gennes superconductivity near the bottom of the upper subband with the negative helicity shifted by the RSOC. Our theory overcomes the limitations present so far due to common BCS approximations used in previous theoretical works on superconductivity in the presence of spin-orbit interactions which mostly describe superconductivity only at very high Fermi energy. The work in Ref. [249] constitutes an important exception, focussing on superconductivity in low-density semimetals in the presence of strong spin-orbit coupling and analysing the superconducting instability in different pairing channels. This latter work clearly shows the need to systematically develop the extension of the BCS theory in strongly spin-orbit coupled systems (see also [250]). We have shown the key role of quantum configuration interaction between the gaps in the self-consistent mean-field equation which need the calculation of the exchange interactions between singlet pairs in subbands with different quantum number and different helicity. The exchange interactions are local contact interactions which have been shown to be essential in condensation phenomena in fermionic quantum ultracold gases. In our theory the contact interactions are in action together with phonon exchange Cooper pairing. The key result of this work has been the calculations of the overlap of the electron wavefunctions by solving the non relativistic Dirac equation in order to account for the spin-orbit coupling. We believe that the results obtained here provide a roadmap for the quantum material design of a superlattice of periodicity d made of superconducting atomic flakes of thickness L separated by spacers of thickness W.

As a first step, we have shown that resonant and crossover phenomena in the normal state are amplified when the transverse energy dispersion of electrons in the superlattice is of the same order of magnitude of the energy cut-off $\Delta E_z \sim \hbar\omega_0$ of the effective pairing interaction. Under these conditions the introduction of a RSOC, of amplitude of the order of the 3D superlattice period, creates a completely unexpected variation

in the topology of the Fermi surface, especially for the negative helicity band. In particular, the RSOC induces an unconventional Lifshitz transition with an associated extanded van Hove singularity. For the non-BCS superconducting phase we have solved the Bogoliubov-de Gennes equation for the multiple gaps numerically. The unusual complexity in the properties of the normal phase is reflected in an amplification of the gap and the critical temperature in precise energy ranges. We have found that the enhancement of the superconducting parameters takes place when the chemical potential is tuned around the Lifshitz transition. Under these circumstances it is necessary to include the configuration interaction between different gaps in different subbands.

In the BCS theory the pairing interaction is assumed originated from an effective contact interaction mediated by phonons between electrons with opposite momentum and spin. The wavefunction of the superconducting ground state has been constructed by the configuration interaction of all electron pairs on the Fermi surface in an energy window that is the energy cut-off of the interaction. In a multiband anisotropic superconductor we have seen that the effective pairing interaction entering in the gap equation needs to be reconfigured by the effects of the quantization through the single-particle wavefunctions determined by the external confining potential. The BCS-like self-consistency relation shows in this case a matrix structure whose elements depend on the subband index and on the wavevector transversal to the layers. This implies a structure in the k-dependence interband coupling interaction for the electrons that determines interference effects between the single-particle wavefunctions of the pairing electrons in different subbands of the superlattice. In this case, both a conventional intraband coupling and an interband coupling strictly connected to the amplification of the critical temperature become possible. We have shown that the interband and intraband distributions show different shapes and widths and have different range of values and that in order to have a strong amplification of the critical temperature it is necessary to create a strong anisotropy in the gaps. This can be achieved by increasing the superconducting coupling in the higher energy subband with respect to the interband and intraband term relating to the first subband.

The issue of superconducting fluctuations in a multiband and multigap configuration deserves a comment at this point. Whereas amplitude and phase fluctuations of the order parameter are in general detrimental and a source of large suppression of the (otherwise enhanced) critical temperature in low dimensional and/or strongly coupled superconductors, their effect can be reduced by the recently proposed mechanism [192,193] of the screening of superconducting fluctuations in a (at least) two-band system. References [192,193] demonstrated that a coexistence of a shallow carrier band with strong pairing and a deep band with weak pairing, together with the exchange-like pair transfer between the bands to couple the two condensates, realizes an optimal and robust multicomponent superconductivity regime: it preserves strong pairing to generate large gaps and a very high critical temperature but screens the detrimental superconducting fluctuations, thereby suppressing the pseudo-gap state. The screening is found to be very efficient even when the pair exchange is very small. Thus, a multiband superconductor with a coherent mixture of condensates in the BCS regime (deep band) and in the BCS-BEC crossover regime (shallow band) offers a promising route to enhance critical temperatures, eliminating at the same time the suppression effect due to fluctuations. In the light of these considerations, a quantitative calculation of the screening in the system here considered, requiring the inclusion of the spin-orbit coupling terms in the fluctuation propagator, is postponed to a future work.

The coexistence of at least one large Fermi surface and at least one small Fermi

surface appearing or disappearing with small changes in the chemical potential is the key ingredient for the shape-resonance idea in superconducting gaps [164, 165] which is a type of Fano-Feshbach resonance. By changing the chemical potential, the critical temperature (T_C) decreases towards 0 K when the chemical potential is tuned to the band edge, because of the Fano antiresonance, and the T_C maximum appears (as in Fano resonances) at higher energy, between one and two times the pairing interaction above the band edge [164, 165, 167].

The most interesting aspects that emerged from this thesis are the possibility of to vary the RSOC by varying the parameters of the model and the possibility to obtain a critical temperature typical of high T_C compounds by suitably and parallel varying the parameters that define the superconducting phase, the RSOC coupling and the geometry of the heterostructure of quantum layers. This allows us to provide precise indications for any experimental tests and practical applications. In a second phase of our work, we have, indeed, seen that by choosing a RSOC of the order of the cut-off energy and greater than the dispersion of the second subband and keeping the lattice periodicity fixed, it is possible to suitably vary the electron-phonon interaction constant in order to reach critical temperatures of the order of 208 K. Furthermore, our work shows how by adding the spin degree of freedom in the equations describing the system as well as being able to model the behaviour of real systems in a more realistic way, it is possible to justify the most recent results on superconductors at room temperature in a week coupling regime.

9.1 Future prospectives

The works [192, 193], cited above, should first be extended to include the realistic electronic structure of the superlattice in the $3D$-$2D$ dimensional crossover, subject of this thesis. This involves going beyond the parabolic-band approximation used in [192, 193]. To this end, as a preliminary study, it is possible to consider an analytical fit-model of the superlattice bands as obtained in the *Section* 5.2. Another aspect that should be analysed is the extension of the Ginzburg-Landau theory (the GL theory) in the presence of fluctuations for multiband systems [251]. The next step could be to study the effect of thermal fluctuations in a multiband superconductor in the presence of a spin-orbit coupling (SOC). This greatly complicates an already controversial problem, but it could open up the possibility to study entirely new and fascinating phenomena.

The theory of GL in the presence of a Rashba spin-orbit interaction (RSOC) has been investigated in several papers [48, 149, 252–264]. In the Ref. [256] it is emphasized that for such systems there are two transition temperatures the higher of which is the conventional critical temperature, T_C, while the lower one, T^*, corresponds to the crossover from a mixed singlet-triplet phase, at lower temperatures, to only a spin-singlet or spin-triplet (depending on the sign of the interband scattering potential) phase at higher temperatures. Currently, the problem of superconducting fluctuations in the presence of SOC has been addressed only for single-band [149, 252, 254–264] systems, where the fluctuations with SOC are studied in BCS-BEC crossover, an important aspect for our work. In fact, the crossing of a shape-resonance and the passage of the chemical potential through a Lifshitz transition determines the tuning of the superlattice through this crossover. In the works [149, 252–254, 256, 257, 259, 262, 264] the BCS-BEC crossover in the presence of RSOC was analysed. It has been shown that the SOC causes fluctuations to mediate an attractive pairing coupling, strongly dependent on the momentum and the spin, in the channel with odd-parity (p- or f-wave). Contrary

to what was expected, the addition of a transversal Zeeman field does not destroy the superconductivity, but it suppresses the s-wave coupling promoting a coupling with odd-parity that increases as the SOC increases. This behaviour supports an unconventional topological superconductivity. As underlined in [255, 261, 263] for sufficiently large SOC the singlet contribution improves in the BCS channel, but is suppressed in the BEC channel, therefore, as the spin-orbit coupling increases the system passes from a BCS-BEC superfluid to a condensate BEC.

The above leads, as a major effort, to the need to develop a new theoretical and computational research project aimed at the study of BCS-BEC fluctuations and the crossover phenomena in the presence of multiband systems, such as those generated by a superlattice, and at the same time, in the presence of spin-orbit coupling and, possibly, in the presence both parallel and transverse Zeeman magnetic fields. This will be a promising future development of the work of this thesis.

A

The origin of the spin-orbit interaction

The spin-orbit interaction (SOI) arises in the non-relativistic limit of the Dirac equation. The Dirac equation reads

$$i\hbar\partial_t\psi = (\boldsymbol{\alpha}\cdot\mathbf{p} + \beta mc^2 + V)\psi, \tag{A.1}$$

with

$$\boldsymbol{\alpha} = \begin{pmatrix} 0 & \boldsymbol{\sigma} \\ \boldsymbol{\sigma} & 0 \end{pmatrix},\ \beta = \begin{pmatrix} 1 & 0 \\ 0 & -1 \end{pmatrix},\ V = eV\begin{pmatrix} 1 & 0 \\ 0 & 1 \end{pmatrix},\ \psi = \begin{pmatrix} \psi_1 \\ \psi_2 \end{pmatrix}, \tag{A.2}$$

where we consider the presence of a static electric field described by eV, ψ_1 and ψ_2 are the upper and lower components of the spinor ψ. While $\boldsymbol{\sigma}$ are the Pauli matrices linked to the spin of the electron $\boldsymbol{\sigma} = 2\mathbf{S}/\hbar$. Taking mc^2 as the zero of energy, the Dirac equation becomes

$$\begin{cases} i\hbar\partial_t\psi_1 = eV\psi_1 + c(\boldsymbol{\sigma}\cdot\mathbf{p})\psi_2 \\ i\hbar\partial_t\psi_1 = (eV - 2mc^2)\psi_2 + c(\boldsymbol{\sigma}\cdot\mathbf{p})\psi_1 \end{cases} \tag{A.3}$$

which shows that when eV and cp are small compared to the so-called Dirac gap $2mc^2$ (the non-relativistic limit), $\psi_1 \sim e^{-imc^2t/\hbar}$ and $\psi_2 \sim e^{imc^2t/\hbar}$. Now we want to derive an equation for the upper component ψ_1 when the Dirac gap is the largest energy scale. To this end we use the second equation in (A.3) expressing ψ_2 in terms of ψ_1, and we make an expansion in the parameter $1/(2mc^2)$.

$$\psi_2 \simeq \frac{1}{2mc}\left(1 - \frac{i\hbar\partial_t}{2mc^2} + \frac{eV}{2mc^2}\right)(\boldsymbol{\sigma}\cdot\mathbf{p})\psi_1. \tag{A.4}$$

In this way we can eliminate ψ_2 in the equation for ψ_1. The normalization condition for the original wavefunction $<\psi|\psi>=1$ implies

$$<\psi|\psi>=<\psi_1|\psi_1> + <\psi_2|\psi_2>= 1. \tag{A.5}$$

Therefore, if we define

$$\tilde{\psi} = \left(1 + \frac{(\boldsymbol{\sigma}\cdot\mathbf{p})^2}{8m^2c^2}\right)\psi_1, \tag{A.6}$$

where $\tilde{\psi}$ satisfies $<\psi|\psi>=1$ at order $1/(2mc^2)$. The equation for $<\psi|\psi>=1$ reads

$$i\hbar\partial_t\tilde{\psi} = \left(1-\frac{p^2}{8m^2c^2}\right)\left[eV+\frac{p^2}{2m}+(\boldsymbol{\sigma}\cdot\mathbf{p})\frac{eV}{4m^2c^2}(\boldsymbol{\sigma}\cdot\mathbf{p})\right]\left(1+\frac{p^2}{8m^2c^2}\right)\tilde{\psi}. \tag{A.7}$$

By calculating the product up to the terms of order $1/c^2$, we get

$$H_{eff} = e\phi+\frac{p^2}{2m}-\frac{p^4}{8m^3c^2}+\frac{e\hbar\Delta V}{8m^2c^2}+\frac{e\hbar}{4m^2c^2}[\boldsymbol{\sigma}\cdot(\boldsymbol{\nabla}V\times\mathbf{p})], \tag{A.8}$$

where the first two terms represent the classical non-relativistic Hamiltonian, the third term is the first relativistic correction to the kinetic energy, the fourth term is the so-called Darwin term, and finally the last one is the spin-orbit interaction. Let us examine this term more carefully; it can be expressed as

$$H_{SO} = \frac{e\tilde{\lambda}_0^2}{4}(\boldsymbol{\sigma}\times\boldsymbol{\nabla}V)\cdot\mathbf{p}, \tag{A.9}$$

where $\tilde{\lambda}_0 = \hbar/(mc) \simeq 10^{10}cm$ is the Compton wavelength in a vacuum, which is very small compared with the characteristic lengths in solids. However, when considering the spin-orbit interaction in solids one must take into account that an effective Compton wavelength, $\tilde{\lambda}$, may appear. In some cases this brings a big enhancement of the strength of the spin-orbit interaction. For example, in $GaAs$ the effective Compton wavelength $\tilde{\lambda}$ is about three orders of magnitude larger than the vacuum value $\tilde{\lambda}_0$. In atoms, the potential eV, in equation (A.9), is the central field due to the nucleus and to the screening of electrons and the SOI term is responsible for the fine structure of the atomic spectra.

In solids, in principle, the Eq.(A.9) applies to all potentials acting on the electrons. In this respect one may speak of different spin-orbit mechanisms depending on the origin of the potential. Those which, due to the potential from impurities and defects, break the translational symmetry of a periodic lattice, are called extrinsic mechanisms. On the other hand, those mechanisms arising from the potential of the host lattice or from the confining potential determining an electronic device, as in the case of a two-dimensional electron gas, are called intrinsic. In the present thesis we are interested in the latter class of mechanisms.

B

The DOS and the occupation number for a 2DEG in the presence of RSOC

The density of states, commonly referred by the acronym DOS, tells us how many states there are with an energy between E and $E + dE$, given a volume element dp

$$dE = N(p)dp = \frac{dE}{dp}dp \qquad \Rightarrow \qquad N(p) = \frac{dE}{dp}.$$

It is possible to introduce this quantity in a more formal way by defining

$$N(E) = \frac{1}{V}\sum_{p}\delta(E - E_p).$$

This function gives the number of elements in the volume dE. In the case of infinite volume we have

$$N(E) = \int \frac{d^2p}{(2\pi)^2}\delta(E - E_p)$$

and the important report holds true

$$\frac{1}{V}\sum_{p}F(E - E_p) = \int dEN(E)F(E).$$

In the case under consideration

$$N(E) = \sum_{p,\alpha}\delta(E - E_p^{\alpha}). \tag{B.1}$$

E_p^{α} is a continuous function of p, hence

$$N(E) = \int \frac{d^2p}{(2\pi)^2}[\delta(E - E_p^{+}) + \delta(E - E_p^{-})].$$

Since p is defined as in Fig.(2.2), we solve in polar coordinates

$$N(E) = \int_0^\infty \frac{pdp}{(2\pi)^2} \int_0^{2\pi} d\vartheta[\delta(E - E_p^+) + \delta(E - E_p^-)],$$

$$N(E) = \frac{1}{2\pi} \int_0^\infty pdp[\delta(E - \frac{p^2}{2m} - \alpha p) + \delta(E - E - \frac{p^2}{2m} + \alpha p)].$$

We take advantage of the properties of the $\delta - Dirac$ function and proceed as follows:

1. Let's solve the equation $p^2 \pm 2m\alpha p - 2mE = 0 \Rightarrow p_\pm(E) = \mp m\alpha \pm \sqrt{(m\alpha)^2 + 2mE}$ e $\frac{dE}{dp} = \frac{p}{m} \pm \alpha$.
2. We see what are the acceptable solutions
   - $p_1(E) = m\alpha + \sqrt{(m\alpha)^2 + 2mE}$ always $> 0 \Rightarrow$ always valid,
   - $p_2(E) = m\alpha - \sqrt{(m\alpha)^2 + 2mE} > 0 \iff E < 0$,
   - $p_3(E) = -m\alpha - \sqrt{(m\alpha)^2 + 2mE}$ never $> 0 \Rightarrow$ never valid,
   - $p_4(E) = -m\alpha + \sqrt{(m\alpha)^2 + 2mE}$ always $> 0 \iff E > 0$.
3. We distinguish two cases: $E \lessgtr 0$.
   - For $E < 0$ we have

     $$N(E) = \frac{1}{2\pi} \int pdp \frac{\delta(p - p_1)}{|\frac{p_1}{m} - \alpha|} + \frac{\delta(p - p_2)}{|\frac{p_2}{m} - \alpha|} = \frac{m}{2\pi} \frac{2m\alpha}{\sqrt{(m\alpha)^2 + 2mE}}. \quad \text{(B.2)}$$

     This function tends to $+\infty$ when $E = -E_0$ and to $m\pi$ for $E = 0$.
   - For $E > 0$ we have

     $$\begin{aligned} N(E) &= \frac{1}{2\pi} \int pdp \frac{\delta(p - p_1)}{|\frac{p_1}{m} - \alpha|} + \frac{\delta(p - p_4)}{|\frac{p_4}{m} + \alpha|} = \\ &= \frac{m}{2\pi} \frac{m\alpha + \sqrt{(m\alpha)^2 + 2mE}}{\sqrt{(m\alpha)^2 + 2mE}} + \frac{-m\alpha + \sqrt{(m\alpha)^2 + 2mE}}{\sqrt{(m\alpha)^2 + 2mE}} = \\ &= \frac{m}{2\pi} N(E)_- + N(E)_+ = \frac{m}{\pi} \end{aligned} \quad , \quad \text{(B.3)}$$

     where we have defined

     $$N(E)_\pm = \frac{m}{2\pi}(1 \mp \frac{m\alpha}{\sqrt{(m\alpha)^2 + 2mE_\pm}}). \quad \text{(B.4)}$$

The graphic result is shown in the Fig.(2.3). Therefore, a discontinuity in the derivative is observed at $E = 0$ and a van Hove singularity at $-E_0$.

Known the DOS, can determine the occupation number. In the standard case we have

$$n = \int_{-E_0}^{E_F} N(E)dE = \int_{-E_0}^{E_F} \frac{m}{\pi} dE = \frac{m}{\pi}(E_F - E_0).$$

In the RSOC case we will have instead

$$n = \int_{-E_0}^{E_F<0} N(E)dE = \frac{m^2\alpha}{\pi} \int_{-E_0}^{E_F} \frac{dE}{\sqrt{(m\alpha)^2 + 2mE}} = \frac{m\alpha}{\pi} \sqrt{2m(E_0 + E_F)},$$

if the Fermi energy is less than zero and

$$n = \int_{-E_0}^{E_F>0} N(E)dE = \int_{-E_0}^{0} N(E)dE + \int_{0}^{E_F} N(E)dE = \frac{m}{\pi}\int_{-E_0}^{0} \frac{m\alpha dE}{\sqrt{(m\alpha)^2 + 2mE}}$$

$$+\frac{m}{\pi}\int_{0}^{E_F} dE = \frac{m}{\pi}(E_F + 2E_0),$$

if the Fermi energy is greater than zero.

What we have seen in this *Appendix*, supports the idea that in the presence of a RSOC the 2DEG manifests an anomalous behaviour already in the properties that define the normal phase.

C

The Dirac Comb

In the Kronig-Penney model we consider a potential made of a repeated succession of potential barriers with high V, wide W and sprawling of a distance L. The solution of the Schrödinger equation is found by imposing the continuity of the wavefunction and its first derivative on the discontinuities of the potential. Following this procedure you will get to calculate the determinant of matrices 4×4 (if there is a RSOC these matrices become 8×8). The problem can be simplified by imposing a potential known as *Dirac comb*: infinite sequence of Dirac delta-function centred in the nL sites (Fig. C.1).

The analytical form of the aforementioned potential is the following

$$V(z) = v_0 \sum_{n=-\infty}^{\infty} \delta(z - nL),$$

where v_0 is a positive constant with the dimensions of an energy for a length and n is an integer or zero.

In each of the ranges $(nL, (n+1)L)$ the particle is free, so the time-independent Schrödinger equation (3.4) admits plane-waves as fundamental solutions.

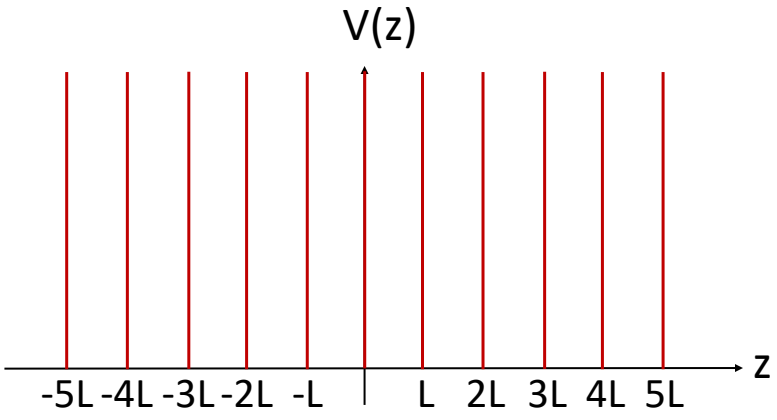

Figure C.1: *Periodic potential: Dirac comb.*

Formally

$$-\frac{\partial_z^2}{2m}\psi(z)+v_0\sum_n\delta(z-nL)\psi(z)=E\psi(z). \tag{C.1}$$

For $z\neq nL$:

$$-\frac{\partial_z^2}{2m}\psi(x)=E\psi(z)\Rightarrow\begin{cases}\psi(z)=e^{\pm ipz}\\ p=\sqrt{2mE} & for E>0\\ q=i\sqrt{2mE}=ip & for E<0.\end{cases} \tag{C.2}$$

We are now search solutions of the form:

$$\psi(z)=Ae^{ipz}+Be^{-ipz}. \tag{C.3}$$

The first condition to impose is that ψ satisfies Bloch theorem

$$\psi(L)=e^{ikL}\psi(0)\qquad I\ CONDITION. \tag{C.4}$$

Given that on the border there is a δ-Dirac function as a further condition we can impose the discontinuity of the first derivative. The idea is to integrate the stationary Schrödinger equation from $-\varepsilon$ to ε, with $\varepsilon>0$, and analyse the behaviour in the limit $\varepsilon\to L$ (point where we find the first discontinuity)

$$\lim_{\varepsilon\to0}\left(-\frac{1}{2m}\int_{-\varepsilon}^{\varepsilon}\frac{d^2\psi_(z)}{d^2z}dz+\int_{-\varepsilon}^{\varepsilon}V(z)\psi_(z)dz\right)=\lim_{\varepsilon\to0}\left(E\int_{-\varepsilon}^{\varepsilon}\psi_(z)dz\right). \tag{C.5}$$

Let's analyse the different contributions

$$\lim_{\varepsilon\to0}\left(-\frac{1}{2m}\int_{-\varepsilon}^{\varepsilon}\frac{d^2\psi_(z)}{d^2z}dz\right)=\lim_{\varepsilon\to0}\left(\frac{d\psi}{dz}\Big|_{z=\varepsilon}-\frac{d\psi}{dz}\Big|_{z=-\varepsilon}\right)=\left(\frac{d\psi}{dz}\Big|_{+}-\frac{d\psi}{dz}\Big|_{-}\right). \tag{C.6}$$

From the Bloch theorem and from the fact that the factor e^{ikL} does not depend on z, we have that the relation (C.4) must also hold for the derivatives

$$\frac{d\psi}{dz}\Big|_{z=0}=e^{-ikL}\frac{d\psi}{dz}\Big|_{z=L} \tag{C.7}$$

which replaced in equation (C.6) leads to

$$\frac{d\psi}{dz}\Big|_{z=0}-e^{-ikL}\frac{d\psi}{dz}\Big|_{z=L}. \tag{C.8}$$

Then, we used the Bloch theorem to replace the left derivative with the derivative calculated in $z=L$, thus passing to a condition at the edges of the barrier. Now consider the second contribution of the equation (C.5)

$$\lim_{\varepsilon\to0}\int_{-\varepsilon}^{\varepsilon}V(z)\psi_(z)dz\Rightarrow v_0\int_{-\varepsilon}^{\varepsilon}\delta(z-\varepsilon)\psi(z)dz=v_0\psi(\varepsilon)\longrightarrow_{\varepsilon\to0}v_0\psi(0). \tag{C.9}$$

Now consider the third contribution of the equation (C.5). For the first condition, ψ is a continuous function, for the Weiestrass theorem, in the compact $[-\varepsilon,\varepsilon]$, admits minimum, m, and maximum, M

$$m\int_{-\varepsilon}^{\varepsilon}dz\leqslant\int_{-\varepsilon}^{\varepsilon}\psi(z)dz\leqslant M\int_{-\varepsilon}^{\varepsilon}dz.$$

For the theorem of the *carabinieri* it follows that

$$\lim_{\varepsilon\to 0}\int_{-\varepsilon}^{\varepsilon}\psi_(z)dz = 0.$$

In conclusion we have

$$\begin{cases} -\frac{1}{2m}\left(\frac{d\psi}{dz}\Big|_{z=0} - \frac{d\psi}{dz}\Big|_{z=L} e^{-ikL}\right) + v_0\psi(0) = 0 \\ \Rightarrow \psi'(L)e^{-ikL} = \psi'(0) - 2mv_0\psi(0) \\ \Rightarrow \psi'(L) = e^{ikL}(\psi'(0) - 2mv_0\psi(0)) \quad II\ \ CONDITION. \end{cases} \tag{C.10}$$

It is therefore necessary to solve the following system:

$$\begin{cases} \psi(L) = e^{ikL}\psi \\ \psi'(L) = e^{ikL}(\psi'(0) - 2mv_0\psi(0)). \end{cases} \tag{C.11}$$

For $E > 0$ we have

$$\begin{cases} Ae^{ipL} + Be^{-ipL} = e^{ikL}(A+B) \\ Ae^{ipL} - Be^{-ipL} = (A-B) - \frac{2mv_0}{ip}(A+B), \end{cases} \tag{C.12}$$

placing $\mathcal{Z} = \frac{2mv_0}{ip}$, we have

$$\begin{cases} A(e^{ipL} - e^{ikL}) + B(e^{-ipL} - e^{ikL}) = 0 \\ A(e^{i(p-k)L} - 1 + \mathcal{Z}) + B(e^{-i(p+k)L} + 1 + \mathcal{Z}) = 0, \end{cases} \tag{C.13}$$

writing the coefficients matrix we have

$$\begin{pmatrix} e^{ipL} - e^{ikL} & e^{-ipL} - e^{ikL} \\ e^{i(p-k)L} - 1 + \mathcal{Z} & e^{-i(p+k)L} + 1 + \mathcal{Z} \end{pmatrix} \begin{pmatrix} A \\ B \end{pmatrix} = 0. \tag{C.14}$$

This system admits non-trivial solutions if the coefficient matrix has a null determinant, or

$$\begin{gathered} (e^{ipL} - e^{ikL})(e^{-i(p+k)L} + 1 + \mathcal{Z}) - (e^{-ipL} - e^{ikL})(e^{i(p-k)L} - 1 + \mathcal{Z}) = 0 \\ \Rightarrow -e^{-ikL} + e^{ipL} + e^{-ipL} - e^{ikL} + z(e^{ipL} - e^{-ipL}) = 0 \\ 2\cos(pL) - 2\cos(kL) + 2\mathcal{Z}i\sin(pL) = 0 \\ \Rightarrow \cos(pL) + \frac{2mv_0}{p}\sin(pL) = \cos(kL) = \mathcal{F}(E) \quad Solution\ for\ E > 0. \end{gathered} \tag{C.15}$$

For $E < 0$ we have

$$\begin{gathered} (e^{-pL} + e^{pL}) - (e^{-ikL} + e^{ikL})) + z(e^{-pL} - e^{pL}) = 0 \\ \Rightarrow \cosh(pL) + \frac{2mv_0 i}{p}\sinh(pL) = \cos(kL) = \mathcal{F}(E) \quad Solution\ for\ E < 0. \end{gathered} \tag{C.16}$$

The plot of the $\mathcal{F}(E)$ functions have been obtained with Mathematica software and shown in the Fig. C.2.

We will now consider the case $E > 0$. Since that $\mathcal{F}(E)$ must equal a cosine function (equation (C.14)), there are no values of k that satisfy this equation in the zones where the left member is between -1 and 1, or

$$|\cos(pL) + \frac{2mv_0}{p}\sin(pL)| \leq 1. \tag{C.17}$$

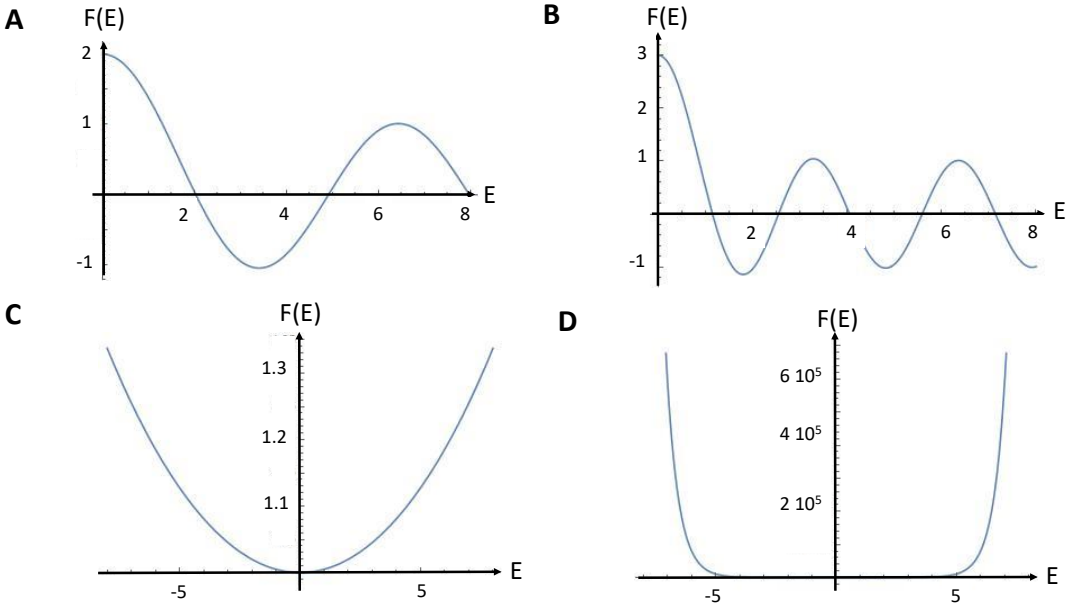

Figure C.2: In the *panel* **A** and **B** we plot equation (C.15) for different values of the parameters $a = L$ and $b = 2mv_0$. In particular in *panel* **A**, $a = b = 1$, while in *panel* **B** $a = 2,\ b = 1$. As a increases, the periodicity of the function decreases, while damping increases as b increases. In *panels* **C** and **D** we have plotted the real part of equation (C.16) for $a = 0.1$ and $a = 2$, respectively. It is observed that as a increases, the parabola widens and squeezes against the x-axis, while the effect of b is negligible. Similar considerations apply to the imaginary part of equation (C.16).

Once the values of p satisfying this inequality have been found, in correspondence with each of them it is possible to determine from the equation (C.14)the values of k which characterizes the Bloch functions. While the level energy is derived from the equation $E = p^2/2m$. The graphic solution of equation (C.17) obtained with Mathematica software is shown in the Fig. C.3.

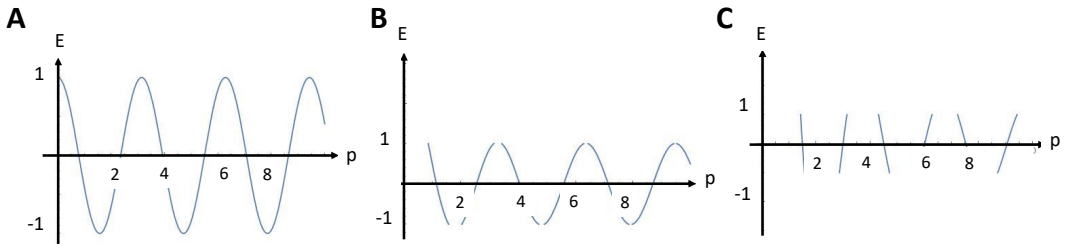

Figure C.3: In the *panel* **A**, **B** and **C** we plot the equation (C.17) for different values of the parameters $a = L$ and $b = 2mv_0$. In particular in *panel* **A**, $a = 2,\ b = 0$, in *panel* **B** $a = 2,\ b = 1$ and in *panel* **C** $a = 2,\ b = 10$. As a increases the periodicity of the function decreases, while as b increases the forbidden energies increase.

We see that there are ranges of energies in which the graph goes out of the allowed interval $(-1 \leq \mathcal{F}(E) \leq 1)$, alternating with values in which it is included. This ultimately means that we have allowed intervals of energies called "*bands*" and ranges of forbidden energies called "*gaps*". For very high energies, $2mv_0/p \to 0$, the left member tends to be a cosine function and, therefore, there are no prohibited energies. In reality

this is a limit behaviour, in fact the gaps are always present even at high energies, even if, as can be seen from the results obtained with Mathematica, they are shrinking more and more. The graphic solution is shown in Fig. C.4. The same result was obtained in Fortran Fig. C.5.

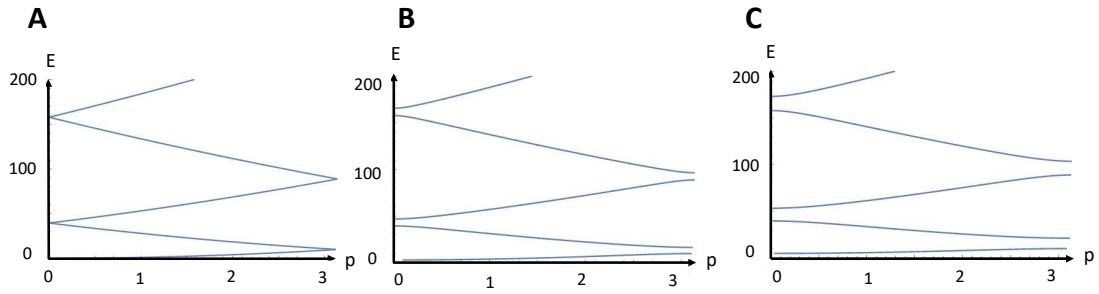

Figure C.4: *The energy bands in the Dirac Comb model obtained with Mathematica.* In the *panel* **A**, **B** and **C** we plot the dispersion obtained be inverted the equation (C.17) for different values of the parameter $b = 2mv_0$. In particular in *panel* **A**, $b = 0$, in *panel* **B** $b = 2$ and in *panel* **C** $b = 4$. As b increases the forbidden energies increase.

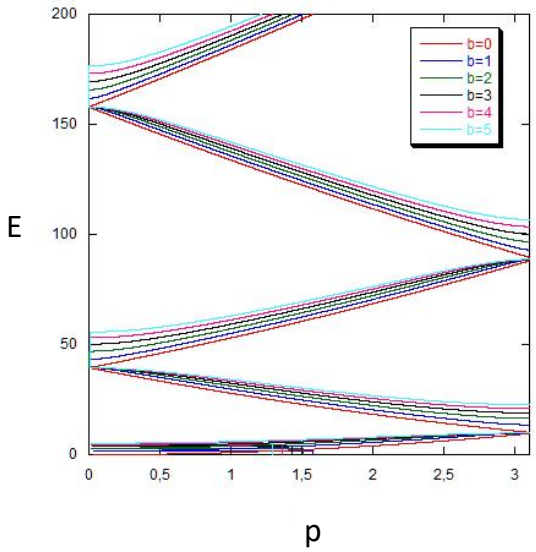

Figure C.5: *The energy bands in the Dirac Comb model with Fortran.* We plot the dispersion obtained be inverted the equation (C.17) for different values of the parameter $b = 2mv_0$. As b increases the forbidden energies increase.

D

The effect of phase factor on the gap equation

In this *Appendix* we consider the Rashba Hamiltonian with pairing interaction of the BCS type. The aim is to clarify if and how the gap equation may change by changing the orientation of the electric field responsible for the Rashba spin-orbit coupling (RSOC). The Rashba Hamiltonian will be considered with two different orientations. The first, as supposed in this thesis, has the traditional form with the electric field along the z-axis

$$H_z = \alpha(\sigma_x p_y - \sigma_y p_x), \tag{D.1}$$

whereas the second, considered in the works [17, 148], has the electric field along the y-axis

$$H_y = \alpha(\sigma_x p_z - \sigma_z p_x). \tag{D.2}$$

Let us consider now a rotation around the x-axis counterclockwise by $\pi/2$. The matrix of the transformation reads

$$U = \frac{1}{\sqrt{2}}\left(\sigma_0 - i\sigma_x\right). \tag{D.3}$$

Then one obtains the following transformation rules

$$\sigma_x \to \sigma_x, \quad \sigma_y \to \sigma_z, \quad \sigma_z \to -\sigma_y$$

and the equivalent for the momenta

$$p_x \to p_x, \quad p_y \to p_z, \quad p_z \to -p_y.$$

By using the above transformation rules, one has the transformation

$$H_z \to H_y.$$

The eigenvalues of H_z are $E_\lambda = \lambda\alpha p$ with $\lambda = \pm 1$. The corresponding eigenvectors read

$$\eta_\lambda(\vartheta) = \frac{1}{\sqrt{2}}\begin{pmatrix} 1 \\ -i\lambda e^{i\vartheta} \end{pmatrix}. \tag{D.4}$$

The angle ϑ defines the direction of the momentum $p_x = p\cos(\vartheta)$ with respect to the x-axis.

By applying the rotation U to the eigenvectors $\eta_\lambda(\vartheta)$ one gets

$$U\eta_\lambda(\vartheta) \longrightarrow \xi_\lambda(\vartheta) = \frac{1}{\sqrt{2}} \begin{pmatrix} \sqrt{1-\lambda\cos(\vartheta)} \\ \lambda\sqrt{1+\lambda\cos(\vartheta)} \end{pmatrix} e^{i\vartheta/2} e^{-i\pi(\lambda+1)/2}. \tag{D.5}$$

The vectors $\xi_\lambda(\vartheta)$ are the eigenvectors of the rotated Hamiltonian H_y. The overall phase factor of the eigenvectors $\xi_\lambda(\vartheta)$ is inherited by the eigenvectors $\eta_\lambda(\vartheta)$. Of course one could have diagonalized directly the Hamiltonian H_y getting as eigenvectors

$$\varsigma_\lambda(\vartheta) = \frac{1}{\sqrt{2}} \begin{pmatrix} \sqrt{1-\lambda\cos(\vartheta)} \\ \lambda\sqrt{1+\lambda\cos(\vartheta)} \end{pmatrix}. \tag{D.6}$$

The eigenvectors $\varsigma_\lambda(\vartheta)$ and $\xi_\lambda(\vartheta)$ differ by an overall phase factor. A key observation is that the choice of the phase factor determines the form of the gap function via the effective interaction in the helicity basis.

By following Gor'kov and Rashba [133], one defines the effective interaction as

$$U_{\lambda\lambda\mu\mu}(\vartheta,\vartheta') = \frac{U_0}{2} \left\langle \xi_\lambda(\vartheta) \left| \xi_\mu(\vartheta') \right\rangle \left\langle \xi_\lambda(\vartheta+\pi) \left| \xi_\mu(\vartheta'+\pi) \right\rangle \right.,$$

which leads to

$$U_{\lambda\lambda\mu\mu}(\vartheta,\vartheta') = \frac{U_0}{4} e^{-i(\vartheta-\vartheta')} e^{-i\pi(\lambda-\mu)/2} \left[\lambda\mu + \cos(\vartheta-\vartheta')\right].$$

One may remember that the inversion of momentum amounts to shift the angle ϑ by π.

Within the gap equation one has the combination of the effective potential

$$U_{\lambda\lambda\mu\mu}(\vartheta,\vartheta') - U_{\lambda\lambda\mu\mu}(\vartheta+\pi,\vartheta') = \frac{U_0}{2}\lambda\mu e^{-i(\vartheta-\vartheta')} e^{-i\pi(\lambda-\mu)/2}. \tag{D.7}$$

The above form of the potential in the gap equation is precisely the one obtained by Gor'kov and Rashba [133]. The second key observation is the following. Should one have used the eigenvectors (D.6), which do not have the overall phase factor, one would have obtained the combination

$$U_{\lambda\lambda\mu\mu}(\vartheta,\vartheta') - U_{\lambda\lambda\mu\mu}(\vartheta+\pi,\vartheta') = \frac{U_0}{2}\cos(\vartheta-\vartheta'). \tag{D.8}$$

The two forms (D.7) and (D.8) lead to different gap equations. It may be useful to recall the comment in the paper by Gor'kov and Rashba [133], soon after the equation (17):

> "Before we turn to the discussion of the nature of the order parameter in the new SC state, let us mention that the "gap function" $\Delta(\mathbf{p})$ depends on $\mathbf{p}$ through its phase. This dependence is inherent in the non-perturbative character of the spinor basis functions of equation (2) after spin degeneracy is lifted. It cannot be eliminated but can be changed by a different choice of phase factors in equation (2)."

Hence, one may use the eigenvectors (D.5) and obtain the same gap equation as in Gor'kov and Rashba [133].

E

Three-dimensional Rashba metal

Given the importance of the density of the states in the study of the properties of the normal and superconducting phase of a quantum system, in the following we will analyse the simple case of a three-dimensional (3D) system in the presence of RSOC, in which the electrons along the direction of the Rashba electric field are supposed free [19]. We start from the following Hamiltonian

$$H_0 = \frac{\hbar^2 k_\parallel^2 \boldsymbol{\sigma}_0}{2m} + \frac{\hbar^2 k_z^2 \boldsymbol{\sigma}_0}{2m_z} + \hbar\alpha(\hat{z} \times \mathbf{k}) \cdot \boldsymbol{\sigma}, \tag{E.1}$$

where $\mathbf{k} = (k_x, k_y, k_z)$ is the electron wave number, $\boldsymbol{\alpha} = \alpha\hat{z}$ is the Rashba vector pointing along the z-direction, $k_\parallel = \sqrt{k_x^2 + k_y^2}$ and $\boldsymbol{\sigma}_0$ is the identity matrix, while $\boldsymbol{\sigma} = (\sigma_x, \sigma_y, \sigma_z)$ is the Pauli matrix vector.

Diagonalization of equation (E.1) gives an electron dispersion consisting of two bands, that apart from a constant energy shift (as see in the following), are given by

$$E(\mathbf{k}, \lambda) = \frac{\hbar^2 k_z^2}{2m_z} + \frac{\hbar^2}{2m}(k_\parallel + \lambda k_0)^2, \tag{E.2}$$

where $k_0 = \alpha m/\hbar$ is the Rashba momentum, while $E_0 = \frac{\hbar^2 k_0^2}{2m} = m\alpha^2/2$ is the energy splitting RSOC and $\lambda = \pm 1$. In the equation (E.2) by imposing that $E(\mathbf{k}, \lambda) = E_F = \frac{\hbar^2 k_F^2}{2m}$, where E_F is the Fermi energy, we have

$$k_F^2 = \frac{m}{m_z} k_z^2 + (k_\parallel + \lambda k_0)^2 = \tilde{k}_z^2 + (k_\parallel + \lambda k_0)^2. \tag{E.3}$$

At this point we can distinguish two cases. The first case is $k_0 > k_F$ in where the only possible solution is that for $\lambda = -1$ and equation (E.3) is reduced to $k_F^2 = \tilde{k}_z^2 + (k_\parallel - k_0)^2$. This means that the surfaces of the retainers have a toroidal geometry (Fig. E.1 **A**). For the second case, $k_0 < k_F$, we have both the solutions for $\lambda = \pm 1$, the equation (E.3) is reduced to $k_F^2 = \tilde{k}_z^2 + (k_\parallel + \lambda k_0)^2$ and the Fermi surface has a more complex geometry (Fig. E.1 **B**).

Now we can to evaluate the DOS. Let us consider the case with $\lambda = -1$

$$N(E_F, -1) = \int_0^\infty \frac{k_\parallel dk_\parallel}{2\pi} \int_{-\infty}^\infty \frac{dk_z}{2\pi} \delta(k_z^2 + (k_\parallel - k_0)^2 - E_F). \tag{E.4}$$

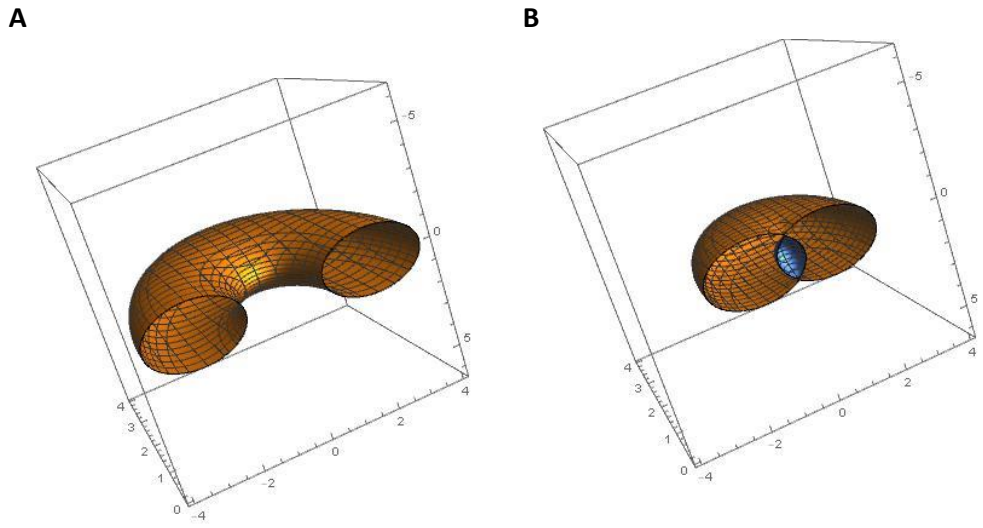

Figure E.1: *Evolution of the Fermi surface. Panel* **A**: case in which $k_0 > k_F$. *Panel* **B**: case in which $k_0 < k_F$. For $k_0 > k_F$ the Fermi level crosses only the $\lambda = -1$ band and the Fermi surface is a torus. In the case in which $k_0 > k_F$ we have two-solution and two toroidal Fermi surfaces with inner and outer surfaces corresponding to $\lambda = 1$ (blue) and $\lambda = -1$ (orange).

Notice that we put the integration over k_z first. It is equivalent and easier.

Let us make the change of variable $k' = k_{\|} - k_0$

$$N(E_F, -1) = \int_{-k_0}^{\infty} \frac{dk'}{2\pi}(k' + k_0) \int_0^{\infty} \frac{dk_z}{2\pi} \delta(k_z^2 + (k')^2 - E_F). \tag{E.5}$$

Define $\tilde{E} = k_z^2$, hence, $dk_z = 1/\sqrt{\tilde{E}} d\tilde{E}$

$$\begin{aligned} N(E_F, -1) &= \int_{-k_0}^{\infty} \frac{dk'}{2\pi}(k' + k_0) \int_0^{\infty} \frac{d\tilde{E}}{2\pi\sqrt{\tilde{E}}} \delta(\tilde{E} - E_F + k') \\ &= \int_{-k_0}^{\infty} \frac{dk'}{2\pi}(k' + k_0) \frac{1}{2\pi} \frac{\theta(E_F - k'^2)}{\sqrt{E_F - k'^2}}. \end{aligned} \tag{E.6}$$

The theta-function requires that $-\sqrt{E_F} < k' < \sqrt{E_F}$. There is no problem for $k' > 0$, but for $k' < 0$ we must distinguish:

- $\sqrt{E_F} < k_0$

$$\begin{aligned} N(E_F, -1) &= \frac{1}{4\pi^2} \int_{-k_0}^{-\sqrt{E_F}} \frac{k' + k_0}{\sqrt{E_F - k'^2}} \\ &= \frac{1}{4\pi^2} 2k_0 \int_0^1 \frac{x}{\sqrt{1 - x^2}} = \frac{k_0}{4\pi} \equiv \frac{\sqrt{E_0}}{4\pi}. \end{aligned} \tag{E.7}$$

- $\sqrt{E_F} > k_0$

$$\begin{aligned} N(E_F, -1) &= \frac{1}{4\pi^2} \int_{-k_0}^{-\sqrt{E_F}} dk' \frac{k' + k_0}{\sqrt{E_F - k'^2}} \\ &= \frac{1}{4\pi^2} \left[\int_{-k_0^2}^{\sqrt{E_F}} dx \frac{1}{2\sqrt{E_F - x}} + k_0 \int_{-k_0/\sqrt{E_F}}^{1} dx \frac{1}{\sqrt{1 - x^2}} \right]. \end{aligned} \tag{E.8}$$

Let us consider $\lambda = 1$

$$\begin{aligned} N(E_F, 1) &= \int_0^\infty \frac{dk_\parallel k_\parallel}{2\pi} \int_{-\infty}^\infty \frac{dk_z}{2\pi} \delta(k_z^2 + (k_\parallel + k_0)^2 - E_F) \\ &= \int_{k_0}^\infty \frac{dk'}{2\pi}(k' - k_0) \int_0^\infty \frac{dk_z}{2\pi} \delta(k_z^2 + k'^2 - E_F) \\ &= \int_{k_0}^\infty \frac{dk'}{2\pi}(k' - k_0) \frac{1}{2\pi} \frac{\theta(E_F - k'^2)}{\sqrt{E_F - k'^2}} = \frac{1}{4\pi^2} \int_{k_0}^{\sqrt{E_F}} dk' \frac{k' - k_0}{\sqrt{E_F - k'^2}} \\ &= \frac{1}{4\pi^2} \left[\int_{k_0^2}^{E_F} dx \frac{1}{2\sqrt{E_F - x}} - k_0 \int_{k_0/\sqrt{E_F}}^1 dx \frac{1}{\sqrt{1 - x^2}} \right] \\ &= \frac{1}{4\pi^2} \left[\sqrt{E_F - k_0^2} - k_0 \left(\frac{\pi}{2} - \arcsin\left(\frac{k_0}{\sqrt{E_F}} \right) \right) \right]. \end{aligned} \tag{E.9}$$

Finally

$$N(E_F) = \theta(E_0 - E_F) \frac{\sqrt{E_0}}{4\pi} + \theta(E_F - E_0) \frac{1}{2\pi^2} \left[\sqrt{E_F - E_0} + \sqrt{E_0} \arcsin\left(\frac{E_0}{E_F} \right) \right], \tag{E.10}$$

where $\arcsin(\frac{E_0}{E_F}) = \arctan(\frac{E_0}{E_F - E_0})$.

In the $k_0 < k_F$ regime the Fermi level crosses the bands of both helicity and the Fermi surface is a spindle torus, with the inner and outer sheets corresponding respectively to $\lambda = 1$ and $\lambda = -1$, as shown in the *panel* **B** of Fig. E.1. In this regime, the density of state (DOS) at the Fermi level is given by reduces the well-known expression for the density of states of a 3D electron gas asymptotically. In the $k_0 > k_F$ regime the Fermi level crosses only the $\lambda = -1$ band and the Fermi surface becomes a ring torus (Fig. E.1 **A**). In this regime the DOS is independent of Fermi energy, as in 2D electron gases (see *Chapter 2*)[1].

[1] The equation (E.2) is defined up to a constant term equal to $-k_0^2$ this is reflected in DOS with the simple substitution $N(E_F) \longrightarrow N(E_F + k_0^2)$

F

Complete derivation of the gap equation in a quantum layer heterostructure with RSOC

In the *Chapter 5* we have determined eigenvalues and eigenvectors of the Hamiltonian Rashba, $H_{RSOC}(x,y)$, see equations (5.15) and (5.19). From this equation it is possible to define the base change matrix that diagonalizes H_{RSOC}, as is known, this matrix has eigenvectors (equation (5.15)) for columns, therefore

$$\mathcal{M} = \frac{1}{\sqrt{2}} \begin{pmatrix} 1 & 1 \\ -ie^{i\vartheta} & ie^{i\vartheta} \end{pmatrix} =< s|\lambda >= \begin{bmatrix} < 1/2|1 > & < 1/2|-1 > \\ < -1/2|1 > & < -1/2|1 > \end{bmatrix}. \tag{F.1}$$

As seen, we can therefore define a two-component spinor in the helicity base

$$\eta^s_\lambda(\vartheta) =< s|\lambda >= \frac{1}{\sqrt{2}} \begin{bmatrix} 1 \\ i\lambda e^{i\vartheta} \end{bmatrix} \qquad \lambda = \pm 1. \tag{F.2}$$

The relationships that lead from the helicity to that spin base, and viceversa, therefore will be

$$\begin{cases} a_\lambda = \sum_s < \lambda|s > c_s = \sum_s U^\dagger_{\lambda,s} c_s = \sum_s (\eta^s_\lambda(\vartheta))^* c_s \\ c_s = \sum_\lambda < s|\lambda > a_\lambda = \sum_\lambda U_{s,\lambda} a_\lambda = \sum_\lambda (\eta^s_\lambda(\vartheta)) a_\lambda \end{cases}. \tag{F.3}$$

At this point we can introduce the interaction Hamiltonian in order to study the properties of the superconductive phase

$$H_I = \frac{1}{2} \int \Psi^\dagger(\mathbf{r}) \Psi^\dagger(\mathbf{r}') U_0 \delta(\mathbf{r} - \mathbf{r}') \Psi(\mathbf{r}) \Psi(\mathbf{r}'), \tag{F.4}$$

where the interaction is supposed punctual, $U(\mathbf{r} - \mathbf{r}') = U_0 \delta(\mathbf{r} - \mathbf{r}')$ and Ψ are the field operators

$$\Psi(\mathbf{r}) = \sum_{k,s} \psi_k(\mathbf{r}) \chi_s c_s(k), \tag{F.5}$$

with:

- $k = n, k_x, k_y, k_z$,

- $\psi_k(\mathbf{r}) = \frac{1}{\sqrt{L_x L_y}} e^{ik_x x} e^{ik_y y} \psi_{nk_z}(z)$,
- χ_s is the two-component spinor in the spin base.

It is therefore possible to rewrite the interaction Hamiltonian as

$$H_I = \frac{U_0}{2} \sum_{k_1,k_2,k_3,k_4} \sum_{s_1,s_2,s_3,s_4} \int [\psi^*_{k_1}(\mathbf{r}_1)\chi^\dagger_{s_1}(1)\psi^*_{k_2}(\mathbf{r}_2)\chi^\dagger_{s_2}(2)\delta(\mathbf{r}_1 - \mathbf{r}_2) \\ \psi_{k_3}(\mathbf{r}_2)\chi_{s_3}(2)]\psi_{k_4}(\mathbf{r}_1)\chi_{s_4}(1)d\mathbf{r}_1 d\mathbf{r}_2] c^\dagger_{s_1}(k_1)c^\dagger_{s_2}(k_2)c_{s_3}(k_3)c_{s_4}(k_4). \tag{F.6}$$

The basic vectors in the case of spin 1/2 are

$$\begin{cases} |+ >= \chi_+ = \begin{pmatrix} 1 \\ 0 \end{pmatrix} \\ |- >= \chi_- = \begin{pmatrix} 0 \\ 1 \end{pmatrix} \end{cases} , \tag{F.7}$$

then

$$\begin{cases} \chi^\dagger_{s_1}(1)\chi_{s_4}(1) = \delta_{s_1,s_4} \\ \chi^\dagger_{s_2}(2)\chi_{s_3}(2) = \delta_{s_2,s_3} \end{cases} . \tag{F.8}$$

Therefore, it is possible to write the interaction Hamiltonian as

$$H_I = \frac{U_0}{2} \sum_{k_1,k_2,k_3,k_4} \sum_{s_1,s_2} \int [\psi^*_{k_1}(\mathbf{r})\psi^*_{k_2}(\mathbf{r})\psi_{k_3}(\mathbf{r})\psi_{k_4}(\mathbf{r})d\mathbf{r}] c^\dagger_{s_1}(k_1)c^\dagger_{s_2}(k_2)c_{s_2}(k_3)c_{s_1}(k_4). \tag{F.9}$$

First we calculated $c^\dagger_{s_1}(k_1)c^\dagger_{s_2}(k_2)c_{s_2}(k_3)c_{s_1}(k_4)$, using the relationships (F.3)

$$c^\dagger_{s_1}(k_1)c^\dagger_{s_2}(k_2)c_{s_2}(k_3)c_{s_1}(k_4) = \sum_{\lambda_1,\lambda_2,\lambda_3,\lambda_4} a^\dagger_{\lambda_1}(k_1)a^\dagger_{\lambda_2}(k_2)a_{\lambda_3}(k_3)a_{\lambda_4}(k_4) \\ < \lambda_1|s_1 >< s_1|\lambda_4 >< \lambda_2|s_2 >< s_2|\lambda_3 >. \tag{F.10}$$

Now let's calculate the sum on the spin indices in the equation (F.9)

$$\begin{aligned} &\sum_{s_1,s_2} < \lambda_1|s_1 >< s_1|\lambda_4 >< \lambda_2|s_2 >< s_2|\lambda_3 > \\ &= \sum_{s_1} < \lambda_1|s_1 >< s_1|\lambda_4 > \sum_{s_2} < \lambda_2|s_2 >< s_2|\lambda_3 > \\ &= \sum_{s_1} (\eta^{s_1}_{\lambda_1}(k_1))^* \eta^{s_1}_{\lambda_4}(k_4) \sum_{s_2} (\eta^{s_2}_{\lambda_2}(k_2))^* \eta^{s_2}_{\lambda_3}(k_3) \\ &= \frac{1}{4}(1 + \lambda_1\lambda_4 e^{-i(\vartheta_1 - \vartheta_4)})(1 + \lambda_2\lambda_3 e^{-i(\vartheta_2 - \vartheta_3)}) \\ &= M_{\lambda_1,\lambda_4}(\vartheta_{k_1} - \vartheta_{k_4}) M_{\lambda_2,\lambda_3}(\vartheta_{k_2} - \vartheta_{k_3}) \end{aligned} . \tag{F.11}$$

We can now calculate the integral that appears in the equation (F.9)

$$I_{k_1,k_2,k_3,k_4} = \int \frac{1}{L^2_\parallel} e^{-i(k_{1\parallel} - k_{3\parallel})} e^{-i(k_{2\parallel} - k_{4\parallel})} dr_\parallel$$

$$\int \psi^*_{n_1 k_{1z}}(z)\psi^*_{n_2 k_{2z}}(z)\psi_{n_3 k_{3z}}(z)\psi_{n_4 k_{4z}}(z)dz. \tag{F.12}$$

Exploiting the properties of the δ-Dirac function, the integral in $dr_\parallel$ leads to the conservation law $k_{1\parallel} + k_{2\parallel} = k_{3\parallel} + k_{4\parallel}$. We can therefore put: $k_1 = k$, $k_2 = -k + q$, $k_3 = -k' + q$ and $k_4 = k'$, where $k = \{nk_z\}$, in this case the equation (F.12) becomes

$$I_{k,k',q} = \frac{2\pi}{L_\parallel^2} \int \psi_k^*(z)\psi_{-k+q}^*(z)\psi_{-k'+q}(z)\psi_{k'}(z)dz. \tag{F.13}$$

So for $q = 0$ we have

$$I_{k,k'} = \frac{2\pi}{L_\parallel^2} \int \psi_k^*(z)\psi_{-k}^*(z)\psi_{-k'}(z)\psi_{k'}(z)dz. \tag{F.14}$$

Recalling that $\psi_{nk_z}(z)$ is a Bloch function that holds $(\psi_{nk_z}(z))^* = \psi_{n-k_z}(z)$, we have:

$$I_{k,k'} = \frac{2\pi}{L_\parallel^2} \int |\psi_k(z)|^2|\psi_{k'}(z)|^2dz = \frac{2\pi}{L_\parallel^2} \int |\psi_{nk_z}(z)|^2|\psi_{n'k'_z}(z)|^2dz. \tag{F.15}$$

In conclusion, the interaction Hamiltonian is

$$\begin{aligned} H_I =& \frac{U_0}{2} \sum_{kk'q} I_{k,k',q} \sum_{\lambda_1,\lambda_2,\lambda_3,\lambda_4} M_{\lambda_1,\lambda_4}(\vartheta_k - \vartheta_{k'}) M_{\lambda_2,\lambda_3}(\vartheta_{-k+q} - \vartheta_{-k'+q}) \\ & a^\dagger_{\lambda_1}(k) a^\dagger_{\lambda_2}(-k+q) a_{\lambda_3}(-k'+q) a_{\lambda_4}(k') \\ =& \frac{1}{2} \sum_{kk'q} U_{\lambda_1,\lambda_2,\lambda_3,\lambda_4}(k,k',q) a^\dagger_{\lambda_1}(k) a^\dagger_{\lambda_2}(-k+q) a_{\lambda_3}(-k'+q) a_{\lambda_4}(k') \ , \end{aligned} \tag{F.16}$$

where we have defined

$$U_{\lambda_1,\lambda_2,\lambda_3,\lambda_4}(k,k',q) = U_0 I_{k,k',q} M_{\lambda_1,\lambda_4}(\vartheta_k - \vartheta_{k'}) M_{\lambda_2,\lambda_3}(\vartheta_{-k+q} - \vartheta_{-k'+q}). \tag{F.17}$$

At this point it is necessary to determine the equations of motion for the creation and destruction operators, $a^\dagger$ and a. What we get is

$$i\partial_t a_\lambda(k,t) = \xi_{k\lambda} a_\lambda(k,t) + \frac{1}{2} \sum_{q,\nu} [U_{\lambda\mu\nu\nu}(k,q) - U_{\mu\lambda\nu\nu}(-k,q)] a^\dagger_\mu(-k,t) a_\nu(-q,t) a_\nu(q,t), \tag{F.18}$$

$$i\partial_t a^\dagger_\lambda(-k,t) = -\xi_{-k\lambda} a^\dagger_\lambda(-k,t) + \frac{1}{2} \sum_{q,\nu} [U_{\lambda\mu\nu\nu}(-k,q) - U_{\mu\lambda\nu\nu}(k,q)] a^\dagger_\nu(q,t) a^\dagger_\nu(-q,t) a_\mu(k,t). \tag{F.19}$$

Starting from these equation we can determine the equations of motion of the normal and anomalous Green function. Whose definitions are, respectively, the following

$$\begin{aligned} G_\lambda(k,t-t') =& -i < T a_\lambda(k,t) a^\dagger_\lambda(k,t') > \\ =& -i\vartheta(t-t') a_\lambda(k,t) a^\dagger_\lambda(k,t') + i\vartheta(t'-t) a^\dagger_\lambda(k,-t) a_\lambda(k,t), \end{aligned} \tag{F.20}$$

$$\begin{aligned} -iF^\dagger_\lambda(k,t-t') =& < T a^\dagger_\lambda(-k,t) a^\dagger_\lambda(k,t') > \\ =& \vartheta(t-t') a^\dagger_\lambda(-k,t) a^\dagger_\lambda(k,t') - \vartheta(t'-t) a^\dagger_\lambda(k,t') a^\dagger_\lambda(-k,t). \end{aligned} \tag{F.21}$$

For these functions we have the following equations of motion

$$\begin{aligned} i\delta_t G_\lambda(k,t-t') =& \delta(t-t') + \xi_{k\lambda} G_\lambda(k,t-t') + \\ & + \frac{i}{2} \sum_{q,\nu} [U_{\lambda\lambda\nu\nu}(k,q) - U_{\lambda\lambda\nu\nu}(-k,q)] F_\nu(q,0^+) F^\dagger(k,t-t'), \end{aligned} \tag{F.22}$$

$$i\delta_t(-iF^\dagger_\lambda(k,t-t')) = -\xi_{-k\lambda}(-iF^\dagger_\lambda(k,t-t'))+ \\ -\frac{1}{2}\sum_{q,\nu}[U_{\lambda\lambda\nu\nu}(-k,-q)-U_{\lambda\lambda\nu\nu}(k,-q)](-iF^\dagger_\nu(q,0^+))(-iG_\lambda(k,t-t')). \tag{F.23}$$

Calling

$$\begin{cases}\Delta_\lambda(k) = -\frac{1}{2}\sum_{q,\nu}[U_{\lambda\lambda\nu\nu}(k,q)-U_{\lambda\lambda\nu\nu}(k,-q)]F_\nu(q,0^+) \\ \Delta^\dagger_\lambda(k) = -\frac{1}{2}\sum_{q,\nu}[U_{\lambda\lambda\nu\nu}(-k,-q)-U_{\lambda\lambda\nu\nu}(k,-q)]F^\dagger_\nu(q,0^+)\end{cases} \tag{F.24}$$

and solving the equations (F.22, F.23) in Fourier space, remembering that the anti-transform is

$$G_\lambda(k,t-t') = T\sum_\omega e^{-i\omega(t-t')}G_\lambda(k,\omega)$$

and that

- $\partial_t \to i\omega$,
- $\nabla^2 \to k^2$,
- $\delta \to f(\omega,k) = 1$ constant function,

where the choice $\omega = (2n+1)\pi/\beta$ guarantees that they are fermions.

What we get is

$$(\omega-\xi_{k\lambda})G_\lambda(k,\omega) + i\Delta_\lambda(k)F^\dagger_\lambda(k,\omega) = 1. \tag{F.25}$$

Proceeding in a completely similar way, we obtain the equation of motion for the anomalous Green function

$$(\omega+\xi_{-k\lambda})F^\dagger_\lambda(k,\omega) - i\Delta^\dagger(\lambda)(k)G_\lambda(k,\omega) = 0. \tag{F.26}$$

In matrix form we have

$$\begin{pmatrix}\omega-\xi_{k\lambda} & i\Delta_\lambda(k) \\ -i\Delta^\dagger_\lambda(k) & \omega+\xi_{-k\lambda}\end{pmatrix}\begin{pmatrix}G_\lambda(k,\omega) \\ F^\dagger_\lambda(k,\omega)\end{pmatrix} = \begin{pmatrix}1\\0\end{pmatrix}. \tag{F.27}$$

In compact form it is possible to write $Ax = y \Rightarrow x = A^{-1}y$, where the inverse of a 2x2 matrix is calculated as

$$A = \begin{pmatrix}a & b\\ c & d\end{pmatrix} \Rightarrow A^{-1} = \frac{1}{det(A)}\begin{pmatrix}d & -b\\ -c & a\end{pmatrix}.$$

Then, we compute $det(A)$

$$det(A) = (\omega-\xi_{k\lambda})(\omega+\xi_{-k\lambda}) - |\Delta_\lambda(k)|^2 = \omega^2 - \xi^2_{k\lambda} - |\Delta_\lambda(k)|^2.$$

Defining the quasiparticle energy of the superconducting state as

$$E_{k\lambda} = \sqrt{\xi^2_{k\lambda}+|\Delta_\lambda(k)|^2} \Rightarrow det(A) = (\omega-E_{k\lambda})(\omega+E_{k\lambda}).$$

Then, the solution for the system (F.27) is

$$\begin{cases}G_\lambda(k,\omega) = \frac{\omega+\xi_{-k\lambda}}{\omega^2+E^2_{k\lambda}} \\ F^\dagger_\lambda(k,\omega) = \frac{i\Delta^{\dagger *}_\lambda(k)}{\omega^2+E^2_{k,\lambda}}\end{cases}. \tag{F.28}$$

At this point from the definitions (F.24) it is possible to derive the gap equation.

First you need to calculate $[U_{\lambda\lambda\nu\nu}(-k,-q) - U_{\lambda\lambda\nu\nu}(k,-q)]$, where

$$\begin{cases} U_{\lambda\lambda\nu\nu}(k,q) = U_0 I_{k,-k,-q,q} M_{\lambda\nu}(\vartheta_k - \vartheta_q) M_{\lambda\nu}(\vartheta_{-k} - \vartheta_{-q}) \\ U_{\lambda\lambda\nu\nu}(-k,-q) = U_0 I_{-k,k,q,-q} M_{\lambda\nu}(\vartheta_{-k} - \vartheta_{-q}) M_{\lambda\nu}(\vartheta_k - \vartheta_q) \end{cases} . \tag{F.29}$$

By taking that $\vartheta_{-k} - \vartheta_{-q} = \vartheta_k - \vartheta_q$ and that

$$M_{\lambda\nu}(\vartheta_k - \vartheta_q) = U^\dagger(\vartheta_k) U(\vartheta_q) = e^{-i\frac{\vartheta_k - \vartheta_q}{2}} \begin{pmatrix} cos(\vartheta_k - \vartheta_q/2) & isin(\vartheta_k - \vartheta_q/2) \\ isin(\vartheta_k - \vartheta_q/2) & cos(\vartheta_k - \vartheta_q/2) \end{pmatrix}, \tag{F.30}$$

we have

$$[U_{\lambda\lambda\nu\nu}(-k,-q) - U_{\lambda\lambda\nu\nu}(k,-q)] = U_0 I_{kq} \lambda\nu e^{i(\vartheta_k - \vartheta_q)}. \tag{F.31}$$

In conclusion the gap equation becomes

$$\Delta^\dagger_\lambda(k) = -\frac{U_0}{2} \sum_q \sum_\nu I_{kq} \lambda\nu e^{i(\vartheta_k - \vartheta_q)} T \sum_\omega \frac{\Delta^\dagger_\nu(q)}{\omega^2 + E^2_{q\nu}}. \tag{F.32}$$

All that remains is to calculate the sum on the Matsubara frequencies, ω, we start from the following equation

$$T \sum_\omega \frac{1}{\omega^2 + E^2_{k\lambda}} = T \sum_\omega \frac{1}{(\omega - E_{k\lambda})(\omega + E_{k\lambda})}.$$

At this point it is possible to use the simple fract method:

$$\frac{1}{ab} = \left(\frac{1}{a} - \frac{1}{b}\right) \frac{1}{b-a},$$

hence

$$T \sum_\omega \frac{1}{\omega^2 + E^2_{k\lambda}} = T \sum_\omega \frac{1}{2E_{k\lambda}} \left(\frac{1}{(\omega - E_{k\lambda})} - \frac{1}{(\omega + E_{k\lambda})} \right).$$

Recalling that the function of Fermi is defined as

$$f(a) = T \sum_{\varepsilon_n} \frac{1}{\omega - a} = \frac{1}{e^{\beta a} + 1}$$

and that the following property holds for it

$$f(-a) = 1 - f(a).$$

In conclusion, we can write

$$T \sum_\omega \frac{1}{\omega^2 + E^2_{k\lambda}} = \frac{\tanh(\frac{\beta E_{k\lambda}}{2})}{2E_{k\lambda}}. \tag{F.33}$$

In the limit $T \to 0$, $\frac{\beta E_{k\lambda}}{2} \to \infty$, remembering that $lim_{x\to\infty} \tanh(x) = 1$, in conclusion the following relationships of self-consistency is obtained

$$\begin{cases} \Delta^\dagger_\lambda(k) = -\frac{U_0}{2} \sum_q \sum_\nu I_{kq} \lambda\nu e^{-i(\vartheta_k - \vartheta_q)} \frac{\Delta^\dagger_\nu(q)}{2E_{q\nu}} \\ \Delta_\lambda(k) = -\frac{U_0}{2} \sum_q \sum_\nu I_{kq} \lambda\nu e^{i(\vartheta_k - \vartheta_q)} \frac{\Delta_\nu(q)}{2E_{q\nu}} \end{cases} . \tag{F.34}$$

Considering, for example, the second relationship of (F.34) it possible to write

$$\begin{cases} \Delta_\lambda(k) = \lambda e^{i\vartheta_{k_\parallel}} \Delta(n, k_z) \\ \Delta(n, k_z) = -\frac{U_0}{2} \sum_{n', k'_z} I^{nn'}_{k_z, k'_z} \Delta(n', k'_z) \sum_\nu \sum_{k'_x, k'_y} \frac{1}{2E_{k'\nu}} \end{cases} . \tag{F.35}$$

One notices that the pairing potential has a dependence on momentum via the exponential factor and a dependence on the helicity index via λ. The quantity $\Delta(n, k_z)$ does not depend explicitly on momentum and helicity according to Gor'kov and Rashba paper [133].

In the equation (F.35)

$$\begin{aligned} E_{k'\nu} &= \sqrt{\left(\frac{\hbar^2}{2m} k'^2_\parallel - \nu\alpha\hbar k'_\parallel + E_{n'}(k'_z) - E_F\right) + |\Delta_\nu(n', k'_z, \vartheta_{k'_\parallel})|^2} \\ &= \sqrt{(\varepsilon_\nu(k'_x, k'_y) + E_{n'}(k'_z) - E_F)^2 + |\Delta_\nu(n', k'_z)|^2} = f(\varepsilon_\nu(k'_x, k'_y)). \end{aligned} \tag{F.36}$$

The function $f(\varepsilon_\nu(k'_x, k'_y))$ is independent of $\vartheta_{k'}$ so integration in k'_x and k'_y is reduced to a single integration on k' or, passing to the density of states (equation (F.37)), to an integration on ε. Going to the density of the states simplifies the problem of calculating the integrals that appear in the definition of the gap that would otherwise be elliptical integrals.

$$\begin{aligned} \sum_{k_x, k_y} f(\varepsilon_\nu(k_\parallel)) &= \frac{L_x L_y}{(2\pi)^2} \int 2\pi k_\parallel f(\varepsilon_\nu(k_\parallel)) dk_\parallel \\ &= \frac{L_x L_y}{(2\pi)^2} \int 2\pi k_\nu(\varepsilon) f(\varepsilon) \left|\frac{dk_\nu(\varepsilon)}{d\varepsilon}\right| d\varepsilon, \end{aligned} \tag{F.37}$$

where $k_\nu(\varepsilon)$ is obtained by inverting the following equation

$$\varepsilon_\nu(k_\parallel) = \frac{\hbar^2}{2m} k^2_\parallel - \hbar\nu\alpha k_\parallel = a(k_\parallel - k_0)^2 + E_0, \tag{F.38}$$

with

$$\begin{cases} a = \frac{\hbar^2}{2m} \\ k_0 = \frac{m\nu\alpha}{\hbar} \\ E_0 = \frac{m\alpha^2}{2} = \frac{\hbar^2 k_0^2}{2m} \end{cases} . \tag{F.39}$$

In order to determine the gap equation we considered the zero temperature limit, that is $T \longrightarrow 0$, $\beta E_{k\lambda}/2 \longrightarrow \infty$, and thus obtained the equation (F.34). We want to see now what happens at the finished temperature, that is, in the opposite limit: $T \longrightarrow T_C$, $\Delta \longrightarrow 0$.

In this case it is necessary to use the equation (F.35) for the sums on the Matsubara frequencies and then evaluate the following equation numerically and in a self-consistent way

$$\Delta(n, k_z) = -\frac{U_0}{2} \sum_{n', k'_z} I^{nn'}_{k_z k'_z} \Delta(n', k'_z) \sum_\nu \sum_{k'_x, k'_y} \frac{\tanh(\frac{\beta E_{k\lambda}}{2})}{2E_{k'\nu}}. \tag{F.40}$$

Taking into account the fact that the critical temperature is by definition the temperature at which all the gaps cancel each other out.

G

Numerical simulation

In the following we attach the numerical model implemented with Fortran to solve the normal and superconducting phase of a heterostructure of quantum layers in the presence of RSOC.

```
!______________________________________________________________________


!************* SUPERLATTICE OF LAYERS WITH RSOC COUPLING***************

! This program compute, with BPV theory, the properties of the normal
! and superconductive phase of a superlattice of layers in the isotropic
! case (mx=mz) and in presence of an RSOC coupling.
! In this system the electrons in the plane (x,y) are free and the
! energy bands are split, depending on the helicity, by the RSOC
! coupling based, the electrons along the z direction are subjected to a
! Kronig-Penney potential and subjected to an electric field along z.
!______________________________________________________________________

! Compile with
! parallel version:
!  gfortran -O -Wno-align-commons -fopenmp
!                           -o RSOC_KP_3d RSOC_KP_3d.f dqags.f d1mach.f
!
! Serial version:
!  gfortran -O -Wno-align-commons
!                           -o RSOC_KP_3d RSOC_KP_3d.f dqags.f d1mach.f
!______________________________________________________________________

program 3D System with RSOC

include 'RSOC_KP_3d_inc.f'
!The global variables are defined in this file
```

```
character*12 Name,Name1,Name2, Namex, Namez

Ending = '.C04'

call Initialize

!_____Normal Phase_____________________________________________________

BandBottom = minimum_energy - 0.01
BandTop = 2.0d0
Name = 'DOS'
call DensityStates(Name)

!____Superconductive Phase_____________________________________________

Name = 'Gap'
Name1= 'NSuper'
Name2= 'DSuper'
call GapvsEf(Name)

Name = 'Tc'
call TcvsEf(Name)

stop
end


!**********************************************************************
!************************** NORMAL PHASE ******************************
!**********************************************************************


!______________________________________________________________________

! ______________ Initializes parametres of model _____________________
!______________________________________________________________________

subroutine Initialize
include 'RSOC_KP_3d_inc.f'
integer n,i,nn,np
character*12 Name
real*8 deltaE_RSOC

Vb = 500.d-3            ! potential barrier (V)

h = 7.00d0              ! barrier width (A)
L = 23.00d0             ! well width    (A)
d = h + L               ! period        (A)
```

```
mw = 1.0d0                ! effective mass in the well     (adim)
mb = 1.0d0                ! effective mass on the barrier  (adim)
mx = 1.0d0                ! effective mass along x         (adim)
mz = 1.0d0                ! effective mass along z         (adim)

! Order of magnitude of the strength of the spin-orbit coupling
deltaE_RSOC = 2.0 * ht2up2m * (2.d0*Pi/d)

DensityLimit = 0.01d0

! Interval for Ef in the plots of Gap vs Ef and Tc vs Ef
BottomEf    = -0.66
TopEf    = -0.16
GapPlot = LeaveHighEnergy

! The following code defines the strength
! of the spin-orbit coupling
! for each subband alphaRSOC(n)
alphaRSOC(1) = 0.7 * deltaE_RSOC
alphaRSOC(2) = 0.7 * deltaE_RSOC

! The following code initializes the coupling SC: lambda(nn,np)
do nn = 1,NBands
do np = 1,NBands
if (nn .eq. np) then
lambda(nn,np) = 0.4
else
lambda(nn,np) = 0.4
end if
end do
end do

! The following code initializes the energy cut-off: omegad(nn,np)
do nn = 1,NBands
do np = 1,NBands
if (nn .eq. np) then
omegad(nn,np) = 60.0D-3  ! [eV]
else
omegad(nn,np) = 60.0D-3
end if
end do
end do

! omegadmax is the cut-off beyond which the gap is certainly zero
omegadmax = -1.d0
do nn = 1,NBands
do np = 1,NBands
if (omegad(nn,np) .gt. omegadmax) then
omegadmax = omegad(nn,np)
```

```
end if
end do
end do

! End of inputs ____________________________________________________

! The bands are searched within this interval
BandBottom = -Vb
BandTop =  -0.16d0

ZByExtended = 2.d0*Pi/d
ZBy = ZByExtended

Name = 'cqd'
call GraphCqd(Name)

call ExtremeBand
write (6,*) 'Found bands extrema:'
write (6,'  (4E18.10)') ((EEdge(n,i),i=1,4),n=1,NBands)

ZBxExtended = 2.d0*dsqrt((EEdge(NBands,2)+2.d0*Vb)/ht2up2m*mx)
ZBx = ZBxExtended

ZBzExtended = 2.d0*dsqrt((EEdge(NBands,2)+2.d0*Vb)/ht2up2m*mz)
ZBz = ZBzExtended

Name = 'BandsKy'
call BandupKy(Name)
call compute_minimum_energy

write (6,*) 'Bands Compute'

call FunctionCoefficients
write (6,*) 'Calculated AutoFunctions Coefficients'

call CalculateCoupling
write (6,*) 'Calculated Coupling Coefficients'

end

! 1) DOS and Dispersion Equation


!_____________________________________________________________________

! _______________ Computes Bottom and Top of the bands _________________

!_____________________________________________________________________
```

```
subroutine ExtremeBand
include 'RSOC_KP_3d_inc.f'
integer nb
real*8 ee,de,e1,e2,e3,emin,emax,minq,maxq

minq = 0.5d0*ZBy/2.d0/dfloat(NPointsZB)
maxq = (dfloat(NPointsZB)-0.5d0)*ZBy/2.d0/dfloat(NPointsZB)
write (6,*) minq,maxq
de = (BandTop-BandBottom)/50000.d0
write (6,*) 'BandTop ',BandTop
write (6,*) 'BandBottom ',BandBottom
ee = BandBottom+de
do nb = 1,NBands
call ThreePoints(ee,de,e1,e2,e3)
call BinaryResearch(dfloat((-1)**(nb+1)),
+       e1,e2,EEdge(nb,1),EEdge(nb,3),(-1)**nb)
call BinaryResearch(dfloat((-1)**(nb+2)),
+       e2,e3,EEdge(nb,2),EEdge(nb,4),(-1)**nb)
ee = e3

if ( mod(nb,2) .eq. 1) then
if ( EEdge(nb,3) .gt. minq .or. EEdge(nb,4) .lt. maxq) then
write (6,*) 'Problems ...'
stop
end if
else
if ( EEdge(nb,3) .lt. maxq .or. EEdge(nb,4) .gt. minq) then
write (6,*) 'Problems ...'
stop
end if
end if

end do
end

!_____________________________________________________________________
subroutine BinaryResearch(target,e1,e2,ee,q,verso)
include 'RSOC_KP_3d_inc.f'
integer verso,f,ss
real*8 target,emin,emax,ee,q,cqd,dq,pee,e1,e2

emin = e1
emax = e2

ee = (emin+emax)/2.d0
pee = ee + 1.d0

call EquationKP(ee,q,cqd,f)
ss = dsign(1.d0,cqd-target)
```

```
do while (pee .ne. ee)

if (ss * verso .eq. 1) then
emax = ee
else
emin = ee
end if
pee = ee
ee = (emax+emin)/2.d0
call EquationKP(ee,q,cqd,f)
ss = dsign(1.d0,cqd-target)
end do
write (6,*) 'ee,q',ee,cqd,q
end

!-----------------------------------------------------------------------
subroutine ThreePoints(es,de,e1,e2,e3)
include 'RSOC_KP_3d_inc.f'
real*8 e1,e2,e3,es,de,q,dq,cqd,ee,emin,emax
integer scqd,pscqd,f

ee = es
e1 = ee
call EquationKP(ee,q,cqd,f)
pscqd = dsign(1.d0,cqd)
scqd = pscqd
do while ( scqd .eq. pscqd .or. dabs(cqd) .lt. 1.d0)
ee = ee + de
call EquationKP(ee,q,cqd,f)
scqd = dsign(1.d0,cqd)
end do
e3 = ee
emax = e3
emin = e1
ee = ( e1 + e3 )/2.d0
call EquationKP(ee,q,cqd,f)
scqd = dsign(1.d0,cqd)
do while ( dabs(cqd) .gt. 1.d0 )

if (pscqd * scqd .eq. 1) then
e1 = ee
else
e3 = ee
end if
ee = ( e1 + e3 )/2.d0
call EquationKP(ee,q,cqd,f)
scqd = dsign(1.d0,cqd)
end do
```

```
e2 = ee

call EquationKP(e1,q,cqd,f)
write (6,*) e1,cqd
call EquationKP(e2,q,cqd,f)
write (6,*) e2,cqd
call EquationKP(e3,q,cqd,f)
write (6,*) e3,cqd
end


!_____________________________________________________________________

!__ Solution of the implicit Kronig-Penney equation for the energies ___

!_____________________________________________________________________
subroutine EquationKP(ee,q,cqd,f)
include 'RSOC_KP_3d_inc.f'
real*8 Kb,Kw,csi,cqd,dF,dKb,dKw,ee,q,dcsi
integer f

!For positive energies
if (ee .gt. 0.d0) then
Kb = dsqrt(mb/ht2up2m*ee)
Kw = dsqrt(mw/ht2up2m*(ee+Vb))
csi = Kb/Kw
cqd = dcos(Kw*L)*dcos(Kb*h)
+       -0.5*( csi+1.d0/csi)*dsin(Kw*L)*dsin(Kb*h)
end if

!For negative energies
if (ee .le. 0.d0) then
Kb = dsqrt(-mb/ht2up2m*ee)
Kw = dsqrt(mw/ht2up2m*(ee+Vb))
csi = Kb/Kw
cqd = dcos(Kw*L)*dcosh(Kb*h)
+       -0.5*(-csi+1.d0/csi)*dsin(Kw*L)*dsinh(Kb*h)
end if

!Check that |cos(qd)|<=1
if (dabs(cqd) .le. 1.d0) then
f = 1
q = dacos(cqd)/d
else
f = 0
end if
end
```

```
!_____________________________________________________________________

!____ Graph of the implicit Kronig-Penney Equation for the energies ____

!_____________________________________________________________________

subroutine GraphCqd(Name)
include 'RSOC_KP_3d_inc.f'
real*8 ee,cqd,q,dq,de
integer f,i
character*12 Name

open (12,file=Name(1:Len_Trim(Name))//Ending,
+    form='FORMATTED',status='UNKNOWN')
de = ((BandTop - BandBottom)/500.d0)
do i = 0,500
ee = BandBottom+(dfloat(i))*de
call EquationKP(ee,q,cqd,f)
write (12,*) ee,cqd,dq,f
end do
close(12)
end

!_____________________________________________________________________

!____________ Density of states vs chemical potential (Mu) _____________

!_____________________________________________________________________

subroutine DensNormvsMu(Name)
include 'RSOC_KP_3d_inc.f'
character*12 Name,NameFile
real*8 de,ddos,A,dens,mu
integer n,i

de = (TopEf-BottomEf)/dfloat(NPointsGDvsMu)
ddos = (BandTop-BandBottom)/dfloat(NPointsDOS)

write (NameFile,"(A,A)")
+    Name(1:Len_Trim(Name)),
+    Ending(1:Len_Trim(Ending))
open (20,file=NameFile,
+            form='FORMATTED',status='UNKNOWN')

A = 32. * Pi**2 * d * (NPointsZBDOS ** 3.) / (ZBx*ZBz)
do i = NPointsGDvsMu,1,-1
Ef = BottomEf+(dfloat(i)-0.5d0)*de
n = 1
mu = BandBottom+(dfloat(n)-0.5d0)*ddos
```

```
dens = 0.
do while (mu .lt. Ef)
dens = dens + DOS(0,n)*2./A
n = n+1
mu = BandBottom+(dfloat(n)-0.5d0)*ddos
end do
write (20,*) Ef,dens
end do
close(20)
end

!_____________________________________________________________________

!________ This routine computes the bands filling known the DOS ________

!_____________________________________________________________________

subroutine MuvsDens(Name)
include 'RSOC_KP_3d_inc.f'
character*12 Name,NameFile
real*8 n,dn,dens,dens1,EEf,dMu,A
integer i

write (NameFile,'(A,A)') Name(1:Len_Trim(Name)),Ending
open (12,file=NameFile,form='FORMATTED',status='UNKNOWN')

A = 32. * Pi**2 * d * (NPointsZBDOS**3.) / (ZBx*ZBz)
dn = DensityLimit/NPointsMu
i = 0
dMu = (BandTop-BandBottom)/dfloat(NPointsDOS)
dens = 0.d0
n = 0.d0
do while (n .lt. DensityLimit)
do while (dens .le. n)
i = i + 1
dens1 = dens
dens = dens1 + dfloat(DOS(0,i))*2./A ! *dMu
end do
EEf = dMu*(n-dens1)/(dens-dens1)+
+       BandBottom+
+       dfloat(i-1)/dfloat(NPointsDOS)*(BandTop-BandBottom)
write (12,*) n,EEf
n = n+dn
end do

close (12)
end
```

```
!_____________________________________________________________________

!_ This subroutine makes a histogram to find the density of the states _

!_____________________________________________________________________

subroutine DensityStates(Name)
include 'RSOC_KP_3d_inc.f'
real*8 dkx,dky,dkz, EE1, EE2
real*8 kx0,ky0,kz0
integer nkx0,nky0,nkz0
real*8 Enky0(NBands)
integer n,j
integer*8 conta
character*12 Name,NameBands,outputFile

common /privateDOS/ private_DOS
integer             private_DOS(0:2*NBands,NPointsDOS)
write (*,*) 'Computing DOS ...'
call InitializesDOS


!----------------- If NPointsZBDOS < 70 --------------------------------
!--------opens n files where it saves the dispersion--------------------
if (NPointsZBDOS .lt. 70) then
do n = 1,NBands
write (NameBands,'(A,I2.2,A)') 'Band',n,Ending
open (FileBandsBase+n,file=NameBands,
+         form='FORMATTED',status='UNKNOWN')
end do
end if
!---------------------------------------------------------------------

conta = 0
dkx = ZBx/dfloat(NPointsZBDOS)/2.d0
dkz = ZBz/dfloat(NPointsZBDOS)/2.d0
dky = ZBy/dfloat(NPointsZBDOS)/2.d0


! each thread clean its own private_DOS
do n = 0,(2*NBands)
do j = 1,NPointsDOS
private_DOS(n,j) = 0
end do
end do

do nky0 = 1,NPointsZBDOS
ky0 = (dfloat(nky0)-0.5d0)*dky
```

```
call EdiQ(ky0,Enky0)

do nkx0 = 1,NPointsZBDOS
kx0 = (dfloat(nkx0)-0.5d0)*dkx
do nkz0 = 1,NPointsZBDOS
kz0 = (dfloat(nkz0)-0.5d0)*dkz
do n = 1,NBands
EE1= Enky0(n) + ht2up2m/mx*kx0**2 + ht2up2m/mz*kz0**2
+                  + alphaRSOC(n)*sqrt(kx0**2 + kz0**2)
EE2= Enky0(n) + ht2up2m/mx*kx0**2 + ht2up2m/mz*kz0**2
+                  - alphaRSOC(n)*sqrt(kx0**2 + kz0**2)

!Total DOS for the band with chirality + and -
call AddtoDOS(ee1,0)
call AddtoDOS(ee2,0)
!DOS for each upbband with chirality   +
call AddtoDOS(ee1,n)
!DOS for each upbband with chirality   -
call AddtoDOS(ee2,NBands+n)
if (NPointsZBDOS .lt. 70) then
write (FileBandsBase+n,*) kx0,ky0,kz0,ee1,ee2

end if
end do
end do
end do
end do

do n = 0,2*NBands
do j = 1,NPointsDOS
DOS(n,j) = DOS(n,j) + private_DOS(n,j)
end do
end do

call WriteDOS(Name)
if (NPointsZBDOS .lt. 70) then
do n = 1,NBands
close(FileBandsBase+n)
end do
end if
write (*,*) 'DOS computed!'
end

!_____________________________________________________________________

!___________ Initialize the histogram that calculates the DOS __________

!_____________________________________________________________________
```

```
subroutine InitializesDOS
include 'RSOC_KP_3d_inc.f'
integer n,i
do n = 0,(2*NBands)
do i = 1,NPointsDOS
DOS(n,i) = 0
end do
!        NStati(n) = 0
end do
end

!-----------------------------------------------------------------------

!_____________________ DOS on the complete ZB _____________________

!-----------------------------------------------------------------------

subroutine AddtoDOS(ee,nb)
include 'RSOC_KP_3d_inc.f'
real*8 ee
integer n,nb

common /privateDOS/ private_DOS
integer             private_DOS(0:2*NBands,NPointsDOS)

n=1+(ee-BandBottom)/(BandTop-BandBottom)*dfloat(NPointsDOS)
if (n.ge.1 .and. n.le.NPointsDOS) then
private_DOS(nb,n) = private_DOS(nb,n) + 8
end if
end

!-----------------------------------------------------------------------

!_____________________ Writes the DOS histogram to file _____________________

!-----------------------------------------------------------------------

subroutine WriteDOS(Name)
include 'RSOC_KP_3d_inc.f'
character*12 Name,NameDOS
real*8 ee,de,g,A
integer n,nb

de = (BandTop-BandBottom)/NPointsDOS

! A is the area of the system: to calculate it, we have that:
!   1)  the number of kx vectors present overall in the ZBx is
!       2 * NPointsZBDOS, the 2 there is because in the DensityStates
!       cycle we add only up the positive kx, but I must also take into
```

```
!       account the negative kx (as well as ky and kz).
!   2)  ZBx = 2*Pi/Lx * (2*NPointsZBDOS).
!   3)  ZBz = 2*Pi/Lz * (2*NPointsZBDOS).
!   4)  Ly = (2*NPointsZBDOS) * d.
! Then A = Lx * Ly * Lz =

A = 32. * Pi**2 * d * (NPointsZBDOS**3.) / (ZBx*ZBz)
do nb = 0,(2*NBands)
write (NameDOS,'(A,I2.2,A)') Name(1:Len_Trim(Name)),
+          nb,Ending

open (12,file=NameDOS,form='FORMATTED',status='UNKNOWN')
do n = 1,NPointsDOS
ee = (dfloat(n-1)+0.5d0)*de+BandBottom
g = dfloat(DOS(nb,n))/de/A
write (12,*) ee,g
end do
close(12)
end do
end


subroutine DOSAnalytical(Name)
include 'RSOC_KP_3d_inc.f'
real*8 de,ee,g,arg
integer iky,nb,i
character*12 Name

open(12,file=Name//Ending,form='FORMATTED',status='UNKNOWN')
de = (BandTop-BandBottom)/NPointsDOS
do i = 1,NPointsDOS
ee = BandBottom + (dfloat(i)-0.5d0) * de
g = 0.d0
do nb = 1,NBands
do iky = 1,NPointsZB
arg = ht2up2m/mx*(ee - Eq(nb,iky))
if (arg .gt. 0.d0) g = g + 1.d0/dsqrt(arg + 1.d-15)
end do
end do
g = g/(2.d0*Pi*d*NPointsZB)
write (12,*) ee,g
end do
close (12)
end


!_____________________________________________________________________

!___________ For each q, compute the corresponding energy _____________
```

```
!---------------------------------------------------------------------

subroutine EdiQ(q,Enky)
include 'RSOC_KP_3d_inc.f'
real*8 q,qq,Emin,Emax,ee,cqd,dq,PrecEmax,PrecEmin
real*8 Enky(NBands)

!Verso takes in account all the possible band curvatures
integer Verso
integer nb,f

do nb = 1,NBands
verso = mod(nb,2)
Emin = EEdge(nb,1)
Emax = EEdge(nb,2)
PrecEmax = 1.d12
PrecEmin = 1.d12
qq = 1.d10
do while ( dabs(q-qq) .gt. 1.d-13 .and.
+          ( (PrecEmax .ne. Emax) .or. (PrecEmin .ne. Emin) ) )
ee = (Emax+Emin)/2.d0
call EquationKP(ee,qq,cqd,f)
PrecEmax = Emax
PrecEmin = Emin
if (Verso .eq. 1 .and. qq .gt. q) Emax = ee
if (Verso .eq. 1 .and. qq .le. q) Emin = ee
if (Verso .eq. 0 .and. qq .gt. q) Emin = ee
if (Verso .eq. 0 .and. qq .le. q) Emax = ee

end do
Enky(nb) = ee
end do
end

!---------------------------------------------------------------------

! Writes the first and second derivatives of energy and the energy vs q
!---------------------------------------------------------------------

subroutine BandsupKy(Name)
include 'RSOC_KP_3d_inc.f'
integer n,i,f
character*12 Name
character*20 NameBanda
real*8 q,cqd,deedq,d2eedq2,energy(NBands)

open (12,file=Name(1:Len_Trim(Name))//Ending,
+    form='FORMATTED',status='UNKNOWN')
```

```
do n = 1,NPointsZB
q = (dfloat(n) - 0.5d0) * ZBy/2.d0/dfloat(NPointsZB)
call EdiQ(q,E)
do i = 1,NBands
Eq(i,n) = E(i)
call EquationKP(E(i),q,cqd,f)
write (12,'(2(E21.15,1X))') q,Eq(i,n)
end do
end do
close(12)

do n = 1,NBands
write (NameBanda,'(A,I2.2,A)')
+       Name(1:Len_Trim(Name)),n,Ending
open (12,file=NameBanda(1:Len_Trim(NameBanda)),
+      form='FORMATTED',status='UNKNOWN')
do i = 1,NPointsZB
q = (dfloat(i) - 0.5d0) * ZBy/2.d0/dfloat(NPointsZB)
write (12,'(4(E21.15,1X))') q,Eq(n,i),dEdq(n,i),d2Edq2(n,i)
end do
close(12)
end do
end



! FDO


!_____________________________________________________________________

!___________ The following subroutines allow us to compute  ____________
!                           the FDO along y
!_____________________________________________________________________

subroutine FunctionCoefficients
include 'RSOC_KP_3d_inc.f'
complex*16 Kb,Kw,x(4)
integer n,iky,i

do n = 1,NBands
do iky = 1,NPointsZB
ky = (dfloat(iky)-0.5d0)*ZBy/2.d0/dfloat(NPointsZB)
call SolutionSys(n,iky,x,Kb,Kw)
do i = 1,4
abgd(i,n,iky) = x(i)
end do
end do
end do
```

```
end

!_____________ Definition of coefficients matrix ____________________

subroutine SolutionSys(n,iky,x,Kb,Kw)
include 'RSOC_KP_3d_inc.f'
complex*16 A(4,4),i,x(4),Kb,Kw
real*8 Enky,Ekx
integer n,iky

Enky = Eq(n,iky)
Ekx = kx**2*ht2up2m/mx

i = dcmplx(0.,1.)

Kb = cdsqrt(dcmplx(Enky/ht2up2m*mb))
Kw = cdsqrt(dcmplx((Enky+Vb)/ht2up2m*mw))

! The first period of the periodic potential is between -l/2 and L/2+h.
! The period is d = L + h
! Up the first period
!      The well       is between -L/2 and L/2     -> V(well) = 0
!      The barrier    is between  L/2 ad L/2+h    -> V(barr) = Vb
! Then we need to replicate this potential along the y axis,in this way
! the periodic potential is symmetrical (V(x) = V(-x))
! The FDO between -L/2 and L/2+h is
!
!   for the well:
!       psi(y) = psi_well(y) = A exp(i Kw y) + B exp(-i Kw y)
!   on the barrier
!       psi(y) = psi_barr(y) = C exp(i Kb(y-d/2)) + D exp(-i Kb(y-d/2))
!
! The d/2 in the psi_barr is an additional phase on C and D
!
! The condixction for compute A,B,C e D are:
!   1)     psi_well(L/2)     = psi_barr(L/2)
!   2)     dpsi_well/dx(L/2) = dpsi_barr/dx (L/2)
!   3)     exp(i ky d) psi_well(-L/2)    = psi_barr(L/2+h)
!   4)     exp(i ky d) dpsi_well/dx(L/2) = dpsi_barr/dx(L/2+h)
! A homogeneous system is obtained whose solution is normalized by
! imposing that the integral on the period of the square module
! of psi (x) is equal to 1

A(1,1) =  cdexp( i*Kw*L/2.)
A(1,2) =  cdexp(-i*Kw*L/2.)
A(1,3) = -cdexp(-i*Kb*h/2.)
A(1,4) = -cdexp( i*Kb*h/2.)

A(2,1) =  i*Kw*cdexp( i*Kw*L/2.)
```

```
A(2,2) = -i*Kw*cdexp(-i*Kw*L/2.)
A(2,3) = -i*Kb*cdexp(-i*Kb*h/2.)
A(2,4) =  i*Kb*cdexp( i*Kb*h/2.)

A(3,1) =  cdexp(-i*Kw*L/2.+i*ky*d)
A(3,2) =  cdexp( i*Kw*L/2.+i*ky*d)
A(3,3) = -cdexp( i*Kb*h/2.)
A(3,4) = -cdexp(-i*Kb*h/2.)

A(4,1) =  i*Kw*cdexp(-i*Kw*L/2.+i*ky*d)
A(4,2) = -i*Kw*cdexp( i*Kw*L/2.+i*ky*d)
A(4,3) = -i*Kb*cdexp( i*Kb*h/2.)
A(4,4) =  i*Kb*cdexp(-i*Kb*h/2.)

call RisolviSysOmo(A,4,4,x,Kw,Kb)
end

!_________________________ Gauss Method _________________________________

subroutine RisolviSysOmo(A,n,m,x,Kw,Kb)
include 'RSOC_KP_3d_inc.f'
integer n,m,jm,cm,t,i,j,k,r(4),c(4)
complex*16 A(n,m),Am,Amm,x(n),Norm,Kw,Kb,iii,Norm1,Norm2

integer ii,jj
complex*16 det

real*8 PrecisionDet
parameter (PrecisionDet = 1.d-7)
do i = 1,n
r(i) = i
c(i) = i
end do

i = 1
call FindMax(A,n,m,jm,cm,Am,r,i)

do while (cdabs(Am) .gt. PrecisionDet .and. i .le. n)
t = r(i)
r(i) = r(jm)
r(jm) = t
do j = 1,m
if (c(j) .eq. cm) jm = j
end do
c(jm) = c(i)
c(i) = cm

do j = i+1,n
Amm = A(r(j),cm)
```

```
do k = 1,m
A(r(j),k) = A(r(j),k) - A(r(i),k)/Am*Amm
end do
end do
i = i+1
call FindMax(A,n,m,jm,cm,Am,r,i)

end do
i = i-1

do j = 4,i+1,-1
x(c(j)) = 1.
end do
do j = i,1,-1
x(c(j)) = 0.
do k = j+1,4
x(c(j)) = x(c(j)) - A(r(j),c(k))*x(c(k))
end do

x(c(j)) = x(c(j))/A(r(j),c(j))
end do

iii = dcmplx(0.,1.)
if (dabs(dreal(Kw)) .gt. 1.d-10) then
Norm1 = (cdabs(x(1))**2+cdabs(x(2))**2)*L+
+          2.*dreal(x(1)*dconjg(x(2))) * dsin(dreal(Kw*L))/Kw
else
Norm1 = (cdabs(x(1))**2+cdabs(x(2))**2)*
+           dsinh(dimag(Kw)*L)/dimag(Kw)+
+          2.*dreal(x(1)*dconjg(x(2)))*L
end if
if (dabs(dreal(Kb)) .gt. 1.d-10) then
Norm2 = (cdabs(x(3))**2+cdabs(x(4))**2)*h+
+          2.*dreal(x(3)*dconjg(x(4))) * dsin(dreal(Kb*h))/Kb
else
Norm2 = (cdabs(x(3))**2+cdabs(x(4))**2)*
+          (dexp(dimag(Kb)*h)-dexp(-dimag(Kb)*h))/(2.*dimag(Kb))+
+          2.*dreal(x(3)*dconjg(x(4)))*h
end if

Norm = (Norm1+Norm2)*Lx*Ny

do j = 1,4
x(j) = x(j)/dsqrt(cdabs(Norm))
if ( isnan(dreal(x(j))) .or. isnan(dimag(x(j))) ) then
write (6,*) "IsNan x(j)"
stop
end if
end do
```

```
end

!---------------------------------------------------------------------
subroutine FindMax(A,n,m,jm,cm,Am,r,i)
implicit none
integer n,m,jm,cm,i,j,k,r(n)
complex*16 A(n,m),Am
real*8 d,dm

dm = 0.
do j = i,n
do k = 1,m
d = cdabs(A(r(j),k))
if (d .gt. dm) then
dm = d
jm = j
cm = k
end if
end do
end do
Am = A(r(jm),cm)
end


!---------------------------------------------------------------------
!---------------------------------------------------------------------



!*********************************************************************
!************************SUPERCONDUCTIVE PHASE************************
!*********************************************************************



!---------------------------------------------------------------------

!__ The following subroutines allow to determine the exchange integral__

!---------------------------------------------------------------------
subroutine CalculateCoupling
include 'RSOC_KP_3d_inc.f'
integer nn,ikyn,np,ikyp

do nn = 1,NBands
do np = 1,NBands
do ikyn = 1,NPointsZB
do ikyp = 1,NPointsZB
```

```
call
+         CouplingFast(nn,ikyn,np,ikyp,Acc(nn,ikyn,np,ikyp))
write (12,*) nn,ikyn, np,ikyp, Acc(nn,ikyn,np,ikyp)
end do
end do
write (6,*) 'Ho fatto gli Accoppiamenti',nn,np
end do
end do
end

!_____________________________________________________________________
subroutine CouplingFast(nn,ikyn,np,ikyp,a)
include 'RSOC_KP_3d_inc.f'
complex*16 Kbn,Kwn,Kbp,Kwp,aa
real*8 a,Enky
complex*16 an,bn,cn,dn,ap,bp,cp,dp,a1,a2
integer nn,np,ikyn,ikyp

an = abgd(1,nn,ikyn)
bn = abgd(2,nn,ikyn)
cn = abgd(3,nn,ikyn)
dn = abgd(4,nn,ikyn)
Enky = Eq(nn,ikyn)
Kbn = cdsqrt(dcmplx(Enky/ht2up2m*mb))
Kwn = cdsqrt(dcmplx((Enky+Vb)/ht2up2m*mw))

ap = abgd(1,np,ikyp)
bp = abgd(2,np,ikyp)
cp = abgd(3,np,ikyp)
dp = abgd(4,np,ikyp)
Enky = Eq(np,ikyp)
Kbp = cdsqrt(dcmplx(Enky/ht2up2m*mb))
Kwp = cdsqrt(dcmplx((Enky+Vb)/ht2up2m*mw))

call Coupling2(an,bn,Kwn,ap,bp,Kwp,L,a1)
call Coupling2(cn,dn,Kbn,cp,dp,Kbp,h,a2)

aa = a1+a2
if (dabs(dimag(aa)) .gt. 1.d-12) then
write(6,*) 'Coupling Complesso !!'
stop
end if
a = dreal(aa)
end

!_____________________________________________________________________
subroutine Coupling2(an,bn,kn,ap,bp,kp,ll,a)
include 'RSOC_KP_3d_inc.f'
complex*16 an,bn,kn,ap,bp,kp,a
```

```
complex*16 a1,a2,a3,a4
complex*16 MySin
external MySin
real*8 ll

a1 = cdabs(an)**2* (
+ cdabs(ap)**2*MySin(-dcmplx(dimag(kn)),-dcmplx(dimag(kp)),ll)+
+ cdabs(bp)**2*MySin(-dcmplx(dimag(kn)),dcmplx(dimag(kp)),ll) +
+ dconjg(ap)*bp*MySin(-dcmplx(dimag(kn)),dcmplx(0.,-dreal(kp)),ll)+
+ ap*dconjg(bp)*MySin(-dcmplx(dimag(kn)),dcmplx(0.,dreal(kp)),ll) )

a2 = cdabs(bn)**2* (
+ cdabs(ap)**2*MySin(dcmplx(dimag(kn)),-dcmplx(dimag(kp)),ll)+
+ cdabs(bp)**2*MySin(dcmplx(dimag(kn)),dcmplx(dimag(kp)),ll) +
+ dconjg(ap)*bp*MySin(dcmplx(dimag(kn)),dcmplx(0.,-dreal(kp)),ll)+
+ ap*dconjg(bp)*MySin(dcmplx(dimag(kn)),dcmplx(0.,dreal(kp)),ll) )

a3 = dconjg(an)*bn * (
+ cdabs(ap)**2*MySin(dcmplx(0.,-dreal(kn)),-dcmplx(dimag(kp)),ll)+
+ cdabs(bp)**2*MySin(dcmplx(0.,-dreal(kn)),dcmplx(dimag(kp)),ll) +
+ dconjg(ap)*bp*MySin(dcmplx(0.,-dreal(kn)),
+                     dcmplx(0.,-dreal(kp)),ll)+
+ ap*dconjg(bp)*MySin(dcmplx(0.,-dreal(kn)),
+                   dcmplx(0.,dreal(kp)),ll) )

a4 = an*dconjg(bn) * (
+ cdabs(ap)**2*MySin(dcmplx(0.,dreal(kn)),-dcmplx(dimag(kp)),ll)+
+ cdabs(bp)**2*MySin(dcmplx(0.,dreal(kn)),dcmplx(dimag(kp)),ll) +
+ dconjg(ap)*bp*MySin(dcmplx(0.,dreal(kn)),
+       dcmplx(0.,-dreal(kp)),ll)+
+ ap*dconjg(bp)*MySin(dcmplx(0.,dreal(kn)),
+                     dcmplx(0.,dreal(kp)),ll) )

a = a1 + a2 + a3 + a4
end

!_____________________________________________________________________
complex*16 function MySin(k1,k2,ll)
complex*16 k1,k2,z,z1
real*8 ll

z = k1+k2
if (cdabs(z) .le. 1.d-10) then
MySin = ll
else
z1 = cdexp(z*ll)
MySin = (z1-1./z1)/(2.*z)
end if
end
```

```
!_____________________________________________________________________

!_____________________________________________________________________

!_________The following subroutines allow to determine the Gap__________

!_____________________________________________________________________

subroutine ComputeLambda(nn,np,ll)
include 'RSOC_KP_3d_inc.f'
integer nn,np
real*8 ll,x

! In this particular case, lambda has no dependence on Ef
! and this subroutine always returns the same values for lambda.
ll = lambda(nn,np)
end


!_____________________________________________________________________________
subroutine GapvsEf (NameGap)
include 'RSOC_KP_3d_inc.f'
real*8 energy, rel_tol, abs_tol, de, gapBCS
real*8 deltaE,minimumEnergy,minBandsnergy
integer*4 maxiter,i,j
integer n,iky, Base

parameter (Base = 20)
character*12 NameGap,NameFile

rel_tol = 1e-5 ! relative (normalized) change at which two gap
               !can be considere equal
abs_tol = 1e-9 ![eV] energy at which gap can be considered 0
maxiter = 1000

! Initialize gap, basically starts with a gap equal to omegad __________
call init_gap(omegadmax)

de = (TopEf-BottomEf)/(dfloat(NPointsGDvsMu))
do n = 1,NBands
write (NameFile,"(A,I2.2,A)")
+      NameGap(1:Len_Trim(NameGap)),
+      n,
+      Ending(1:Len_Trim(Ending))

open (Base+n,
+        file=NameFile,
+        form='FORMATTED',
```

```
+        status='UNKNOWN')
end do

! We start the cycle on Ef, start with a very large value
! and go towards the bottom of the RSOC band
j = 0
do i = NPointsGDvsMu, 1,-1

Ef=BottomEf+(dfloat(i)-0.5d0)*de
write (*,*) 'Ef =',Ef

call compute_homogeneous_DOS3D(Ef - minimum_energy)
call compute_gap(rel_tol, abs_tol, maxiter)

! the BCS gap makes sense only if lambda is a constant,
! so we use the lambda(1,1) value
gapBCS = 2.0d0 * omegadmax * dexp(-1.0d0 / dabs( lambda(1,1) ))

do n=1,NBands
do iky=1, NPointsZB
Gap(n,iky) = GapNG(n,iky)
end do
write (Base+n,*) Ef,gapBCS,
+                       Gap(n,1),
+                       Gap(n,NPointsZB/2),
+                       Gap(n,NPointsZB)
call flush(Base+n)
end do

j = j + 1
write (6,*) 'Gap plot complete at',
+      dfloat(j)/NPointsGDvsMu*100,'%'

end do

do n = 1,NBands
close(Base+n)
end do
end


!---------------------------------------------------------------------
subroutine compute_minimum_energy
include 'RSOC_KP_3d_inc.f'

real*8 deltaE, minBandsnergy
integer n,nmin

minimum_energy = 1.0d100
```

```
do n = 1,NBands
deltaE = alphaRSOC(n) * alphaRSOC(n) / (4.0d0 * ht2up2m)
minBandsnergy = EEdge(n,1) - deltaE

write (6,'("alphaRSOC  for band",I2," =",E18.10)')
+         n, alphaRSOC(n)
write (6,'("deltaE     for band",I2," =",E18.10)')
+         n, deltaE
write (6,'("min energy for band",I2," =",E18.10)')
+         n, minBandsnergy

if (minBandsnergy .lt. minimum_energy) then
minimum_energy = minBandsnergy
nmin = n
end if
end do
write (6,'("overall min energy =",E18.10,"   for band ",I2)')
+         minimum_energy,nmin
end

subroutine compute_homogeneous_DOS3D(energy)
include 'RSOC_KP_3d_inc.f'

real*8 energy

g0 = 1.D0/(4.0d0 * pi**2)  *
+     1.D0/(ht2up2m**1.5d0) *
+     dsqrt(energy)

end


!---------------------------------------------------------------------
subroutine init_gap(g)
! set the whole matrix Gap() to g
include 'RSOC_KP_3d_inc.f'
real*8 g
integer nn,ikyn
do nn = 1,NBands
do ikyn = 1,NPointsZB
Gap(nn,ikyn) = g
end do
end do
end

! Function that calculates gap with a cycle from which you exit if
! we reach max interactions (no convergence)
! or if we have obtained convergence <rel_tol
subroutine compute_gap(rel_tol,abs_tol,max_iter)
```

```
include 'RSOC_KP_3d_inc.f'

integer*4 niter,max_iter
real*8  rel_tol,abs_tol,dG,average
integer n,iky

niter = 1
do while (niter .lt. max_iter)
call compute_selfcon_integral
call compute_normalized_deltaG(dG,abs_tol,average)
call copy_gap

write (*,*) ' niter = ', niter
write (*,*) '   normalized_delta_G = ', dG ,
+              ' mean gap = ', average

if (dG .lt. rel_tol) return

niter = niter + 1
end do
end

!---------------------------------------------------------------------
subroutine compute_normalized_deltaG(dG,abs_tol,average)
include 'RSOC_KP_3d_inc.f'

real*8  dG,abs_tol
integer n,iky,n_average
real*8  average

dG      = 0.d0
average = 0.d0
n_average = 1
do n=1,NBands
do iky=1,NPointsZB
if (dabs(GapNG(n,iky)) .gt. 0.d0) then
dG      = dG + dabs(GapNG (n,iky) - Gap(n,iky))
average = average+dabs(Gap(n,iky))
n_average = n_average+1
end if
end do
end do

average=average/n_average
dG = dG / (average + abs_tol)
end

subroutine copy_gap
include 'RSOC_KP_3d_inc.f'
```

```
integer n,iky
do n = 1,NBands
do iky = 1,NPointsZB
Gap(n,iky) = GapNG(n,iky)
end do
end do
end


!_____________This is the parallelized version of ComputeGap__________
subroutine compute_selfcon_integral()
include 'RSOC_KP_3d_inc.f'

real*8    S, deltaE, sum_nu,emin,emax,i1,s1
real*8    Enky, gg
integer*4 nu
integer n,iky,np,ikyp,NPointsy

!$OMP PARALLEL DEFAULT(PRIVATE)
!$OMP+   SHARED(ht2up2m,alphaRSOC,Eq,omegadmax,Ef)
!$OMP+   SHARED(Acc,Gap,GapNG,Jo,pi)

!$OMP DO
do iky=1,NPointsZB
do n=1,NBands
call compute_selfcon_integral_element(n,iky,gg)
GapNG(n,iky) = gg
end do ! next n
end do !next iky
!$OMP END PARALLEL
end

! compute the self consistency integral (gg) for a specific ky (iky)
! on a specific band (n)
subroutine compute_selfcon_integral_element(n,iky,gg)
include 'RSOC_KP_3d_inc.f'

integer n,iky
real*8 gg

real*8    S, deltaE, sum_nu,emin,emax,i1,s1
real*8    Enky, U0, omegad_n_np
integer*4 nu,np,ikyp,NPointsy

double precision abserr,epsabs,epsrel,result,work
integer ier,iwork,last,lenw,limit,neval
dimension iwork(100),work(4*100)

external SelfConIntegrand
```

```
common /SelfConInt12/ k0,e0,a,Ef1,G,Enkyp,T
real*8                k0,e0,a,Ef1,G,Enkyp,T
!$OMP THREADPRIVATE( /SelfConInt12/ )

deltaE = (alphaRSOC(n)*alphaRSOC(n))/(4.0d0 * ht2up2m)
Enky = Eq(n,iky)
if ((Enky - deltaE) .gt. (Ef + omegadmax)) then
gg = 0.d0
return
end if

S = 0.0d0   ! S accumulate the sum over np and ikyp

Ef1 = Ef    ! copy global variable in the THREADPRIVATE common block
T   = Temp

do np =1,NBands
omegad_n_np = omegad(n,np)
do ikyp=1,NPointsZB

Enkyp = Eq(np,ikyp)

a  =  ht2up2m
e0 =  - alphaRSOC(np) * alphaRSOC(np) / (4.0d0 * a)
sum_nu = 0

do nu = -1,1,2
k0 = dfloat(nu) * alphaRSOC(np) / (2.0d0 * a);
if (nu .eq. -1) then
emax = dmax1(  omegad_n_np - (Enkyp - Ef) , 0.0d0 )
emin = dmax1( -omegad_n_np - (Enkyp - Ef) , 0.0d0 )
else ! nu=+1
emax = dmax1(  omegad_n_np - (Enkyp - Ef) , e0)
emin = dmax1( -omegad_n_np - (Enkyp - Ef) , e0)
end if

if (emax .gt. emin) then
G = Gap(np,ikyp)
epsabs = 0.0E0
epsrel = 1.0E-5
limit = 100
lenw = limit*4
call DQAGS(
+              SelfConIntegrand,emin,emax, !***** Now SelfConIntegrad
+              EPSABS,EPSREL,
+              RESULT,ABSERR,
+              NEVAL,IER,
+              LIMIT,LENW,LAST,IWORK,WORK
```

```
+          )
U0 = -lambda(n,np) / g0; ! g0 is the 3D density of states
i1= U0 * RESULT;
else
i1 = 0
end if

sum_nu = sum_nu + i1
end do

! Ink;n'k' = Acc / (Ny * Lx * Lz)
!            kydegeneracy
!            ky = 0 and ky = pi/d should be counted once,
!            all the others should be counted twice because energy and
!            overlaps dont't changes for ky -> -ky

s1 = 2.0d0 * Acc(n,iky,np,ikyp) * Gap(np,ikyp) * sum_nu
S  = S + s1
end do
end do

NPointsy = 2.0d0 * NPointsZB
gg = -S/(4.0d0 * pi * NPointsy)
end

!-----------------------------------------------------------------------
real*8 function SelfConIntegrand(energy)
real*8 energy,Ef
real*8 csi, absG,Ep,s,abs_dknu_de,knu,num

common /SelfConInt12/ k0,e0,a,Ef1,G,enkyp,T
real*8                k0,e0,a,Ef1,G,enkyp,T
!$OMP THREADPRIVATE( /SelfConInt12/ )

! e is the RSOC part of the energy
! e = ht2m * k .* k - nu * alphaRSOC(n) * k
! that has been written as
! e = a * (k - k0) + e0

! Ef is local in this function
! (the "global" include file is not included)
Ef = Ef1
absG = dabs(G)
csi =  energy + enkyp - Ef
Ep  = dsqrt(csi * csi + absG * absG)

s = dsqrt((energy - e0) / a)

abs_dknu_de = 1.0d0 / (2.0d0 * a * s)
```

```
if (k0 .gt. 0)  then          !(k0 > 0) [ mean nu = +1, positive helicity ]
if (s .gt. k0)  then        !(k0 - s) < 0 and must be excluded
knu = k0 + s
num = knu * abs_dknu_de
else
! num = (k0 + s) * abs_dknu_de + (k0 - s) * abs_dknu_de
num = 2.0d0 * k0 * abs_dknu_de
end if
else                           !(k0 < 0) [ mean nu = -1, negative helicity ]
knu = k0 + s
num = knu * abs_dknu_de
end if

if ( T .eq. 0) then
SelfConIntegrand = num / (2.0d0 * Ep)
else
SelfConIntegrand = num / (2.0d0 * Ep) * dtanh(Ep/2./T)
end if

end

!_____________________________________________________________________
subroutine TcvsEf(NameTc)
include 'RSOC_KP_3d_inc.f'

integer i,j,iky
integer ciclostart,ciclostop,ciclostep
character*12 NameTc,NameFile
real*8 de,nn
real*8 TcBCS

real*8 rel_tol, abs_tol
integer maxiter

Temp = 0.d0
de = (TopEf-BottomEf)/dfloat(NPointsGDvsMu)

write (NameFile,"(A,A)")
+    NameTc(1:Len_Trim(NameTc)),
+     Ending(1:Len_Trim(Ending))
open (20,file=NameFile,
+            form='FORMATTED',status='UNKNOWN')

j = 0
if (GapPlot .eq. LeaveHighEnergy) then
ciclostart = NPointsGDvsMu
ciclostop  = 1
ciclostep  = -1
```

```
else
ciclostart = 1
ciclostop  = NPointsGDvsMu
ciclostep  = 1
end if

rel_tol = 1e-4 ! relative (normalized) change at which
               ! two gap can be considere equal
abs_tol = 1e-9 ![eV] energy at which gap can be considered 0
maxiter = 20

do i =  ciclostart,ciclostop,ciclostep
j = j+1

Ef = BottomEf+(dfloat(i)-0.5d0)*de
call compute_homogeneous_DOS3D(Ef - minimum_energy)

if (Temp .eq. 0.d0) then

call init_gap(omegadmax)
call compute_gap(rel_tol, abs_tol, maxiter)
Temp = Gap(1,NPointsZB/2)*2.d0/3.52d0
write (6,*) Temp/KBoltz

if (dabs(Temp/KBoltz) .lt. 1.d-3) Temp = 1.d0*KBoltz
call init_gap(1.d0*KBoltz) ! a gap "small"
end if

call compute_Tc(1.d-3,1500)
TcBCS = 1.14 * omegadmax * dexp( -1.0 / lambda(1,1) )

write (20,*) Ef, Temp/KBoltz, TcBCS/KBoltz
call flush(20)
write (6,*) ' ***** Grafico Tc completo al',
+        dfloat(j)/NPointsGDvsMu*100,'%'
end do
close(20)
end


!---------------------------------------------------------------------
subroutine compute_Tc(tol,maxiter)
include 'RSOC_KP_3d_inc.f'
integer maxiter,i
real*8 dd,sdd,psdd,Temp2,Temp1,l3,l2,l1,tol,Perc

Temp1 = 0.d0
Temp2 = 0.d0
l1 = 0.d0
```

```
l2 = 0.d0
write (6,*) 'Input: Temp ',Temp/KBoltz,' Ef ',Ef

call MaxEigenvalue(l3,1.d-3,100)
dd = dabs(l3-1.d0)
sdd = dsign(1.d0,l3-1.d0)
psdd = sdd
if (sdd .eq. 1.d0) then
Temp2 = Temp
l2 = l3
else
Temp1 = Temp
l1 = l3
end if

i = 1
do while (sdd .eq. psdd .and. i .le. maxiter)
i = i+1
Perc = 0.2
if (dd .le. 0.10) Perc = 0.10
if (dd .le. 0.05) Perc = 0.05
Temp = Temp*(1.d0 + sdd * Perc)
call MaxEigenvalue(l3,1.d-3,100)
dd = dabs(l3-1.d0)
sdd = dsign(1.d0,l3-1.d0)
if (sdd .eq. 1.d0) then
Temp2 = Temp
l2 = l3
else
Temp1 = Temp
l1 = l3
end if
write (6,*) 'T1 ',Temp1/KBoltz,' l1 ',l1
write (6,*) 'T2 ',Temp2/KBoltz,' l2 ',l2
end do

write (6,*) 'compute_Tc init terminated sdd = ',sdd,
+               '  psdd = ',psdd,' i = ',i

if (i .le. maxiter) then
i = 1
do while (dabs((Temp2-Temp1)/Temp1) .gt. tol .and.
+                         i .le. maxiter)
Temp = Temp1 + (1.d0-l1)*(Temp2-Temp1)/(l2-l1)
call MaxEigenvalue(l3,1.d-3,100)
sdd = dsign(1.d0,l3-1.d0)
if (dabs(l3-1.d0) .le. 1.d-5) then
Temp1 = Temp
Temp2 = Temp
```

```
write (6,*) 'T ',Temp/KBoltz,' l3 ',l3
else
if (sdd .eq. 1.d0) then
Temp2 = Temp
l2 = l3
else
Temp1 = Temp
l1 = l3
end if
write (6,*) 'T1 ',Temp1/KBoltz,' l1 ',l1
write (6,*) 'T2 ',Temp2/KBoltz,' l2 ',l2
end if
i = i+1
end do
if (i .ge. maxiter) call init_gap(1.d0*KBoltz)
Temp = (Temp2+Temp1)/2.d0
else
Temp = 0.d0
end if
end

subroutine MaxEigenvalue(ll,tol,maxiter)
include 'RSOC_KP_3d_inc.f'
integer n,i,j,maxiter
real*8 ll,lmax,lmin,rap,atttol,tol

n = 0
write (6,*)
write (6,*) 'Temp,Ef',Temp/KBoltz,Ef

call compute_selfcon_integral
call copy_gap
lmax = -100.d0
lmin = 1.d50
do while ( n .le. maxiter .and. dabs((lmax-lmin)/lmin) .gt. tol)
n = n+1
write (6,*) 'Massimo Autoval Iterazione n# ',n
call compute_selfcon_integral

lmax = -100.d0
lmin = 1.d50
write (6,*) 'Gap'
write (6,"(6(E12.3,2X))") ((Gap(i,j)/KBoltz,j = 1,6),i=1,3)
write (6,*) 'GapNG'
write (6,"(6(E12.3,2X))") ((GapNG(i,j)/KBoltz,j = 1,6),i=1,3)
do i = 1,NBands
do j = 1,NPointsZB
if ( GapNG(i,j) .ne. 0.d0 .and. Gap(i,j) .ne. 0.d0) then
rap = GapNG(i,j)/Gap(i,j)
```

```
if (rap .gt. lmax) lmax = rap
if (rap .lt. lmin) lmin = rap
end if
end do
end do
write (6,*) 'lmax,lmin',lmax,lmin
call copy_gap
end do
if (n .gt. maxiter) write (6,*)
+     'Massimo autovalore non ha convergiuto !'
write (6,*) lmax,lmin
ll = (lmax+lmin)/2.d0
write (6,*) 'll -> ',ll
end

!---------------------------------------------------------------------
!---------------------------------------------------------------------
block data CostantiFisicheFondamentali
include 'RSOC_KP_3d_inc.f'

data Pi /  3.1415926535897960d0  /
data dsqrt2 /  1.414213562373d0  /
data ht2up2m / 3.8100d0 /    ! in eV * A**2
data Kboltz / 8.617718D-5 /  ! in eV/K
data d / 18.33d0 /
data L / 12.83d0 /
data h / 5.50d0 /
data Lx / 1.d0 /
data Ny / 1 /
data mw / 1.d0 /
data mb / 1.d0 /
data mx / 1.d0 /
data mz / 1.0d0 /

end
```

In the file

```
RSOC_KP_3d_inc.f
```

we have defined the global variables as follows:

```
! RSOC_KP_3d_inc.f - Here are the definitions of the global variables

implicit NONE

integer
+        NBands,NDim,
+        NPointsDOS,NPointsZB,NPointsZBDOS,NPointsGDvsMu,
```

```
+        NPointsBanda,NPointsMu,OgniQuanti,
+        FileBandsBase,LeaveHighEnergy,
+        PartoEnergieBasse,Debug
parameter (NBands = 2,              ! Self-explanatory
+           NDim = 3,                ! We are in NDim dimensions
+           NPointsDOS = 500,        ! DOS array size
+           NPointsZB = 100,         ! NPointsZB ** 3 on the ZB for the
                                     ! Gap are examined
+           NPointsZBDOS = 700,      ! NPointsZBDOS ** 3 on the ZB for the
                                     ! DOS are examined
+           NPointsGDvsMu =500,      ! Number of points for scanning in Ef
+           NPointsBanda = 150,      ! N points with which the Band is
                                     ! drawn
+           NPointsMu = 150,         ! N points fort the Mu vs Dens plot
+           OgniQuanti = 100000,     ! Each (kx, ky, kz) one is transcribed
+           FileBandsBase = 30,      ! Start numbering .TMP file
+           LeaveHighEnergy  = 1,    ! These are the two possible values
                                     ! of the variable
+           PartoEnergieBasse = 0,   ! the variable GapPlot

common /Global/
+       Pi,                         ! Pi greek
+       dsqrt2,                     ! dsqrt(2.d0)
+       ht2up2m,                    ! ht**2/(2*me)
+       Kboltz,                     ! The Boltzmann constant
+       mb,mw,mx,mz,                ! Effective masses of the electron
+       h,L,d,                      ! Geometry of the Potential
+                                   ! (L size well, h size barrier, d = L + h)
+       Lx,Ny,                      ! Length in x and Number of cells in y
+       GapPlot,                    ! Graf.Gap starting from en. high or low
+       Vb,                         ! Height of the Barrier (eV)
+       Jo,                         ! Coupling parameter
+       g0,                         ! density of states in an homogeneous system
+       kx,ky,kz,nkx,nky,nkz,       ! Point of the ZB considered
+       altri_quattro_bytes,        ! Padding required by the compiler
+       ZBx,ZBy,ZBz,                ! Extension of the ZB long kx,ky e kz
+       ZBxExtended,ZByExtended,    ! Extension of the ZB without sup-cell
+       ZBzExtended,
+       E,                          ! Eigenvalues (spectrum) for the point
                                    ! under consideration
+       gradEx,gradEy,              ! Partial derivatives of the eigenvalues
+       Eq,UnE,EEdge,               ! Scan on the ky axis
+       minimum_energy,             ! lowest energy in the spectrum considering
                                    ! also RSOC
+       dEdq,d2Edq2,                ! first and second derivatives of E (q)
+       abgd,                       ! Coefficients of the eigenfunctions
+       D0x,D0z,D0xNG,D0zNG,        ! Gap BCS
+       prefattore,                 ! prefactor used in ValutaIntSelfCon
+       Temp,                       ! Temperature under examination
```

```
+       DOS,                        ! Density of states
+       DensitaSuper,               ! Electronic Density (when there is a Gap)
+       Ef,                         ! Fermi level set
+       omegadmax,                  ! Maximum Debye frequency (energy cutoff
                                    ! for the Gap)
+       omegad,                     ! Debye frequency (now it's a matrix)
+       lambda,                     ! Dimensionless Coupling (now it's a matrix)
+       Ending,                     ! Extension (.DAT .PAT etc ..) of the files
+       rho,                        ! superfluid density
+       Gap,GapNG,                  ! Gap BCS
+       ancora_quattro_bytes,       ! Padding required by the compiler
+       BandBottom,BandTop,         ! Energy extremes for DOS
+       BottomEf,TopEf,             ! Extremes of variation of Ef
+       alphaRSOC, al, Kso,
+       DensityLimit                ! Extremum sup for the mu vs dens graph

real*8
+       Pi,
+       dsqrt2,
+       ht2up2m,Kboltz,
+       mb,mw,mx,mz,
+       h,L,d,
+       Lx,
+       alphaRSOC(NBands), al, Kso
real*8
+       Gap(NBands,NPointsZB),GapNG(NBands,NPointsZB)

integer
+       Ny
integer
+       GapPlot
real*8
+       Vb,Jo,g0,
+       kx,ky,kz
integer
+       nkx,nky,nkz,altri_quattro_bytes
real*8
+       ZBx,ZBy,ZBz,
+       ZBxExtended,ZByExtended,ZBzExtended
real*8
+       E(NBands),
+       gradEx(NBands),gradEy(NBands),
+       Eq(NBands,NPointsZB),UnE(NBands),EEdge(NBands,4),
+       minimum_energy,
+       dEdq(NBands,NPointsZB),d2Edq2(NBands,NPointsZB)
complex*16
+       abgd(4,NBands,NPointsZB)
real*8
+       D0x(NBands,NPointsZB),D0z(NBands,NPointsZB),
```

```
+       D0xNG(NBands,NPointsZB),D0zNG(NBands,NPointsZB),
+       prefattore,
+       Temp
integer
+       DOS(0:2*NBands,NPointsDOS)
real*8
+       DensitaSuper(NPointsGDvsMu),
+       Ef,omegadmax,omegad(NBands,NBands),lambda(NBands,NBands)
character*4
+       Ending

real*8
+       rho(0:NBands,0:NDim)
integer*8
+       ancora_quattro_bytes
real*8
+       BandBottom,BandTop,
+       BottomEf,TopEf,
+       DensityLimit

common Acc    Couplings between the SubBands
real*8 Acc(NBands,NPointsZB,NBands,NPointsZB)
```

Acknowledgement

I would like to dedicate this space to those who, with dedication and patience, have contributed to the realization of this paper.

First I would like to thank the *University of Roma Tre* for giving me the opportunity to carry out this course of study in a serene and stimulating way.

Special thanks go to my supervisor, prof. Roberto Raimondi, for his immense patience, for his indispensable advice and for the knowledge transmitted throughout the course of writing the thesis.

I infinitely thank *RICMASS* and in particular the prof. Antonio Bianconi, an inexhaustible source of knowledge, who in addition to having guided, stimulated and encouraged me throughout my entire course of study, gave me the passion and enthusiasm necessary for the thesis to take shape day after day.

I thank the prof. Antonio Valletta of the *Computing Center of the CNR Institute of Microelectronics and Microsystems*, the prof. Gaetano Campi of the *CNR Institute of Crystallography* and the prof. Andrea Perali of *Condensed Matter Physics at the University of Camerino*, for their infinite availability and theirs enormous skills.

A special dedication goes to my partner, my animals and my family, who every day shared joys, sacrifices and successes with me, without ever turning their backs on me. The affection and support they have shown me make this milestone even more valuable. Thank you all, without you I would never have made it.

Bibliography

[1] S. Weinberg, "Superconductivity for particular theorists," *PThPS*, vol. 86, pp. 43–53, 1986. 3

[2] L. P. Gor'kov, "Developing *BCS* ideas in the former soviet union," *International Journal of Modern Physics B*, vol. 24, no. 20n21, pp. 3835–3854, 2010. 3, 6

[3] B. Josephson, "Possible new effect in superconducting tunneling," *Phys. Lett.*, vol. 1, pp. 251–253, 1962. 3, 6

[4] J. Kondo, "Superconductivity in transition metals," *Progress of Theoretical Physics*, vol. 29, no. 1, pp. 1–9, 1963. 3, 6

[5] J. M. Blatt, "Theory of superconductivity," 1964. 3, 6, 8

[6] A. Leggett, "Modern trends in the theory of condensed matter ed *A. Pekalski* and *J. Przystawa*," *Lecture Notes in Physics*, vol. 115, 1980. 3, 6, 8

[7] J. F. Annett *et al.*, *Superconductivity, superfluids and condensates*, vol. 5. Oxford University Press, 2004. 3, 6

[8] B. V. Svistunov, E. S. Babaev, and N. V. Prokof'ev, *Superfluid states of matter*. Crc Press, 2015. 3, 6

[9] A. J. Coleman and V. I. Yukalov, *Reduced density matrices: Coulson's challenge*, vol. 72. Springer Science & Business Media, 2000. 3, 8

[10] A. Bianconi, "Process of increasing the critical temperature T_C of a bulk superconductor by making metal heterostructures at the atomic limit," July 24 2001. US Patent 6,265,019. 3, 8, 27, 29, 38, 40

[11] A. Bianconi, "On the possibility of new high T_C superconductors by producing metal heterostructures as in the cuprate perovskites," *Solid state communications*, vol. 89, no. 11, pp. 933–936, 1994. 3, 8, 27, 38, 44

[12] A. Bianconi, "On the fermi liquid coupled with a generalized wigner polaronic *CDW* giving high T_C superconductivity," *Solid State Communications*, vol. 91, no. 1, pp. 1–5, 1994. 3, 8, 27, 38, 44

[13] A. Bianconi, "The instability close to the $2D$ generalized wigner polaron crystal density: A possible pairing mechanism indicated by a key experiment," *Physica C: Superconductivity*, vol. 235, pp. 269–272, 1994. 3, 8, 27, 38, 44

[14] A. Bianconi and T. Jarlborg, "Lifshitz transitions and zero point lattice fluctuations in sulfur hydride showing near room temperature superconductivity," *Novel Superconducting Materials*, vol. 1, no. open-issue, 2015. 3, 8, 27, 29, 38, 42

[15] S.-Q. Shen, *Topological insulators*, vol. 174. Springer, 2012. 3

[16] S. M. Bhattacharjee, M. Mj, and A. Bandyopadhyay, *Topology and Condensed Matter Physics*, vol. 19. Springer, 2017. 3

[17] C. Perroni, D. Bercioux, V. M. Ramaglia, and V. Cataudella, "Rashba quantum wire: exact solution and ballistic transport," *Journal of Physics: Condensed Matter*, vol. 19, no. 18, p. 186227, 2007. 3, 10, 22, 54, 119

[18] V. M. Ramaglia, V. Cataudella, G. De Filippis, and C. Perroni, "Ballistic transport in one-dimensional loops with rashba and dresselhaus spin-orbit coupling," *Physical Review B*, vol. 73, no. 15, p. 155328, 2006. 3, 10, 22, 65

[19] V. Brosco and C. Grimaldi, "Anisotropy of transport in bulk rashba metals," *Physical Review B*, vol. 95, no. 19, p. 195164, 2017. 3, 10, 11, 22, 54, 62, 121

[20] G. Volovik and K. Zhang, "Lifshitz transitions, type-II dirac and weyl fermions, event horizon and all that," *Journal of Low Temperature Physics*, vol. 189, no. 5-6, pp. 276–299, 2017. 3, 14, 38, 41

[21] G. Volovik, "Topological lifshitz transitions," *Low Temperature Physics*, vol. 43, no. 1, pp. 47–55, 2017. 3, 14, 28, 38, 41

[22] G. E. Volovik, "Exotic lifshitz transitions in topological materials," *Physics-Uspekhi*, vol. 61, no. 1, p. 89, 2018. 3, 11, 14, 28, 38, 41, 54

[23] H. Kamerlingh Onnes, "The resistance of pure mercury at helium temperatures," *Commun. Phys. Lab. Univ. Leiden, b*, vol. 120, 1911. 3, 4

[24] W. Meissner and R. Ochsenfeld, "Ein neuer effekt bei eintritt der supraleitfähigkeit," *Naturwissenschaften*, vol. 21, no. 44, pp. 787–788, 1933. 3, 4

[25] F. London and H. London, "The electromagnetic equations of the supraconductor," *Proceedings of the Royal Society of London. Series A-Mathematical and Physical Sciences*, vol. 149, no. 866, pp. 71–88, 1935. 3

[26] V. M. Vinokur and T. I. Baturina, "Ginzburg-Landau equations," *100 Years of Superconduct.*, vol. 1, pp. 51–65, 2011. 3, 4

[27] J. Schrieffer and D. Ginsberg, "Calculation of the quasiparticle recombination time in a superconductor," *Physical Review Letters*, vol. 8, no. 5, p. 207, 1962. 3, 4

[28] A. Migdal, "Interaction between electrons and lattice vibrations in a normal metal," *Sov. Phys. JETP*, vol. 7, no. 6, pp. 996–1001, 1958. 3, 5, 41, 44, 89

[29] W. McMillan, "Transition temperature of strong-coupled superconductors," *Physical Review*, vol. 167, no. 2, p. 331, 1968. 3, 5, 41

[30] R. Dynes, "Mcmillan's equation and the T_C of superconductors," *Solid State Communications*, vol. 10, no. 7, pp. 615–618, 1972. 3, 5, 41

[31] G. Eliashberg, "Interactions between electrons and lattice vibrations in a superconductor," *Sov. Phys. JETP*, vol. 11, no. 3, pp. 696–702, 1960. 3, 5, 41

[32] A. Drozdov, M. Eremets, I. Troyan, V. Ksenofontov, and S. I. Shylin, "Conventional superconductivity at 203 kelvin at high pressures in the sulfur hydride system," *Nature*, vol. 525, no. 7567, pp. 73–76, 2015. 3, 7, 8, 28, 37, 38, 98, 102, 104

[33] M. Somayazulu, M. Ahart, A. K. Mishra, Z. M. Geballe, M. Baldini, Y. Meng, V. V. Struzhkin, and R. J. Hemley, "Evidence for superconductivity above 260 K in lanthanum superhydride at megabar pressures," *Phys. Rev. Lett.*, vol. 122, p. 027001, Jan 2019. 3, 7

[34] E. Snider, N. Dasenbrock-Gammon, R. McBride, M. Debessai, H. Vindana, K. Vencatasamy, K. V. Lawler, A. Salamat, and R. P. Dias, "Room-temperature superconductivity in a carbonaceous sulfur hydride," *Nature*, vol. 586, no. 7829, pp. 373–377, 2020. 3, 7, 9, 28, 37, 38

[35] b. N. Bogoliubov, V. Tolmachev, and D. Shirkov, "A new method in the theory of superconductivity I," *Soviet Physics JETP*, vol. 34, no. 7, p. 1, 1958. 3, 5, 6

[36] Y. Nambu, "Axial vector current conservation in weak interactions," *Physical Review Letters*, vol. 4, no. 7, p. 380, 1960. 3, 8

[37] J. F. Prins, "The diamond–vacuum interface: II. electron extraction from n-type diamond: evidence for superconduction at room temperature," *Semiconductor science and technology*, vol. 18, no. 3, p. S131, 2003. 3

[38] P. Tripodi, D. Di Gioacchino, R. Borelli, and J. D. Vinko, "Possibility of high temperature superconducting phases in PdH," *Physica C: Superconductivity*, vol. 388, pp. 571–572, 2003. 3

[39] P. Tripodi, D. Di Gioacchino, and J. D. Vinko, "Superconductivity in PdH: phenomenological explanation," *Physica C: Superconductivity*, vol. 408, pp. 350–352, 2004. 3

[40] P. Tripodi, D. Di Gioacchino, and J. D. Vinko, "A review of high temperature superconducting property of PdH system," *International Journal of Modern Physics B*, vol. 21, no. 18n19, pp. 3343–3347, 2007. 3

[41] T. Scheike, W. Böhlmann, P. Esquinazi, J. Barzola-Quiquia, A. Ballestar, and A. Setzer, "Can doping graphite trigger room temperature superconductivity. Evidence for granular high-temperature superconductivity in water-treated graphite powder," *Advanced Materials*, vol. 24, no. 43, pp. 5826–5831, 2012. 3

[42] R. Mankowsky, A. Subedi, M. Först, S. O. Mariager, M. Chollet, H. Lemke, J. S. Robinson, J. M. Glownia, M. P. Minitti, A. Frano, *et al.*, "Nonlinear lattice dynamics as a basis for enhanced superconductivity in $YBa_2Cu_3O_{6.5}$," *Nature*, vol. 516, no. 7529, pp. 71–73, 2014. 3

[43] E. Cartlidge, "Superconductivity record sparks wave of follow-up physics," 2015. 3

[44] Y. Ge, F. Zhang, and Y. Yao, "First-principles demonstration of superconductivity at 280 K in hydrogen sulfide with low phosphorus substitution," *Physical Review B*, vol. 93, no. 22, p. 224513, 2016. 3

[45] D. K. Thapa and A. Pandey, "Evidence for superconductivity at ambient temperature and pressure in nanostructures," *arXiv preprint arXiv:1807.08571*, 2018. 3

[46] M. Somayazulu, M. Ahart, A. K. Mishra, Z. M. Geballe, M. Baldini, Y. Meng, V. V. Struzhkin, and R. J. Hemley, "Evidence for superconductivity above 260 K in lanthanum superhydride at megabar pressures," *Physical review letters*, vol. 122, no. 2, p. 027001, 2019. 3, 41

[47] A. Drozdov, P. Kong, V. Minkov, S. Besedin, M. Kuzovnikov, S. Mozaffari, L. Balicas, F. Balakirev, D. Graf, V. Prakapenka, *et al.*, "Superconductivity at 250 K in lanthanum hydride under high pressures," *Nature*, vol. 569, no. 7757, pp. 528–531, 2019. 3, 28, 38, 40, 41, 98, 104

[48] H. Suhl, B. Matthias, and L. Walker, "Bardeen-cooper-schrieffer theory of superconductivity in the case of overlapping bands," *Physical Review Letters*, vol. 3, no. 12, p. 552, 1959. 3, 8, 107

[49] N. Ashcroft, "Hydrogen dominant metallic alloys: high temperature superconductors," *Physical Review Letters*, vol. 92, no. 18, p. 187002, 2004. 3, 8, 9, 37

[50] Y. Li, J. Hao, H. Liu, Y. Li, and Y. Ma, "The metallization and superconductivity of dense hydrogen sulfide," *The Journal of chemical physics*, vol. 140, no. 17, p. 174712, 2014. 3, 8, 37

[51] D. Duan, X. Huang, F. Tian, D. Li, H. Yu, Y. Liu, Y. Ma, B. Liu, and T. Cui, "Pressure-induced decomposition of solid hydrogen sulfide," *Physical Review B*, vol. 91, no. 18, p. 180502, 2015. 3, 8, 37, 38

[52] J. M. McMahon, M. A. Morales, C. Pierleoni, and D. M. Ceperley, "The properties of hydrogen and helium under extreme conditions," *Reviews of modern physics*, vol. 84, no. 4, p. 1607, 2012. 3, 8, 37

[53] V. Ginzburg and D. Kirzhnitz, "High temperature superconductivity. consultants bureau," *New York (English translation*, 1982. 3, 9

[54] E. Maksimov and D. Y. Savrasov, "Lattice stability and superconductivity of the metallic hydrogen at high pressure," *Solid state communications*, vol. 119, no. 10-11, pp. 569–572, 2001. 3, 9

[55] E. G. Maksimov and O. V. Dolgov, "A note on the possible mechanisms of high-temperature superconductivity," *Physics-Uspekhi*, vol. 50, no. 9, p. 933, 2007. 3, 9

[56] N. W. Ashcroft, "Metallic hydrogen: A high-temperature superconductor," *Physical Review Letters*, vol. 21, no. 26, p. 1748, 1968. 3, 9

[57] C. Richardson and N. Ashcroft, "High temperature superconductivity in metallic hydrogen: Electron-electron enhancements," *Physical review letters*, vol. 78, no. 1, p. 118, 1997. 3, 9

[58] N. Ashcroft, "Symmetry and higher superconductivity in the lower elements," in *Symmetry and Heterogeneity in High Temperature Superconductors*, pp. 3–20, Springer, 2006. 3, 9

[59] E. Babaev, A. Sudbø, and N. Ashcroft, "A superconductor to superfluid phase transition in liquid metallic hydrogen," *Nature*, vol. 431, no. 7009, pp. 666–668, 2004. 3, 9

[60] K. Abe and N. Ashcroft, "Quantum disproportionation: The high hydrides at elevated pressures," *Physical Review B*, vol. 88, no. 17, p. 174110, 2013. 3, 9

[61] A. Vittorini-Orgeas and A. Bianconi, "From Majorana theory of atomic autoionization to Feshbach resonances in high temperature superconductors," *Journal of superconductivity and novel magnetism*, vol. 22, no. 3, pp. 215–221, 2009. 3, 40

[62] A. Perali, A. Bianconi, A. Lanzara, and N. L. Saini, "The gap amplification at a shape resonance in a superlattice of quantum stripes: A mechanism for high T_C," *Solid State Communications*, vol. 100, no. 3, pp. 181–186, 1996. 3, 8, 27, 29, 38, 40

[63] A. Valletta, G. Bardelloni, M. Brunelli, A. Lanzara, A. Bianconi, and N. Saini, "T_C amplication and pseudogap at a shape resonance in a superlattice of quantum stripes," *Journal of Superconductivity*, vol. 10, no. 4, pp. 383–387, 1997. 3, 8, 27, 38

[64] A. Valletta, A. Bianconi, A. Perali, and N. Saini, "Electronic and superconducting properties of a superlattice of quantum stripes at the atomic limit," *Zeitschrift für Physik B Condensed Matter*, vol. 104, no. 4, pp. 707–713, 1997. 3, 8, 11, 27, 29, 38, 40, 44, 54

[65] A. Bianconi, "European patent N.0733271: High T_C superconductors made by metal heterostuctures at the atomic limit (priority date 7 Dec 1993), published in european patent bulletin 98/22, 27 May 1998); a. bianconi, a. valletta, a. perali, and nl saini," *Physica C*, vol. 296, p. 269, 1998. 3, 8, 27, 38

[66] A. Bianconi, "Shape resonances in multi-condensate granular superconductors formed by networks of nanoscale-striped puddles," in *Journal of Physics: Conference Series*, vol. 449, p. 012002, IOP Publishing, 2013. 3, 8, 27, 29, 38, 40

[67] C. Chin, R. Grimm, P. Julienne, and E. Tiesinga, "Feshbach resonances in ultracold gases," *Reviews of Modern Physics*, vol. 82, no. 2, p. 1225, 2010. 3, 8

[68] M. Greiner, C. A. Regal, and D. S. Jin, "Emergence of a molecular bose-Einstein condensate from a fermi gas," *Nature*, vol. 426, no. 6966, pp. 537–540, 2003. 3, 8

[69] A. Perali, P. Pieri, L. Pisani, and G. Strinati, "$BCS - BEC$ crossover at finite temperature for superfluid trapped fermi atoms," *Physical review letters*, vol. 92, no. 22, p. 220404, 2004. 3, 8, 27, 38, 94

[70] Q. Chen, J. Stajic, S. Tan, and K. Levin, "$BCS - BEC$ crossover: From high temperature superconductors to ultracold superfluids," *Physics Reports*, vol. 412, no. 1, pp. 1–88, 2005. 3, 8

[71] A. Perali, P. Pieri, and G. Strinati, "Quantitative comparison between theoretical predictions and experimental results for the $BCS-BEC$ crossover," *Physical review letters*, vol. 93, no. 10, p. 100404, 2004. 3, 8, 27, 38, 81

[72] G. Campi, A. Bianconi, N. Poccia, G. Bianconi, L. Barba, G. Arrighetti, D. Innocenti, J. Karpinski, N. D. Zhigadlo, S. M. Kazakov, *et al.*, "Inhomogeneity of charge-density-wave order and quenched disorder in a high-T_C superconductor," *Nature*, vol. 525, no. 7569, pp. 359–362, 2015. 3

[73] A. Bianconi, S. Agrestini, G. Bianconi, D. Di Castro, and N. Saini, "A quantum phase transition driven by the electron lattice interaction gives high T_C superconductivity," *Journal of alloys and compounds*, vol. 317, pp. 537–541, 2001. 3, 27, 38

[74] G. Bianconi, "Superconductor-insulator transition on annealed complex networks," *Physical Review E*, vol. 85, no. 6, p. 061113, 2012. 3, 27, 38

[75] P. Turner and L. Nottale, "The origins of macroscopic quantum coherence in high temperature superconductivity," *Physica C: Superconductivity and its Applications*, vol. 515, pp. 15–30, 2015. 3

[76] M. A. Continentino, I. T. Padilha, and H. Caldas, "Mechanism for enhancement of superconductivity in multi-band systems with odd parity hybridization," *Journal of Statistical Mechanics: Theory and Experiment*, vol. 2014, no. 7, p. P07015, 2014. 3

[77] M. V. Milošević and A. Perali, "Emergent phenomena in multicomponent superconductivity: an introduction to the focus issue," *arXiv preprint arXiv:1504.06995*, 2015. 3, 8

[78] H. Takahashi, K. Igawa, K. Arii, Y. Kamihara, M. Hirano, and H. Hosono, "Superconductivity at 43 K in an iron-based layered compound $LaO_{1-x}F_xFeAs$," *Nature*, vol. 453, no. 7193, pp. 376–378, 2008. 3

[79] A. Guidini and A. Perali, "Band-edge $BCS-BEC$ crossover in a two-band superconductor: physical properties and detection parameters," *Superconductor Science and Technology*, vol. 27, no. 12, p. 124002, 2014. 3

[80] Z. Tang, L. Zhang, N. Wang, X. Zhang, G. Wen, G. Li, J. Wang, C. T. Chan, and P. Sheng, "Superconductivity in 4 angstrom single-walled carbon nanotubes," *Science*, vol. 292, no. 5526, pp. 2462–2465, 2001. 3

[81] M. V. Mazziotti, A. Valletta, G. Campi, D. Innocenti, A. Perali, and A. Bianconi, "Possible Fano resonance for high-T_C multi-gap superconductivity in p-terphenyl doped by K at the lifshitz transition," *EPL (Europhysics Letters)*, vol. 118, no. 3, p. 37003, 2017. 3, 11, 27, 28, 29, 38, 40, 54

[82] S. N. Bose, "Plancks gesetz und lichtquantenhypothese," 1924. 3

[83] L. Landau, "Theory of the superfluidity of helium II," *Physical Review*, vol. 60, no. 4, p. 356, 1941. 3

[84] M. H. Anderson, J. R. Ensher, M. R. Matthews, C. E. Wieman, and E. A. Cornell, "Observation of bose-Einstein condensation in a dilute atomic vapor," *science*, vol. 269, no. 5221, pp. 198–201, 1995. 3

[85] T. Bourdel, L. Khaykovich, J. Cubizolles, J. Zhang, F. Chevy, M. Teichmann, L. Tarruell, S. Kokkelmans, and C. Salomon, "Experimental study of the $BCS-BEC$ crossover region in lithium 6," *Physical Review Letters*, vol. 93, no. 5, p. 050401, 2004. 3

[86] M. F. Sacchi, "Optimal discrimination of quantum operations," *Physical Review A*, vol. 71, no. 6, p. 062340, 2005. 3

[87] P. Courteille, R. Freeland, D. Heinzen, F. Van Abeelen, and B. Verhaar, "Observation of a Feshbach resonance in cold atom scattering," *Physical Review Letters*, vol. 81, no. 1, p. 69, 1998. 3

[88] M. Zwierlein, C. Stan, C. Schunck, S. Raupach, A. Kerman, and W. Ketterle, "Condensation of pairs of fermionic atoms near a Feshbach resonance," *Physical Review Letters*, vol. 92, no. 12, p. 120403, 2004. 3

[89] S. Inouye, M. Andrews, J. Stenger, H.-J. Miesner, D. Stamper-Kurn, and W. Ketterle, "Observation of Feshbach resonances in a bose–Einstein condensate," *Nature*, vol. 392, no. 6672, pp. 151–154, 1998. 3

[90] B. Marcelis, E. Van Kempen, B. Verhaar, and S. Kokkelmans, "Feshbach resonances with large background scattering length: Interplay with open-channel resonances," *Physical Review A*, vol. 70, no. 1, p. 012701, 2004. 3

[91] I. Lifshitz *et al.*, "Anomalies of electron characteristics of a metal in the high pressure region," *Sov. Phys. JETP*, vol. 11, no. 5, pp. 1130–1135, 1960. 3, 28, 72

[92] Y. A. Bychkov and E. I. Rashba, "Oscillatory effects and the magnetic susceptibility of carriers in inversion layers," *Journal of physics C: Solid state physics*, vol. 17, no. 33, p. 6039, 1984. 9, 17, 18

[93] Y. A. Bychkov and É. I. Rashba, "Properties of a $2D$ electron gas with lifted spectral degeneracy," *JETP lett*, vol. 39, no. 2, p. 78, 1984. 9, 10, 17, 18

[94] G. Seibold, S. Caprara, M. Grilli, and R. Raimondi, "Non-equilibrium spin currents in systems with striped rashba spin-orbit coupling," *Journal of Superconductivity and Novel Magnetism*, vol. 30, no. 1, pp. 123–128, 2017. 9, 10, 17

[95] A. M. Sheikhabadi, I. Miatka, E. Y. Sherman, and R. Raimondi, "Theory of the inverse spin galvanic effect in quantum wells," *Physical Review B*, vol. 97, no. 23, p. 235412, 2018. 9, 10

[96] G. Dresselhaus, "Spin-orbit coupling effects in zinc blende structures," *Physical Review*, vol. 100, no. 2, p. 580, 1955. 9, 18

[97] S. Wolf, D. Awschalom, R. Buhrman, J. Daughton, v. S. von Molnár, M. Roukes, A. Y. Chtchelkanova, and D. Treger, "Spintronics: a spin-based electronics vision for the future," *science*, vol. 294, no. 5546, pp. 1488–1495, 2001. 9

[98] I. Žutić, J. Fabian, and S. D. Sarma, "Spintronics: Fundamentals and applications," *Reviews of modern physics*, vol. 76, no. 2, p. 323, 2004. 9

[99] M. N. Baibich, J. M. Broto, A. Fert, F. N. Van Dau, F. Petroff, P. Etienne, G. Creuzet, A. Friederich, and J. Chazelas, "Giant magnetoresistance of $(001)Fe/(001)Cr$ magnetic superlattices," *Physical review letters*, vol. 61, no. 21, p. 2472, 1988. 9

[100] G. Binasch, P. Grünberg, F. Saurenbach, and W. Zinn, "Enhanced magnetoresistance in layered magnetic structures with antiferromagnetic interlayer exchange," *Physical review B*, vol. 39, no. 7, p. 4828, 1989. 9

[101] S. S. Parkin, C. Kaiser, A. Panchula, P. M. Rice, B. Hughes, M. Samant, and S.-H. Yang, "Giant tunnelling magnetoresistance at room temperature with MgO (100) tunnel barriers," *Nature materials*, vol. 3, no. 12, pp. 862–867, 2004. 9

[102] Y. Ando and M. Shiraishi, "Spin to charge interconversion phenomena in the interface and surface states," *Journal of the Physical Society of Japan*, vol. 86, no. 1, p. 011001, 2017. 9

[103] S. D. Ganichev, M. Trushin, and J. Schliemann, "Spin polarization by current," 2012. 9

[104] A. Soumyanarayanan, N. Reyren, A. Fert, and C. Panagopoulos, "Emergent phenomena induced by spin-orbit coupling at surfaces and interfaces," *Nature*, vol. 539, no. 7630, pp. 509–517, 2016. 9

[105] G. Lancaster, J. Van Wyk, and E. Schneider, "Spin-lattice relaxation of conduction electrons in silicon," *Proceedings of the Physical Society*, vol. 84, no. 1, p. 19, 1964. 9

[106] M. B. Lifshits and M. I. Dyakonov, "Swapping spin currents: Interchanging spin and flow directions," *Physical review letters*, vol. 103, no. 18, p. 186601, 2009. 9

[107] J. Nitta, T. Akazaki, H. Takayanagi, and T. Enoki, "Gate control of spin-orbit interaction in an inverted." 9

[108] S. Datta and B. Das, "Electronic analog of the electro-optic modulator," *Applied Physics Letters*, vol. 56, no. 7, pp. 665–667, 1990. 9

[109] T. Schäpers, J. Knobbe, A. van der Hart, and H. Hardtdegen, "Rashba effect in strained $InGaAs/InP$ quantum wire structures," *Science and Technology of Advanced Materials*, vol. 4, no. 1, p. 19, 2003. 9, 17

[110] M. Z. Hasan and C. L. Kane, "Colloquium: topological insulators," *Reviews of modern physics*, vol. 82, no. 4, p. 3045, 2010. 9, 10

[111] B. A. Bernevig, T. L. Hughes, and S.-C. Zhang, "Quantum spin hall effect and topological phase transition in $HgTe$ quantum wells," *science*, vol. 314, no. 5806, pp. 1757–1761, 2006. 9

[112] M. König, S. Wiedmann, C. Brüne, A. Roth, H. Buhmann, L. W. Molenkamp, X.-L. Qi, and S.-C. Zhang, "Quantum spin hall insulator state in hgte quantum wells," *Science*, vol. 318, no. 5851, pp. 766–770, 2007. 9

[113] K. C. Nowack, E. M. Spanton, M. Baenninger, M. König, J. R. Kirtley, B. Kalisky, C. Ames, P. Leubner, C. Brüne, H. Buhmann, *et al.*, "Imaging currents in $HgTe$ quantum wells in the quantum spin hall regime," *Nature materials*, vol. 12, no. 9, pp. 787–791, 2013. 9

[114] H. Zhang, C.-X. Liu, X.-L. Qi, X. Dai, Z. Fang, and S.-C. Zhang, "Topological insulators in Bi_2Se_3, Bi_2Te_3 and Sb_2Te_3 with a single dirac cone on the surface," *Nature physics*, vol. 5, no. 6, pp. 438–442, 2009. 9

[115] C. Beenakker, "Search for Majorana fermions in superconductors," *Annu. Rev. Condens. Matter Phys.*, vol. 4, no. 1, pp. 113–136, 2013. 9

[116] L. Fu and C. L. Kane, "Superconducting proximity effect and Majorana fermions at the surface of a topological insulator," *Physical review letters*, vol. 100, no. 9, p. 096407, 2008. 9

[117] P. Středa and P. Šeba, "Antisymmetric spin filtering in one-dimensional electron systems with uniform spin-orbit coupling," *Physical review letters*, vol. 90, no. 25, p. 256601, 2003. 9

[118] R. M. Lutchyn, J. D. Sau, and S. D. Sarma, "Majorana fermions and a topological phase transition in semiconductor-superconductor heterostructures," *Physical review letters*, vol. 105, no. 7, p. 077001, 2010. 9

[119] Y. Oreg, G. Refael, and F. Von Oppen, "Helical liquids and Majorana bound states in quantum wires," *Physical review letters*, vol. 105, no. 17, p. 177002, 2010. 9

[120] V. Mourik, K. Zuo, S. M. Frolov, S. Plissard, E. P. Bakkers, and L. P. Kouwenhoven, "Signatures of Majorana fermions in hybrid superconductor-semiconductor nanowire devices," *Science*, vol. 336, no. 6084, pp. 1003–1007, 2012. 9

[121] S. Nadj-Perge, I. K. Drozdov, J. Li, H. Chen, S. Jeon, J. Seo, A. H. MacDonald, B. A. Bernevig, and A. Yazdani, "Observation of Majorana fermions in ferromagnetic atomic chains on a superconductor," *Science*, vol. 346, no. 6209, pp. 602–607, 2014. 9

[122] G. Moore and N. Read, "Nonabelions in the fractional quantum hall effect," *Nuclear Physics B*, vol. 360, no. 2-3, pp. 362–396, 1991. 9

[123] C. Nayak, S. H. Simon, A. Stern, M. Freedman, and S. D. Sarma, "Non-abelian anyons and topological quantum computation," *Reviews of Modern Physics*, vol. 80, no. 3, p. 1083, 2008. 9

[124] J. Alicea, "New directions in the pursuit of Majorana fermions in solid state systems," *Reports on progress in physics*, vol. 75, no. 7, p. 076501, 2012. 9, 26

[125] M. Leijnse and K. Flensberg, "Introduction to topological superconductivity and Majorana fermions," *Semiconductor Science and Technology*, vol. 27, no. 12, p. 124003, 2012. 9

[126] S. R. Elliott and M. Franz, "Colloquium: Majorana fermions in nuclear, particle, and solid-state physics," *Reviews of Modern Physics*, vol. 87, no. 1, p. 137, 2015. 9

[127] J. Alicea, Y. Oreg, G. Refael, F. Von Oppen, and M. P. Fisher, "Non-abelian statistics and topological quantum information processing in 1D wire networks," *Nature Physics*, vol. 7, no. 5, pp. 412–417, 2011. 9, 26

[128] A. M. Sheikhabadi, R. Raimondi, and K. Shen, "The edelstein effect in the presence of impurity spin-orbit scattering," *Acta Physica Polonica, A.*, vol. 132, no. 1, 2017. 9, 10

[129] V. Dugaev, I. Tralle, A. Wal, and J. Barna, "Spin orbitronics and topological properties of nanostructures." 9, 10

[130] M. V. Mazziotti, N. Scopigno, M. Grilli, and S. Caprara, "Majorana fermions in one-dimensional structures at $LaAlO_3/SrTiO_3$ oxide interfaces," *Condensed Matter*, vol. 3, no. 4, p. 37, 2018. 10, 26

[131] E. Majorana, "Teoria simmetrica dell'elettrone e del positrone," *Il Nuovo Cimento (1924-1942)*, vol. 14, no. 4, p. 171, 1937. 10

[132] M. Smidman, M. Salamon, H. Yuan, and D. Agterberg, "Superconductivity and spin–orbit coupling in non-centrosymmetric materials: A review," *Reports on Progress in Physics*, vol. 80, no. 3, p. 036501, 2017. 10, 17, 26, 54

[133] L. P. Gor'kov and E. I. Rashba, "Superconducting $2D$ system with lifted spin degeneracy: mixed singlet-triplet state," *Physical Review Letters*, vol. 87, no. 3, p. 037004, 2001. 10, 11, 17, 22, 24, 25, 26, 54, 65, 75, 80, 120, 129

[134] G. Seibold, S. Caprara, M. Grilli, and R. Raimondi, "Theory of the spin galvanic effect at oxide interfaces," *Physical review letters*, vol. 119, no. 25, p. 256801, 2017. 10

[135] G. Vignale and I. Tokatly, "Theory of the nonlinear rashba-edelstein effect: The clean electron gas limit," *Physical Review B*, vol. 93, no. 3, p. 035310, 2016. 10

[136] E. I. Rashba, "Properties of semiconductors with an extremum loop. I. cyclotron and combinational resonance in a magnetic field perpendicular to the plane of the loop," *Soviet Physics, Solid State*, vol. 2, pp. 1109–1122, 1960. 10

[137] V. M. Ramaglia, D. Bercioux, V. Cataudella, G. De Filippis, C. Perroni, and F. Ventriglia, "Conductance of a large point contact with rashba effect," *The European Physical Journal B-Condensed Matter and Complex Systems*, vol. 36, no. 3, pp. 365–375, 2003. 10, 65

[138] J. Zhang, H. Hu, X.-J. Liu, and H. Pu, "Fermi gases with synthetic spin-orbit coupling," in *Annual Review of Cold Atoms and Molecules*, pp. 81–143, World Scientific, 2014. 10

[139] S. Caprara, F. Peronaci, and M. Grilli, "Intrinsic instability of electronic interfaces with strong rashba coupling," *Physical Review Letters*, vol. 109, no. 19, p. 196401, 2012. 10

[140] D. Bucheli, M. Grilli, F. Peronaci, G. Seibold, and S. Caprara, "Phase diagrams of voltage-gated oxide interfaces with strong rashba coupling," *Physical Review B*, vol. 89, no. 19, p. 195448, 2014. 10

[141] S. Caprara, D. Bucheli, M. Grilli, J. Biscaras, N. Bergeal, S. Hurand, C. Feuillet-Palma, J. Lesueur, A. Rastogi, and R. Budhani, "Inhomogeneous electron gas at oxide interfaces with strong rashba spin–orbit coupling," in *Spin*, vol. 4, p. 1440004, World Scientific, 2014. 10

[142] C. R. Ast, J. Henk, A. Ernst, L. Moreschini, M. C. Falub, D. Pacilé, P. Bruno, K. Kern, and M. Grioni, "Giant spin splitting through surface alloying," *Physical Review Letters*, vol. 98, no. 18, p. 186807, 2007. 10

[143] M. Sakano, J. Miyawaki, A. Chainani, Y. Takata, T. Sonobe, T. Shimojima, M. Oura, S. Shin, M. Bahramy, R. Arita, *et al.*, "Three-dimensional bulk band

dispersion in polar $BiTeI$ with giant rashba-type spin splitting," *Physical Review B*, vol. 86, no. 8, p. 085204, 2012. 10

[144] K. Ishizaka, M. Bahramy, H. Murakawa, M. Sakano, T. Shimojima, T. Sonobe, K. Koizumi, S. Shin, H. Miyahara, A. Kimura, *et al.*, "Giant rashba-type spin splitting in bulk $BiTeI$," *Nature materials*, vol. 10, no. 7, pp. 521–526, 2011. 10

[145] M. Liebmann, C. Rinaldi, D. Di Sante, J. Kellner, C. Pauly, R. N. Wang, J. E. Boschker, A. Giussani, S. Bertoli, M. Cantoni, *et al.*, "Giant rashba-type spin splitting in ferroelectric $GeTe$ (111)," *Advanced Materials*, vol. 28, no. 3, pp. 560–565, 2016. 10

[146] Y. Feng, Q. Jiang, B. Feng, M. Yang, T. Xu, W. Liu, X. Yang, M. Arita, E. F. Schwier, K. Shimada, *et al.*, "Rashba-like spin splitting along three momentum directions in trigonal layered $PtBi_2$," *Nature communications*, vol. 10, no. 1, pp. 1–8, 2019. 10

[147] A. Chaplik and L. Magarill, "Bound states in a two-dimensional short range potential induced by the spin-orbit interaction," *Physical review letters*, vol. 96, no. 12, p. 126402, 2006. 10, 54

[148] E. Cappelluti, C. Grimaldi, and F. Marsiglio, "Topological change of the fermi surface in low-density rashba gases: application to superconductivity," *Physical review letters*, vol. 98, no. 16, p. 167002, 2007. 10, 54, 119

[149] J. P. Vyasanakere and V. B. Shenoy, "Bound states of two spin-$\frac{1}{2}$ fermions in a synthetic non-abelian gauge field," *Physical Review B*, vol. 83, no. 9, p. 094515, 2011. 10, 54, 107

[150] S. Takei, C.-H. Lin, B. M. Anderson, and V. Galitski, "Low-density molecular gas of tightly bound rashba-dresselhaus fermions," *Physical Review A*, vol. 85, no. 2, p. 023626, 2012. 10, 54

[151] G. Goldstein, C. Aron, and C. Chamon, "Band-edge superconductivity," *Physical Review B*, vol. 92, no. 2, p. 020504, 2015. 10, 54

[152] J. Hutchinson, J. Hirsch, and F. Marsiglio, "Enhancement of superconducting T_C due to the spin-orbit interaction," *Physical Review B*, vol. 97, no. 18, p. 184513, 2018. 10, 54

[153] H. Allami, O. Starykh, and D. Pesin, "Superfluid-insulator transition and the $BCS - BEC$ crossover in the rashba moat band," *Physical Review B*, vol. 99, no. 10, p. 104505, 2019. 10, 54

[154] D. Stornaiuolo, D. Massarotti, R. Di Capua, P. Lucignano, G. Pepe, M. Salluzzo, and F. Tafuri, "Signatures of unconventional superconductivity in the $LaAlO_3/SrTiO_3$ two-dimensional system," *Physical Review B*, vol. 95, no. 14, p. 140502, 2017. 10

[155] D. Massarotti, A. Miano, F. Tafuri, and D. Stornaiuolo, "High efficiency superconducting field effect devices for oxide electronic applications," *Superconductor Science and Technology*, vol. 33, no. 3, p. 034007, 2020. 10

[156] P. Rout, E. Maniv, and Y. Dagan, "Link between the superconducting dome and spin-orbit interaction in the (111) $LaAlO_3/SrTiO_3$ interface," *Physical Review Letters*, vol. 119, no. 23, p. 237002, 2017. 10

[157] A. Ptok, K. Rodríguez, and K. J. Kapcia, "Superconducting monolayer deposited on substrate: Effects of the spin-orbit coupling induced by proximity effects," *Physical Review Materials*, vol. 2, no. 2, p. 024801, 2018. 10

[158] C. Liu, X. Yan, D. Jin, Y. Ma, H.-W. Hsiao, Y. Lin, T. M. Bretz-Sullivan, X. Zhou, J. Pearson, B. Fisher, *et al.*, "Discovery of two-dimensional anisotropic superconductivity at $KTaO_3$ (111) interfaces," *arXiv preprint arXiv:2004.07416*, 2020. 10

[159] R. Mori, P. B. Marshall, K. Ahadi, J. D. Denlinger, S. Stemmer, and A. Lanzara, "Controlling a van hove singularity and fermi surface topology at a complex oxide heterostructure interface," *Nature communications*, vol. 10, no. 1, pp. 1–7, 2019. 10

[160] K. Gotlieb, C.-Y. Lin, M. Serbyn, W. Zhang, C. L. Smallwood, C. Jozwiak, H. Eisaki, Z. Hussain, A. Vishwanath, and A. Lanzara, "Revealing hidden spin-momentum locking in a high-temperature cuprate superconductor," *Science*, vol. 362, no. 6420, pp. 1271–1275, 2018. 10

[161] D. Stornaiuolo and F. Tafuri, "High critical temperature superconductor josephson junctions and other exotic structures," in *Fundamentals and Frontiers of the Josephson Effect*, pp. 275–337, Springer, 2019. 10

[162] R. Caruso, H. G. Ahmad, A. Pal, G. P. Pepe, D. Massarotti, M. G. Blamire, and F. Tafuri, "Low temperature characterization of high efficiency spin-filter josephson junctions," in *EPJ Web of Conferences*, vol. 233, p. 05007, EDP Sciences, 2020. 10

[163] A. Bianconi, A. Valletta, A. Perali, and N. L. Saini, "Superconductivity of a striped phase at the atomic limit," *Physica C: Superconductivity*, vol. 296, no. 3-4, pp. 269–280, 1998. 11, 27, 29, 38, 40, 42, 54

[164] A. Bianconi, "Feshbach shape resonance in multiband superconductivity in heterostructures," *Journal of Superconductivity*, vol. 18, no. 5-6, pp. 625–636, 2005. 11, 27, 29, 38, 40, 54, 107

[165] D. Innocenti, N. Poccia, A. Ricci, A. Valletta, S. Caprara, A. Perali, and A. Bianconi, "Resonant and crossover phenomena in a multiband superconductor: Tuning the chemical potential near a band edge," *Physical Review B*, vol. 82, no. 18, p. 184528, 2010. 11, 27, 29, 38, 40, 44, 54, 73, 74, 85, 107

[166] A. Shanenko, M. D. Croitoru, A. Vagov, V. M. Axt, A. Perali, and F. Peeters, "Atypical $BCS-BEC$ crossover induced by quantum-size effects," *Physical Review A*, vol. 86, no. 3, p. 033612, 2012. 11, 54

[167] A. Bianconi, D. Innocenti, A. Valletta, and A. Perali, "Shape resonances in superconducting gaps in a $2DEG$ at oxide-oxide interface," in *Journal of Physics: Conference Series*, vol. 529, p. 012007, IOP Publishing, 2014. 11, 27, 38, 54, 107

[168] T. Jarlborg and A. Bianconi, "Breakdown of the migdal approximation at lifshitz transitions with giant zero-point motion in the H_3S superconductor," *Scientific reports*, vol. 6, p. 24816, 2016. 11, 14, 38, 40, 49, 54, 102

[169] M. Cariglia, A. Vargas-Paredes, M. M. Doria, A. Bianconi, M. V. Milošević, and A. Perali, "Shape-resonant superconductivity in nanofilms: from weak to strong coupling," *Journal of Superconductivity and Novel Magnetism*, vol. 29, no. 12, pp. 3081–3086, 2016. 11, 40, 54

[170] D. Innocenti, S. Caprara, N. Poccia, A. Ricci, A. Valletta, and A. Bianconi, "Shape resonance for the anisotropic superconducting gaps near a lifshitz transition: the effect of electron hopping between layers," *Superconductor Science and Technology*, vol. 24, no. 1, p. 015012, 2010. 11, 12, 27, 29, 38, 40, 54, 73, 85

[171] A. Perali, D. Innocenti, A. Valletta, and A. Bianconi, "Anomalous isotope effect near a 2.5 lifshitz transition in a multi-band multi-condensate superconductor made of a superlattice of stripes," *Superconductor Science and Technology*, vol. 25, no. 12, p. 124002, 2012. 11, 12, 27, 29, 38, 40, 83

[172] A. Bianconi, A. Valletta, A. Perali, and N. Saini, "High T_C superconductivity in a superlattice of quantum stripes," *Solid State Communications*, vol. 102, no. 5, pp. 369–374, 1997. 11, 12, 27, 29, 38, 40

[173] R. Caivano, M. Fratini, N. Poccia, A. Ricci, A. Puri, Z.-A. Ren, X.-L. Dong, J. Yang, W. Lu, Z.-X. Zhao, *et al.*, "Feshbach resonance and mesoscopic phase separation near a quantum critical point in multiband $FeAs$-based superconductors," *Superconductor Science and Technology*, vol. 22, no. 1, p. 014004, 2008. 11, 12

[174] C. Di Castro and R. Raimondi, *Statistical mechanics and applications in condensed matter*. Cambridge University Press, 2015. 11

[175] A. Bianconi, D. Di Castro, S. Agrestini, G. Campi, N. Saini, A. Saccone, S. De Negri, and M. Giovannini, "A superconductor made by a metal heterostructure at the atomic limit tuned at theshape resonance': MgB_2," *Journal of Physics: Condensed Matter*, vol. 13, no. 33, p. 7383, 2001. 12, 27, 29, 38, 40

[176] D. R. Harshman and A. T. Fiory, "On the isotope effect in compressed superconducting H_3S and D_3S," *Superconductor Science and Technology*, vol. 30, no. 4, p. 045011, 2017. 14, 38, 40

[177] R. Szczesniak and A. Durajski, "The isotope effect in H_3S superconductor," *Solid State Communications*, vol. 249, pp. 30–33, 2017. 14, 38, 40

[178] R. Szczesniak and A. P. Durajski, "Unusual sulfur isotope effect and extremely high critical temperature in H_3S superconductor," *Scientific reports*, vol. 8, no. 1, pp. 1–9, 2018. 14, 40

[179] Y. A. Bychkov and V. M. E. Rashba, "Effect of spin-orbit coupling on the energy spectrum of a $2D$ electron system in a tilted magnetic field," *Zh. Eksp. Teor. Fiz*, vol. 98, p. 726, 1990. 17, 18

[180] R. S. Calsaverini, E. Bernardes, J. C. Egues, and D. Loss, "Intersubband-induced spin-orbit interaction in quantum wells," *Physical Review B*, vol. 78, no. 15, p. 155313, 2008. 17

[181] R. Winkler, "Spin-orbit coupling effects in two-dimensional electron and hole systems," *Springer Tracts in Modern Physics*, vol. 191, pp. 1–8, 2003. 18

[182] T. Matsubara and J. M. Blatt, "Bose-Einstein condensation of correlated pairs," *Progress of Theoretical Physics*, vol. 23, no. 3, pp. 451–474, 1960. 27

[183] J. M. Blatt and C. J. Thompson, "Shape resonances in superconducting thin films," *Physical Review Letters*, vol. 10, no. 8, p. 332, 1963. 27

[184] N. Pinto, S. J. Rezvani, A. Perali, L. Flammia, M. V. Milošević, M. Fretto, C. Cassiago, and N. De Leo, "Dimensional crossover and incipient quantum size effects in superconducting niobium nanofilms," *Scientific reports*, vol. 8, no. 1, pp. 1–12, 2018. 27

[185] A. Bianconi, N. Saini, S. Agrestini, D. D. Castro, and G. Bianconi, "The strain quantum critical point for superstripes in the phase diagram of all cuprate perovskites," *International Journal of Modern Physics B*, vol. 14, no. 29n31, pp. 3342–3355, 2000. 27, 29, 38, 40

[186] A. Bianconi, "Ugo Fano and shape resonances," in *AIP Conference Proceedings*, vol. 652, pp. 13–18, American Institute of Physics, 2003. 27, 29, 38, 40

[187] A. Bianconi, "Feshbach shape resonance in multiband superconductivity in heterostructures," *Journal of Superconductivity*, vol. 18, no. 5-6, pp. 625–636, 2005. 27, 29, 38, 40

[188] A. Bianconi and T. Jarlborg, "Superconductivity above the lowest *Earth* temperature in pressurized sulfur hydride," *EPL (Europhysics Letters)*, vol. 112, no. 3, p. 37001, 2015. 27, 29, 38, 42

[189] A. Bianconi, "Superconductivity in quantum complex matter: the superstripes landscape," *Journal of Superconductivity and Novel Magnetism*, vol. 33, no. 8, pp. 2269–2277, 2020. 27, 29, 38, 41

[190] D. Innocenti and A. Bianconi, "Isotope effect at the Fano resonance in superconducting gaps for multiband superconductors at a 2.5 lifshitz transition," *Journal of superconductivity and novel magnetism*, vol. 26, no. 4, pp. 1319–1324, 2013. 27, 38, 40

[191] A. Perali, A. Valletta, G. Bardeiloni, A. Bianconi, A. Lanzara, and N. Saint, "The isotope effect in a superlattice of quantum stripes," *Journal of Superconductivity*, vol. 10, no. 4, pp. 355–359, 1997. 27, 29, 38, 40, 44, 83

[192] L. Salasnich, A. Shanenko, A. Vagov, J. A. Aguiar, and A. Perali, "Screening of pair fluctuations in superconductors with coupled shallow and deep bands: A route to higher-temperature superconductivity," *Physical Review B*, vol. 100, no. 6, p. 064510, 2019. 29, 40, 106, 107

[193] T. Saraiva, P. Cavalcanti, A. Vagov, A. Vasenko, A. Perali, L. Dell'Anna, and A. Shanenko, "Multiband material with a quasi-1D band as a robust high-temperature superconductor," *Physical Review Letters*, vol. 125, no. 21, p. 217003, 2020. 29, 106, 107

[194] D. Li, Y. Liu, F.-B. Tian, S.-L. Wei, Z. Liu, D.-F. Duan, B.-B. Liu, and T. Cui, "Pressure-induced superconducting ternary hydride H_3SXe: A theoretical investigation," *Frontiers of Physics*, vol. 13, no. 5, p. 137107, 2018. 37

[195] J. G. Bednorz and K. A. Müller, "Perovskite-type oxides—the new approach to high-T_C superconductivity," *Reviews of Modern Physics*, vol. 60, no. 3, p. 585, 1988. 37

[196] L. Gao, Y. Xue, F. Chen, Q. Xiong, R. Meng, D. Ramirez, C. Chu, J. Eggert, and H. Mao, "Superconductivity up to 164 K in $HgBa_2Ca_{m-1}Cu_mO_{2m+2+\delta}$ (m = 1, 2, *and* 3) under quasihydrostatic pressures," *Physical Review B*, vol. 50, no. 6, p. 4260, 1994. 37

[197] M. Kostrzewa, K. Szczęśniak, A. Durajski, and R. Szczęśniak, "From LaH_10 to room–temperature superconductors," *Scientific Reports*, vol. 10, no. 1, pp. 1–8, 2020. 37

[198] T. X. Souza and F. Marsiglio, "The possible role of van hove singularities in the high T_C of superconducting H_3S," *International Journal of Modern Physics B*, vol. 31, no. 25, p. 1745003, 2017. 38, 40

[199] A. F. Goncharov, S. S. Lobanov, V. B. Prakapenka, and E. Greenberg, "Stable high-pressure phases in the HS system determined by chemically reacting hydrogen and sulfur," *Physical Review B*, vol. 95, no. 14, p. 140101, 2017. 38

[200] D. Duan, Y. Liu, Y. Ma, Z. Shao, B. Liu, and T. Cui, "Structure and superconductivity of hydrides at high pressures," *National Science Review*, vol. 4, no. 1, pp. 121–135, 2017. 38

[201] I. Kruglov, R. Akashi, S. Yoshikawa, A. R. Oganov, and M. M. D. Esfahani, "Refined phase diagram of the HS system with high-T_C superconductivity," *Physical Review B*, vol. 96, no. 22, p. 220101, 2017. 38

[202] D. Duan, Y. Liu, F. Tian, D. Li, X. Huang, Z. Zhao, H. Yu, B. Liu, W. Tian, and T. Cui, "Pressure-induced metallization of dense $(H_2S)_2H_2$ with high-T_C superconductivity," *Scientific reports*, vol. 4, p. 6968, 2014. 38

[203] M. Einaga, M. Sakata, T. Ishikawa, K. Shimizu, M. I. Eremets, A. P. Drozdov, I. A. Troyan, N. Hirao, and Y. Ohishi, "Crystal structure of the superconducting phase of sulfur hydride," *Nature physics*, vol. 12, no. 9, pp. 835–838, 2016. 38, 102, 104

[204] Y. Quan and W. E. Pickett, "Van hove singularities and spectral smearing in high-temperature superconducting H_3S," *Physical Review B*, vol. 93, no. 10, p. 104526, 2016. 38, 40

[205] B. Guigue, A. Marizy, and P. Loubeyre, "Direct synthesis of pure H_3S from S and H elements: No evidence of the cubic superconducting phase up to 160 GPa," *Physical Review B*, vol. 95, no. 2, p. 020104, 2017. 38

[206] Y. Chen, A. Shanenko, A. Perali, and F. Peeters, "Superconducting nanofilms: molecule-like pairing induced by quantum confinement," *Journal of Physics: Condensed Matter*, vol. 24, no. 18, p. 185701, 2012. 40

[207] A. Vargas-Paredes, A. Shanenko, A. Vagov, M. Milošević, and A. Perali, "Cross-band versus intraband pairing in superconductors: Signatures and consequences of the interplay," *Physical Review B*, vol. 101, no. 9, p. 094516, 2020. 40

[208] M. M. Doria, M. Cariglia, and A. Perali, "Multigap superconductivity and barrier-driven resonances in superconducting nanofilms with an inner potential barrier," *Physical Review B*, vol. 94, no. 22, p. 224513, 2016. 40

[209] A. Guidini, L. Flammia, M. V. Milošević, and A. Perali, "$BCS-BEC$ crossover in quantum confined superconductors," *Journal of Superconductivity and Novel Magnetism*, vol. 29, no. 3, pp. 711–715, 2016. 40

[210] D. Valentinis, D. Van Der Marel, and C. Berthod, "BCS superconductivity near the band edge: Exact results for one and several bands," *Physical Review B*, vol. 94, no. 2, p. 024511, 2016. 40

[211] A. V. Chubukov and D. Mozyrsky, "Evolution of the dynamics of neutral superconductors between BCS and BEC regimes: The variational approach," *Low Temperature Physics*, vol. 44, no. 6, pp. 528–533, 2018. 40

[212] P. A. Tajima, H. and P. Pieri, "$BCS-BEC$ crossover and pairing fluctuations in a two band superfluid/superconductor: At matrix approach," *Condensed Matter*, vol. 5(1), no. 10. 40

[213] K. J. S. A. W. M. H. B. A. Bussmann-Holder, A. and A. Perali, "The road map toward room-temperature superconductivity: Manipulating different pairing channels in systems composed of multiple electronic components," *Condensed Matter*, vol. 2(3), no. 24. 40

[214] . B. A. Kagan, M. Y., "Fermi-bose mixtures and $BCS-BEC$ crossover in high-T_C superconductors," *Condensed Matter*, vol. 4(2), no. 51. 40

[215] E. Bauer, C. Paul, S. Berger, S. Majumdar, H. Michor, M. Giovannini, A. Saccone, and A. Bianconi, "Thermal conductivity of superconducting MgB_2," *Journal of Physics: Condensed Matter*, vol. 13, no. 22, p. L487, 2001. 40

[216] A. Bussmann-Holder, J. Köhler, M.-H. Whangbo, A. Bianconi, and A. Simon, "High temperature superconductivity in sulfur hydride under ultrahigh pressure: A complex superconducting phase beyond conventional BCS," *Novel Superconducting Materials*, vol. 1, no. open-issue, 2016. 40

[217] A. Bussmann-Holder, H. Keller, A. Simon, and A. Bianconi, "Multi-band superconductivity and the steep band/flat band scenario," *Condensed Matter*, vol. 4, no. 4, p. 91, 2019. 40

[218] S. Agrestini, N. Saini, G. Bianconi, and A. Bianconi, "The strain of CuO_2 lattice: the second variable for the phase diagram of cuprate perovskites," *Journal of Physics A: Mathematical and General*, vol. 36, no. 35, p. 9133, 2003. 40

[219] D. Di Castro, G. Bianconi, M. Colapietro, A. Pifferi, N. Saini, S. Agrestini, and A. Bianconi, "Evidence for the strain critical point in high T_C superconductors," *The European Physical Journal B-Condensed Matter and Complex Systems*, vol. 18, no. 4, pp. 617–624, 2000. 40

[220] I. Makarov, V. Gavrichkov, E. Shneyder, I. Nekrasov, A. Slobodchikov, S. Ovchinnikov, and A. Bianconi, "Effect of CuO_2 lattice strain on the electronic structure and properties of high-T_C cuprate family," *Journal of Superconductivity and Novel Magnetism*, vol. 32, no. 7, pp. 1927–1935, 2019. 40

[221] S. Agrestini, D. Di Castro, M. Sansone, N. Saini, A. Saccone, S. De Negri, M. Giovannini, M. Colapietro, and A. Bianconi, "High T_C superconductivity in a critical range of micro-strain and charge density in diborides," *Journal of Physics: Condensed Matter*, vol. 13, no. 50, p. 11689, 2001. 40

[222] D. Di Castro, S. Agrestini, G. Campi, A. Cassetta, M. Colapietro, A. Congeduti, A. Continenza, S. De Negri, M. Giovannini, S. Massidda, *et al.*, "The amplification of the superconducting T_C by combined effect of tuning of the fermi level and the tensile micro-strain in $Al_{1-x}Mg_xB_2$," *EPL (Europhysics Letters)*, vol. 58, no. 2, p. 278, 2002. 40

[223] S. Agrestini, C. Metallo, M. Filippi, L. Simonelli, G. Campi, C. Sanipoli, E. Liarokapis, S. De Negri, M. Giovannini, A. Saccone, *et al.*, "Substitution of sc for Mg in MgB_2: Effects on transition temperature and kohn anomaly," *Physical Review B*, vol. 70, no. 13, p. 134514, 2004. 40

[224] M. Fratini, R. Caivano, A. Puri, A. Ricci, Z.-A. Ren, X.-L. Dong, J. Yang, W. Lu, Z.-X. Zhao, L. Barba, *et al.*, "The effect of internal pressure on the tetragonal to monoclinic structural phase transition in $ReOFeAs$: the case of $NdOFeAs$," *Superconductor Science and Technology*, vol. 21, no. 9, p. 092002, 2008. 40

[225] A. Ricci, N. Poccia, G. Ciasca, M. Fratini, and A. Bianconi, "The microstrain-doping phase diagram of the iron pnictides: heterostructures at atomic limit," *Journal of superconductivity and novel magnetism*, vol. 22, no. 6, pp. 589–593, 2009. 40

[226] L. Simonelli, V. Palmisano, M. Fratini, M. Filippi, P. Parisiades, D. Lampakis, E. Liarokapis, and A. Bianconi, "Isotope effect on the E_{2g} phonon and mesoscopic phase separation near the electronic topological transition in $Mg_{1-x}Al_xB_2$," *Physical Review B*, vol. 80, no. 1, p. 014520, 2009. 40

[227] L. P. Gorkov and V. Z. Kresin, "Pressure and high-T_C superconductivity in sulfur hydrides," *Scientific reports*, vol. 6, no. 1, pp. 1–7, 2016. 41

[228] L. P. Gorkov and V. Z. Kresin, "Colloquium: High pressure and road to room temperature superconductivity," *Reviews of Modern Physics*, vol. 90, no. 1, p. 011001, 2018. 41

[229] L. P. Gorkov and V. Z. Kresin, "Sulfur hydrides: Phase diagram and the transition into the record-high T_C state," *Journal of Superconductivity and Novel Magnetism*, vol. 31, no. 1, pp. 1–5, 2018. 41

[230] V. Z. Kresin, "High-T_C hydrides: interplay of optical and acoustic modes and comments regarding the upper limit of T_C," *Journal of Superconductivity and Novel Magnetism*, vol. 31, no. 11, pp. 3391–3395, 2018. 41

[231] H. Aoki, "Theoretical possibilities for flat band superconductivity," *Journal of Superconductivity and Novel Magnetism*, pp. 1–6, 2020. 41

[232] H. Song, D. Duan, T. Cui, and V. Z. Kresin, "High-T_C state of lanthanum hydrides," *Physical Review B*, vol. 102, no. 1, p. 014510, 2020. 41

[233] I. A. Kruglov, D. V. Semenok, H. Song, R. Szczęśniak, I. A. Wrona, R. Akashi, M. M. D. Esfahani, D. Duan, T. Cui, A. G. Kvashnin, *et al.*, "Superconductivity of LaH_10 and LaH_16 polyhydrides," *Physical Review B*, vol. 101, no. 2, p. 024508, 2020. 41

[234] V. Z. Kresin and Y. N. Ovchinnikov, "Pair correlation in nano systems," *Annals of Physics*, p. 168141, 2020. 41

[235] M. Y. Kagan, "Unconventional superconductivity in low density electron systems and conventional superconductivity in hydrogen metallic alloys," *JETP letters*, vol. 103, no. 11, pp. 728–738, 2016. 41

[236] E. Talantsev, "Classifying superconductivity in compressed H_3S," *Modern Physics Letters B*, vol. 33, no. 17, p. 1950195, 2019. 41

[237] A. P. Durajski, "Quantitative analysis of nonadiabatic effects in dense H_3S and PH_3 superconductors," *Scientific reports*, vol. 6, p. 38570, 2016. 41

[238] A. P. Durajski and R. Szczęśniak, "First-principles study of superconducting hydrogen sulfide at pressure up to 500 GPa," *Scientific Reports*, vol. 7, no. 1, pp. 1–8, 2017. 41

[239] R. Akashi, W. Sano, R. Arita, and S. Tsuneyuki, "Possible "magnéli" phases and self-alloying in the superconducting sulfur hydride," *Physical review letters*, vol. 117, no. 7, p. 075503, 2016. 41

[240] A. Majumdar, S. T. John, and Y. Yao, "Mechanism for the structural transformation to the modulated superconducting phase of compressed hydrogen sulfide," *Scientific reports*, vol. 9, no. 1, pp. 1–10, 2019. 41

[241] L. Wu, J. Yang, S. Wang, P. Wei, J. Yang, W. Zhang, and L. Chen, "Two-dimensional thermoelectrics with rashba spin-split bands in bulk $BiTeI$," *Physical Review B*, vol. 90, no. 19, p. 195210, 2014. 54

[242] C. Li, C. Wang, B. Wan, X. Wan, H.-Z. Lu, and X. Xie, "Rules for phase shifts of quantum oscillations in topological nodal-line semimetals," *Physical review letters*, vol. 120, no. 14, p. 146602, 2018. 54

[243] Y. Uemura, "Bose-Einstein to BCS crossover picture for high-T_C cuprates," *Physica C: Superconductivity*, vol. 282, pp. 194–197, 1997. 81, 94

[244] N. Andrenacci, A. Perali, P. Pieri, and G. Strinati, "Density-induced BCS to bose-Einstein crossover," *Physical Review B*, vol. 60, no. 17, p. 12410, 1999. 81, 94

[245] F. Pistolesi and G. C. Strinati, "Evolution from BCS superconductivity to bose condensation: role of the parameter$k_F\xi$," *Physical Review B*, vol. 49, no. 9, p. 6356, 1994. 81, 94

[246] A. Bussmann-Holder and A. Bianconi, "Raising the diboride superconductor transition temperature using quantum interference effects," *Phys. Rev. B*, vol. 67, p. 132509, Apr 2003. 83

[247] Y. Bang and H.-Y. Choi, "Possible pairing states of the Fe-based superconductors," *Phys. Rev. B*, vol. 78, p. 134523, Oct 2008. 83

[248] O. V. Dolgov, I. I. Mazin, D. Parker, and A. A. Golubov, "Interband superconductivity: Contrasts between bardeen-cooper-schrieffer and eliashberg theories," *Phys. Rev. B*, vol. 79, p. 060502, Feb 2009. 83

[249] L. Savary, J. Ruhman, J. W. F. Venderbos, L. Fu, and P. A. Lee, "Superconductivity in three-dimensional spin-orbit coupled semimetals," *Phys. Rev. B*, vol. 96, p. 214514, Dec 2017. 105

[250] P. M. R. Brydon, L. Wang, M. Weinert, and D. F. Agterberg, "Pairing of $j = 3/2$ fermions in half-heusler superconductors," *Phys. Rev. Lett.*, vol. 116, p. 177001, Apr 2016. 105

[251] N. Orlova, A. Shanenko, M. Milošević, F. Peeters, A. Vagov, and V. M. Axt, "Ginzburg-Landau theory for multiband superconductors: microscopic derivation," *Physical Review B*, vol. 87, no. 13, p. 134510, 2013. 107

[252] L. He and X.-G. Huang, "Superfluidity and collective modes in rashba $spin-orbit$ coupled fermi gases," *Annals of Physics*, vol. 337, pp. 163–207, 2013. 107

[253] F. N. Krohg and A. Sudbø, "Derivation of a Ginzburg-Landau free energy density containing mixed gradient terms of a $p + ip$ superconductor with spin-orbit coupling," *arXiv preprint arXiv:1804.01808*, 2018. 107

[254] V. Kozii, *Exotic superconductivity in quantum materials*. PhD thesis, Massachusetts Institute of Technology, 2019. 107

[255] P. D. Powell, G. Baym, and C. de Melo, "Superfluid transition temperature of spin-orbit and rabi coupled fermions with tunable interactions," *arXiv preprint arXiv:1709.07042*, 2017. 107, 108

[256] S. P. Mukherjee and S. S. Mandal, "Ginzburg-Landau theory of noncentrosymmetric superconductors," *Physical Review B*, vol. 77, no. 1, p. 014513, 2008. 107

[257] L. Dell'Anna, G. Mazzarella, and L. Salasnich, "Condensate fraction of a resonant fermi gas with $spin-orbit$ coupling in three and two dimensions," *Physical Review A*, vol. 84, no. 3, p. 033633, 2011. 107

[258] V. Moskalenko, "Superconductivity in metals with overlapping energy bands," *Fiz. Metal. Metalloved*, vol. 8, no. 503513, pp. 2518–2520, 1959. 107

[259] Z. Zheng, H. Pu, X. Zou, and G. Guo, "Thermodynamic properties of rashba spin-orbit-coupled fermi gas," *Physical Review A*, vol. 90, no. 6, p. 063623, 2014. 107

[260] L. Jiang, X.-J. Liu, H. Hu, and H. Pu, "Rashba spin-orbit-coupled atomic fermi gases," *Physical Review A*, vol. 84, no. 6, p. 063618, 2011. 107

[261] L. Han and C. S. de Melo, "Evolution from BCS to BEC superfluidity in the presence of spin-orbit coupling," *Physical Review A*, vol. 85, no. 1, p. 011606, 2012. 107, 108

[262] L. He, H. Lü, G. Cao, H. Hu, and X.-J. Liu, "Quantum fluctuations in the $BCS-BEC$ crossover of two-dimensional fermi gases," *Physical Review A*, vol. 92, no. 2, p. 023620, 2015. 107

[263] J. P. Devreese, J. Tempere, and C. A. S. de Melo, "Quantum phase transitions and berezinskii-kosterlitz-thouless temperature in a two-dimensional spin-orbit-coupled fermi gas," *Physical Review A*, vol. 92, no. 4, p. 043618, 2015. 107, 108

[264] Z.-Q. Yu and H. Zhai, "Spin-orbit coupled fermi gases across a Feshbach resonance," *Physical review letters*, vol. 107, no. 19, p. 195305, 2011. 107